NAVAL POSTGRADUATE SCHOOL
Monterey, California

DISSERTATION

AN INTERPRETATION OF
EXTRATROPICAL CYCLOGENESIS
USING ADJOINT METHODS

by

Rolf H. Langland

June 1996

Dissertation Advisor: R. L. Elsberry

Approved for public release, distribution is unlimited.

19960910 133

REPORT DOCUMENTATION PAGE

1. AGENCY USE ONLY *(Leave blank)*	2. REPORT DATE	3. REPORT TYPE AND DATES COVERED
	June 1996	Doctoral Dissertation

4. TITLE AND SUBTITLE

AN INTERPRETATION OF EXTRATROPICAL CYCLOGENESIS
USING ADJOINT METHODS

5. FUNDING NUMBERS

6. AUTHOR(S)

Langland, Rolf Harold

7. PERFORMING ORGANIZATION NAME(S) AND ADDRESS(ES)

Naval Research Laboratory
Marine Meteorology Division
7 Grace Hopper Avenue
Monterey, CA 93943-5502

8. PERFORMING ORGANIZATION REPORT NUMBER

9. SPONSORING/MONITORING AGENCY NAME(S) AND ADDRESS(ES)

10. SPONSORING/MONITORING AGENCY REPORT NUMBER

11. SUPPLEMENTARY NOTES

The views expressed in this thesis are those of the author and do not reflect the official policy or position of the Department of Defense or the United States Government.

12a. DISTRIBUTION/AVAILABILITY STATEMENT

Approved for public release; distribution unlimited.

12b. DISTRIBUTION CODE

13. ABSTRACT *(Maximum 200 words)*

Adjoint methods are used to examine the development of idealized and real extratropical cyclones. This research represents the first use of adjoint sensitivity that includes moist physical processes to study complete cyclone life cycles. Adjoint sensitivity is a computationally efficient technique for determining, in a comprehensive sense, the sensitivity of a forecast aspect (J) to small perturbations of model variables at earlier times in a numerical forecast, including initial conditions. In these simulations, J is selected to represent central pressure or vorticity of forecast cyclones. Specification of lower tropospheric (500-800 hPa) temperature and moisture near the incipient cyclone at the beginning of the storm track appears especially critical to cyclone prediction. Rapid cyclone intensification appears related to enhancement of dry baroclinic instability by latent heat release from nonconvective precipitation near the cyclone warm front. Cyclones can also be intensified by reduced surface stress and higher sea-surface temperature in the warm sector of the storm. The cyclone life cycle may be viewed in terms of an initially small-scale instability that propagates upward from a baroclinic zone in the lower troposphere, and leads to intensification of anomalies in both the upper and lower troposphere at the end of the storm track.

14. SUBJECT TERMS

adjoint methods, sensitivity studies, baroclinic instability, cyclogenesis, air-sea interaction, precipitation processes

15. NUMBER OF PAGES

227

16. PRICE CODE

17. SECURITY CLASSIFICATION OF REPORT	18. SECURITY CLASSIFICATION OF THIS PAGE	19. SECURITY CLASSIFICATION OF ABSTRACT	20. LIMITATION OF ABSTRACT
UNCLASSIFIED	UNCLASSIFIED	UNCLASSIFIED	UL

[THIS PAGE INTENTIONALLY LEFT BLANK]

AN INTERPRETATION OF EXTRATROPICAL CYCLOGENESIS USING ADJOINT METHODS

Rolf Harold Langland
B.A., The University of Georgia-Athens, 1978
M.S., The University of Wisconsin-Madison, 1984

Submitted in partial fulfillment of the
requirements for the degree of

DOCTOR OF PHILOSOPHY IN METEOROLOGY

from the

NAVAL POSTGRADUATE SCHOOL
June 1996

Author: _____
Rolf Harold Langland

Approved by:

_____   _____
Russell L. Elsberry   R. Terry Williams
Professor of Meteorology   Professor of Meteorology
Dissertation Supervisor

_____   _____
Carlyle H. Wash   Wendell A. Nuss
Professor of Meteorology   Associate Professor of Meteorology

_____   _____
Roland W. Garwood   Beny Neta
Professor of Oceanography   Professor of Mathematics

_____
Ronald M. Errico
National Center for Atmospheric Research

Approved by: _____
Robert L. Haney, Chairman, Department of Meteorology

Approved by: _____
Maurice D. Weir, Associate Provost for Instruction

iii

[THIS PAGE INTENTIONALLY LEFT BLANK]

ABSTRACT

Adjoint methods are used to examine the development of idealized and real extratropical cyclones. This research represents the first use of adjoint sensitivity that includes moist physical processes to study complete cyclone life cycles. Adjoint sensitivity is a computationally efficient technique for determining, in a comprehensive sense, the sensitivity of a forecast aspect (J) to small perturbations of model variables at earlier times in a numerical forecast, including initial conditions. In these simulations, J is selected to represent central pressure or vorticity of forecast cyclones. Specification of lower tropospheric (500-800 hPa) temperature and moisture near the incipient cyclone at the beginning of the storm track appears especially critical to cyclone prediction. Rapid cyclone intensification appears related to enhancement of dry baroclinic instability by latent heat release from nonconvective precipitation near the cyclone warm front. Cyclones can also be intensified by reduced surface stress and higher sea-surface temperature in the warm sector of the storm. The cyclone life cycle may be viewed in terms of an initially small-scale instability that propagates upward from a baroclinic zone in the lower troposphere, and leads to intensification of anomalies in both the upper and lower troposphere at the end of the storm track.

[THIS PAGE INTENTIONALLY LEFT BLANK]

TABLE OF CONTENTS

LIST OF FIGURES

xi

xvi

[THIS PAGE INTENTIONALLY LEFT BLANK]

LIST OF TABLES

ACKNOWLEDGMENTS

[THIS PAGE INTENTIONALLY LEFT BLANK]

I. INTRODUCTION

A.   REVIEW OF PREVIOUS RESEARCH

Synoptic-scale cyclones are a predominant feature of extratropical weather. They are responsible for many extreme wind events, and produce a considerable proportion of the total precipitation in middle latitudes. Much of what is called "weather" (clouds, rain, snow, wind) is related to the development and generally west to east progression of these storm systems. The strongest extratropical cyclones (explosive deepeners) are responsible for significant property damage and loss of life both on land and at sea. Improved prediction of these storms remains a primary goal of the atmospheric science community.

The modern understanding of extratropical cyclone development dates to the Norwegian school established in Bergen in the early 1900s. The Norwegian frontal cyclone model depicts how cyclones can be initiated along the polar front, developing from a frontal wave through the fully occluded stage (Fig. 1.1). Although this conceptual model (Bjerknes 1919, Bjerknes and Solberg 1922) is still useful today, certain modifications and enhancements have been made as our ability to observe and simulate storms in more detail has increased (Petterssen et al. 1962, Neiman and Shapiro 1993, Mass and Schultz 1993)

The theoretical studies by Charney (1947) and Eady (1949) used linearized solutions to the quasi-geostrophic equations to show that baroclinic instability provides a basis for explaining synoptic-scale cyclone development. Their results show that a spectrum of *infinitesimally small perturbations* in an unstable basic state eventually leads to the dominance of an exponentially growing normal mode, with a
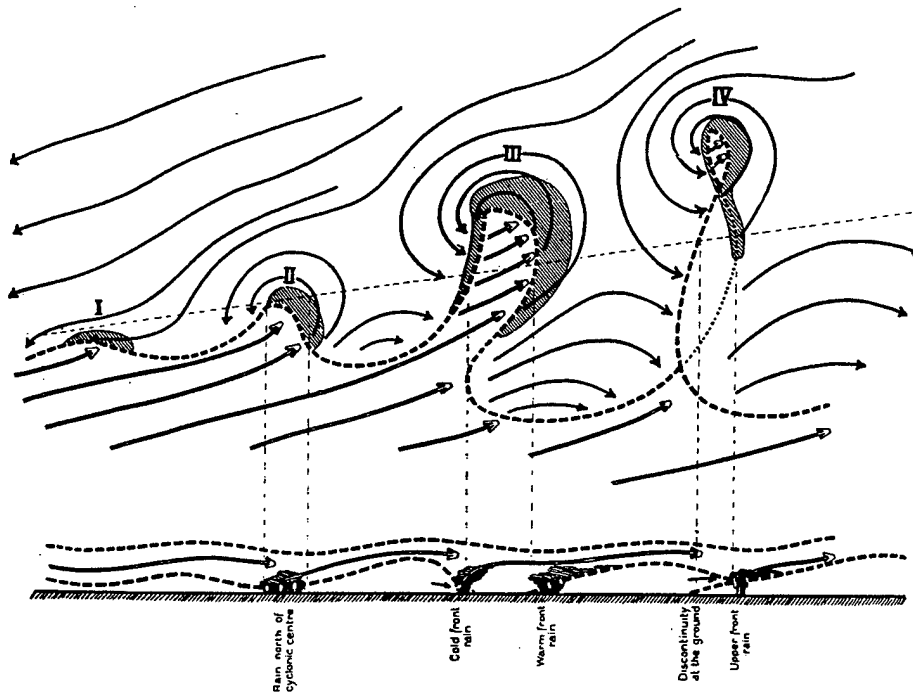
Figure 1.1: Norwegian frontal cyclone model from Neiman and Shapiro (1993) describing amplification of a frontal wave from initiation (I) through cyclogenesis (II, III), to frontal occlusion (IV).

wavelength similar to the scale (3000-4000 km) of observed mid-latitude cyclones. The wavelength of the most baroclinically unstable wave is inversely related to ambient static stability. Baroclinic growth rates depend on the amount of vertical wind shear, which corresponds to horizontal temperature gradients through the thermal wind relation.

Although the linear solutions described by Charney and Eady have certain unrealistic features (including excessive amplitude near the surface), it is now recognized that baroclinic instability is the primary mechanism through which synoptic-scale atmospheric waves convert available potential energy into storm kinetic energy. Simmons and Hoskins (1978, 1979) extended the original results of Charney and Eady into the nonlinear regime, and simulated the mature frontal development and occlusion phases of cyclone development.

2

Farrell (1982, 1984, 1985) recognized that certain favorably configured atmospheric perturbations can produce transient growth rates larger than those predicted by linear normal mode considerations. The growth of these "nonmodal" waves can be described using quasi-geostrophic theory in terms of the continuous spectrum of singular neutral modes, and thus complement the discrete eigenmodes. Inclusion of the continuous spectrum allows an initial value problem to be solved for any particular perturbation configuration, rather than just those of normal mode form.

According to Farrell (1985), one effect of the continuous spectrum is to excite the normal modes, even when they might otherwise be stable, as in the presence of an Ekman layer (frictional boundary layer). Nonmodal perturbations control transient growth rates, while long-term growth is dominated by the normal mode solution as the continuous spectrum decays. Modal waves can grow or decay while retaining the same structure, while nonmodal waves continue to change structure and amplitude.

The nonmodal initial value interpretation provides a framework for understanding the type-B cyclogenesis described by Petterssen and Smebye (1971), in which cyclone development is initiated by a pre-existing upper-level trough. In the real atmosphere, cyclogenesis (at least during the stage of most rapid development) usually involves the growth and interaction of large amplitude (rather than infinitesimal) disturbances. Often this takes the form of an upper-level trough moving over a lower-tropospheric vorticity center such as a frontal zone.

Type-B cyclone development may also be viewed as the interaction of two potential vorticity (PV) anomalies, as described by Hoskins et al. (1985, HMR hereafter) and McIntyre (1988). In this perspective, properly aligned anomalies of potential vorticity (PV) in the upper and lower troposphere can interact and amplify

3
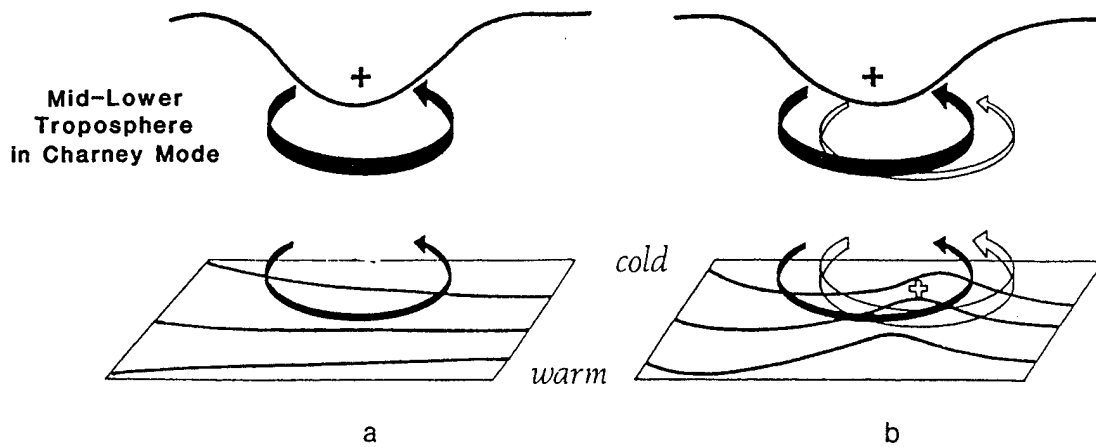
Figure 1.2: Schematic after Hoskins et al. (1985) of cyclogenesis associated with (a) arrival of an "upper-air" potential vorticity anomaly over a region of significant low-level baroclinity, and (b) the circulations resulting from this configuration.

a cyclonic circulation through a "phase lock" mechanism (Fig. 1.2). Favorable PV anomaly positions correspond to the upstream "tilt" that is characteristic of developing baroclinic waves. The effects of PV incorporate both vorticity advection *and* temperature advection from traditional quasi-geostrophic dynamics (e.g., Holton 1992). It should be noted that the "upper" PV feature referred to in HMR and shown in Fig. 1.2 may exist in the "mid-troposphere or lower" during cyclone intensification.

The alternative type-A development described by Petterssen and Smebye (1971) involves *simultaneous* growth of the surface cyclone and upper-level trough, which corresponds more closely to a pure normal mode development. Farrell (1985) has suggested that type-A cyclogenesis may occur in the vicinity of coastal fronts. Another cyclone development type is suggested by the observational study of North Atlantic cyclones by Rogers and Bosart (1986). A "composite" model of many Atlantic cyclones

4

reveals initial intensification in the lower troposphere, with later development of a cyclone vortex through the entire troposphere. This conceptualization appears to differ from both type-B (initial development forced by an upper-tropospheric feature) and type-A (simultaneous development at all levels), but resembles more closely the type-A development.

A similar view of the cyclone life cycle is provided in Hoskins et al. (1983), based on diagnosis of Eliassen-Palm fluxes. According to this study, eddy activity associated with baroclinic development begins at low levels at the beginning of storm tracks, then propagates upward as the disturbance moves in an eastward direction, and reaches the upper troposphere by the end of the storm track (Fig. 1.3). The upward propagation of baroclinic eddies shown in Fig. 1.3 is consistent with the interpretation in HMR85 of instability saturation at the steering level in the mid-lower troposphere and subsequent propagation of Rossby wave energy into the upper troposphere. For the fastest growing Charney mode of baroclinic instability, the
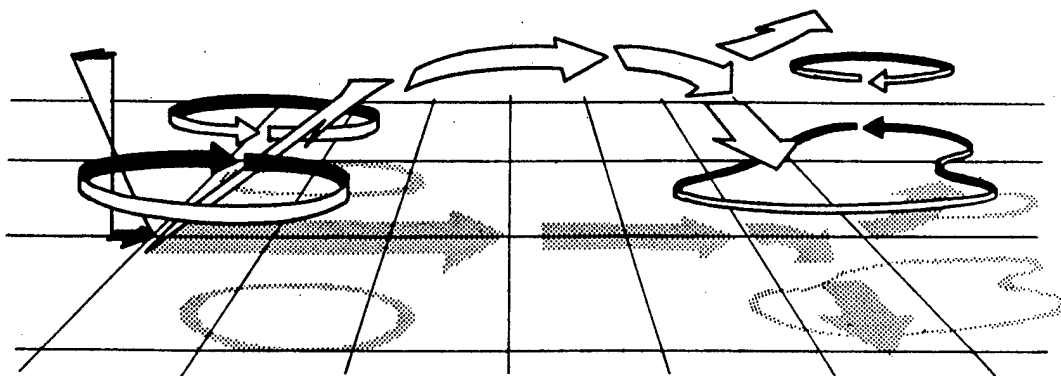
Figure 1.3: Schematic from Hoskins et al. (1983) of eddy activity within a storm track.

"upper" anomaly is located at the steering level, between 600 and 700 hPa (HMR85, p. 924).

A pressure deepening rate of 1 hPa h^{-1} is commonly referred to as a unit of 1 Bergeron, and represents a threshold for "explosive" cyclone intensification. For geostrophic equivalence, the Bergeron is multiplied by a factor of sin ϕ/sin 60, where ϕ is the latitude of the storm, and 60 deg. represents the approximate latitude of Bergen, Norway, where the Norwegian cyclone model was developed.

Observational evidence and numerical studies show that explosive deepening of extratropical cyclones usually occurs in the vicinity of strong sea-surface temperature gradients, including the Gulf Stream and Kuroshio currents (Sanders and Gyakum 1980, Roebber 1984, Chen et al. 1992). These are regions of intense low-level baroclinicity, low static stability, and large transfers of heat and moisture from the ocean to atmosphere. The most rapid deepening usually takes place as cyclones pass over sea-surface temperature fronts (Sanders 1986, Roebber 1989), which indicates the importance of near-surface processes. Hoskins and Valdes (1990) suggest that the Northern Hemisphere storm track regions are "self maintaining." The existence of warm western boundary currents in the oceans leads to strong diabatic heating and baroclinity in the atmosphere. In turn, the resulting storm "eddies" help maintain a mean atmospheric flow that enhances the oceanic currents.

Shallow mesoscale vortices in the lower troposphere are a significant feature in the early phase of extratropical cyclone life cycles. These small-scale features can develop where strong sea-surface temperature gradients exist along the north wall of the Gulf Stream (Fig. 1.4), and in conjunction with coastal fronts (Doyle and Warner 1993b). Strong upward fluxes of heat from the sea lead to negative pressure

6
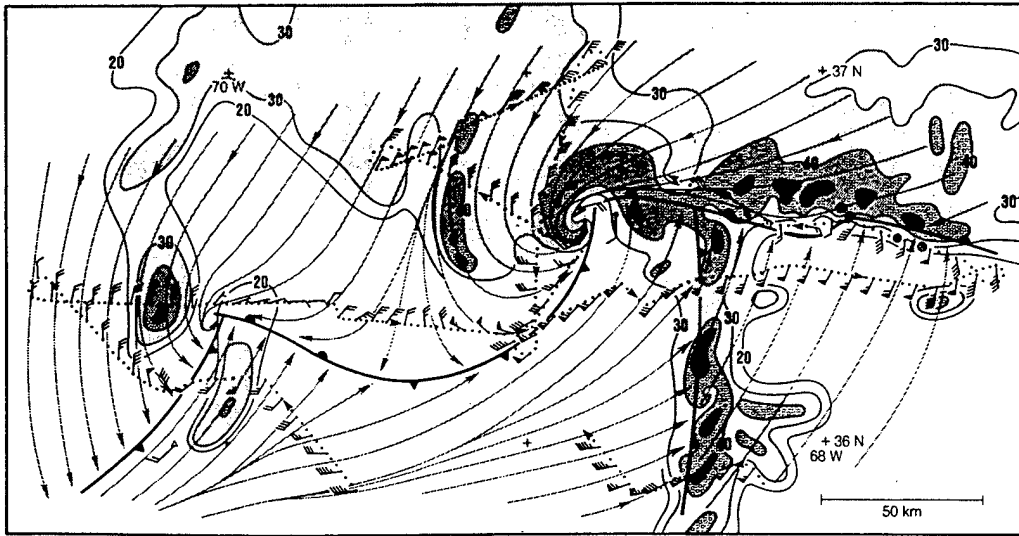
Figure 1.4: Finescale analysis of Doppler radar reflectivity (dBZ, gray-shaded) and 350-m streamlines depicting mesoscale vortices in the lower troposphere during the early stage of the ERICA IOP-4 cyclone at 0600 UTC 4 January 1989 (from Neiman et al. 1993).

perturbations, enhanced convergence, upward motion, and shear vorticity, and increased near-surface baroclinity. The existence of significant lower-tropospheric vorticity preceding explosive cyclogenesis is supported by the diagnostic studies of Bosart and Lin (1984), Hoskins and Berrisford (1988), Whitaker et al. (1988), Gyakum et al. (1992), and others.

Based on analysis of the QE II storm (September 1978), Gyakum (1991) discusses a two-stage cyclogenesis process, in which lower-tropospheric development occurs independently and prior to arrival of the upper-tropospheric disturbance. The QE II cyclone appears to develop independently of upper-level processes during an "antecedent" period. Rapid deepening occurs when a 500 hPa polar trough overruns the pre-existing surface cyclone. A weaker cyclone associated with the upper-level trough is absorbed into the Gulf Stream cyclone, which persists as the "primary" QE

II storm system. This two-stage development apparently conflicts with classical "type-B" development (Petterssen and Smebye 1971) in which an approaching midtropospheric, short-wave trough *initiates* development of the surface low.

Over the past decade, major field experiments have been conducted to study extratropical cyclone development and structure. ERICA (Experiment on Rapidly Intensifying Cyclones over the Atlantic) had a field phase from December 1988 to February 1989. ERICA was preceded by GALE (Genesis of Atlantic Lows Experiment) and CASP (Canadian Atlantic Storms Program), which took place from January to March 1986. These field experiments were designed to examine cyclone development in the western Atlantic ocean. The Fronts and Atlantic Storm Track Experiment (FASTEX, Thorpe and Shapiro 1995) will study "end-of-stormtrack" cyclones that affect western Europe during an observational phase in January and February 1997.

The goals of ERICA were stated as: (1) obtain detailed observations to understand the fundamental physical processes occurring in the atmosphere during rapid intensification of cyclones, (2) determine those physical processes that need to be incorporated in dynamical prediction models, and (3) identify measurable precursors that must be incorporated into the initial analysis for accurate and detailed operational model predictions (Hadlock and Kreitzberg 1988). Roebber (1984) postulated that explosive cyclogenesis might involve some physical mechanism in addition to ordinary baroclinic instability that might explain the extreme deepening rates observed in some events. It was a search for this physical mechanism, in part, that led to the considerable observational and research efforts represented by GALE, CASP, and ERICA.

It is now accepted that explosive cyclogenesis is driven by baroclinic instability, enhanced by convective and stable precipitation processes (Sanders 1986, Whitaker et al. 1988, Manobianco 1989, Uccellini 1990). Diabatic processes do not represent a fundamentally different mechanism that can initiate and develop extratropical cyclones apart from dry baroclinic processes (Robertson and Smith 1983, Chen and Dell'Osso 1987, Kuo et al. 1991b, Davis et al. 1993, and others). However, diabatic heating from precipitation processes can increase the cyclone deepening rate into the explosive range (Kuo and Low-Nam 1990), accelerate cyclone motion (Chang et al. 1989, Davis et al. 1993), and alter the cyclone track (Anthes et al. 1983, Mullen and Baumhefner 1988). No additional unique physical or dynamical mechanism has been found that distinguishes rapid deepeners from less intense extratropical cyclones.

In many cyclones, rapid deepening of the surface low is associated with short-wave troughs in the middle and upper troposphere (Uccellini and Kocin 1987, Liou et al. 1990, Rogers and Bosart 1991). However, end-of-stormtrack (e.g., FASTEX-type) cyclones may approach or exceed explosive development rates *without the presence of a short-wave trough in the middle or upper troposphere*, although strong cyclonic vorticity advection still exists in association with an upper-tropospheric jet streak.

Warm advection associated with tropopause depressions may also be significant for some cyclone developments, at least in a near-instantaneous sense, since the effects of small temperature changes on net column air pressure are relatively large at the tropopause level (Boyle and Bosart 1986, Hirschberg and Fritsch 1991). In a hydrostatic atmosphere, the surface low is, by definition, located under the net warmest column of air.

Although the skill of numerical model forecasts of explosive cyclogenesis has improved in the last decade (Sanders 1992), some important issues regarding cyclone development remain unresolved. For example, the relative importance of upper versus lower-tropospheric forcing at various stages of cyclone life cycles is still a matter of controversy, and has implications for improvements in numerical forecast skill. The sequence of events as shallow, mesoscale vortices in the lower troposphere interact with upper-level forcing has not been explained in a satisfactory way. Efforts can be made to improve three- to five-day predictions of cyclone track and intensity, as well as precipitation forecasts. Other questions include: What types of features serve as reliable precursors to explosive cyclogenesis? How do boundary layer processes (including surface momentum stress) influence the track followed by the surface low? Is upper-tropospheric cyclonic vorticity advection and divergence necessary for spin-up of low-level vorticity during the early development phase? In what location is diabatic heating from precipitation processes most critical to cyclone intensification? Does convective or nonconvective precipitation contribute more to cyclone intensification? During which phases of the cyclone life cycle and in what locations do sensible and latent heat fluxes from the sea contribute most strongly to the cyclone development?

Many numerical model-based investigations of extratropical cyclogenesis have included *sensitivity experiments* in which certain variables or parameterizations in a model are altered to determine their effect on a forecast of a cyclone event. For example, the model sea-surface temperature in a particular region could be modified, the nonlinear model re-run, and the altered forecast compared to an unaltered (control) simulation. The effects of latent heat release on cyclone development are

10

examined in sensitivity studies by Reed et al. (1988), Pauley and Smith (1988), Kuo et al. (1991b), and others.

The results of model sensitivity experiments have provided considerable insight, but also some apparently inconsistent conclusions. For example, sensitivity studies by Kuo et al. (1991a) state that surface fluxes have little or no direct effect during the rapid deepening phase. This finding is supported by Kuo and Reed (1988), Manobianco (1989), Kuo and Low-Nam (1990), Reed and Simmons (1991), and others. A possible explanation for this conclusion is provided by Danard and Ellenton (1980), who note that heating by surface fluxes in the cold air behind the low center destroys available storm potential energy.

However, numerical studies by Atlas (1987), Chen and Dell'Osso (1987), Reed and Simmons (1991), and Lapenta and Seaman (1992) indicate that surface fluxes concurrent with the rapid deepening may directly contribute to the development in a positive way. Nuss and Kamikawa (1990) provide observational evidence that fluxes in the updraft region (northeast quadrant) of the cyclone remain important during the rapid deepening phase by increasing convergence into the surface low. Sensitivity studies related to the importance of moist convection in maritime cyclogenesis also report differing conclusions (Anthes et al. 1983, Danard 1986, Mailhot and Chouinard 1989).

The inconclusive nature of many cyclone sensitivity studies is due partly to case dependency, but also to inherent limitations of forward sensitivity evaluation. For example, when a model is run in a forward sensitivity test with one parameter (such as the sea-surface temperature) changed, only the sensitivity of the forecast to that one parameter can be evaluated. A series of sensitivity tests in which various

11

parameters are tested in turn is computationally expensive and does not assure that the most significant model parameters have been evaluated.

In addition, removal of model physical processes in forward sensitivity experiments can alter the behavior of other processes, which makes it difficult to isolate the effect of the process under investigation. Because they are not linearly additive, the various components of the model dynamics and physics cannot be considered as separate pieces to be removed or added together as independent contributions to the complete cyclogenesis. When an entire model process (such as surface sensible heat flux) is removed from a numerical simulation at some arbitrary time, some insight into spatial variability is lost. It is possible that a physical process may be contributing to storm development in one area while opposing development another. Therefore, it is appropriate to develop and apply new diagnostic methods using numerical models to understand physical processes in cyclogenesis.

B.   ADJOINT METHODS

Adjoint methods provide a new and powerful approach to numerical sensitivity analysis in meteorology and oceanography. In adjoint sensitivity evaluation, a *forecast aspect* (*J*) is selected as a starting condition, and the adjoint model determines, in a quantitative sense, the partial derivatives (or "sensitivity" gradient) of *J* with respect to perturbations of variables and parameters at earlier times during the forecast, including initial conditions. The adjoint forecast aspect *J* can be defined as any model variable or differentiable scalar function of model variables, including forecast error. The choice of *J* determines the type of sensitivity question to be investigated; for example, cyclone development can be investigated by defining *J* as forecast cyclone pressure or vorticity.

12

Adjoint sensitivity provides quantitative information describing how perturbations of model variables and parameters will influence the feature represented by the forecast aspect (J). Physical processes and instability mechanisms provide a link between the initial perturbation and J. To determine the mechanisms that are involved, it is necessary to select an appropriate forecast aspect, and examine in detail the adjoint sensitivity fields at various times during the cyclone life cycle.

The earliest uses of adjoint methods in meteorology are attributed to Lorenz (1965), who investigated predictability using tangent linear and adjoint operators, and Marchuk (1974). Hall et al. (1982) and Hall (1986) demonstrated that the adjoint approach could be used to efficiently evaluate parameter sensitivity in simple atmospheric models. Thomson and Sykes (1990) used the adjoint method to examine sensitivity in a sea-ice model.

More recently, the adjoints of primitive equation meteorological models have been developed and used in sensitivity studies. Adjoint sensitivity with dry models has been investigated for idealized extratropical cyclones by Rabier et al. (1992, RCT92 hereafter), and in real-data cases by Errico and Vukićević (1992), Errico et al. (1993a,b), Rabier et al. (1996) and Vukićević and Raeder (1995). These studies suggest the localized nature of high-sensitivity regions in which small perturbations can have relatively large effects on forecast features in mid-latitude situations, and examine several choices of forecast aspect (J). They also demonstrate that adjoint sensitivity provides an acceptable approximation for describing perturbation growth in nonlinear models.

The model used for this research is Version 1 of the National Center for Atmospheric Research (NCAR) Mesoscale Adjoint Modeling System (MAMS1, Errico

et al. 1994). As described in Chapt. II.A and Appendix A, MAMS1 includes a nonlinear model, a tangent linear model (TLM), and an adjoint model. Chapt. II.B describes how sensitivity is evaluated in the context of adjoint methods.

The uses of adjoint models include a wide range of research and operational applications. Adjoint methods provide a basis for next-generation, four-dimensional variational data assimilation (Rabier et al. 1993, Thépaut et al. 1993, M. Županski 1993, Courtier et al. 1994). Ensemble forecasting in the operational environment can use dynamically-conditioned perturbations derived using adjoint models (Mureau et al. 1993, Molteni et al. 1994, Buizza 1994, 1995). Predictability can be studied using adjoint-derived singular vectors (Molteni and Palmer 1993, Hartmann et al. 1995), and optimal perturbations (Farrell 1990, Ehrendorfer and Errico 1995, Oortwijn and Barkmeijer 1995).

For numerical sensitivity studies, the adjoint method has several advantages compared to conventional sensitivity tests performed in the forward sense. A single adjoint run is computationally inexpensive and, for one choice of J, can provide the sensitivity to all model fields and to model parameters, such as albedo, roughness length, or drag coefficient. Similar guidance can be obtained from forward sensitivity only by re-running and successively perturbing each variable in the initial conditions at every grid point. In a forward sensitivity experiment, it is not usually known in advance which variables or parameters actually have the most influence on the forecast, so a given experiment may not relate to the most significant variable or process. For example, a perturbed sea-surface temperature field may appear to have a beneficial effect on cyclone prediction in a forward sensitivity experiment, but the specific areas of positive contributions may be difficult to determine, and more

significant improvements may be controlled by other factors that an adjoint model is able to identify.

Adjoint sensitivity allows identification of the area(s) of strongest sensitivity, which may be highly localized. Without this domain-wide sensitivity information, forward sensitivity experiments must rely on intuition or trial and error regarding locations where changes to initial conditions might influence a forecast feature of interest. Changes to initial conditions at one location may be significant, but be partially canceled by the effects of changes made elsewhere, so that the combined effect is relatively small. This situation is easily identified with adjoint sensitivity, whereas a forward sensitivity experiment may lead to erroneous conclusions (e.g., that local sensitivity is smaller than it actually is). In addition, adjoint sensitivity is obtained with respect to the unmodified forecast of the complete nonlinear model so that parameterized physics are not removed.

A limitation of adjoint sensitivity is that the adjoint model is linearized with respect to a nonlinear forecast (time-varying basic state), so that sensitivity in the adjoint framework is actually obtained as a first-order approximation along a trajectory that is tangent to the nonlinear forecast. The tangent-linear assumption implies that the accuracy of adjoint sensitivity (compared to fully nonlinear sensitivity) diminishes with increasing time, and tangent linear models estimate most accurately the growth of small perturbations (of a size comparable to or smaller than typical analysis errors). In general, adjoint and tangent linear models can provide useful information for at least 48 - 72 h (Errico et al. 1993a).

Moist processes have been included in several adjoint studies. In Vukićević and Errico (1993), the accuracy of TLM and adjoint solutions with moist physics (including

a Kuo-Anthes convective parameterization) was examined using an early version of MAMS1. Because characteristics of the Kuo-Anthes parameterization created problems in development of the TLM and adjoint codes, the Kuo-Anthes parameterization was replaced by the Hack convective scheme (Errico et al. 1994), and later by a version of the relaxed Arakawa-Schubert cumulus paramterization. In Park et al. (1994), the tangent linear and adjoint versions of a 1-D convective cloud model were used in a sensitivity study. Although they found that TLM accuracy was acceptable for small perturbations, problems were encountered with transitions between precipitating and non-precipitating conditions. Variational data assimilation including adjoint models with moist processes is described by Zou et al. (1993), Bao and Warner (1993), Verlinde and Cotton (1993), D. Županski (1993), and Županski and Mesinger (1995). These papers illustrate some of the approaches to overcome the difficulties of applying an adjoint involving moist processes.

C.   HYPOTHESES AND RESEARCH GOALS

The main objectives of this research are to demonstrate that adjoint sensitivity information is consistent with previous understanding of physical processes in extratropical cyclogenesis, and to use adjoint sensitivity to provide new insights into cyclogenesis. The sensitivity provided by adjoint methods contains important clues related to the development of extratropical cyclones. If this sensitivity exists, there must be physical or dynamical mechanisms that transmit the effect of a small, localized, perturbation of initial conditions into larger scale effects on cyclone features at later times. Therefore, adjoint sensitivity can be used to develop and revise conceptual models of the cyclone life cycle and cyclone predictability.

16

Whereas diagnostic equations such as the Petterssen Development Equation, height tendency equations, or potential vorticity (PV) inversion techniques pertain to more-or-less *instantaneous* effects on cyclone development, adjoint sensitivity describes, in a cause and effect sense, how perturbations influence the *future* state of selected forecast features. Adjoint sensitivity includes the complete dynamics and physics of a nonlinear primitive equation forecast model and does not rely on conservation or balance assumptions involved in other techniques, such as trajectory analysis or PV inversion. Thus, adjoint models can provide new insights into cyclone development by providing highly accurate and comprehensive information about sensitivity effects over the entire cyclone life cycle.

It is proposed that by conducting a systematic series of adjoint model sensitivity experiments involving dry idealized, moist idealized, and real cyclone simulations, it will be possible to gain substantial insight into physical processes of extratropical cyclogenesis. A synthesis of these results can lead to refinements of current conceptual models describing the life cycle of extratropical cyclones, as well as indicate where improvements might be made in numerical prediction of these storms. A number of hypotheses can be defined as starting points for investigation with adjoint sensitivity:

- *Lower tropospheric vorticity in the incipient stage of marine cyclogenesis can spin-up during the early development phase independently from middle and upper tropospheric features. Lower tropospheric precursors include small-scale thermal waves, coastal fronts, convergence zones, and enhanced cyclonic vorticity.*

- *During the rapid deepening stage, cyclone intensification is significantly influenced by upper-tropospheric cyclonic vorticity anomalies.*

- *Surface fluxes of sensible and latent heat contribute to cyclone development mainly during a "preconditioning" phase early in the cyclone life cycle*

- *Latent heat release from nonconvective precipitation near the warm front in the lower troposphere contributes to explosive cyclone intensification.*

- *The development of upper-tropospheric potential vorticity anomalies is influenced by instabilities that originate in the lower troposphere.*

- *The predictability of extratropical cyclones over periods of 24-48 h depends primarily on resolving initial small-scale features in the middle and lower troposphere, rather than large-scale features near the tropopause level.*

In Chapt. III.A, the MAMS1 adjoint is used to evaluate sensitivity under the controlled conditions of an idealized cyclogenesis (near-adiabatic, without moist processes) in a channel domain. The results of this work are published in Langland et al. (1995). The effects of moist processes (convective and nonconvective precipitation, surface latent heat flux) for an idealized cyclogenesis are considered in Chapt. III.B, and published in Langland et al. (1996). In Chapt. IV, adjoint sensitivity is used to interpret the development of an actual cyclone that formed in the North Atlantic ocean during January 1995. A summary and discussion of research results is provided in Chapt. V.

II. ADJOINT METHODOLOGY

A.   DERIVATION OF TANGENT LINEAR AND ADJOINT MODELS

To obtain sensitivity via the adjoint method, it is necessary to use an adjoint version of a numerical model. The adjoint model in this study is a component of the Mesoscale Adjoint Modeling System Version I (MAMS1). A detailed description of MAMS1 is provided by Errico et al (1994), including the development of discretized finite difference versions of the tangent linear and adjoint subroutines. The following discussion summarizes the basic mathematical representation of tangent linear model (TLM) and adjoint model development.

The nonlinear model may be expressed as

$$\frac{d\mathbf{x}}{dt} = \mathbf{M}_N(\mathbf{x}, t) \quad , \tag{2.1}$$

where $\mathbf{M}_N$ is a nonlinear function of the model component vector ($\mathbf{x}$) defined in orthogonal Cartesian coordinates (i,j,k), and time (t). The discretized nonlinear model is

$$\mathbf{x}_f = \mathbf{R}_N(\mathbf{x}_0) \quad , \tag{2.2}$$

where $\mathbf{R}_N$ denotes the resolvent nonlinear operator. The resolvent represents a complete integration of the model from the initial conditions ($\mathbf{x}_0$) to the final state ($\mathbf{x}_f$). The TLM is a first-order linearization of the discretized nonlinear model with respect to a time-varying basic state (nonlinear forecast). For sufficiently small perturbations, the TLM can be used to forecast the development of an initial perturbation vector ($\mathbf{x}'_0$), according to

$$\mathbf{x}'_f = \mathbf{R}_L(\mathbf{x}'_0) \quad , \tag{2.3}$$

19

where $\mathbf{x}'_f$ is a first-order approximation of the difference between perturbed and nonperturbed nonlinear solutions, and $\mathbf{R}_L$ is the resolvent tangent linear operator (Jacobian of the nonlinear operator $\mathbf{R}_N$).

A forecast aspect, J, is defined as a differentiable scalar function of the components of $\mathbf{x}_f$, ($J(\mathbf{x}_f)$). The nonlinear response of J to a change in $\mathbf{x}_0$ is

$$\Delta J = J(\tilde{\mathbf{x}}_f) - J(\bar{\mathbf{x}}_f) = J\{\mathbf{R}_N(\bar{\mathbf{x}}_0 + \mathbf{x}'_0)\} - J\{\mathbf{R}_N(\bar{\mathbf{x}}_0)\} \quad , \tag{2.4}$$

where $\tilde{\mathbf{x}}_f$ is a perturbed and $\bar{\mathbf{x}}_f$ a nonperturbed nonlinear forecast. This ΔJ must be obtained from two integrations of the nonlinear model, and ΔJ can be approximated using first-order perturbations in a Taylor series, as

$$J' = \mathbf{x}'_f \cdot \frac{\partial J}{\partial \mathbf{x}_f} \quad . \tag{2.5}$$

The adjoint of (2.3) can be written as

$$\frac{\partial J}{\partial \mathbf{x}_0} = \mathbf{R}_L^T \left(\frac{\partial J}{\partial \mathbf{x}_f} \right) \quad , \tag{2.6}$$

where $\mathbf{R}_L^T$ is the adjoint operator corresponding to the transpose (interchange of matrix rows and columns) of $\mathbf{R}_L$. The vector of adjoint variables $\partial J/\partial \mathbf{x}_0$ denotes the gradient (sensitivity) of J with respect to the initial state vector $\mathbf{x}_0$. The operator $\mathbf{R}_L^T$ represents a complete integration of the adjoint model from the starting condition $\partial J/\partial \mathbf{x}_f$ to $\partial J/\partial \mathbf{x}_0$, with the order of operations reversed from the tangent linear model. The tangent linear and adjoint systems satisfy the scalar dot product relationship

$$\mathbf{R}_L(\mathbf{x}'_0) \cdot \frac{\partial J}{\partial \mathbf{x}_f} = \mathbf{x}'_0 \cdot \mathbf{R}_L^T \left(\frac{\partial J}{\partial \mathbf{x}_f} \right) \quad . \tag{2.7}$$

20

From the right side of (2.7), J' may also be obtained as a product of the adjoint sensitivity and initial perturbation vector, which may include any number of model grid points

$$J' = \mathbf{x}_0' \cdot \frac{\partial J}{\partial \mathbf{x}_0} \quad . \tag{2.8}$$

Equation (2.8) is a first-order estimate of J' resulting from a perturbation of model initial conditions. Note that (2.4) provides the response ΔJ for a particular $\mathbf{x}_0'$, while (2.6) provides the sensitivity $(\partial J/\partial \mathbf{x}_0)$ for a particular J.

The tangent linear model determines the evolution of a perturbation forward in time, while the adjoint model determines the evolution of sensitivity backward in time. It is not necessary to use the tangent linear model to obtain adjoint sensitivity; however, the TLM is extremely useful for examining perturbation growth in the forward-time sense, and for validating the adjoint model gradient test, via (2.7). Adjoint sensitivity in this context is not a direct inversion technique, or backward-in-time integration of the forward nonlinear or tangent linear model.

The TLM in MAMS1 is a complete linearization of the nonlinear model except for several terms that have negligible impact on perturbation growth in realistic situations. Validation of the TLM consists of verifying that the ratio of progressively smaller perturbations in tangent linear forecasts approaches that found in the nonlinear model. That is,

$$\frac{\mathbf{R}_N(\overline{\mathbf{x}}_0 + \mathbf{x}_0') - \mathbf{R}_N(\overline{\mathbf{x}}_0)}{\mathbf{R}_L(\mathbf{x}_0')} \cong 1 \quad , \tag{2.9}$$

as $\mathbf{x}_0'$ approaches zero, but not with $\mathbf{x}_0'$ close to machine precision.

To perform a tangent linear or adjoint model run, the nonlinear model is integrated forward, and the forecast (basic state) fields are saved at some prescribed interval. For the simulations performed in this study, it is not possible to save basic state fields at every model time step, due to file storage capacity limitations. In terms of computational expense, full-physics adjoint and TLM runs require slightly more time than corresponding nonlinear model integrations, because of additional file-reading (basic state input) and evaluation of extra terms arising from model linearization. Adjoint and TLM memory requirements are somewhat higher than in the nonlinear model, because the sensitivity (or perturbation) arrays and basic state arrays must be carried simultaneously.

In MAMS1, the convective and nonconvective precipitation processes are not directly linearized, because of complications involved with code "switches" (if-then-else FORTRAN code statements). Instead, estimates of the Jacobian matrices corresponding to the tangent linear operators are obtained by selectively perturbing the nonlinear forecast (see Errico et al. 1994). The Jacobian matrices are provided to the TLM and adjoint at the times specified for the basic state update.

Differences between nonlinear perturbation growth and tangent linear (or adjoint) results arise from two considerations: (i) the elimination of terms involving products of perturbation variables in first-order linearization, and (ii) the frequency of basic state coefficient update. If the basic state is not updated each time step, the TLM and adjoint are not truly "tangent linear," but can still provide a good approximation to the nonlinear trajectory, depending on forecast length and perturbation size. In general, tangent linear and adjoint information provides acceptable accuracy for up to 48-72 h (Lacarra and Talgarand 1988, Rabier and

Courtier 1992, Errico et al. 1993a). Accuracy is usually better for relatively small magnitude perturbations (smaller than or comparable to typical analysis errors), and, assuming that perturbations are growing with time, over shorter forecast intervals.

For the idealized initial conditions in Chapt. III, there is a "spin-up" period of about 30 h during which perturbation growth is relatively slow, which allows the period of useful adjoint and TLM information to be extended to about 90 h. Examples of tangent linear model accuracy are provided in Chapt. III, and in Chapt. IV for conditions of a real cyclone simulation to 48 h.

B. ADJOINT SENSITIVITY AND FORECAST ASPECT (J)

The adjoint forecast aspect (J) is selected to represent some feature or attribute of the model forecast. In prediction of a cyclone, J might be defined as surface pressure or near-surface vorticity in an area near the center of the cyclone, or J might represent wind speed, kinetic energy, divergence, integrated mixing ratio, or other differentiable function of model variables. In data assimilation applications, J is an error costfunctional that measures the fit between a short-term forecast and observations (e.g., Courtier et al. 1994 or Li et al. 1994).

In singular vector applications (Buizza and Palmer 1995, Ehrendorfer and Errico 1994), J can be a function involving a norm to measure total perturbation energy in a specified region. Singular vectors (also called optimal perturbations) are initial perturbation structures that maximize a quantity, such as perturbation energy, at the end of a specified forecast interval. It is appropriate to determine singular vectors for nonlinear choices of J, since there may be more than one unstable (growing) initial perturbation configuration. When J is defined as a linear function of perturbation variables, it has been demonstrated (Errico and Oortwijn 1995) that

23

evaluation of sensitivity (e.g., equation (2.6)) is a good approximation to optimal perturbation structure. In addition, when singular vectors are constrained to maximize a nonlinear J (such as forecast perturbation energy) over a local area corresponding to a cyclone, there can be strong similarity between initial condition sensitivity for a linear J (such as forecast vorticity) and the structure of the dominant singular vector at initial time. An example is provided in Chapt. IV.B.2.

It will be shown in Chapts. III and IV that linear choices of J (surface pressure and vorticity) are appropriate for obtaining initial condition sensitivity of extratropical cyclone development. This can be demonstrated by placing selected initial perturbations in the nonlinear model, and verifying that the forecast has been modified in a manner consistent with the choice of J. For example, if J is vorticity over a specified area, then there should be differences in zonal and meridional wind components between perturbed and nonperturbed forecasts over the area of interest.

Since adjoint variables are first partial derivatives of J, the choice of J determines the starting condition of the adjoint model ($\partial J/\partial \mathbf{x}_f$). If J is pressure (p*) at some grid point (i,j), then the adjoint variable $\partial J/\partial p^*_f$ (i,j) = 1 is specified at the beginning of the adjoint integration, with all other adjoint variables equal to zero. This choice of J is used in Chapt. III. For any specified choice of J, a single integration of the adjoint model provides the complete initial condition sensitivity vector $\partial J/\partial \mathbf{x}_0$.

For some choices of J, it may be appropriate to introduce a weighting procedure that accounts for variations in the size of model grid volumes. For example, J might represent average temperature within some volume of the atmosphere, including any number of model grid points. One way to accomplish this weighting is to consider the

amount of mass that a grid volume contains. Within a grid volume (i,j,k), the total mass $(M_{grid})_{i,j,k}$ in kg is

$$\left(M_{grid}\right)_{i,j,k} = \frac{\Delta\sigma_k \, p^*_{i,j}\left(\Delta x \, m_{i,j}\right)^2}{g} \quad , \tag{2.10}$$

where $\Delta\sigma_k$ is the sigma thickness of level "k," Δx is the horizontal grid spacing, $p^*_{i,j}$ has units of Pa, and $m_{i,j}$ is a map factor. The mass-weighted value of $(\partial J/\partial T_f)_{i,j,k}$ is then defined as

$$\left(\frac{\partial J}{\partial T_f}\right)^{weighted}_{i,j,k} = \left(\frac{\partial J}{\partial T_f}\right)^{un-weighted}_{i,j,k} \cdot \frac{\left(M_{grid}\right)_{i,j,k}}{M_{ref}} \quad , \tag{2.11}$$

where (M_{ref}) is an arbitrary "reference" mass of 3.67×10^{12} kg. This value represents the approximate mass of a grid volume, which is $(60 \text{ km})^2 \times 100$ hPa. The effect of (2.11) is to ensure that $(\partial J/\partial T_f)_{i,j,k}$ is larger in grid volumes that contain more mass, since temperature perturbations $(T'_f)_{i,j,k}$ in those locations make a larger contributions to *average* temperature (J). This procedure is used in Chapt. IV, where J represents average vorticity.

The initial condition sensitivity obtained directly from the adjoint model provides an accurate representation of perturbation impact on J', within the context of the model grid. However, adjoint sensitivity is influenced by variations in grid volume size, which affects sensitivity magnitude. For example, a grid point representing some particular volume may have a sensitivity value of 1.0. If this volume is divided into two equal parts, then the sensitivity on each grid point will be 0.5, while the total sensitivity for the original volume remains unchanged.

For a less-distorted display of adjoint sensitivity, a normalization procedure can be used to remove the effects of grid volume size variations. The procedure consists

of multiplying the un-normalized sensitivity by the inverse of the mass-weighting factor on the right side of (2.11), as

$$\left(\frac{\partial J}{\partial T_0}\right)^{display}_{i,j,k} = \left(\frac{\partial J}{\partial T_0}\right)^{grid}_{i,j,k} \cdot \frac{M_{ref}}{\left(M_{grid}\right)_{i,j,k}} \qquad (2.12)$$

For the MAMS1 grid configuration used in this study, the sensitivity on the lowest model level, with a pressure thickness of about 10 hPa, is multiplied by a factor of approximately 10.0 for display purposes. In the interior of the MAMS1 grid, where the pressure thickness of model layers is roughly 100 hPa (see. Fig. A.1), the sensitivity normalization factor is approximately 1.0.

The normalization procedure allows comparison of adjoint sensitivity magnitude between various regions of a model that includes differences in grid volume size, and between models with totally different resolutions. For example, sensitivity obtained with the MAMS1 adjoint (60 km horizontal resolution and 14 vertical levels) in Chapt. IV is compared to sensitivity from a T79 global adjoint model (approximately 150 km horizontal resolution) with 18 vertical levels.

Methods other than the one described here could be used for representation of adjoint sensitivity. In addition, it is not necessary that the mass-weighting of J (equation (2.11)) and the normalization of sensitivity (equation (2.12)) have an inverse relation, since they represent two different problems. For the choices of J used in this study, it is convenient for both procedures to involve grid volume mass.

26

III. IDEALIZED EXTRATROPICAL CYCLOGENESIS

Adjoint models provide sensitivity with respect to a particular nonlinear forecast (time-varying basic state). In Chapt. III.A, the nonlinear forecast describes an idealized dry (near-adiabatic) cyclogenesis in an f-plane channel domain with periodic east and west boundaries. Effects of moist physical processes for the idealized cyclone are examined in Chapt. III.B. The horizontal grid spacing is 60 km, with 121 grid points in the east-west direction, 62 grid points in the north-south direction, and 14 vertical levels between the surface and 25 hPa (see Figure A.1 in Appendix A). The model lower boundary consists of a uniform water surface, with sea-surface temperature held constant in time. A description of the model configuration used for this simulation is provided in Appendix A, and the method used to establish the channel boundary conditions is described in Appendix C.

A. DRY (NEAR-ADIABATIC) MAMS1 SIMULATION

The nonlinear simulation of the dry idealized cyclogenesis is described in Chapt. III.A.1. In Chapt. III.A.2, tangent linear model (TLM) forecasts are used to provide an estimate of the accuracy that may be expected from adjoint sensitivity. In Chapt. III.A.3, adjoint sensitivity is interpreted in the context of physical processes at several times during the cyclone life cycle. Chapter III.A.4 addresses the sensitivity to sea-surface temperature and surface sensible heat flux, and Chapt. III.A.5 describes adjoint sensitivity to surface momentum stress.

1. Nonlinear Simulation

The idealized cyclone begins from idealized initial conditions, which are derived according to procedures described in Appendix B. The initial state includes a westerly jet, located in the center of the channel model domain (Fig. 3.1a). A localized anomaly of temperature and wind (Figs. 3.1b-d) is imposed in the upper troposphere to initiate cyclone development.

In the nonlinear MAMS1 forecast, the idealized cyclone deepens over 120 h to a minimum surface pressure of 982 hPa. The maximum deepening rate (approximately 0.5 hPa h^{-1}) is attained near 80 h (Fig. 3.2). The e-folding time of the disturbance is approximately 30 h, which is typical of synoptic-scale extratropical cyclones. Between the initial time and 60 h, the incipient cyclone moves eastward below the jet axis and gradually intensifies. After 60 h, surface pressure decreases more rapidly and the storm moves northeastward into the colder air. At 90 h, the central pressure is 985.7 hPa and the ridge-trough wavelength of the system is about 1500 km. A cold front extends south from the cyclone. After 100 h, the cyclone enters a barotropic decay phase with no further intensification. Certain features of marine cyclogenesis such as a warm air seclusion or bent-back warm front (Shapiro and Keyser 1990) do not appear in this simulation, and may depend on finer grid resolution, moist processes, or more sophisticated parameterizations of surface heat and momentum interchange. More description of features during the idealized cyclogenesis will be provided in later sections related to the adjoint sensitivity results.

The cyclone scale here is somewhat smaller than the idealized simulations of RCT92, or Simmons and Hoskins (1978, SH78 hereafter) using global models. This difference in scale is probably due to the greater north-south extent of the initial
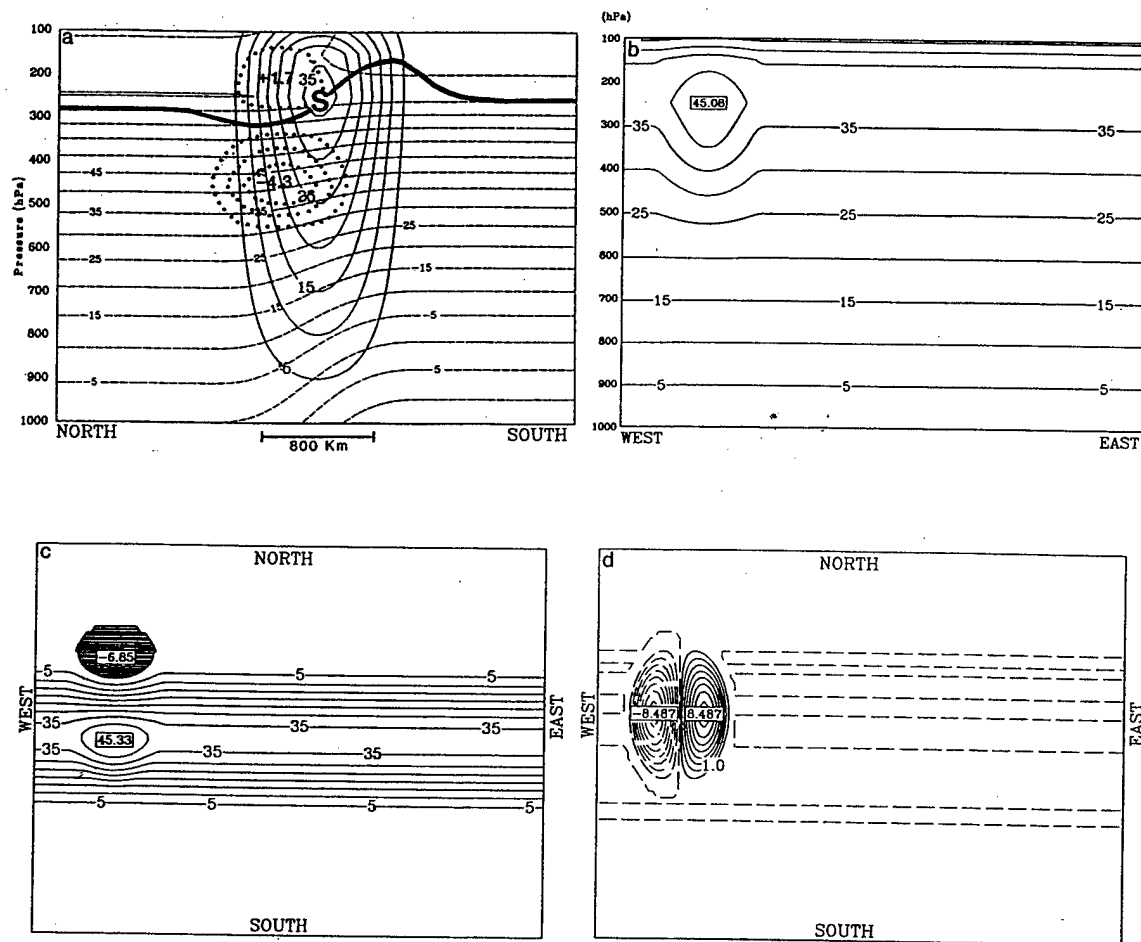
Figure 3.1: (a) North-south vertical cross-section of initial background zonal wind component (solid contour = 5 m s⁻¹) and temperature (dashed contour = 5 °C) for the idealized cyclogenesis case. Initial temperature anomaly (dotted contour = 1 °C) and 2 PVU contour (heavy solid line, 1 PVU = 10⁻⁶ m² K s⁻¹ kg⁻¹). **S** indicates location of 45 m s⁻¹ jet streak associated with temperature anomaly. (b) East-west vertical cross-section of initial zonal wind, including anomaly (contour = 5 m s⁻¹), (c) Initial zonal wind, including anomaly, at 250 hPa (contour = 5 m s⁻¹), and (d) Initial meridional wind anomaly at 250 hPa (contour = 1 m s⁻¹).
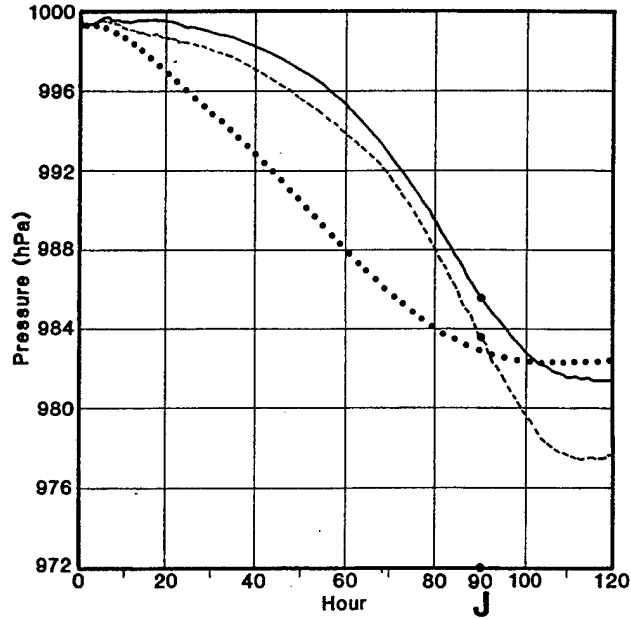
Figure 3.2: Time series of minimum surface pressure in nonlinear simulations with initial anomalies in upper troposphere (solid line) and lower troposphere (dotted line). Time series for simulation with upper-tropospheric initial anomaly and warm sea-surface temperature anomaly (dashed line). Forecast aspect J is pressure at center of 90 h cyclone.
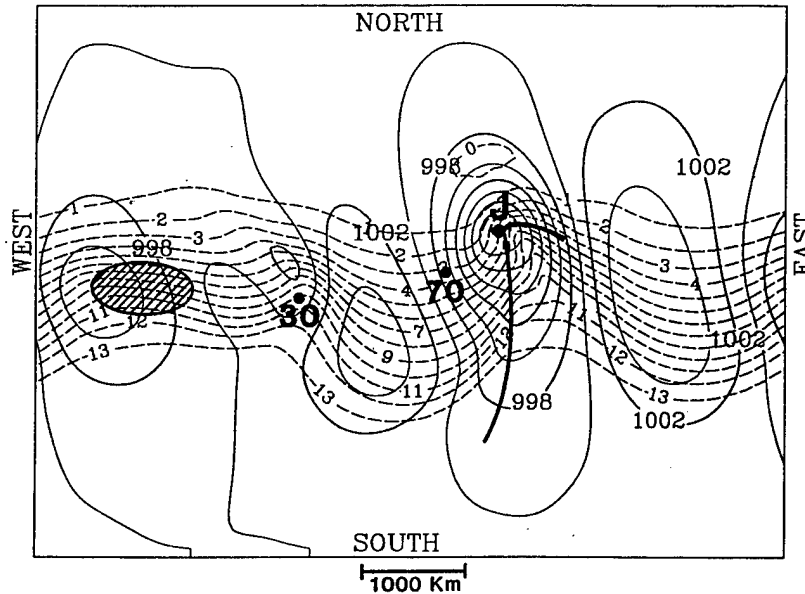
Figure 3.3: Surface pressure (solid contour = 2 hPa) and near-surface air temperature (dashed, contour = 1 °C) at 90 h in the nonlinear run. Solid dots indicate cyclone positions at 30, 70, and 90 h (985.7 hPa). Forecast aspect J is pressure at center of 90 h cyclone. Heavy solid line surrounding cross-hatched area corresponds to the 40 m s^{-1} contour of the jet streak at 250 hPa in the initial conditions.

30

baroclinic zone and jet in SH78 and RCT92. The initial jet speeds in SH78 and RCT92 are similar to that used here. SH78 specified small-amplitude initial disturbances of normal mode form corresponding to wavenumber 6, including surface pressure perturbations. As noted by Thorncroft et al. (1993), the basic features of these idealized cyclone life cycles (scale and intensity) depend more on specification of the mean zonal flow than on initial perturbation amplitude. Over periods of several days or more, small-amplitude perturbations of various forms will evolve asymptotically to a "preferred" normal mode structure, as noted, for example, by Reinhold (1986).

Of course, initial perturbation structure can have significant effects on the timing of cyclone development. A larger scale or more intense initial temperature anomaly in this simulation will produce surface development more quickly, but the final cyclone pressure and scale are similar to Fig. 3.3. A cyclone can also be initiated by placing an anomaly in the lower troposphere instead of in the upper troposphere as described above. In this case, the surface disturbance begins to intensify more quickly (dotted line in Fig. 3.2), but the final cyclone scale and intensity are again similar to the original simulation. The dashed line in Fig. 3.2 corresponds to a simulation including a large sea-surface temperature anomaly, and is discussed in Chapt. III.A.4.

The deepening rate of 12 hPa day^{-1} in this simulation is somewhat larger than the rate of 8 hPa day^{-1} in RCT92, which could be related to the smaller horizontal scale of this cyclone and differences in the specification of initial static stability. In this simulation and those of SH78 and RCT92, the basic mechanism for development is baroclinic instability with some modification by barotropic processes. The features

31

of the simulated cyclones are similar, with well-defined life cycles, including westward-tilting troughs, eastward-tilting temperature perturbations and frontal structures typical of middle-latitude disturbances.

2.   Choice of Forecast Aspect (*J*) and Accuracy Considerations

In Chapt. III.A, adjoint sensitivity results are obtained for a forecast aspect *J* that represents surface pressure in the center of the cyclone at 90 h (Fig. 3.3). That is, $\partial J/\partial p_S = 1.0$ at a single grid point is the starting condition for the adjoint model. For the adjoint sensitivity presented in this paper, the term "cyclogenetic" will imply a decrease of 90 h pressure at the location where *J* has been defined. Sensitivity for several other choices of *J* (including pressure over a larger area surrounding the cyclone center) has been investigated, but does not lead to any substantial differences in the interpretation of the cyclogenesis described here. Cyclone development can be measured by various choices of *J* (such as vorticity or kinetic energy), but they are closely related in a dynamic sense. For example, a change in pressure should be accompanied by changes in vorticity and kinetic energy that have similar sensitivity patterns. An example of sensitivity using *J* as kinetic energy is shown in Fig. 3.10b.

Before describing the adjoint sensitivity results, it is useful to evaluate the accuracy that can be expected for this cyclone simulation. This is best done by comparing forecasts of the tangent linear model with difference fields taken from perturbed and non-perturbed nonlinear model forecasts, to inspect perturbation growth over the entire domain. The adjoint and tangent linear accuracy are identical, in the sense that (2.7) is an identity. The basic state coefficients (from the time-varying nonlinear trajectory) are provided to the tangent linear and adjoint models at

30 min intervals. Experiments with basic state update intervals of 20 min and 10 min did not produce significantly different results.

An accuracy test is made by perturbing the initial temperature field by 2° C in a square of nine grid points on model level 10 (near 760 hPa) in a region of strong temperature sensitivity (location shown as a small square in Fig. 3.8a). Here, sensitivity to initial temperature ($\partial J/\partial T$) provided by the adjoint model has been used to select a location at which to perturb the initial conditions. At this location, initial temperature perturbations will produce a relatively large change in the 90 h cyclone pressure, compared to a perturbation of equal magnitude in regions of weaker sensitivity. Comparison of the tangent linear model 90 h perturbation pressure (Fig. 3.4a) and the corresponding nonlinear difference field (Fig. 3.4b) indicates that, for this perturbation, the TLM accurately depicts the region where 90 h pressure is reduced, but overestimates slightly the magnitude of the pressure change. Similarly, relatively good correspondence in terms of perturbation magnitude and spatial pattern is achieved between the TLM forecast (Fig. 3.4c) and nonlinear difference field (Fig. 3.4d) for a 90 h forecast of 250 hPa zonal wind.

The forecast values of the *largest negative wind, temperature, and pressure perturbations at 90 h* resulting from temperature perturbations at 0 h, 30 h, and 70 h are provided in Table 3.1. In each case, the initial perturbation is placed in a region of strongly negative $\partial J/\partial T$. The forecast perturbations are examined at 90 h for u and v wind components on a model level near 250 hPa, temperature near 760 hPa, and surface pressure. The decision to examine negative forecast perturbations is arbitrary; similar errors occur for positive perturbations.

33

Table 3.1. Comparison of tangent linear and nonlinear perturbation forecasts valid at 90 h, in which perturbations are made at 0 h (90 h forecast), 30 h (60 h forecast), and 70 h (20 h forecast). The 0 h perturbation location is shown in Fig. 3.8a. Entries are largest negative perturbation for u, v, T, or p* with grid point location in parentheses. The initial perturbation consists of + 2° C at nine grid points on sigma level 10 (near 760 hPa) in region of largest negative $\partial J/\partial T$.

Fcst Length	$u(\sigma=0.23)$ m s^{-1}	$v(\sigma=0.23)$ m s^{-1}	$T(\sigma=0.75)$ °C	Pressure hPa
20 h Tangent	-.127 (75,35)	-.155 (81,45)	-.106 (75,32)	-.317 (74,36)
Nonlinear	-.134 (75,36)	-.154 (81,45)	-.127 (76,32)	-.335 (74,37)
60 h Tangent	-.884 (74,38)	-.558 (92,40)	-.469 (72,28)	-1.65 (73,37)
Nonlinear	-.863 (75,38)	-.523 (95,38)	-.444 (73,28)	-1.36 (73,38)
90 h Tangent	-2.80 (105,36)	-1.67 (99,34)	-.928 (72,28)	-3.55 (73,38)
Nonlinear	-2.64 (107,35)	-1.65 (102,32)	-.922 (73,28)	-3.03 (73,39)

As shown in Table 3.1, differences between tangent linear perturbations and perturbations from the nonlinear model are generally smallest for the shortest forecast interval (20 h). For the perturbation inserted at 70 h, the difference between the TLM and nonlinear forecasts of 90 h pressure is 0.018 hPa (five percent), with the TLM perturbation shifted one grid point to the south. Over the full 90 h, the TLM has a 17 percent error in surface pressure and a six percent error in 760 hPa temperature.

The forecast perturbations are largest over 90 h, which indicates that the selected perturbation projects onto a growing instability. As shown in Figs. 3.4c and 3.4d, and in Table 3.1, perturbations of temperature in high sensitivity regions of the lower troposphere can change the wind field in the upper troposphere (250 hPa) by several m s^{-1}. By way of comparison, the same temperature perturbation (2° C, nine grid points) applied in a high-sensitivity region at 250 hPa results in relatively weak 90 h perturbations of surface pressure and upper-tropospheric wind (Table 3.2).

In general, the TLM forecast will be less accurate for larger magnitude initial perturbations, and error patterns will also depend to some extent on the forecast
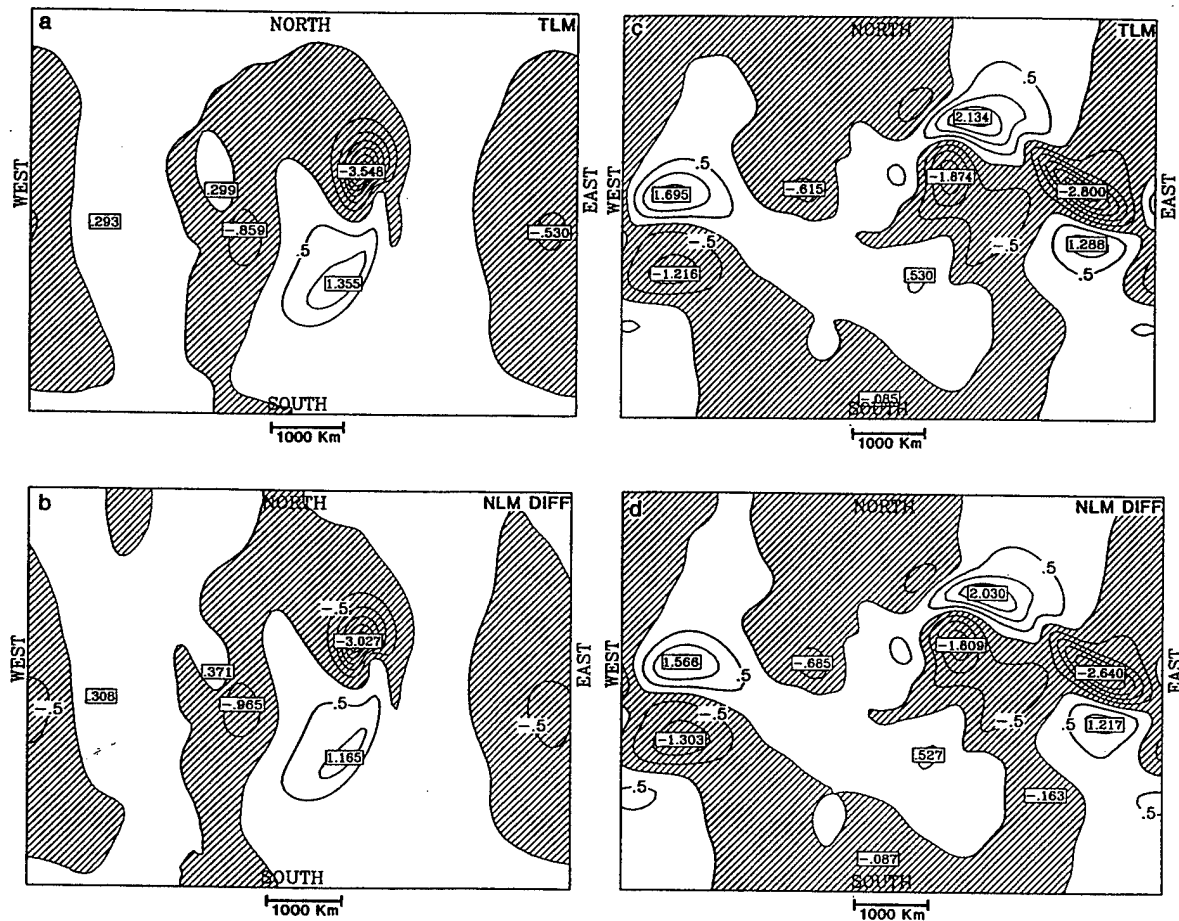
Figure 3.4: (a) 90 h forecast of tangent linear model (TLM) surface pressure perturbations (contour = 0.5 hPa) resulting from initial temperature perturbations near 760 hPa (location shown in Fig. 3.8a); (b) as in (a) except difference between two nonlinear runs; (c) 90 hour forecast of TLM zonal wind perturbations (contour = 0.5 m s^{-1}) near 250 hPa resulting from initial perturbation as in (a); (d) as in (c) except difference between two nonlinear runs. Shading denotes negative values.

35

Table 3.2. Comparison of tangent linear and nonlinear perturbation forecasts as in the lower portion of Table 3.1, except the perturbation consists of + 2° C at nine grid points on sigma level 5 near 250 hPa in the region of largest negative ∂J/∂T at initial time. Forecast length is 90 h.

Forecast	u(σ=0.23) m s⁻¹	v(σ=0.23) m s⁻¹	T(σ=0.75) °C	Pressure hPa
90 h Tangent	-.391 (108,35)	-.224 (104,31)	-.057 (104,30)	-.201 (73,38)
Nonlinear	-.353 (110,34)	-.210 (104,31)	-.055 (106,29)	-.237 (73,39)

situation. Errors due to nonlinearity will be largest for perturbations in high sensitivity regions, that is, for the fastest growing perturbations. Effects of perturbation size and basic state update interval on adjoint accuracy are discussed by Errico et al. (1993a).

Based on these results, it appears that the tangent linear model is able to provide a satisfactory forecast of wind, temperature, and pressure perturbations for this simulation, even over 90 h. *It is therefore possible to have confidence in the validity of the adjoint sensitivity results.* Chapter III.A.3 will describe sensitivity results at the initial time (0 h), in which the adjoint model is integrated backwards in time for 90 hours, at 30 h (60 h adjoint integration), and at 70 h (20 h adjoint integration).

3. Sensitivity to Primary Prognostic Variables

a. *Initial Conditions*

Adjoint sensitivity patterns are first examined for the initial conditions, as determined by a backward integration of the adjoint model over 90 h. The sensitivities to initial temperature (∂J/∂T) and meridional wind (∂J/∂v) are shown in east-west vertical cross-sections through the center of the zonal jet (Fig. 3.5a,b). In areas of negative (positive) sensitivity, a positive perturbation will decrease (increase)

Figure 3.5: East-west vertical cross-sections (A-B indicated in Fig. 3.6) of adjoint sensitivity to (a) initial temperature $\partial J/\partial T$ (contour = 0.01 hPa K^{-1}) and (b) meridional wind, $\partial J/\partial v$ (contour = 0.001 hPa m^{-1} s) at 0 h. Negative values are shaded. Heavy solid line surrounding cross-hatched area corresponds to the 40 m s^{-1} contour of the jet streak in the initial conditions. Forecast aspect J is pressure at center of 90 h cyclone.

90 h pressure (J). Note that the units of the adjoint variables, which are gradients, depend on the choice of J.

The sensitivity to both temperature and meridional wind is largest in the lower troposphere between 600 - 900 hPa, and tilts westward with height. Closer to the surface, the sensitivity is damped by boundary-layer processes. Damping of near-surface perturbation growth is consistent with other adjoint sensitivity studies, e.g., Buizza et al. (1993), and with modeling studies, including Valdes and Hoskins (1988), that show surface friction reduces baroclinic growth rates. The horizontal scale of the sensitivity structures in Fig. 3.5 is similar to that of the 90 h cyclone (Fig. 3.3) and the strongest sensitivity is located below the initial upper tropospheric anomaly (jet streak).

The adjoint sensitivity to initial surface pressure ($\partial J/\partial p_S$) indicates that the 90 h cyclone will be intensified if the initial pressure under the jet streak is reduced (Fig. 3.6, location "L"). The surface pressure sensitivity is geostrophically consistent with lower tropospheric $\partial J/\partial v$ (Fig. 3.5b) and $\partial J/\partial u$ (not shown), which imply a cyclonic circulation around "L" at the initial time. In addition, a reduced pressure at "L" is hydrostatically consistent with the temperature sensitivity, in that $\partial J/\partial T$ implies a net warming of the column (lower average density) above "L" is cyclogenetic.

The vertical variations in sensitivity imply that temperature perturbations at 250 hPa must be on the order of 10 times those at 760 hPa to have comparable effects on the forecast surface pressure. The second column of Table 3.3 summarizes the response of J to one-unit perturbations placed at single grid points having the largest sensitivity on model levels near 250 hPa and 760 hPa.

38
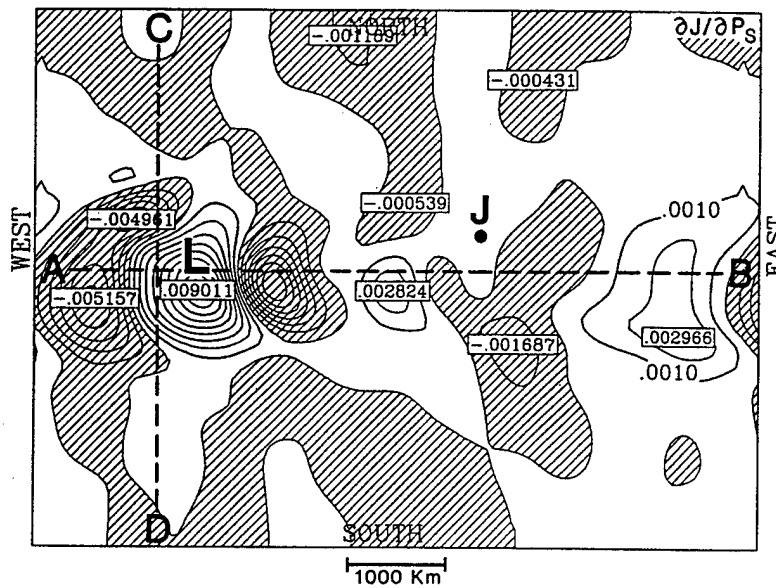
Figure 3.6: Adjoint sensitivity to initial surface pressure $\partial J/\partial p_S$ (contour interval = 0.001). Negative values are shaded. Location "L" indicates a region where a negative pressure perturbation in the initial conditions will deepen the 90 h cyclone. Forecast aspect J is pressure at center of 90 h cyclone.

Table 3.3. The 90 h pressure change (J') implied by adjoint sensitivity resulting from perturbations of basic state wind and temperature near 250 hPa and 760 hPa. Perturbations are located in region of largest negative sensitivity on each level at 0 h. Column 2 uses single-point positive-signed one unit perturbations (1 m s^{-1}, 1° C). Column 3 uses positive-signed perturbations scaled to five percent of basic state value at the same grid point. There is no initial basic state meridional wind at 760 hPa.

Perturbation	One unit	Five percent
250 hPa u	-.0055 hPa	-.0042 hPa
250 hPa v	-.0030	-.0012
250 hPa T	-.0048	-.0495
760 hPa u	-.0122 hPa	-.0067 hPa
760 hPa v	-.0080	---
760 hPa T	-.1186	- 1.573

Perturbations of wind and temperature in the lower troposphere can produce a greater response than equal perturbations in the upper troposphere. The same conclusion applies for perturbations scaled to five percent of the initial basic state field value

39
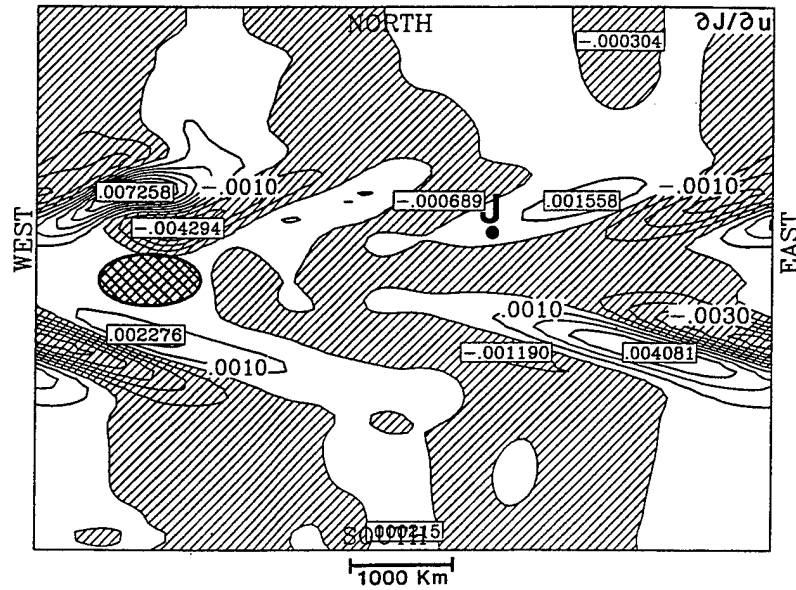
Figure 3.7: Adjoint sensitivity to initial 250 hPa zonal wind $\partial J/\partial u$ (contour = 0.001 hPa m^{-1} s). Negative values are shaded. Heavy solid line surrounding cross-hatched area corresponds to the 40 m s^{-1} contour of the jet streak in the initial conditions. Forecast aspect J is pressure at center of 90 h cyclone.

(third column of Table 3.3). Although zonal wind speed is greater at 250 hPa than at 760 hPa, the effect on J is still larger from lower tropospheric perturbations. The example in Table 3.3 does not rule out possible effects of strong temperature or wind perturbations over large areas of the upper troposphere. However, the impact of very large perturbations cannot be evaluated accurately using tangent linear or adjoint models. In such cases, the complete sensitivity must be resolved with a nonlinear simulation.

Above 500 hPa, the sensitivity structure (Fig. 3.5) is nearly vertical, which suggests a barotropic pattern. The u-component wind sensitivity near 250 hPa (Fig. 3.7) is zonally elongated, with maximum amplitude on either side of the jet core. This pattern seems generally consistent with the discussion of optimal perturbations for barotropic flows in Farrell and Moore (1992) and Molteni and Palmer (1993). As
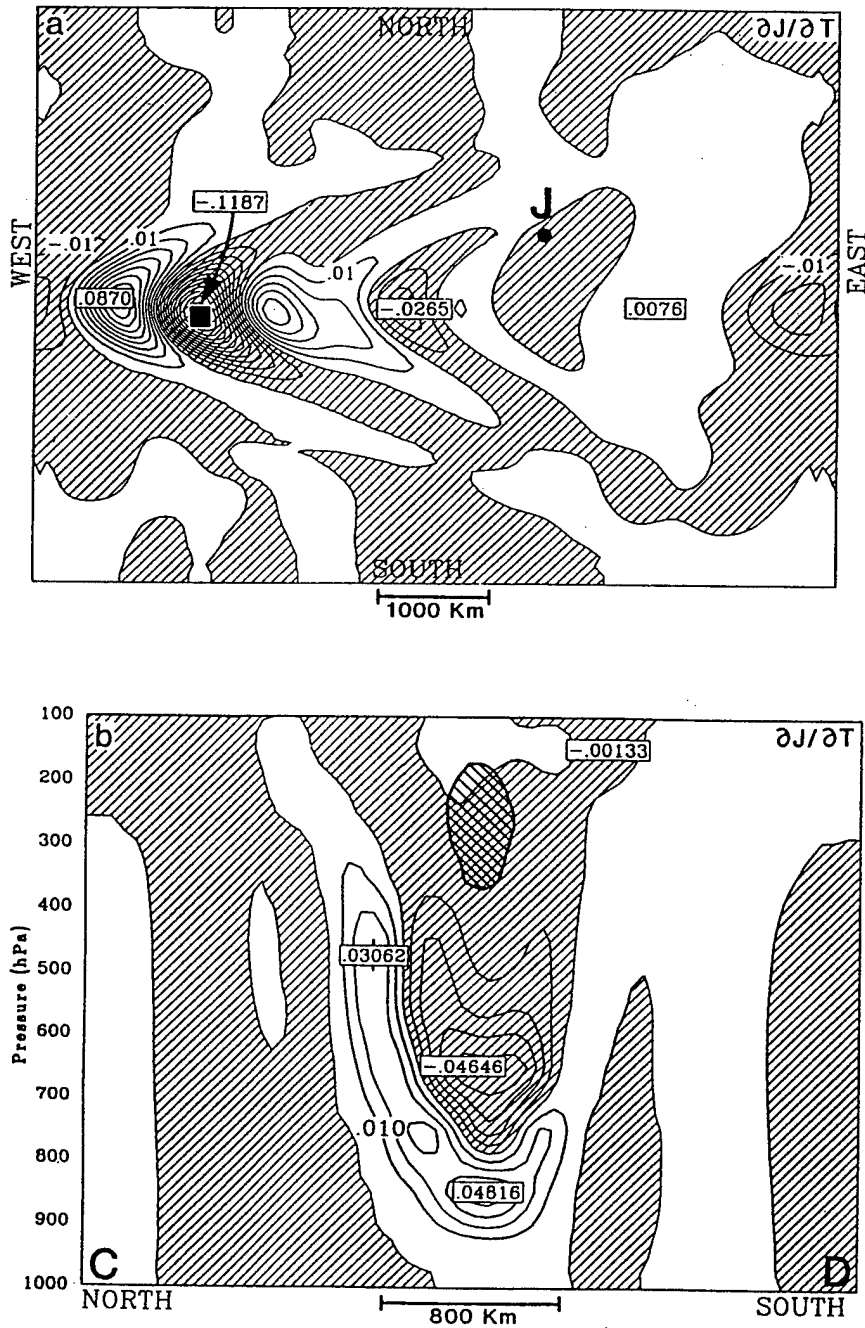
Figure 3.8: (a) Adjoint sensitivity to initial 760 hPa temperature $\partial J/\partial T$ (contour = 0.01 hPa K^{-1}). Solid square is location of test perturbation used in Table 3.1.and Fig. 3.4; (b) $\partial J/\partial T$ at 0 h as in Fig. 3.5a, except for north-south vertical cross-section (C-D indicated in Fig. 3.6). Negative values are shaded. Heavy solid line surrounding cross-hatched area corresponds to the 40 m s^{-1} contour of the jet streak in the initial conditions. Forecast aspect J is pressure at center of 90 h cyclone.

noted by Simmons and Hoskins (1980) and Thorncroft et al. (1993), barotropic mechanisms can have significant influence on baroclinic flows. The sensitivity in Fig. 3.7 depicts how barotropically unstable initial perturbations may be configured to destabilize the shear of the mean zonal flow, and lead to intensification of the 90 h cyclone. However, the sensitivity also includes baroclinic influences that are dynamically consistent with changes to temperature at lower levels.

The temperature sensitivity near 760 hPa (Fig. 3.8a) is largest in the center of the baroclinic zone and is suggestive of normal mode perturbations, with the crescent shape on the sigma level resulting from a combination of upshear tilt of the sensitivity structure and zonal elongation to the side of the jet core. The sensitivity resembles an x-periodic Rossby wave with an alternating +/- potential vorticity pattern as shown in Fig. 17 of HMR85.

A north-south vertical cross-section of $\partial J/\partial T$ through the center of the initial jet streak (Fig. 3.8b) shows that a positive temperature perturbation at 700 hPa (in the region of negative $\partial J/\partial T$ below the jet core) or negative temperature perturbations to the north of the jet axis would be favorable for cyclone intensification. That is, an increase of the north-south temperature gradient and corresponding vertical wind shear in this location is cyclogenetic. However, the effect of warming (or cooling) the entire column under the jet core would be small because $\partial J/\partial T$ has areas of both positive and negative sensitivity and the effect of the perturbations would partially cancel in the vertical integration.

The westward tilt of sensitivity to meridional wind perturbations in the lower troposphere (Fig. 3.5b) corresponds to the streamfunction axis of a developing baroclinic wave. A trough axis is implied by the zero contour of $\partial J/\partial v$, with negative
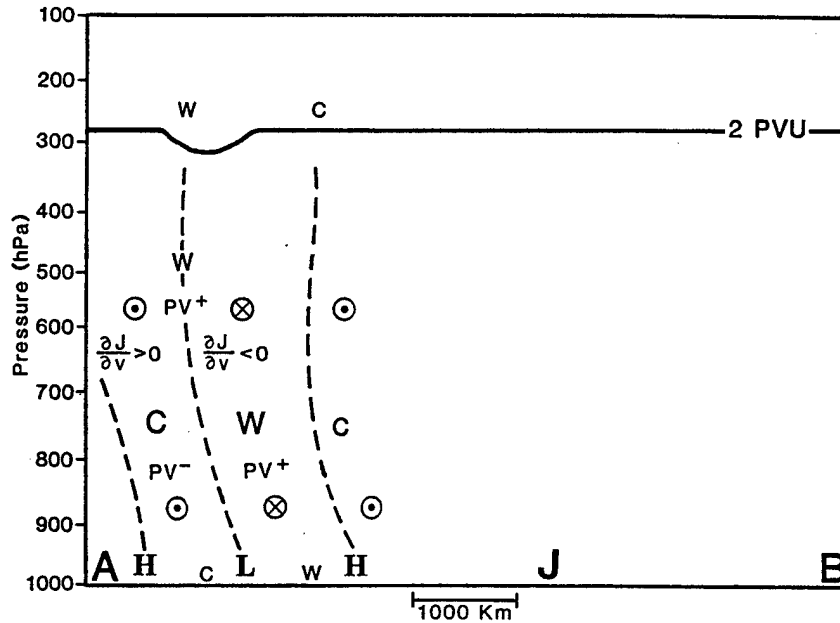
Figure 3.9: Conceptual diagram (scaled to size of east-west vertical cross-section, Fig. 3.5) of trough and ridge axes implied by adjoint sensitivity to meridional wind $\partial J/\partial v$ for initial conditions. Direction of cyclogenetic meridional wind represented by $\otimes$ (northward), $\odot$ (southward). **W** and **C** show where positive and negative temperature perturbations are cyclogenetic (size of letter roughly proportional to sensitivity gradient). **PV+** and **PV -** indicate where positive and negative potential vorticity anomalies are cyclogenetic. **H** and **L** identify ridge and trough axes, respectively. Solid line is 2 PVU contour (1 PVU = 10^{-6} m^2 K s^{-1} kg^{-1}). Forecast aspect J is pressure at center of 90 h cyclone.

sensitivity to the east and positive sensitivity to the west (see conceptual diagram Fig. 3.9). A cyclogenetic perturbation involving meridional wind will slope westward with height according to Fig. 3.5b. The sensitivity structure for temperature perturbations ($\partial J/\partial T$) also slopes westward with height in the lower troposphere (Fig. 3.5a). Near 800 hPa, $\partial J/\partial T$ is offset by about one half wavelength from the trough axis implied by $\partial J/\partial v$, so that initial perturbations configured to enhance thermal advection are strongly cyclogenetic. That is, warm advection ahead of the trough and cold advection behind the trough will decrease J (90 h cyclone pressure). Above 800 hPa, the maximum temperature sensitivity is closer to the implied trough axis, so that thermal

advection will contribute less. This corresponds qualitatively to effects of differential temperature advection, which is the primary mechanism for amplification of midlatitude cyclones in the quasi-geostrophic system (Holton 1992, Chapt. 6).

It is interesting that the westward tilt of the temperature *sensitivity* differs from the typical eastward tilt of temperature in a baroclinic wave (e.g., Hoskins and Heckley 1981). A westward tilt of adjoint temperature sensitivity is also noted by RCT92, who used forecast aspects different from that used here, so this sensitivity feature is probably not anomalous. The axis of warm air in the basic state extends upward from the surface low toward the upper-tropospheric ridge, as must be true for hydrostatic reasons. The adjoint sensitivity therefore implies that cyclone development is not enhanced by temperature perturbations along the basic state thermal axis in the middle and upper troposphere. Instead, middle- and upper-tropospheric temperature perturbations are most influential in the neighborhood of the streamfunction axis, where the strongest sensitivity to wind perturbations is also found. The sensitivity field does not necessarily have to resemble the basic state temperature pattern, since $\partial J/\partial T$ is not a temperature field, but rather a gradient field that describes how temperature perturbations can change the forecast aspect (J).

It is possible to construct a sensitivity to a linearized form of quasi-geostrophic potential vorticity using $\partial J/\partial u$, $\partial J/\partial v$, and $\partial J/\partial T$. The sensitivity to this quantity is also largest in the lower troposphere (indicated by **PV +** in Fig. 3.9). When a potential vorticity anomaly is said to "induce" a cyclonic circulation, this corresponds to effects of wind, temperature and pressure perturbations that represent the anomaly. Conceptually, the potential vorticity viewpoint is another way of describing the integrated effects of forcing that can be considered separately in a

44

quasi-geostrophic context as (differential) thickness and vorticity advection. Adjoint sensitivity includes all physical processes of the nonlinear model, and does not depend on assumptions such as conservation of potential vorticity to transmit the effects of selected perturbations.

According to Fig. 3.5, a temperature or wind perturbation at, say, 500 hPa must be larger and farther upstream than one at 760 hPa to have equivalent effects on the 90 h surface pressure. If perturbations near 500 hPa correspond to a positive potential vorticity anomaly, they can induce a cyclonic circulation (according to "PV-thinking") with warm advection below, and slightly ahead of the anomaly. If the warm advection is to reinforce the 500 hPa PV anomaly, the sensitivity $\partial J/\partial T$ should be negative in the region of warming, which is the pattern in Fig. 3.5. The warm advection ahead of the trough axis has a cyclogenetic effect by inducing cyclonic flow above it that advects higher potential vorticity southward into the upper anomaly, which creates a "phase-locking" situation (HMR85, McIntyre 1988), so long as the upper anomaly is slightly west. The upper PV feature might be a short-wave trough combining wind and temperature anomalies, as in a type-B development (Petterssen and Smebye 1971).

When the initial anomaly used to initiate a cyclone in the nonlinear model is placed in the lower troposphere (centered at 760 hPa, directly below the position in Fig. 3.1), the resulting adjoint sensitivity pattern (Fig. 3.10a) is not that different from the sensitivity for the original basic state (Fig. 3.5a). Maximum sensitivity is still in the lower troposphere and has about the same magnitude. In a nonlinear forecast with the lower-tropospheric anomaly, the surface pressure begins to decrease much more quickly (dotted line, Fig. 3.2) than in the forecast with the

45
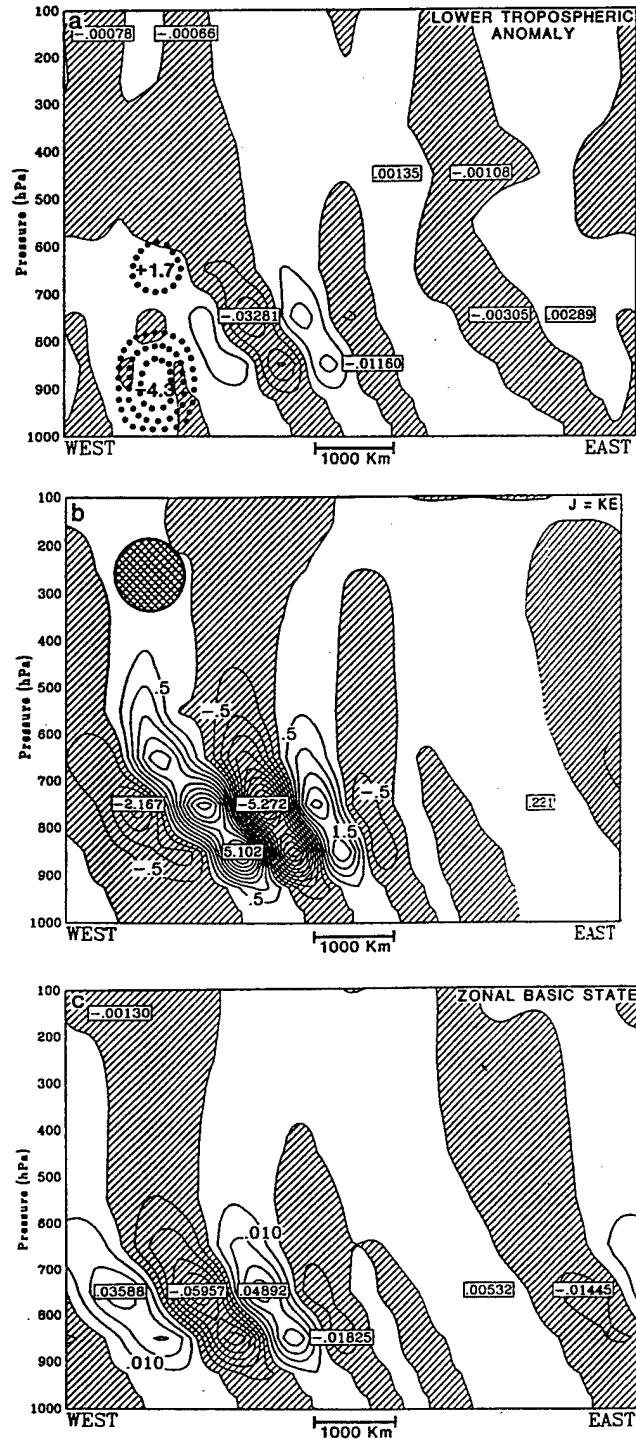
Figure 3.10: East-west vertical cross-sections of adjoint sensitivity to initial temperature $\partial J/\partial T$ as in Fig. 3.5a, for (a) initial anomaly in lower troposphere (dotted contour = 1 °C); (b) J = kinetic energy [$u^2 + v^2$], $\partial J/\partial T$ contour = 0.05 m s^{-1} K^{-1}; and (c) purely zonal basic state (no initial upper tropospheric jet streak). Negative values are shaded. Heavy solid line surrounding cross-hatched area in (b) corresponds to the 40 m s^{-1} contour of the jet streak in the initial conditions.

initial upper-tropospheric anomaly (solid line, Fig. 3.2). Apparently, placing the anomaly in the lower troposphere causes baroclinic instability to develop more rapidly. This is a good example of how changing the initial perturbation structure can influence transient growth rates according to the ideas of Farrell (1989).

The sensitivity is also not highly dependent on specification of the initial lapse rate or drag coefficients. Changes to these factors can alter the intensity or location of the 90 h cyclone to some extent, but the sensitivity to perturbations of initial wind and temperature remains localized in the lower troposphere (not shown).

As an example of sensitivity using a different forecast aspect, J is defined as a simple approximation to near-surface kinetic energy ($u^2 + v^2$) in the center of the 90 h cyclone (Fig. 3.10b). The sensitivity remains concentrated in the lower troposphere, although $\partial J/\partial T$ has changed sign, which indicates that a decrease in 90 h pressure is accompanied by an increase in lower tropospheric kinetic energy.

The adjoint sensitivity does not, by itself, confirm that physical processes in particular locations are important to cyclone development. To illustrate this principle, a vertical cross-section of $\partial J/\partial T$ for a basic state in which all fields are purely zonal over a 90-h period is shown in Fig. 3.10c. No cyclone development occurs, yet the sensitivity pattern is generally similar to one in which the basic state does contain a cyclone (Fig. 3.5a). Therefore, the adjoint sensitivity, by itself, pertains only to the effects of *possible* changes and is not an indicator of physical processes such as temperature advection or surface heat fluxes that actually occurred in the nonlinear basic state forecast. An alternate approach is to consider the adjoint sensitivity in association with tendencies of temperature, wind, or pressure obtained from the nonlinear forecast, as discussed in the remainder of this section.

47

b. Pre-Deepening Phase

Conditions at 30 h are representative of the environment prior to the period of most rapid surface pressure falls. The central pressure of the incipient cyclone is 998 hPa, located below the right-rear quadrant of the main 250 hPa jet streak, which has propagated ahead of the surface disturbance. The basic state trough axis that extends from the surface to 250 hPa tilts westward with height and the axis of basic state temperature tilts eastward with height. The PV anomaly associated with the jet streak is not extremely strong in this simulation compared to many observed cases of extratropical cyclogenesis.

In addition to using adjoint sensitivity to estimate the effect of possible changes to basic state variables, sensitivity effects that correspond to physical processes, such as temperature advection, may also be considered. Sensitivity to a physical process involving more than one predictive variable cannot be obtained directly from the adjoint model. For example, temperature advection ($-\mathbf{V} \cdot \nabla T$) depends on zonal and meridional wind components and temperature. Perturbations (u', v', T') can be combined in different ways to change the magnitude of temperature advection by an equivalent amount, but these perturbation configurations are not likely to have an identical effect when projected (as an inner product) onto adjoint sensitivity fields to obtain J', so that adjoint sensitivity with respect to the physical process of temperature advection is not uniquely defined.

Alternately, a physical process may be considered in terms of an *effect on a prognostic variable*. For example, temperature advection produces a tendency of temperature. If the process is intensified at a particular location, the effect may be considered as a temperature perturbation, and the response of J can be estimated

using the adjoint sensitivity field $\partial J/\partial T$. The response (J') implied by adjoint sensitivity does not depend on the source of a perturbation; T' could be an arbitrary modification, the result of an analysis change, or represent a change to a physical process.

The "total" tendencies (sum of all processes) are obtained from differences of zonal and meridional wind and temperature between 29 and 31 h, and represent the effects of physical processes at this stage of the cyclone development. The tendencies of wind and temperature are largest near jet level in the upper troposphere, decrease towards the middle troposphere, and have a secondary maximum closer to the surface (Fig. 3.11a).

Perturbations of wind and temperature are then chosen to be proportional to the size of these nonlinear tendencies, with larger perturbations in locations where tendencies are largest. Thus, the perturbations represent an increase in the nonlinear tendency, while keeping the relative strength equal at all locations. At each grid point, the perturbation magnitude is equal to an adjustment of wind or temperature over a one-hour interval, as determined from the nonlinear tendencies. The product of these perturbations and the adjoint sensitivity at each grid point (e.g., equation (2.7)) are summed on each model level (Fig. 3.11b). Although temperature and wind *tendencies* are smaller on average in the lower troposphere (Fig. 3.11a), the sensitivity there is considerably larger (as at 0 h), and perturbations of lower tropospheric tendencies can be more significant to cyclone development. In particular, strong cyclogenetic effects appear related to perturbations of meridional wind and temperature below 600 hPa, which implies effects of temperature advection. The spike in Fig. 3.11b related to temperature near 850 hPa suggests a critical layer,

49
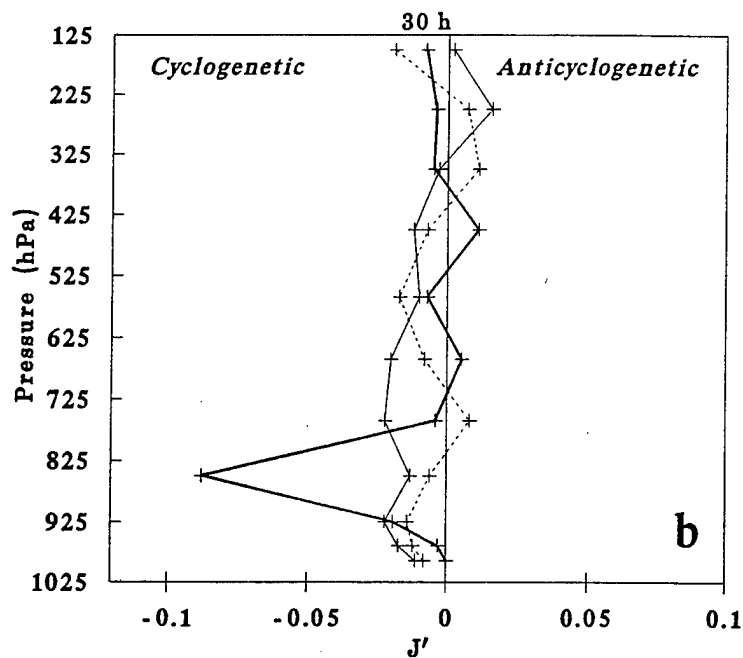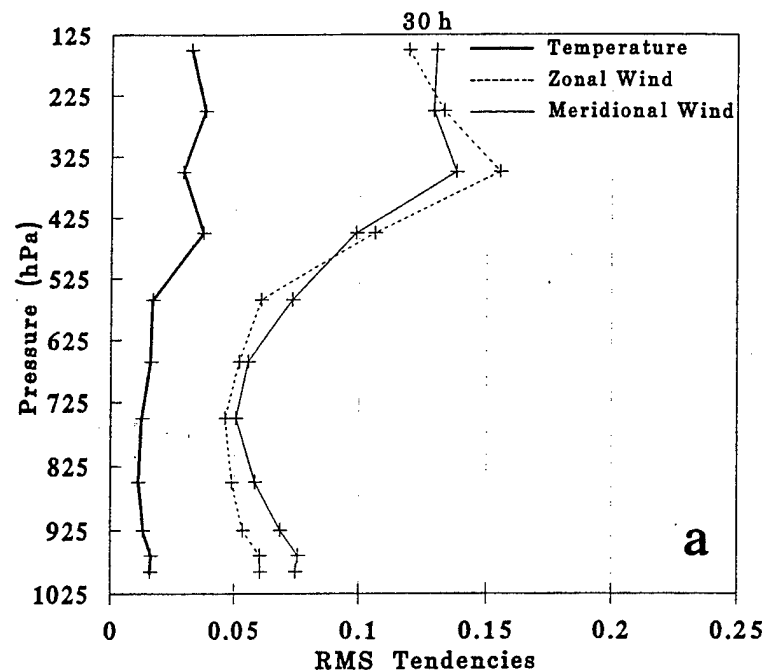
Figure 3.11: (a) Root mean square (on sigma levels) of nonlinear model tendencies of zonal and meridional wind (m s^{-1} h^{-1}) and temperature (K h^{-1}) obtained as a two-hour difference centered at 30 h; (b) Dot product of perturbations (one-hour wind or temperature adjustment) and 30 h adjoint sensitivity, summed on sigma levels. Units of J' are hPa, negative values indicate an increase in nonlinear tendency produces a negative pressure perturbation (J') at center of 90 h cyclone. Crosses correspond to model levels.
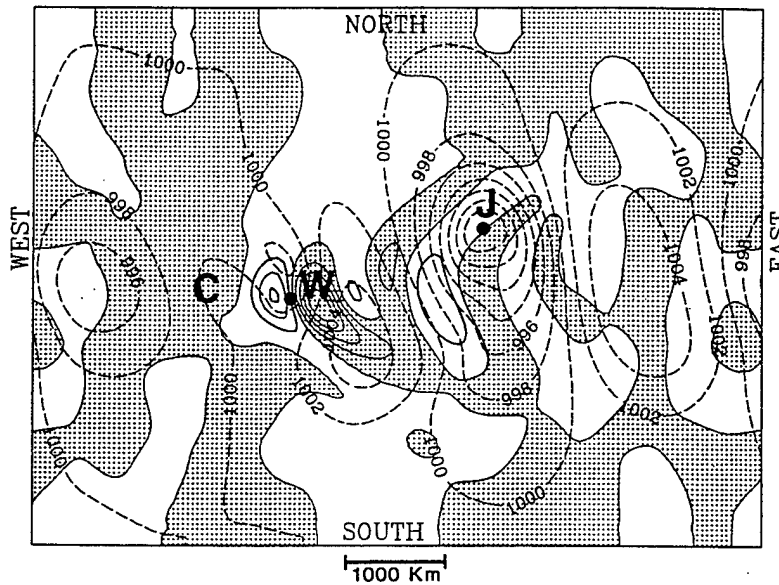
Figure 3.12: Adjoint sensitivity to 850 hPa temperature $\partial J/\partial T$ at 30 h (solid contour = 0.01 hPa K^{-1}). Negative values shaded. Solid dots are cyclone position for 30 h and 90 h (J). 90 h surface pressure (contour = 2 hPa, dashed). **W** and **C** indicate locations of maximum warm and cold temperature advection at 850 hPa. Forecast aspect *J* is pressure at center of 90 h cyclone.

although the largest *sensitivity* is closer to 760 hPa. When this method is applied to the example of the purely zonal basic state (Fig. 3.10c), there are no basic state tendencies and therefore no attribution of cyclogenetic effects to any physical processes, which is the correct interpretation.

The temperature sensitivity ($\partial J/\partial T$) near 850 hPa (Fig. 3.12) depicts localized areas of strong sensitivity near the developing surface pressure center at 30 h. The effect of temperature perturbations will be cyclogenetic for warming ahead of the low and cooling behind the low. In these locations, horizontal temperature advection is the most significant process producing temperature tendencies. An increase in warm advection ahead of the low would be strongly cyclogenetic, since the position of maximum warm advection in the basic state is close to the minimum of $\partial J/\partial T$. Strengthening cold advection behind the low does not appear to have as strong

51

an effect. Adiabatic cooling in the region of upward motion ahead of the cyclone is anticyclogenetic.

Physical processes may produce tendencies of temperature or wind in regions of weak sensitivity. For example, temperature advection in certain regions of the upper troposphere produces relatively large temperature tendencies, but an increase or decrease in strength of this process will have a relatively small effect on the forecast measure (J) in this cyclogenesis. A rule of adjoint sensitivity interpretation is suggested:

> *Physical processes that produce large tendencies in regions of strong*
> *adjoint sensitivity are significant to the feature or statistic represented*
> *by the forecast aspect (J).*

The importance of lower tropospheric processes in this early stage of the cyclone life cycle is supported by conceptual models of baroclinic development presented in Hoskins et al. (1983) and HMR85. According to this view, eddy activity in a storm track originates in the lower troposphere (steering level in the Charney model) through linear baroclinic instability, with subsequent propagation of the instability into the upper troposphere. The steering level in this simulation is between 750 and 800 hPa, where the disturbance phase speed (12 m s^{-1}) and basic state zonal wind are approximately equal, and this is also the region where the adjoint indicates maximum sensitivity. As shown by Edmon et al. (1980) strong divergence of Eliassen-Palm flux (implying a poleward flux of quasi-geostrophic potential vorticity) exists near the steering level in the lower troposphere for the Charney mode. Lindzen et al. (1980) and Robinson (1989) show that Charney and Green baroclinic modes are essentially "critical layer" instabilities that exist between the steering level and the "surface" (thermal anomalies just above the boundary layer), even if unstable

52

eigenmodes exist above the steering level. The strong sensitivity to temperature and wind perturbations at the steering level identified by adjoint sensitivity appears related to the Charney mode interpretation. The steering level instability in this simulation is initiated by a relatively weak upper tropospheric anomaly, and cyclone intensification begins when the lower tropospheric instability is established.

c.   Deepening Phase

At 70 h, the central pressure is 992.8 hPa, and the cyclone is deepening at approximately 0.5 hPa h^{-1}. The surface low pressure center is below the right-rear quadrant of a 42 m s^{-1} jet streak at 250 hPa and the left-front quadrant of an upstream 37 m s^{-1} jet streak at 250 hPa. Strong temperature advection is present in the lower troposphere and also in association with an upper tropospheric trough and sloping tropopause. The maximum sensitivity to wind and temperature determined by the adjoint model is still in the lower troposphere, and localized above the surface cyclone as at 0 h and 30 h.

Tendencies of wind and temperature from the nonlinear forecast (obtained from differences of wind and temperature between 69 and 71 h) are depicted in Fig. 3.13a. Compared to 30 h, the average tendencies are larger on nearly all levels, with most significant increases in the middle and lower troposphere. Following the method applied at 30 h, perturbations that are proportional to the nonlinear tendencies are projected onto the 70 h adjoint sensitivity at each grid point and summed for each model level. As shown in Fig. 3.13b, increases in lower tropospheric temperature tendencies (primarily due to temperature advection) are strongly cyclogenetic, as are perturbations related to meridional wind tendencies in a layer from about 350 hPa to 750 hPa.
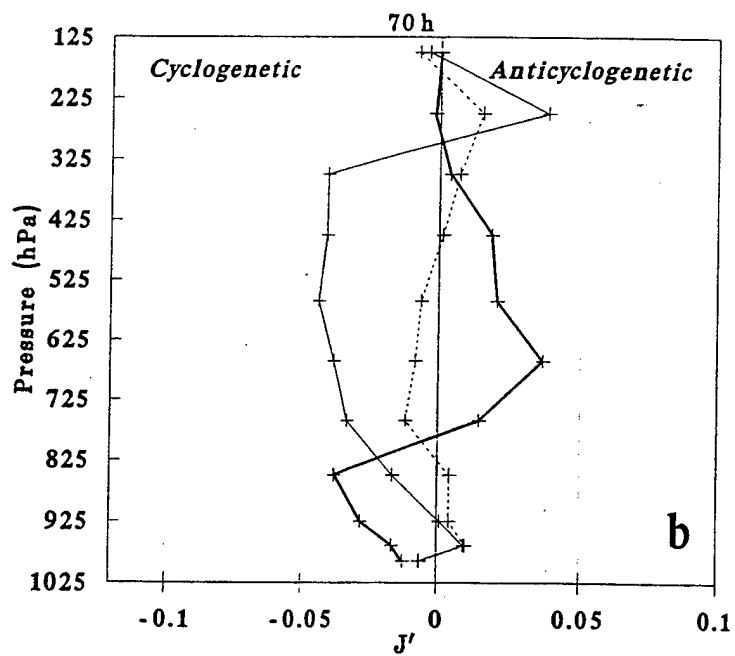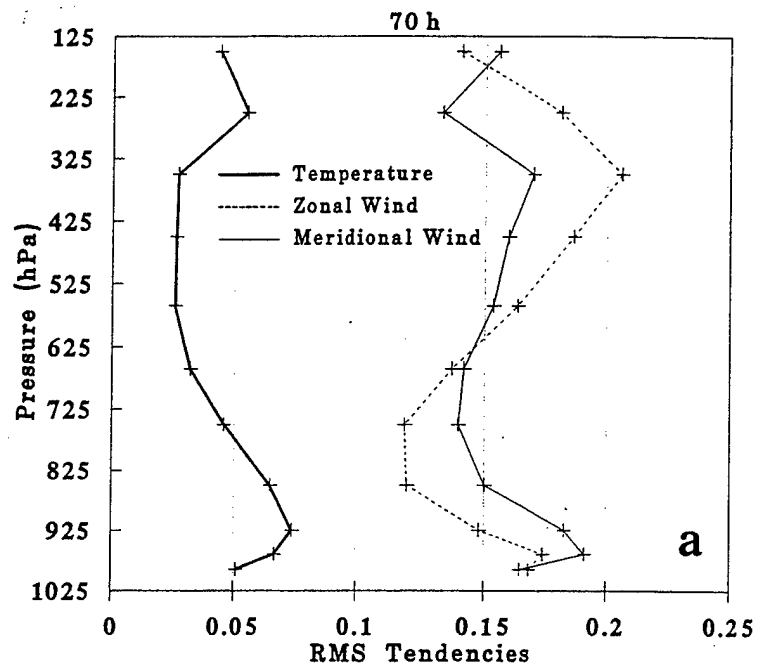
Figure 3.13: As in Fig. 3.11, using nonlinear tendencies and sensitivity at 70 h.
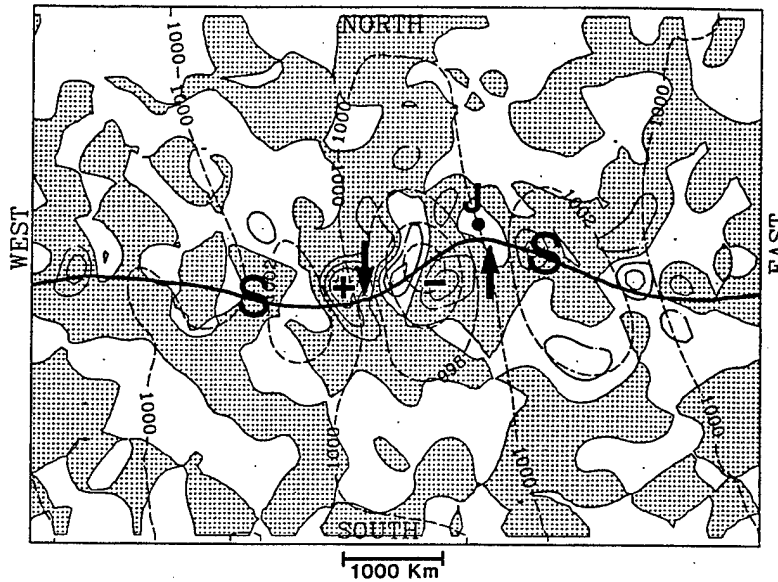
Figure 3.14: Product of 450 hPa adjoint sensitivity to meridional wind $\partial J/\partial v$ (70 h) and v′, with v′ proportional to one-hour basic state tendency (contour = 0.0001 hPa). Negative values are shaded and represent regions in which increasing the nonlinear tendency of meridional wind decreases 90 h central pressure. Basic state surface pressure at 70 h (contour = 2 hPa, dashed). Jet axis indicated by heavy solid line. **S** = positions of jet streaks at 250 hPa. (**+**) and (**-**) indicate centers of positive and negative sensitivity ($\partial J/\partial v$). Arrows pointing upward (downward) indicate nonlinear tendency of meridional wind is northward (southward). Forecast aspect J is pressure at center of 90 h cyclone.

The product (v′ · $\partial J/\partial v$) on a level near 450 hPa is represented in Fig. 3.14. In locations where v′ is negative (southward) and $\partial J/\partial v$ is positive (**+** in Fig. 3.14), an increase in the nonlinear tendency creates a negative J' (decreases the 90 h cyclone pressure). A stronger southward wind at **+** will increase cyclonic vorticity ($\partial v/\partial x$) above the surface low, and divergence ($\partial v/\partial y$) in the jet exit region upstream of the surface low, conditions which are known to be cyclogenetic. Temperature sensitivity (not shown) indicates that cooling below **+** (implying increased trough amplitude) is cyclogenetic. Amplifying the upper tropospheric ridge ahead of the surface disturbance also has a cyclogenetic effect. In this phase of the cyclone life

55

cycle, the forecast central pressure is strongly influenced by physical processes in both the upper and lower troposphere.

It is noted that the regions of significant sensitivity at 30 h and 70 h are much more localized than the sensitivity for the initial conditions, and the sensitivity magnitude is larger at the initial time than at 30 h or 70 h. The increase in sensitivity magnitude at longer times indicates that perturbations in high sensitivity regions result in forecast perturbations that grow with time (demonstrated in Table 3.1). Whereas the initial-time sensitivity appears related to normal mode type structures, the sensitivity at 30 h and 70 h probably includes non-modal (continuous spectrum) features. That is, the cyclone scale and intensity over the full 90 h are determined by normal mode considerations, so the most effective perturbations are those that enhance the normal mode structure (e.g., Figs. 3.5, 3.7, and 3.8). Perturbations of non-modal form may affect short-term growth, but will decay before 90 h. Non-modal perturbations are much more likely to be significant for shorter forecast intervals (Farrell 1984). The highly-localized sensitivity at 30 h and 70 h represents the type of non-modal perturbation structures that can influence cyclone development on shorter time scales. The studies of Borges and Hartman (1992) and Molteni and Palmer (1993) also note increasingly localized structures as optimization time decreases. For intervals of less than about six hours, a gravity wave signal may appear relatively large in the sensitivity. For longer times, the gravity wave contribution to sensitivity remains, but is masked by the effects of other processes.

4. Sensitivity to Sea-surface Temperature and Surface Sensible Heat Flux

The adjoint method can describe sensitivity to external forcing conditions, such as sea-surface temperature (SST). For example, the hypothesis that a higher SST in
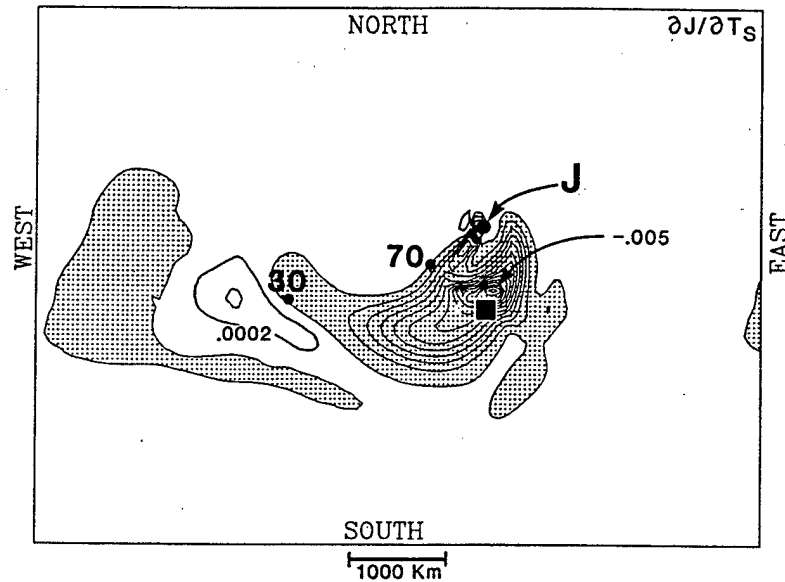
Figure 3.15: Adjoint sensitivity to surface temperature $\partial J/\partial T_S$ accumulated between 0 and 90 h (contour = 0.0004 hPa K^{-1}) for basic state without sea-surface temperature anomaly. Negative values are shaded and are regions where a higher surface temperature will deepen the 90 h cyclone. Solid dots are 30, 70, and 90 h cyclone positions. Solid square is location of test perturbation used in Table 3.4. Forecast aspect J is pressure at center of 90 h cyclone.

a certain region results in a more intense cyclone may be tested. When examining the SST sensitivity, it is appropriate to consider the *accumulated sensitivity* over the entire forecast since SST (in this model) is a lower boundary condition that remains constant in time.

The adjoint field $\partial J/\partial T_S$ in Fig. 3.15 depicts sensitivity to SST perturbations accumulated over 90 h. The most significant sensitivity is negative and located to the east and south of the 70 h cyclone position. This suggests that higher (lower) SST in the cyclone warm sector after 70 h will cause the 90 h central pressure to decrease (increase). There are regions where $\partial J/\partial T_S$ is positive, so that higher SST will increase 90 h central pressure, but this sensitivity is relatively weak.

57

Table 3.4. Comparison of tangent linear and nonlinear perturbation forecasts, in which the initial perturbation consists of + 2° C added to sea-surface temperature at nine grid points in region of negative $\partial J/\partial T_S$ (location shown in Fig. 3.15). Entries are largest negative perturbation for u, v, T, or p* with grid point location in parentheses. Forecast length is 90 h.

Forecast	$u(\sigma=0.23)$ m s^{-1}	$v(\sigma=0.23)$ m s^{-1}	$T(\sigma=0.75)$ °C	Pressure hPa
90 h Tangent	-.012 (18,37)	-.012 (9,32)	-.010 (78,30)	-.088 (78,30)
Nonlinear	-.047 (11,35)	-.049 (12,34)	-.009 (75,38)	-.104 (75,38)

An example of the effect of perturbing SST in the nonlinear and tangent linear models is provided in Table 3.4. Here, the SST perturbation consists of 2° C at nine grid points in a region of negative $\partial J/\partial T_S$ (see Fig. 3.15). For this initial SST perturbation, the TLM provides a fairly accurate estimate of surface pressure and 760 hPa temperature perturbations over 90 h, even though the TLM accuracy is generally better for initial perturbations of air temperature (e.g., Tables 3.1 and 3.2). The maximum sensitivity to SST perturbations is only about 10 percent of the largest sensitivity to atmospheric temperature perturbations, which is found near 760 hPa.

The effects of very large sea-surface temperature perturbations can not be evaluated with high accuracy over long forecast intervals using tangent linear or adjoint models. In such cases, the perturbation forecast can be highly nonlinear, and the complete sensitivity must be resolved with the nonlinear model. For instance, tangent linear systems can not be expected to provide accurate forecasts of situations in which SST perturbations change the surface layer stability over a large area.

The surface sensible heat flux may be expressed as

$$F_S = C_H \rho_K C_P V_K \left(\theta_S - \theta_K\right) \ , \tag{3.1}$$

where F_S has units of (W m^{-2}), ρ_K is surface layer air density, C_P is specific heat, θ_S is surface potential temperature, and θ_K is potential temperature on the lowest model

level. The surface sensible heat transfer coefficient C_H is assigned a fixed value equal to 1.0×10^{-3}. The wind speed V_K in (3.1) includes a convective velocity for light wind conditions (Anthes et al. 1987) that can greatly increase upward heat transfer under conditions of low wind speed in an unstable surface layer (upward heat flux). If surface temperature perturbations change the stability, the convective velocity acts as a switch that can cause the trajectory of the tangent linear forecast to enter a different regime and provide less accurate results.

The original nonlinear simulation contained a zonally invariant SST and relatively small contributions from surface heat transfer. This was useful for isolating the sensitivity to air temperature and winds with a simplified basic state. To explore surface temperature sensitivity under more interesting conditions, an alternate basic state is considered with a circular warm SST anomaly placed somewhat south of the
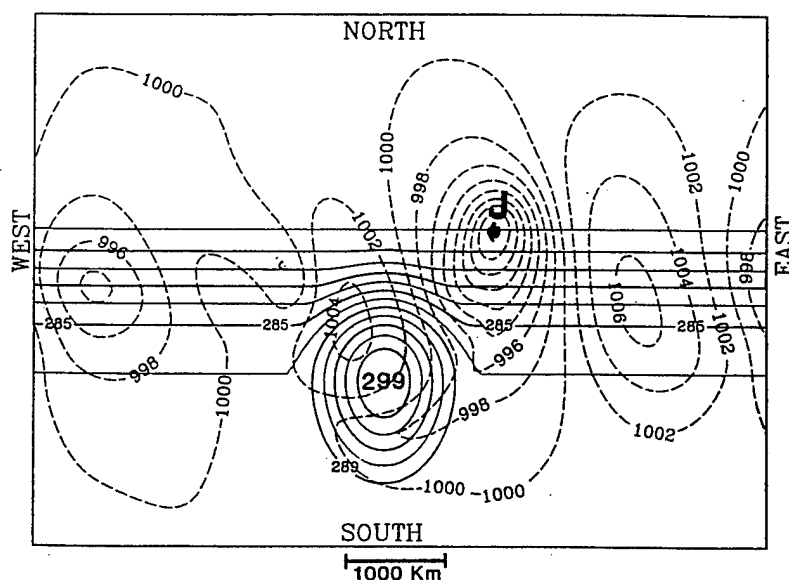
Figure 3.16: Sea-surface temperature (SST, solid contour = 2 K) and 90 h surface pressure (dashed contour = 2 hPa) in the nonlinear simulation with the SST anomaly in which 90 h central pressure = 983.4 hPa. Forecast aspect J is pressure at center of 90 h cyclone.

main baroclinic zone (Fig. 3.16). The anomaly has a magnitude of 12° C in the center, and decreases outward to zero at a radius of 960 km. The initial air-sea temperature difference of 12° C is similar to conditions near the Gulf Stream north wall during cold air outbreaks (Bane and Osgood 1989). This location was selected because the presence of higher sea-surface temperature in the nonlinear model intensifies the cyclone development, and the nonlinear forecast made with the anomaly provides a basic state in which surface heat fluxes have more influence on the cyclone development. A sea-surface temperature anomaly of similar magnitude in a different location (for example, in the cyclone cold sector) can damp, rather than enhance, the development of the cyclone.

The time series of surface pressure for this nonlinear forecast with the SST anomaly appears as a dashed line in Fig. 3.2. The central pressure at 90 h in the simulation with the SST anomaly is reduced by 2.2 hPa and the adjoint approximation to this effect is a pressure reduction of 1.0 hPa. Although the adjoint identifies the correct sign of the forecast pressure perturbation, the difference in magnitude is indicative of the nonlinear effects that may occur over 90 h with a large SST perturbation.

The effect of the warm SST anomaly is communicated through the surface sensible heat flux (F_S), which warms the lower troposphere and creates a strong "pre-conditioning" effect. The heated air is drawn into the cyclone warm sector, where it contributes to a more intense cyclogenesis. The remaining discussion in this section pertains to sensitivity on the basic state trajectory *with the warm SST anomaly present*. The forecast aspect (J) is defined at the center of the 90 h cyclone shown in Fig. 3.16.

The effects of surface sensible heat flux may be investigated by studying sensitivity to the parameter C_H, which appears only in the equation for surface-air heat transfer. Perturbations of C_H are included in the finite difference form of the TLM, as

$$ptten' = \frac{1}{\Delta\sigma_K}\left[C'_{H\,n-1}\overline{\rho}_{K\,n-1}g\overline{V}_{K\,n-1}\left(\overline{\theta}_{S\,n-1} - \overline{\theta}_{K\,n-1}\right)\right] \quad , \qquad (3.2)$$

where ( )' indicates a perturbation variable, ($\overline{}$) indicates a basic state variable, n is a time index, and $\Delta\sigma_K$ is the sigma thickness of the model surface layer. The quantity *ptten'* is used in the TLM to update the next time level of the mass-weighted perturbation temperature (p*T)' using

$$\left(p * T\right)'_{K\,n+1} = \left(p * T\right)'_{K\,n-1} + 2\Delta t \cdot ptten' \quad , \qquad (3.3)$$

where $2\Delta t$ is a leapfrog time step of the model from n-1 to n+1. The finite difference adjoint equation for ptten is derived from (3.3) as

$$\hat{ptten} = 2\Delta t \cdot \left(\hat{p * T}\right)_{K\,n+1} \quad , \qquad (3.4)$$

where $\hat{p*T} = \partial J/\partial(p*T)$ and $\hat{ptten}$ are adjoint variables. The finite difference equation for $\partial J/\partial C_H$ is derived from (3.2) as

$$\left(\frac{\partial J}{\partial C_H}\right)_{n-1} = \frac{1}{\Delta\sigma_K}\left[\hat{ptten}\,\overline{\rho}_{K\,n-1}g\overline{V}_{K\,n-1}\left(\overline{\theta}_{S\,n-1} - \overline{\theta}_{K\,n-1}\right)\right] \quad . \qquad (3.5)$$

Note that (3.4) and (3.5) are simply the transposes of (3.3) and (3.2), respectively. The sensitivity $\partial J/C_H$ in (3.5) can be accumulated over time to estimate the effect due to a perturbation of C_H that remains constant during a particular time interval, which could be the entire forecast.

The interpretation of positive $\partial J/\partial C_H$ is that F_S is anticyclogenetic, since a positive perturbation of C_H will increase F_S (equation (3.1)) and increase 90 h central pressure (J). A negative $\partial J/\partial C_H$ implies that F_S is cyclogenetic, since a positive perturbation of C_H will increase F_S, but J' will be negative.

In considering the effects of sensible heat flux, it is useful to divide the cyclogenesis with the SST anomaly into two phases before and after 60 h. The period before 60 h can be considered a "pre-conditioning" phase, and from 60 - 90 h the "deepening" phase. During the deepening phase, a strong sensitivity to sensible heat flux exists in the cyclone warm sector, where downward heat fluxes exist (shown at 70 h in Fig. 3.17a), but $\partial J/\partial C_H$ from 60 h to 90 h is strongly positive (Fig. 3.17b). Thus, the surface heat flux in the warm sector during the deepening phase *opposes* cyclogenesis. That is, if the downward heat flux in the warm sector were increased (by a positive perturbation of C_H), the 90 h cyclone central pressure would be higher. The upward heat flux in the cold sector is also anticyclogenetic, but the sensitivity is much smaller. The spatial correspondence between $\partial J/\partial C_H$ and F_S confirms the relation of C_H to the surface sensible heat flux.

Downward (or weak upward heat fluxes) are typical for the area immediately east of strong cold fronts in midlatitude cyclones (Petterssen et al. 1962, Fleagle and Nuss 1985, Neiman and Shapiro 1993). The anticyclogenetic effect of sensible heat fluxes during the later stages of cyclogenesis has been noted by Danard and Ellenton (1980), as related to the Laplacian of surface heating, and general weakening of horizontal temperature gradients across the storm center. Other studies that have shown anticyclogenetic (or minimal) effects of surface fluxes during the deepening phase include Kuo and Reed (1988) and Kuo et al. (1991a). However, Nuss and

62
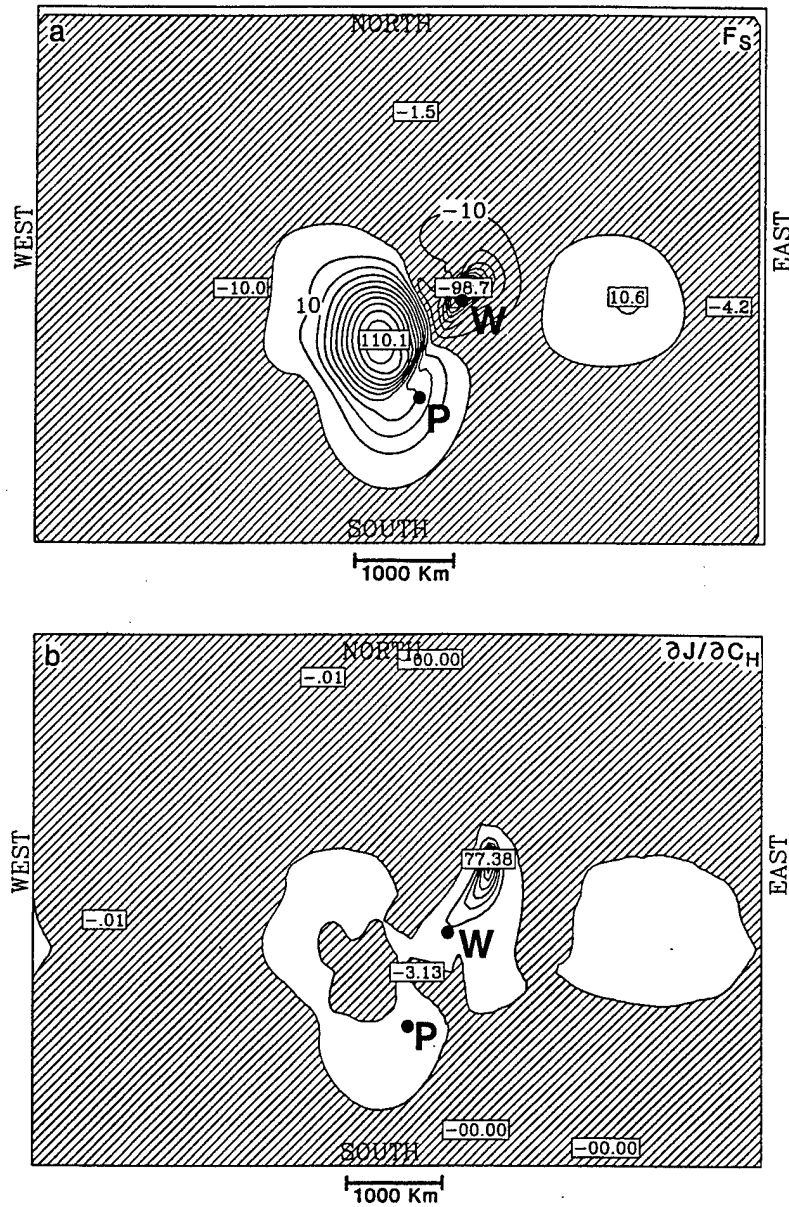
Figure 3.17: (a) Sensible heat flux (F_S, contour = 10 W m^{-2}, positive values are upward) at 70 h in the nonlinear forecast with SST anomaly; (b) adjoint sensitivity to surface heat transfer coefficient $\partial J/\partial C_H$ (contour = 10 hPa) accumulated between 60 and 90 h. Positive $\partial J/\partial C_H$ indicates F_S is anticyclogenetic for 90 h central pressure. Locations "P" and "W" refer to Fig. 3.18. Negative values are shaded.
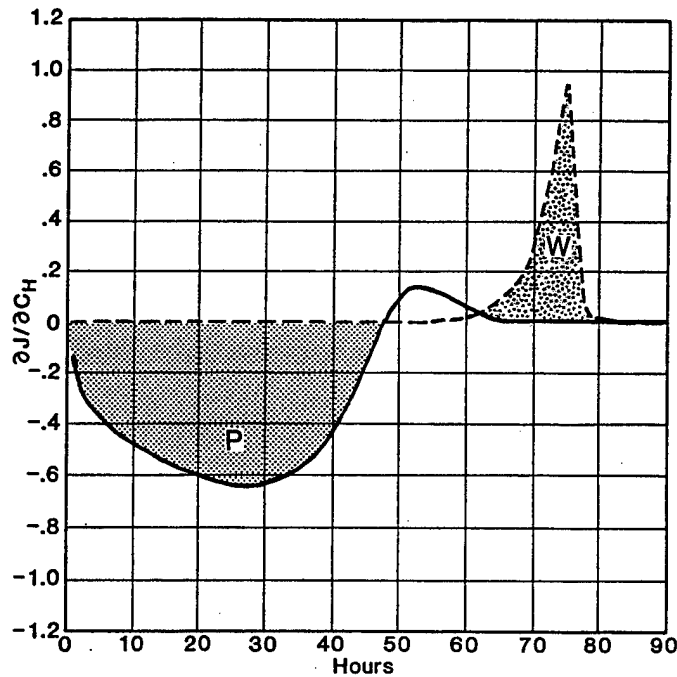
Figure 3.18: Time series of adjoint sensitivity to surface heat transfer coefficient $\partial J/\partial C_H$ (0.01 hPa) at locations "P" (solid line) and "W" (dashed line) for basic state with SST anomaly. Negative values (shaded) indicate period when upward sensible heat flux F_S near P acts to deepen the 90 h cyclone. Positive values (stippling) indicate period when downward F_S near "W" is anticyclogenetic. Locations of P and W shown in Fig. 3.17.

Anthes (1987) show there can be some cyclogenetic effect if surface heat fluxes are upward in parts of the warm sector.

In this cyclogenesis, there must also be a period during which F_S is cyclogenetic (and $\partial J/\partial C_H$ is negative) since surface heat flux associated with the warm SST anomaly produces a deeper cyclone. A time series of $\partial J/\partial C_H$ (Fig. 3.18) at location "P" (position shown in Fig. 3.17) indicates that the heat flux in that location contributes to cyclone deepening from 0 h to about 50 h, as the cyclone approaches and the surface heat flux is upward over the SST anomaly. The interpretation of negative $\partial J/\partial C_H$ here is that larger C_H and increased upward heat flux will deepen the low (decrease J). The cyclogenetic effects of surface heat fluxes during the early stage of cyclogenesis

are noted by Mailhot and Chouinard (1989), Grotjahn and Wang (1989), Fantini (1990), Kuo et al. (1991a), and others.

The time series of $\partial J/\partial C_H$ at location "W" in Fig. 3.18 indicates that anticyclogenetic effects of sensible heat flux occur between 60 h and 80 h, when "W" is in the cyclone warm sector and downward heat fluxes exist. Inspection of $\partial J/\partial C_H$ at 70 h (Fig. 3.17) and other times (not shown) reveals the simultaneous existence of both positive (anticyclogenetic) and negative (cyclogenetic) sensitivity. Thus, the effects of sensible heat flux at various times during the cyclone life cycle may be partially self-cancelling. This type of effect may explain why previous numerical sensitivity experiments in which sensible heat flux was entirely removed during various phases of cyclone development have produced ambiguous results (Kuo et al. 1991a) or concluded that the net effect of sensible heat flux is small (Reed and Simmons 1991). However, these results concerning surface heat flux sensitivity should not be generalized to other basic states in which the surface heat flux is much stronger or weaker, or has a different distribution of upward and downward heat transfer.

The sensitivity to instantaneous perturbations of sea-surface temperature ($\partial J/\partial T_S$) at 70 h (Fig. 3.19) is consistent with the surface heat transfer coefficient sensitivity just discussed. Higher SST in the warm sector where $\partial J/\partial T_S$ is negative will reduce the atmospheric heat loss associated with downward sensible heat flux, increase the baroclinicity between the warm and cold sectors of the cyclone, and result in lower central pressure. A lower SST can be cyclogenetic in some areas (positive $\partial J/\partial T_S$), for example, in a small region west of the surface cold front, but this sensitivity is much weaker.
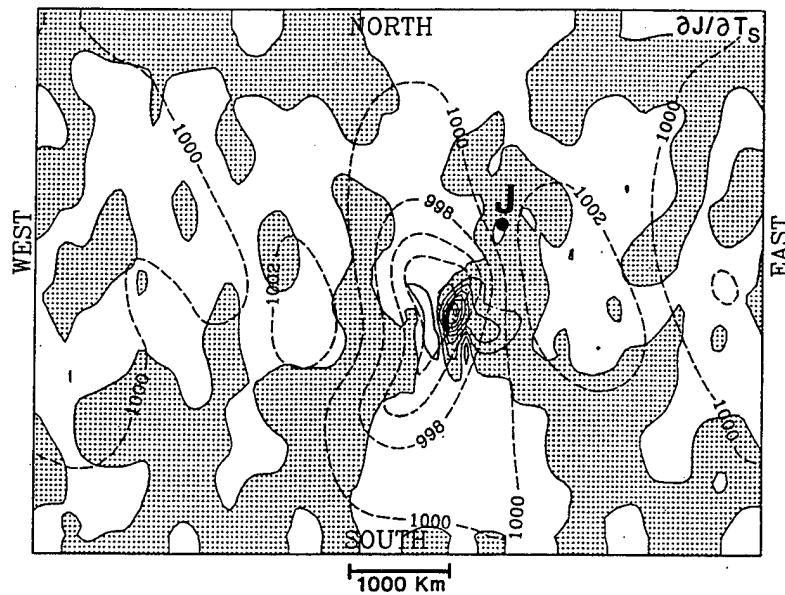
Figure 3.19: Sensitivity to instantaneous perturbations of surface temperature $\partial J/\partial T_s$ at 70 h (contour = 10^{-5} hPa K^{-1}) for basic state with SST anomaly. Negative values (shaded) are regions where higher surface temperature will decrease 90 h central pressure. 70 h basic state surface pressure (contour = 2 hPa, dashed). Forecast aspect J is pressure at center of 90 h cyclone.

Observational and modeling studies demonstrate the relation of intense cyclogenesis to certain "antecedent" features in the lower troposphere, including increased vorticity (Gyakum et al. 1992) and coastal fronts (Bosart and Lin 1984). These features of the marine boundary layer are very sensitive to the SST distribution (Doyle and Warner 1993a). Climatologies of rapidly deepening cyclones show a preference for development near the western boundary currents of the Atlantic and Pacific oceans, and many explosive cyclones follow tracks just poleward of the north walls of the Gulf Stream and Kuroshio currents with the largest SST gradients to the right of the direction of motion. The adjoint sensitivity results (e.g., Figs. 3.15, 3.19) are consistent with these climatologies, as they imply that stronger SST gradients in the warm sector of the idealized cyclone will result in lower central pressure.

66

5. Sensitivity to Surface Stress

The surface momentum stress may be written as

$$\tau = \rho_K C_M V_K^2 \quad , \tag{3.6}$$

where τ is stress (Pa) and ρ_K and V_K are defined as in (3.1). In this simulation, the surface momentum transfer coefficient C_M is specified as a constant 1.0×10^{-3} over the entire model domain. An adjoint equation for $\partial J/\partial C_M$ can be derived in an analogous manner to that for $\partial J/\partial C_H$ (equations (3.2-3.5)) to study sensitivity of J with respect to variations in surface stress. The sensitivity $\partial J/\partial C_M$, accumulated between 0 and 90 h for the basic state without the SST anomaly is shown in Fig. 3.20. The interpretation of Fig. 3.20 is relatively simple. The surface momentum stress is
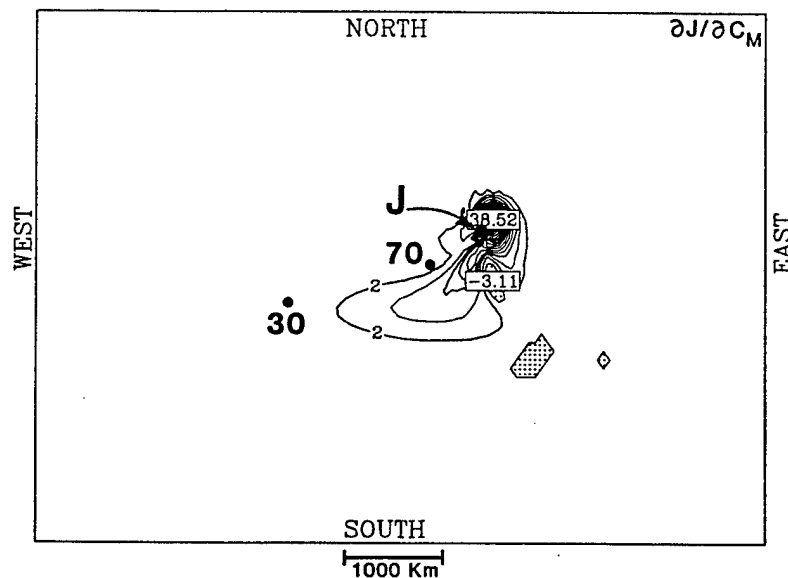
Figure 3.20: Adjoint sensitivity to surface momentum transfer coefficient $\partial J/\partial C_M$ (contour = 2 hPa) accumulated between 0 and 90 h. Positive values indicate surface momentum stress is anticyclogenetic. Cyclone positions at 30 and 70 h indicated by solid dots. Negative values are shaded. Forecast aspect J is pressure at center of 90 h cyclone.

Table 3.5. Comparison of surface pressure perturbations at center of 90 h cyclone (using nonlinear trajectory without sea-surface temperature anomaly) resulting from an increase of 0.0005 (fifty percent) in coefficients for surface fluxes of sensible heat (C_H) and momentum (C_M). Nonlinear model result (ΔJ), and J' obtained as dot product of perturbation and adjoint sensitivity. The surface flux coefficients are perturbed over the entire domain from 0 - 90 h.

Forecast	$C_H + 0.0005$	$C_M + 0.0005$
90 h Adjoint	+ 0.2449 hPa	+ 1.0174 hPa
Nonlinear	+ 0.1713	+ 1.0028

anticyclogenetic during the entire life cycle, with sensitivity strongly localized in the cyclone warm sector after 70 h.

Frictional damping can have significant effects on baroclinic development, as noted by Danard and Ellenton (1980), Branscome et al. (1989), and Hines and Mechoso (1993). An increase in stress will damp thermal advection in the lower troposphere, which may explain the large sensitivity in the cyclone warm sector, where sensitivity to temperature is also greatest. In regions outside the cyclone warm sector, the parameter (C_M) could be changed with little or no effect on the forecast pressure of this cyclone. Lower surface stress over sea-surfaces is a possible explanation for more frequent occurrence of rapidly deepening extratropical cyclones over oceans than over land.

The effect of increasing C_H and C_M from 1.0×10^{-3} to 1.5×10^{-3} in the nonlinear model (basic state with no SST anomaly) is compared in Table 3.5 with the response estimated using the adjoint sensitivity. Increases in both parameters are anticyclogenetic, with a larger effect (about 1 hPa) from increasing C_M. The adjoint accuracy is better for the perturbation related to surface stress (C_M), since C_H is related to more significant nonlinear effects involving surface layer stability and convective velocity.

B.   SIMULATION WITH MOIST PHYSICAL PROCESSES

In this section, the development of an extratropical cyclone, including moist processes, is investigated using adjoint sensitivity methods. These simulations are performed to examine why extratropical cyclone deepening rates can be greater when moist processes (convective and nonconvective precipitation, and surface latent heat flux) are included in model forecasts.

The nonlinear simulation of the idealized cyclone with moist processes is described in Chapt. III.B.1. Tangent linear accuracy is examined in Chapt. III.B.2. In Chapt. III.B.3, adjoint sensitivity during the cyclone rapid deepening phase is described. Effects of convective and nonconvective precipitation are considered in Chapt. III.B.4, and in Chapt. III.B.5, adjoint sensitivity is used to examine the role of surface latent heat flux.

1.   Nonlinear Simulation

The initial conditions are identical to those in Chapt. III.A, except for inclusion of a non-zero mixing ratio field (Fig. 3.21). The largest relative humidity associated with this initial moisture distribution is about 75%. The lower boundary is considered to be a water surface with a fixed sea-surface temperature, and initially small downward surface layer heat fluxes. A cyclone is initiated using an initial perturbation of wind and temperature in the upper troposphere identical to that used for the dry cyclone in Chapt. III.A. The radius of the initial perturbation is about 700 km, with a maximum temperature perturbation of approximately 4° C, and zonal and meridional wind perturbations of about 8 m s^{-1}. The initial perturbation does not include any change to the background moisture field.

Nonconvective (grid-scale resolvable) precipitation in MAMS1 occurs if relative humidity exceeds 100 %, with excess moisture removed and converted to latent heat. This adjustment is performed at the end of each time step. The nonconvective precipitation produces local model tendencies of heating and drying according to

$$\left(p*T\right)_a = \frac{L}{c_p}\Delta\left(p*q\right) \quad , \tag{3.7}$$

$$\left(p*q\right)_a = -\Delta\left(p*q\right) \quad , \tag{3.8}$$

where L is latent heat of condensation, c_p is specific heat, the subscript (a) refers to the field adjustment, and

$$\Delta\left(p*q\right) = p*(q-q_S)(1+\frac{dq_S}{dT}\frac{L}{c_P})^{-1} \quad for\ q-q_S \geq 0 \quad , \tag{3.9}$$

where q_S is saturation mixing ratio.
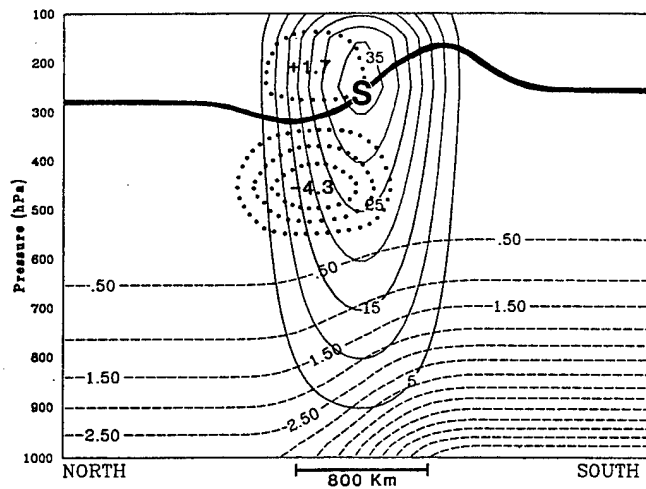
Figure 3.21: North-south vertical cross-section of initial background zonal wind (solid contour = 5 m s^{-1}), mixing ratio (dashed contour = 0.5 g kg^{-1}), initial temperature anomaly (dotted contour = 1 °C), and 2 PVU contour (heavy solid line, 1 PVU = 10^{-6} m^2 K s^{-1} kg^{-1}). S indicates location of 45 m s^{-1} jet streak associated with the imposed temperature anomaly.

70
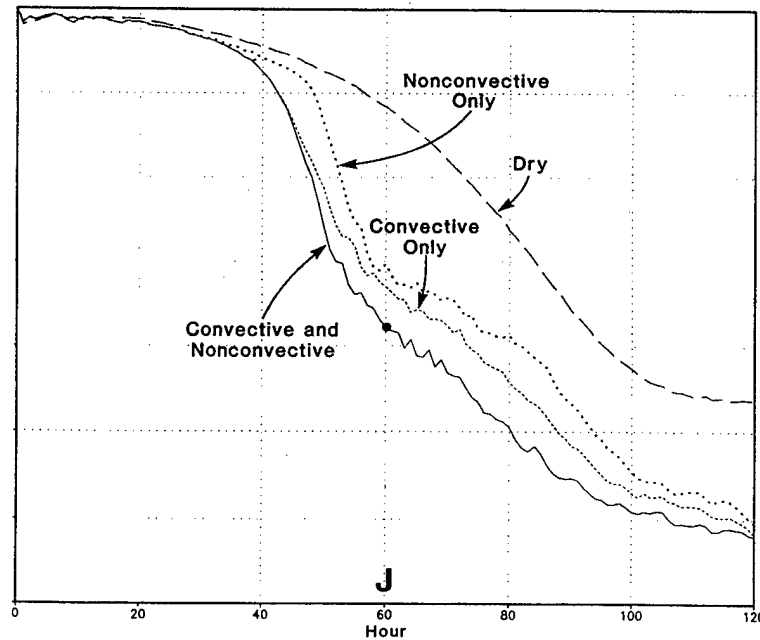
Figure 3.22: Time series of minimum surface pressure in nonlinear simulations: dry (long-dash); with nonconvective precipitation only (dotted); with convective precipitation only (short-dash); with nonconvective and convective precipitation (solid). Forecast aspect J is pressure at center of 60 h cyclone. Simulations with precipitation processes include surface latent heat flux.

The convective parameterization used in this simulation is based on the stability dependent mass-flux adjustment scheme used in version 2 of the NCAR Community Climate model (CCM2; Hack et al. 1993), with some minor differences described in Errico et al. (1994). Convection in this scheme depends on the existence of moist static instability. In addition to heating and drying, local tendencies from convection may include cooling and increases in mixing ratio due to evaporation at some locations. Surface fluxes of moisture are parameterized with a transfer coefficient and bulk differences of mixing ratio in the surface layer (Chapt. III.B.5).

Effects of moisture are small during the first 30 h of the simulation, as a cyclonic circulation gradually develops from the idealized initial conditions. After 30 h, the central pressure of the cyclone in the simulation with convective and

71
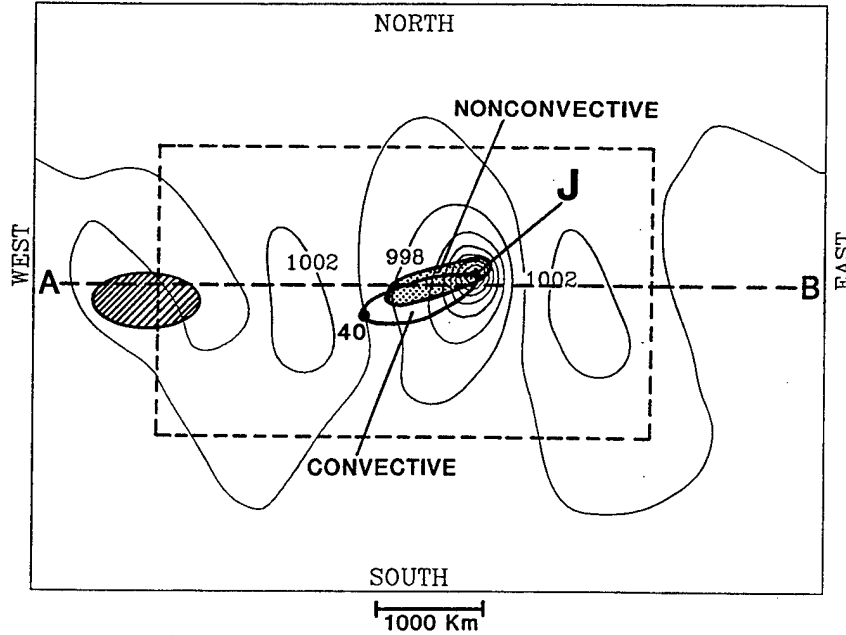
Figure 3.23: Surface pressure (solid contour = 2 hPa) at 60 h in nonlinear run with convective and nonconvective precipitation. Solid dot indicates cyclone position at 40 h (central pressure = 997.0 hPa). Forecast aspect (J) is pressure at center of 60 h cyclone (central pressure = 984.9 hPa). Area of accumulated nonconvective precipitation (40 - 60 h) indicated by shading, area of accumulated convective precipitation outlined by heavy solid line. Solid line surrounding cross-hatched area corresponds to 40 m s^{-1} contour of the jet streak at 250 hPa in the initial conditions. Dashed rectangle is area used in Figs. 3.25 and 3.26.

nonconvective precipitation (Fig. 3.22) decreases earlier and much more rapidly than in the idealized dry cyclone. Between 40 and 50 h, the deepening rate in the moist simulation approaches 1 hPa h^{-1}, which is one criterion for explosive cyclogenesis (Sanders and Gyakum 1980). At 60 h, the central pressure of the cyclone with moist physics is 984.9 hPa (Fig. 3.23), which is more than 10 hPa lower than in the dry cyclone simulation, and the position of the cyclone is about 400 km northeast of the 60 h position in the dry simulation. The horizontal scale (trough to ridge half-wavelength) of the cyclone is roughly 1200 km, or slightly less than in the dry simulation.

When only convective precipitation is included, the period of rapid deepening is again from 40 h - 50 h. When only nonconvective precipitation is used, the rapid deepening is delayed by about 10 h, but then the deepening rate is as large as when both convective and nonconvective precipitation are included. Convective precipitation begins earlier than nonconvective precipitation, since convection does not require supersaturation, and the maximum relative humidity in the initial conditions is only 75 %. Note that the contributions of the convective and nonconvective precipitation may not be simply added (Fig. 3.22) to obtain the same deepening as in the simulation with both included. When either precipitation parameterization is removed, the other tends to partially compensate (a feature also noted by Sardie and Warner 1985), although the lowest central pressure is attained when both convective and nonconvective precipitation are included. An advantage of the adjoint technique is that sensitivity is obtained with respect to a nonlinear forecast that is not modified by removal of physical or dynamical processes, as in forward sensitivity studies.

The surface pressure in the simulation with moist processes begins to decrease when diabatic heating begins near the incipient cyclone center. The sequence of events appears as follows: (i) from 0 h to 30 h, dry processes organize convergence of moisture and upward motion in the incipient cyclone vortex; (ii) the convective parameterization becomes active at about 30 h and heats the lower troposphere near the cyclone center, which causes convergence (divergence) below (above) the heating maximum to increase; (iii) nonconvective precipitation begins at about 40 h as increased moisture convergence provides saturation values of humidity; and (iv) the cyclone enters a 10 h period of explosive deepening at about 40 h as latent heat released from precipitation processes interacts with dry dynamics in a favorable manner.

73

The convective precipitation in this simulation is concentrated near the cyclone center, while the nonconvective precipitation occurs somewhat north and east of the cyclone center in the warm frontal region (the areas of accumulated precipitation are depicted in Fig. 3.23). The relative contributions of convective and nonconvective precipitation will be discussed at greater length in Chapt. III.B.4. Even though the areas of precipitation are not extremely large, moist physics have a significant influence on the cyclone deepening rate, as shown in Fig. 3.22 by comparison with the central pressure evolution in the dry and moist simulations.

2.   Choice of Forecast Aspect (*J*) and Accuracy Considerations

The focus in this simulation is on the rapid cyclone development period between 40 h and 60 h, when moist processes had a significant effect on reducing the central pressure of the idealized cyclone. The forecast aspect (*J*) for the adjoint sensitivity is therefore defined as pressure at the center of the 60 h cyclone. The adjoint sensitivity then provides an estimate of the effect that perturbations of model prognostic variables and parameters will have on 60 h pressure at the position of the cyclone in the original nonlinear forecast. For small perturbations, the cyclone position is likely to remain at its location in the original nonlinear forecast. As perturbation size increases, it becomes more likely that the cyclone position, as well as intensity, may be altered in the perturbed forecast. Other choices of forecast aspect (*J*) have been evaluated but do not lead to different conclusions concerning the cyclone development.

As in the previous section, it is useful to evaluate the accuracy that can be expected for this cyclone simulation, before examining the adjoint sensitivity information. The numerical parameterizations of moist physical processes include on

74

/ off "switches" that can lead to bifurcations of the forecast trajectory. Although the dry adjoint also contains on / off switches (e.g., convective velocity), the effects of these are not nearly as severe as those associated with moist processes. When the effects of on / off switches are significant in the nonlinear forecast, TLM and adjoint solution accuracy may be poor, even for small perturbations and short forecast intervals. Errors in moist TLM and adjoint solutions are likely to be most significant in regions where precipitation is marginal, i.e., when the sense of an on / off switch is altered by a perturbation. This may include frontal regions (Zou et al. 1993), areas of marginal precipitation (Vukićević and Errico 1993), or cloud tops (Park et al. 1994).

An example of tangent linear model accuracy with moist processes is provided by comparing a TLM forecast at 60 h with the difference between perturbed and non-perturbed nonlinear forecasts. The perturbation consists of a 1 g kg^{-1} increase in *mixing ratio* at 40 h at nine adjacent grid points on a model level near 760 hPa. The location is just northeast of the 40 h cyclone center, and was identified as a region of relatively strong sensitivity by examination of an adjoint field (not shown). This perturbation is a severe test of tangent linear model accuracy, since it occurs in a region where precipitation is beginning and the basic state is likely to include more nonlinear effects than in other locations. A perturbation of 1 g kg^{-1} is relatively large, as it represents roughly a 50% increase in the basic-state mixing ratio.

The difference in forecast surface pressure between the perturbed and non-perturbed nonlinear simulations (Fig. 3.24b) contains an area of positive p_s' that is surrounded by a region of negative p_s' to the east that also extends to the north and west. Notice that the cyclone position is not changed when only a localized, small magnitude, perturbation is added. The pattern of Fig. 3.24b is reproduced well by the

75
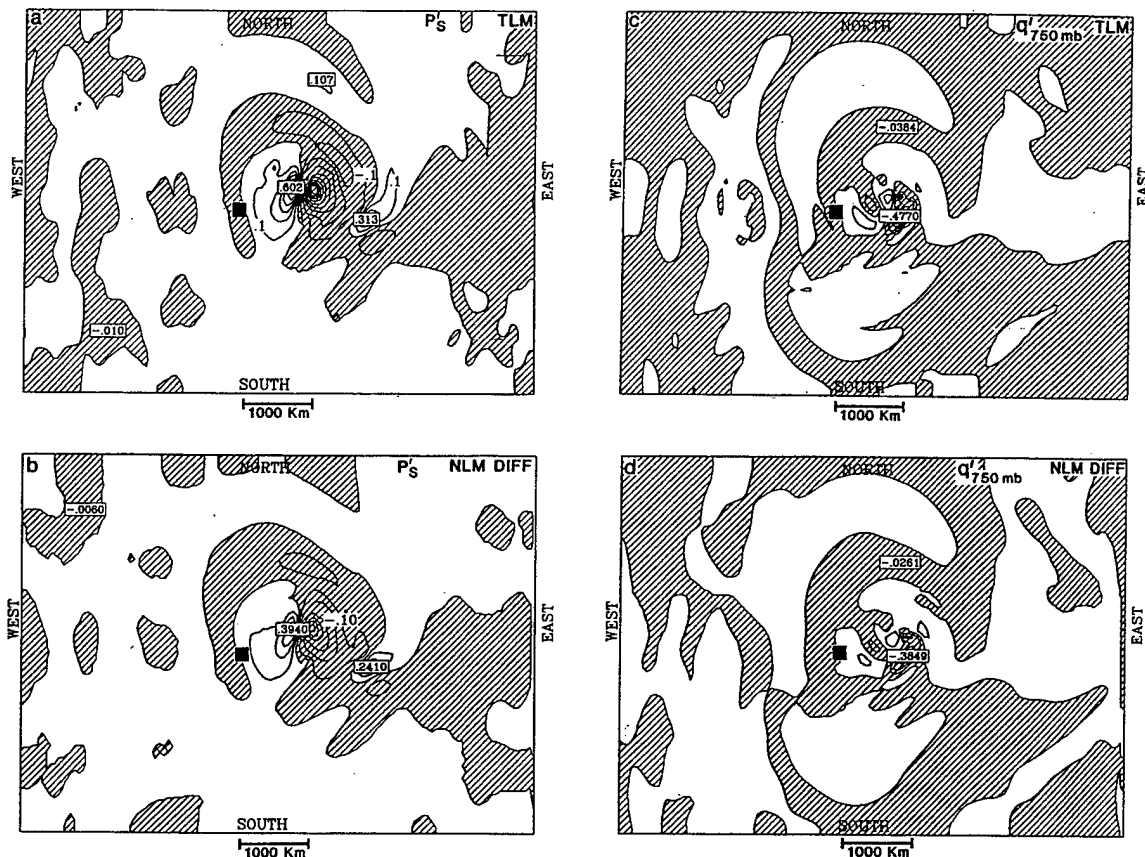
Figure 3.24: (a) 20 h forecast of TLM surface pressure perturbations (contour = 0.1 hPa) resulting from perturbation of mixing ratio (+ 1 g kg^{-1}) at nine grid points on model level near 760 hPa at 40 h. (b) As in (a), except difference between perturbed and non-perturbed nonlinear integrations. (c) 20 hour forecast of TLM mixing ratio perturbations (contour = 0.1 g kg^{-1}) near 760 hPa resulting from initial perturbation as in (a). (d) As in (c), except difference between perturbed and non-perturbed nonlinear integrations. Simulations include convective and nonconvective precipitation. Negative values are shaded. Solid square indicates location of perturbation at 40 h.

TLM (Fig. 3.24a), and the relative sizes of the largest positive and negative pressure perturbations are maintained. The most significant difference is the larger magnitude of p_s' in the TLM forecast, with maximum perturbations about 50 percent larger. A similar comparison for TLM and nonlinear forecasts of mixing ratio perturbations near 760 hPa (Figs. 3.24c,d) indicates good spatial correspondence, although again the TLM overpredicts perturbation magnitude (by about 25 percent).

Table 3.6. Comparison of perturbation forecasts valid at 60 h in which the initial perturbations consist of + 1°C at nine adjacent grid points on sigma level 10 (near 760 hPa). Perturbations are made at 0 h (60 h forecast), 40 h (20 h forecast), and 50 h (10 h forecast). Entries are largest negative perturbation for v, q, T, and p*, with grid point location in parentheses. Nonlinear forecast and moist TLM include convective and nonconvective precipitation, and surface latent heat flux.

Forecast		$v(\sigma=0.23)$ m s^{-1}	$q(\sigma=0.75)$ g kg^{-1}	$T(\sigma=0.75)$ °C	Pressure hPa
10 h	TLM-moist	-0.540 (80,34)	-0.071 (69,33)	-0.128 (64,30)	-0.240 (67,34)
	TLM-dry	-0.153 (80,35)	----	-0.028 (63,29)	-0.031 (67,34)
	Nonlinear	-0.401 (80,34)	-0.056 (69,33)	-0.287 (68,34)	-0.166 (67,34)
20 h	TLM-moist	- 1.19 (71,38)	-0.665 (67,33)	-0.368 (56,32)	-0.776 (69,34)
	TLM-dry	- 0.35 (80,33)	----	-0.046 (66,35)	-0.125 (67,34)
	Nonlinear	- 1.59 (71,38)	-0.551 (69,33)	-0.277 (56,32)	-0.608 (68,35)
60 h	TLM-moist	- 8.52 (64,36)	- 6.93 (67,33)	- 3.74 (65,32)	- 8.60 (69,34)
	TLM-dry	- 1.22 (81,33)	----	- 0.36 (65,30)	- 0.87 (67,34)
	Nonlinear	- 6.32 (65,37)	- 2.62 (69,33)	- 2.36 (66,32)	- 4.05 (70,35)

Table 3.6 is a comparison of perturbation forecasts made with moist and dry versions of the TLM and the moist nonlinear model over forecast intervals of 10 h, 20 h and 60 h. Here, the perturbations consist of a 1° C increase in *temperature* at nine adjacent grid points on a model level near 760 hPa, in areas of relatively strong sensitivity (the sensitivity to temperature, $\partial J/\partial T$, and perturbation locations at 50 h with the moist and dry versions of the adjoint model are shown in Figs. 3.24a and 3.24e, respectively). As expected, larger perturbation growth occurs over longer

forecast intervals (e.g., 60 h in Table 3.6). Over shorter forecast intervals of 10 h, the TLM perturbations are quantitatively more accurate in terms of perturbation magnitude.

The results in Table 3.6 for the dry TLM suggest that inclusion of moist processes in the TLM is necessary to provide a good approximation of perturbation magnitude in the nonlinear model. Perturbation growth in the dry TLM over all time intervals is too small, and contains more significant spatial errors in the perturbation pattern. Nonlinear effects resulting from the perturbation used in Table 3.6 are more significant for certain variables. For example, TLM accuracy over 60 h is much better for 760 hPa temperature and 250 hPa meridional wind than for 760 hPa mixing ratio and surface pressure. These moist TLM and nonlinear model comparisons imply that nonlinear effects neglected by the TLM act to damp perturbation growth over longer time intervals, which can result in TLM over-estimates of forecast perturbation magnitude.

In Chapt. III.A.2, it was shown that TLM / adjoint accuracy may be qualitatively acceptable even to 90 h for a dry model starting from a relatively small perturbation to idealized initial conditions. The inclusion of moist processes constrains the length of time over which the TLM and adjoint can provide acceptable accuracy. Based on the examples of TLM accuracy in Fig. 3.24 and Table 3.6 for this simulation, sensitivity determined with this version of the MAMS1 moist adjoint can be expected to provide qualitatively useful information over a 20 h forecast interval.

3. Sensitivity to Primary Prognostic Variables

The sensitivity of 60-h cyclone central pressure to perturbations of 760 hPa temperature and moisture at 50 h is shown in Fig. 3.25. The 50 h time is selected
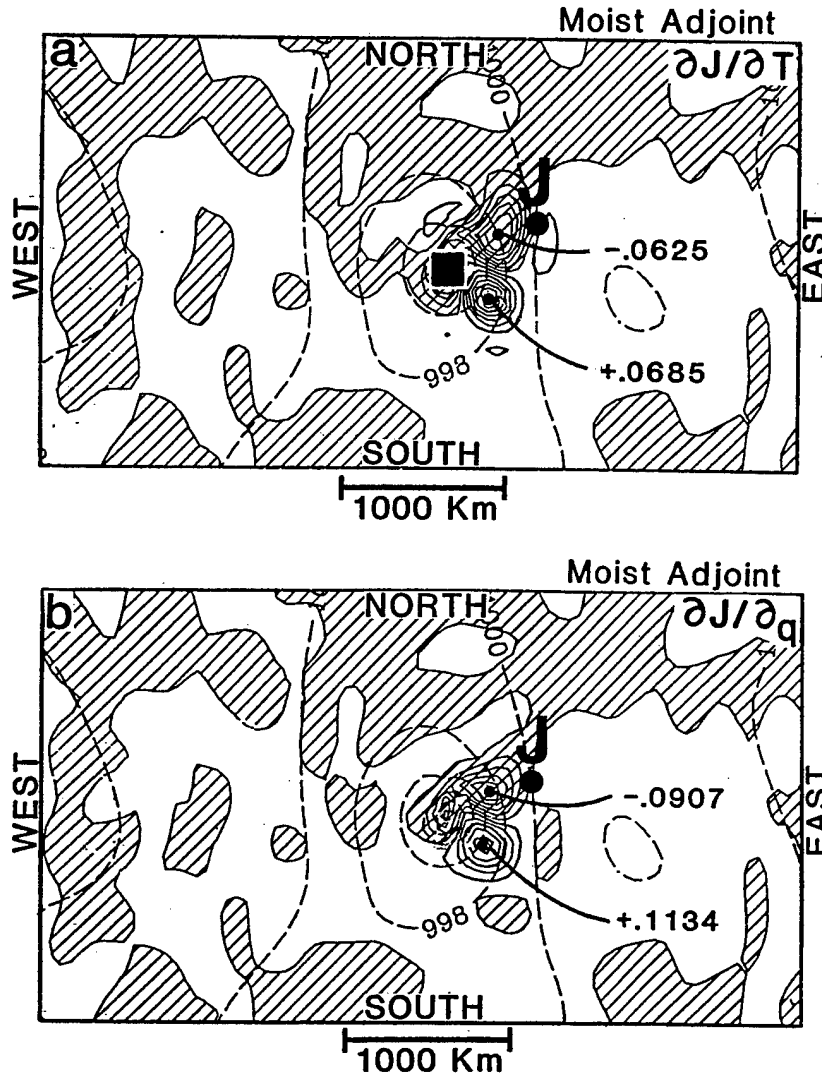
Figure 3.25: Adjoint sensitivity of 60 h cyclone central pressure to (a) temperature $\partial J/\partial T$ at 50 h (solid contour = 0.01 hPa deg^{-1}), and (b) mixing ratio perturbations $\partial J/\partial q$ at 50 h (solid contour = 0.02 hPa g^{-1} kg), where negative values (shaded) indicate regions in which a positive perturbation at 50 h will decrease the cyclone central pressure at 60 h (J); (c) Temperature (solid contour = 1 °C), and (d) relative humidity in the nonlinear forecast at 50 h (solid contour = 10%, greater than 80% shaded); (e) ($\partial J/\partial T$) as in (a), using dry adjoint model and moist basic state. All fields on model level near 760 hPa. Dashed line in (a-d) is surface pressure at 50 h in the nonlinear model forecast (contour = 2 hPa). Moist simulations (a-d) include convective and nonconvective precipitation. Solid squares in (a) and (e) indicate locations of perturbations used for 10 h integrations in Table 3.6. Area of plot shown by dashed rectangle in Fig. 3.23.

79
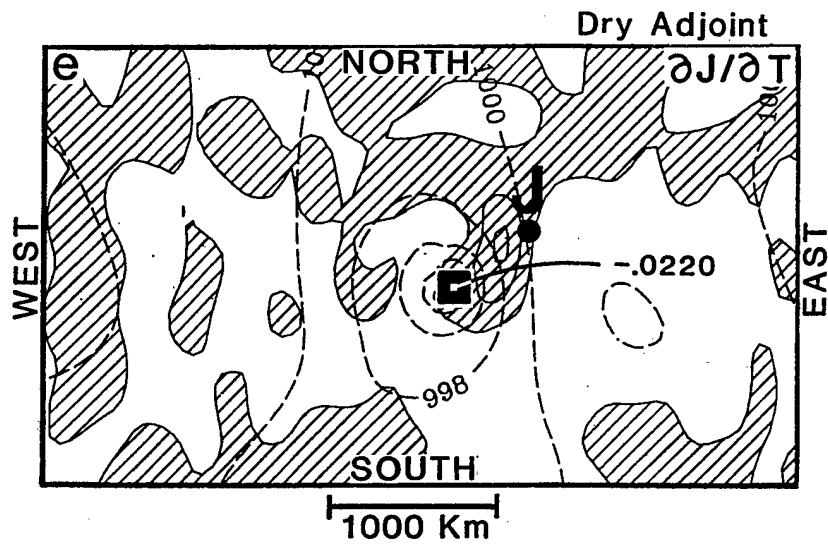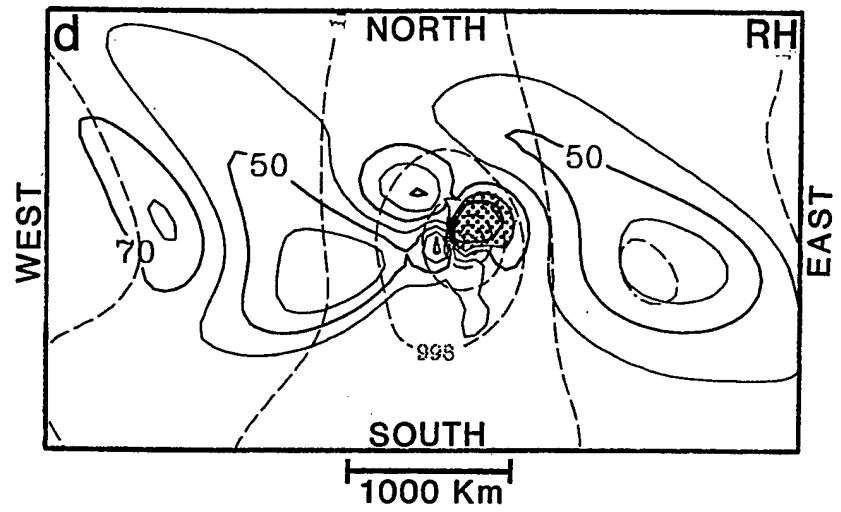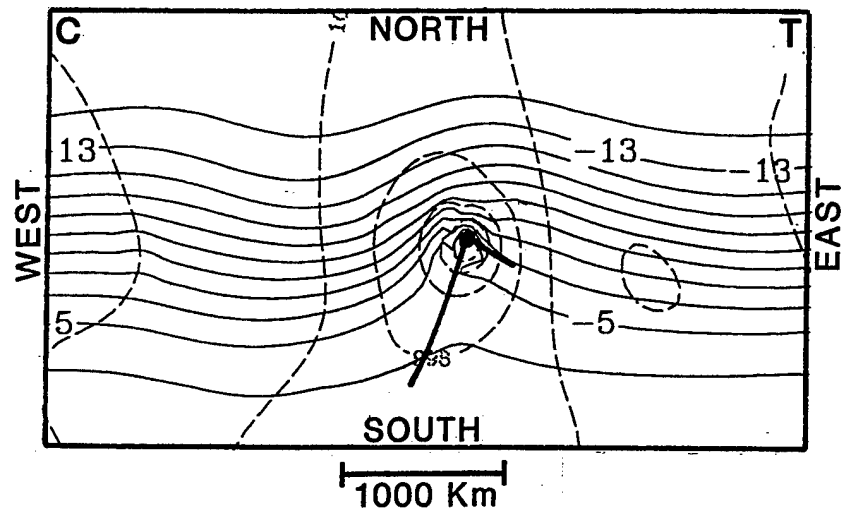
Figure 3.25, continued

because it represents conditions while the most rapid deepening of the cyclone is occurring. At 50 h, a localized area of negative temperature sensitivity ($\partial J/\partial T$) and mixing ratio sensitivity ($\partial J/\partial q$) extends northeast from the 989.2 hPa cyclone center in the region of the warm front. This sensitivity implies that an increase in amplitude of the thermal wave in the warm sector (Fig. 3.25c) will reduce the central pressure of the cyclone at the 60 h forecast position. An increase in mixing ratio northeast of the cyclone center can also intensify the 60 h cyclone. As shown by comparing Figs. 3.25b and 3.25d, the area of strongest sensitivity to mixing ratio perturbations ($\partial J/\partial q$) occurs where relative humidities are largest, which implies that mixing ratio perturbations can intensify the cyclone by making precipitation-related latent heat release stronger. Outside these regions of strong sensitivity, perturbations of temperature or mixing ratio will have relatively small effects on forecast cyclone central pressure.

The minimum $\partial J/\partial T$ at 50 h (Fig. 3.25a) is about -0.06 hPa deg^{-1}, so that a perturbation of +1 deg *at a single grid point in this location of maximum sensitivity (on one level)* will decrease the 60 h pressure in the nonlinear forecast by 0.06 hPa (to first-order approximation). For purposes of comparison, a mixing ratio perturbation of +1 g kg^{-1} (at one grid point) at the location of strongest negative sensitivity ($\partial J/\partial q$ = -0.09 hPa g^{-1} kg, Fig. 3.25b) implies a 0.09 hPa decrease in 60 h central pressure.

As shown in Table 3.6, perturbation growth in the TLM is much larger, and closer to the true nonlinear sensitivity, when moist processes are included. It should be expected, correspondingly, that sensitivity in a dry adjoint model will be reduced in comparison to results obtained with a moist adjoint model. This result is demonstrated by comparing $\partial J/\partial T$ in Fig. 3.25a (moist adjoint) with $\partial J/\partial T$ in Fig. 3.25e

for the dry adjoint (with a moist basic state). Although both the moist and dry adjoint models indicate the main area of negative $\partial J/\partial T$ that extends northeast from the 40 h cyclone center, the sensitivity in the moist adjoint is roughly three times larger. In addition, the dry adjoint does not produce the area of positive $\partial J/\partial T$ southeast of the cyclone center that appears in Fig. 3.25a.

The sensitivities depicted in Figs. 3.25 indicate how temperature and moisture perturbations can enhance or diminish physical processes that develop the cyclone. For example, the spatial correlation of temperature and moisture sensitivity suggests that the primary effect of moisture perturbations on cyclone intensity is accomplished by latent heat release. At 50 h, a strong positive near-surface vorticity tendency in the direction of storm motion (e.g., to the northeast of the cyclone center) is associated with mid-tropospheric vorticity advection and Laplacian of lower-tropospheric thickness advection. An increase in temperature in the lower troposphere to the northeast of the cyclone center (in the area of negative $\partial J/\partial T$) can intensify thermal gradients and forcing of near-surface vorticity tendency by thickness advection. Similarly, an increase in moisture can have the same effect via latent heat release in this region of strong sensitivity to temperature perturbations.

An interesting feature of the sensitivity patterns is the implication that higher (lower) temperature and increased (decreased) mixing ratio in locations of positive sensitivity gradient southeast of the cyclone center (Figs. 3.25a,b) can weaken (strengthen) the cyclone. One interpretation of this sensitivity pattern is that higher temperature and increased moisture will interact unfavorably with existing baroclinic and diabatic processes that are developing the cyclone toward its position in the original forecast. The result could be a weaker cyclone at the original position, or a

change in cyclone position for sufficiently large perturbations of temperature or mixing ratio.

A schematic diagram of the locations of maximum temperature sensitivity at 350, 550, 750, and 925 hPa is given in Fig. 3.26. On all levels, these are the locations where *warming* produces the greatest *decrease* in 60 h central pressure. In the upper troposphere, the maximum sensitivity occurs north and west of the cyclone center. At 750 hPa and 925 hPa, strongest sensitivity to temperature is located ahead of the surface cyclone in the warm sector, so that the axis of maximum sensitivity is tilted upstream with height. This sensitivity pattern can be interpreted in the context of differential temperature advection, or in terms of potential vorticity anomalies, with a cyclogenetic pattern related to an upstream (phase-locked) tilt of upper and lower tropospheric anomalies.
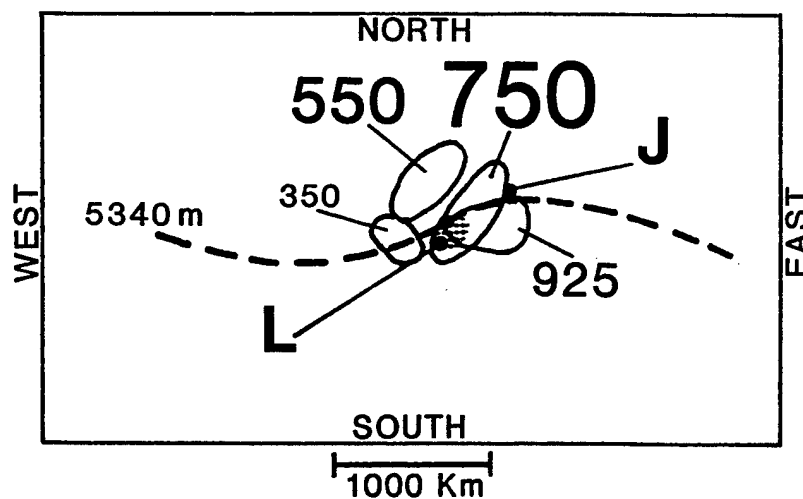
Figure 3.26: Conceptual diagram of sensitivity to temperature ($\partial J/\partial T$) at 50 h. Areas where *positive-signed* temperature perturbations on selected levels (350, 550, 750, 925 hPa) produce greatest decrease in 60 h central pressure (J) are indicated by solid outline. Size of numbers is proportional to sensitivity (e.g., sensitivity at 750 hPa is about four times greater than sensitivity at 350 hPa). **L** indicates position of cyclone at 50 h, position of 5340 height contour indicated by single dashed contour. **J** indicates position of cyclone at 60 h. Shaded area is region of heating from nonconvective precipitation. Area of plot shown by dashed rectangle in Fig. 3.23.

83

With respect to interpretation of adjoint sensitivity, it is important to distinguish between the effects that perturbations can have on cyclone pressure in an instantaneous sense, as opposed to the effects that occur over some time interval and relate to the future state of the cyclone. From simple hydrostatic considerations, heating at any level in a vertical column can decrease the underlying surface pressure in an *instantaneous* sense (if the average column density is thereby reduced). In contrast, adjoint sensitivity can estimate the effects that temperature perturbations have on *future* cyclone intensity. The sensitivity fields indicate where perturbations can have maximum effect on the forecast aspect J, and this sensitivity does not necessarily correspond to the locations of existing features (such as jet streaks or potential vorticity anomalies) that have *already* developed.

Although inclusion of moisture in the basic state and adjoint model increases the magnitude of temperature sensitivity ($\partial J/\partial T$), the primary feature in both moist and dry adjoint results is strong sensitivity in the lower troposphere above the cyclone warm sector. This suggests that *moist physical processes intensify dry baroclinic processes of cyclogenesis, and do not represent a separate, unique cyclone deepening mechanism.* This conceptual idea will be explored in more detail in the following section.

4. Adjoint Interpretation of Precipitation Processes

In the above discussion, the effects of hypothetical temperature and moisture perturbations are considered in the context of adjoint sensitivity fields. A less arbitrary method is to consider perturbations that are scaled to represent the effects of physical processes that are occurring in the nonlinear forecast (a similar approach was used in Chapt. III.A.3 for the idealized dry cyclone simulation). This technique

can also be applied using adjoint sensitivity gradients and tendencies of temperature and mixing ratio associated with convective and nonconvective precipitation. As the nonlinear forecast evolves, these tendencies contribute to anomalies associated with the cyclone, including diabatically-produced potential vorticity anomalies. Rather than using instantaneous (single time step) fields, time-averaged basic state tendencies and sensitivity during the rapid deepening phase will be examined to evaluate effects of moist processes.

Vertical cross-sections of $\partial J/\partial T$ and $\partial J/\partial q$ averaged between 40 h to 60 h are shown in Figs. 3.27a and 3.27b, respectively. The plane of these cross-sections is along the direction of storm motion and includes the zone of maximum sensitivity. In the regions of strong negative sensitivity below 700 hPa, positive perturbations of temperature or mixing ratio will decrease the 60 h central pressure (J). That is, warming and moistening of the lower troposphere above and slightly ahead of the cyclone are cyclogenetic effects. However, regions of positive sensitivity ($\partial J/\partial T$ and $\partial J/\partial q$) at higher levels indicate warming and moistening can *increase* 60 h central pressure. The sensitivity patterns can be used to interpret how the larger deepening rate in the moist cyclogenesis is related to temperature and mixing ratio adjustments that result from the convective and nonconvective precipitation parameterizations.

It is noted that the vertical distribution of sensitivity in this simulation with moist processes is similar to that determined for the dry case described in Chapt. III.A (e.g., compare Fig. 3.27a with Fig. 3.5a). Maximum sensitivity for temperature, winds, and mixing ratio is located between 600 and 900 hPa in the baroclinic zone below the jet core, with sensitivity at 760 hPa approximately 10 times larger than at the jet level near 250 hPa. As in Chapt. III.A, the axis of maximum sensitivity in the lower

85
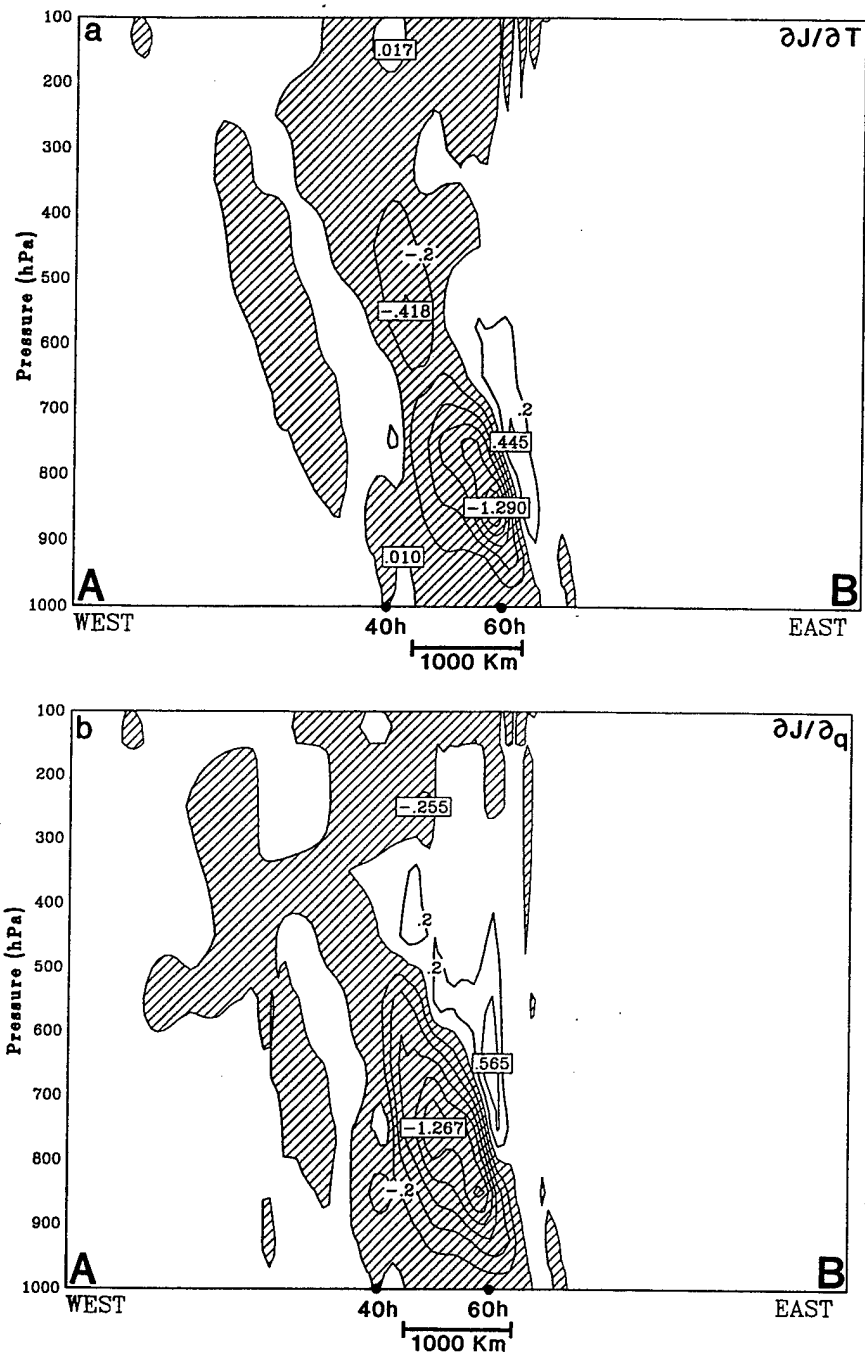
Figure 3.27: East-west vertical cross-sections along the line A-B in Fig. 3.23 of the sensitivity of 60 h cyclone central pressure (J) to (a) temperature perturbations $\partial J/\partial T$ (contour = 0.2 hPa deg^{-1}) and (b) mixing ratio perturbations $\partial J/\partial q$ (contour = 0.2 hPa g^{-1} kg) averaged between 40 and 60 h. Perturbations are in units of (a) deg h^{-1}, and (b) g kg^{-1} h^{-1}. Solid dots indicate cyclone position at 40 h and 60 h. Negative values (shaded) indicate regions in which a positive perturbation will decrease the cyclone central pressure at 60 h.

86
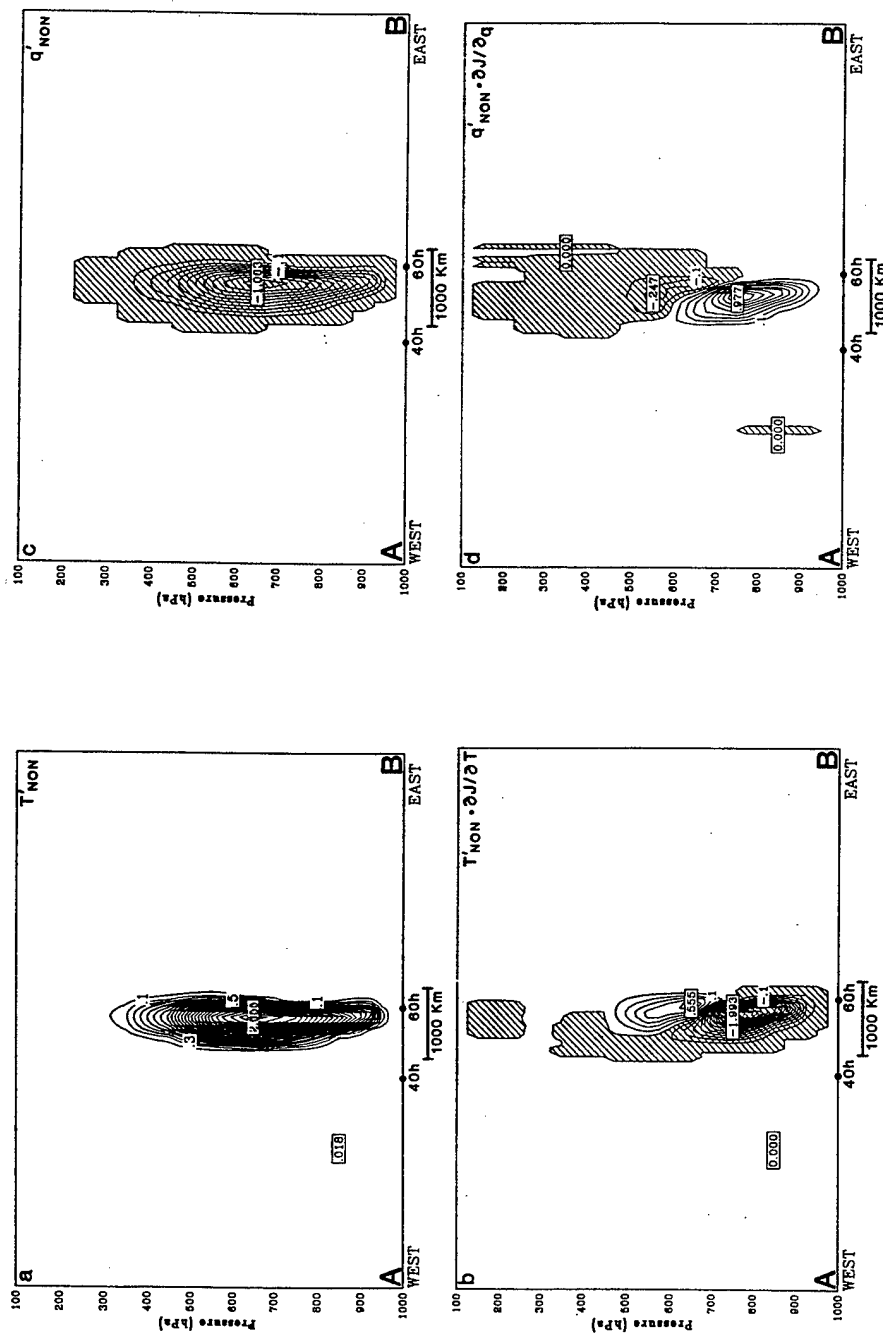
Figure 3.28: East-west vertical cross-sections along the line A-B in Fig. 3.23 of (a) average temperature tendency between 40 and 60 h (contour = 0.1 deg h^{-1}); (b) dot product of perturbation (T' scaled to one-hour temperature tendency in (a)) and sensitivity ($\partial J/\partial T$) in Fig. 3.27a (contour = 0.1 hPa); (c) average mixing ratio tendency between 40 h and 60 h (contour = 0.1 g kg^{-1} h^{-1}); (d) dot product of perturbation (q' scaled to one-hour mixing ratio tendency in (c)) and sensitivity ($\partial J/\partial q$) in Fig. 3.27b (contour = 0.1 hPa).   Tendencies are from **nonconvective** precipitation. Negative values (shaded) in (b) and (d) indicate that the temperature or mixing ratio tendency causes a decrease in 60 h cyclone central pressure (J).

87

troposphere tilts westward with height, which indicates the importance of baroclinic processes to cyclone development.

The nonconvective precipitation parameterization produces maximum heating rates of about 2.6 deg h^{-1} averaged between 40 and 60 h (Fig. 3.28a). This heating occurs between about 350 hPa and 950 hPa with a maximum value near 650 hPa. Since this precipitation represents a loss of moisture from the atmosphere, a similar pattern is found for the drying effect associated with the nonconvective precipitation (Fig. 3.28c). Using these tendencies (which represent the effects of the physical process in model grid-space) to construct perturbations, the effects of heating and drying associated with nonconvective precipitation on the forecast aspect (J) are estimated by computing a scalar dot product with the sensitivities ($\partial J/\partial T$ and $\partial J/\partial q$) shown in Fig. 3.27.

This method shows how small perturbations that represent the effects of precipitation processes influenced cyclone development in the *original nonlinear forecast*. It is re-emphasized that the interpretation in this section pertains to the influence of small perturbations compared in a relative sense at various locations, and not to possible effects of arbitrary or large perturbations that could produce significant differences in cyclone location or intensity. Below 700 hPa, an increase in the heating tendency from nonconvective precipitation would have a cyclogenetic effect (Fig. 3.28b), and is partially compensated by drying tendencies (Fig. 3.28d). Above 700 hPa, the heating tendency from nonconvective precipitation has an anticyclogenetic effect, with some offsetting cyclogenetic effect associated with the drying tendency. The cyclogenetic effect of heating from nonconvective precipitation is strongest in an area near and just north and east of the cyclone center (see Fig. 3.26).

A similar evaluation can be performed for convective precipitation. Between 40 h and 60 h, the largest heating tendency from convective precipitation (Fig. 3.29a) is lower in the troposphere and is only 20% of the maximum associated with nonconvective precipitation. The mixing ratio tendencies arising from convective precipitation (Fig. 3.29c) are also smaller than those from nonconvective precipitation. Taking an inner product of the convective tendencies and the sensitivities (Fig. 3.27), cyclogenetic effects related to diabatic heating are concentrated between 700 and 900 hPa (Fig. 3.29b), and are partially offset by drying (Fig. 3.29d). The effect of heating from convective precipitation is strongest at the grid point representing the cyclone center. Convective precipitation near the storm center was also shown to be important during the initial phase of cyclone development in the study by Tracton (1973).

In terms of projection onto the sensitivity for the entire domain, the net effect of perturbations related to nonconvective precipitation from 40 h to 60 h is about an order of magnitude more significant (to 60 h central pressure) than that from convective precipitation. The nonconvective precipitation produces stronger heating and has a closer spatial correspondence with the region of strongest temperature sensitivity extending from the center of the cyclone to the northeast into the region of the warm front. However, the convective precipitation plays a crucial role during the initial deepening phase of cyclone development, which is not described in Figs. 3.28 and 3.29. Between 30 h and 40 h, heating from convective precipitation occurs in the lower troposphere near the cyclone center, prior to the onset of nonconvective precipitation (which requires full saturation). The convective heating initiates a pattern of vertical motion and divergence above the incipient vortex so that cyclone

89
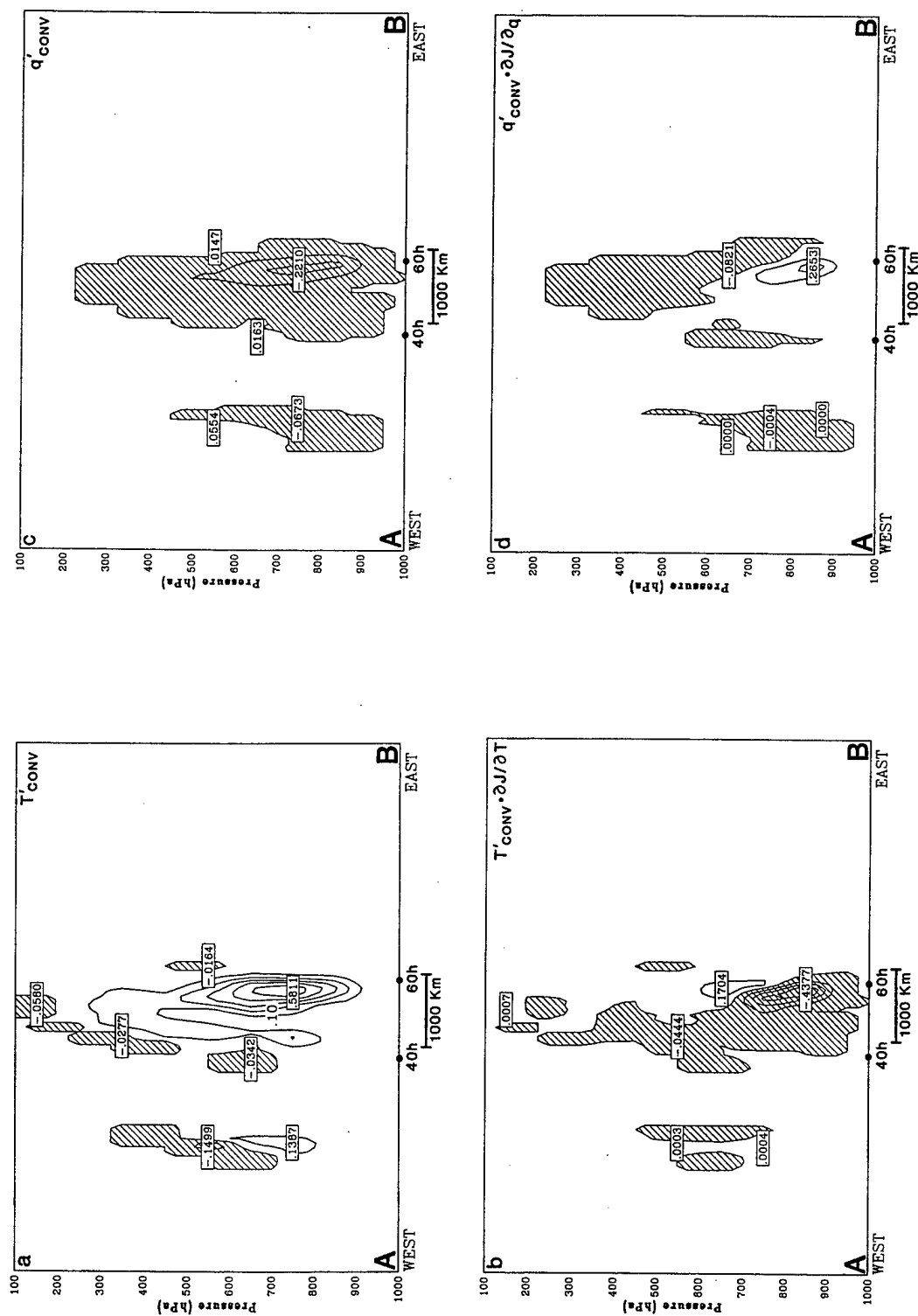
Figure 3.29: As in Fig. 3.28, using tendencies for **convective** precipitation.

central pressure begins decreasing earlier than in the dry simulation or the simulation with only nonconvective precipitation (Fig. 3.22).

As discussed in Chapt. III.B.2 (and documented in Table 3.6), growth of perturbations that originate in regions of strong sensitivity is larger over longer forecast intervals. An optimally-positioned perturbation at 30 h can therefore have more effect on J than the same perturbation 10 h later, which has less time to amplify. This explains why even relatively weak convective heating before 40 h in the region of strong sensitivity near the cyclone center can have such a significant effect on the subsequent cyclone development. Without the early effects of convective heating to initiate moisture convergence, latent heat release in the simulation with only nonconvective precipitation is delayed by about 10 h and the 60 h central pressure of the cyclone is higher.

The adjoint sensitivity information indicates that the vertical distribution of heating (from precipitation or other sources) is very important to future cyclone intensification (this sensitivity feature was also present in the idealized dry cyclone). Heating below about 600 hPa in the warm frontal area will intensify the cyclone, while heating above that level can have a damping effect on the cyclone. Heating in the middle and upper troposphere above the warm front is a stabilizing effect that suppresses cyclone intensification, in the sense that interaction with dry baroclinic processes is apparently not as favorable. The vertical distribution of latent heat release from precipitation processes is therefore likely to be a significant factor in numerical forecasts of extratropical cyclones. This interpretation of vertical sensitivity to temperature perturbations is in agreement with a number of other studies demonstrating that diabatic heating in the lower, rather than the upper, troposphere

is most conducive to cyclogenesis (Tracton 1973, Anthes and Keyser 1979, Sardie and Warner 1985, and Roebber 1989).

An interpretation of cyclone deepening mechanisms associated with nonconvective precipitation in the warm frontal region at 50 h is summarized in the conceptual diagram of Fig. 3.30. Diabatic heating near the warm front in the lower troposphere is optimal in the sense that it amplifies the dry processes of baroclinic instability in the location that potentially has the most impact on cyclone intensification and rate of propagation. If the Laplacian of diabatic heating is large near the warm front in this simulation, this can reinforce a vorticity tendency in the direction of storm motion (to the northeast) related to the Laplacian of thickness advection. In addition, diabatic heating can increase the amplitude of the upper tropospheric ridge above the surface cyclone, and thus strengthen mid-tropospheric vorticity advection and net column mass divergence in the direction of storm motion.

The interpretation of adjoint sensitivity presented in this section lends support to other studies that suggest the importance of diabatic processes in the warm front region during explosive cyclogenesis. In the series of storms analyzed by Kuo and Low-Nam (1990) and also in Kuo et al. (1991b) and Reed et al. (1993), it was determined that nonconvective precipitation near the warm front was crucial for rapid cyclone intensification. It is also interesting to note that the region of strongest temperature and mixing ratio sensitivity, in the lower troposphere and northeast of the cyclone center (Fig. 3.25a,b), corresponds to the location of the "cloud head" feature that Shutts (1990) states is a unique characteristic of many explosively deepening North Atlantic cyclones. The cloud head feature is attributed to stratiform cloud that forms on the main baroclinic zone and frontal surface northeast of the surface low
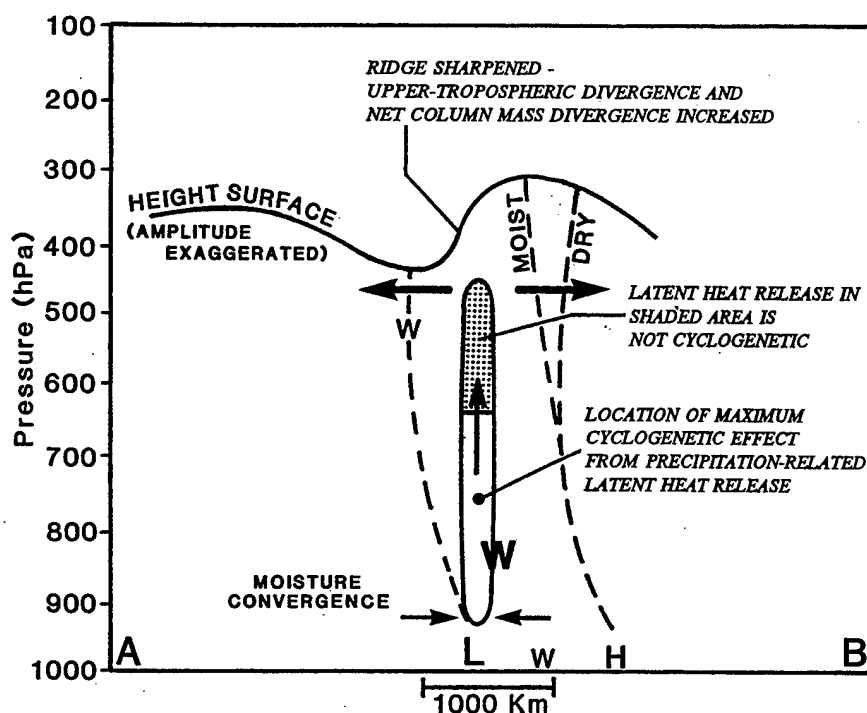
Figure 3.30: Conceptual diagram of sensitivity and latent heat effects at 50 h in an east-west vertical cross-section through the position (L) of the cyclone. Dashed lines are trough and ridge axes. W indicates locations where positive temperature perturbations can decrease 60 h central pressure (size of letters roughly proportional to sensitivity gradient). Area where latent heat release is occurring is contained within the solid oval (this diagram pertains to nonconvective precipitation in the warm frontal region).

center during rapid cyclone intensification. The concept of the cloud head and associated processes seems consistent with the interpretation of moist physical processes and adjoint sensitivity in this idealized simulation, e.g., that latent heat release from nonconvective precipitation in the region of the lower tropospheric warm front is the primary physical process that can increase the deepening rate of extratropical cyclones into the explosive range.

5.   Sensitivity to Surface Latent Heat Flux

The effects of surface sensible heat flux in a dry simulation of an idealized extratropical cyclone were examined in Chapt. III.A.4. The adjoint model is used here

93

to provide sensitivity information related to the surface latent heat flux, which can be expressed as

$$F_L = C_E \rho_K L V_K \left(q_S - q_K \right) \quad , \tag{3.10}$$

where F_L has units of (W m^{-2}), ρ_K is the surface layer air density, L is latent heat of condensation, q_S is surface saturation mixing ratio, and q_K is the mixing ratio on the lowest model level. The surface moisture transfer coefficient C_E is assigned a fixed value equal to 1.0 x 10^{-3}. The wind speed V_K in (3.10) includes a convective velocity in light wind conditions (Anthes et al. 1987). The transfer coefficient C_E is used only to parameterize moisture exchange in the surface layer. The sensitivity $\partial J/\partial C_E$ can be obtained in a manner analogous to the derivation of $\partial J/\partial C_H$ (Eqs. 3.2 - 3.5).

The sensitivity $\partial J/C_E$ can be accumulated over time to estimate the effect due to a perturbation of C_E that remains constant during a particular interval, which could be the entire forecast. In this simulation, the lower boundary is considered to be entirely water-covered with a constant sea-surface temperature, so that sensitivity associated with C_E is related only to surface latent heat flux. In a simulation including a predictive equation for ground surface temperature, the adjoint of another equation related to perturbation surface temperature would be involved in obtaining $\partial J/\partial C_E$.

Largest upward F_L in the nonlinear forecast at 40 h (Fig. 3.31a) is to the west of the cyclone center in the dry air behind the surface cold front (these latent heat flux amounts are relatively weak compared to those found in typical maritime cyclones). Smaller values of upward F_L are found in the cyclone warm sector. The sensitivity of 60 h cyclone central pressure to C_E (Fig. 3.31b) is negative (or near zero) in all locations, with strongest sensitivity in the cyclone warm sector, rather than in the cold sector where the largest moisture fluxes occur. Negative values of $\partial J/\partial C_E$ indicate

94
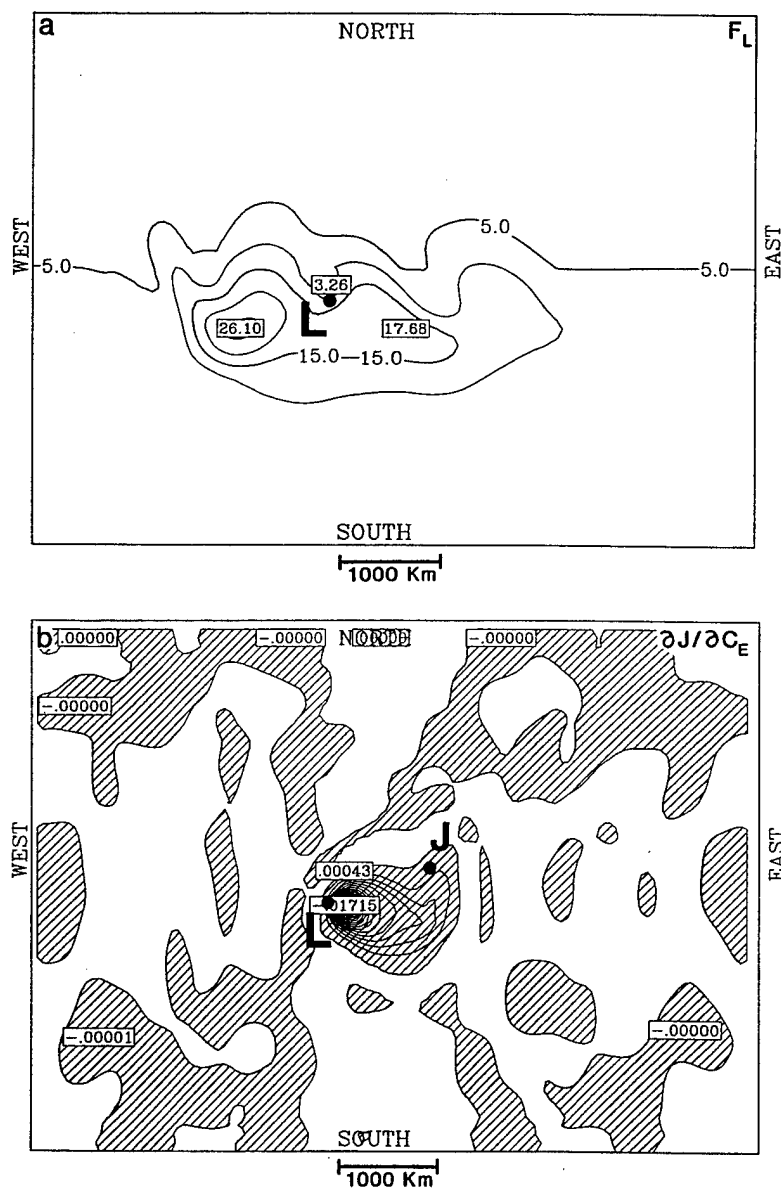
Figure 3.31: (a) Latent heat flux (F_L, contour = 5 W m^{-2}, positive values are upward) at 40 h in the nonlinear forecast; (b) Sensitivity ($\partial J/\partial C_E$) of 60 h cyclone central pressure (J) to perturbations of transfer coefficient for surface latent heat flux (C_E) at 40 h, contour = 0.001 hPa. Negative $\partial J/\partial C_E$ (shaded) indicates F_L is cyclogenetic for 60 h central pressure. L is position of cyclone at 40 h. Simulations include convective and nonconvective precipitation.

95

that if C_E is increased, the 60 h cyclone pressure (J) will decrease. Thus, F_L in the warm sector at 40 h has a cyclogenetic effect (noted also by Emanuel 1994), since an increase in C_E produces an increase in latent heat flux (according to Eq. 3.16) and, through the negative sensitivity, the increase in C_E intensifies the cyclone. Changes to the parameter C_E outside the region of strong sensitivity (for example, in the cyclone cold sector) will have minimal effects on cyclone pressure, even though the latent heat flux may be relatively large in that location.

The adjoint sensitivity to surface transfer parameters during various phases of the cyclone life cycle can be examined by calculating sums over intervals of 10 h of the sensitivity values at all grid points in the model domain. In addition to C_E, the sensitivities to C_H (surface sensible heat transfer coefficient) and C_M (surface momentum stress coefficient) are considered. The sensitivity calculated with the moist (Fig. 3.32a) and dry (Fig. 3.32b) adjoint models is compared with that obtained from moist nonlinear simulations (Fig. 3.32c). The nonlinear sensitivities in Fig. 3.32c are derived from differences between a non-perturbed nonlinear forecast and nonlinear forecasts in which the separate surface transfer coefficients are increased by 0.5×10^{-3} (a 50% perturbation). The sensitivity is obtained by dividing the difference in 60 h central pressure by the transfer coefficient perturbation (0.5×10^{-3}). For example, a perturbation of 0.5×10^{-3} in C_E over the entire model domain between 0 h and 10 h will decrease the 60 h central pressure (J) in a nonlinear forecast by about 0.2 hPa (a product of the perturbation of C_E and the sensitivity $\partial J/\partial C_E$ in Fig. 3.32c).

The sensitivity to C_E is negative at all times, with largest magnitude before 40 h. Thus, F_L is cyclogenetic in a "pre-conditioning" sense before the phase of rapid deepening, since moisture added to the lower troposphere by surface fluxes in the early

96
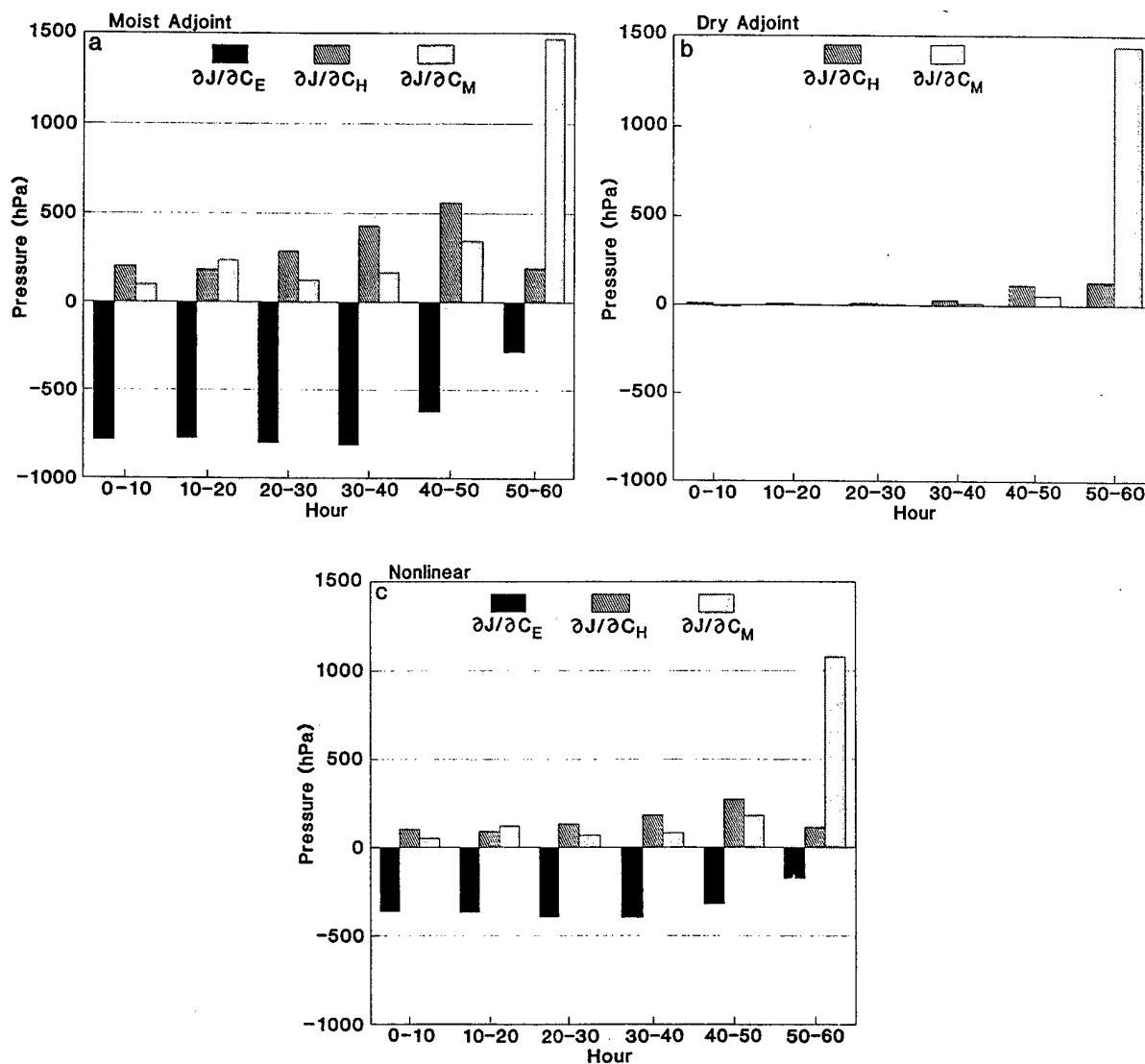
Figure 3.32: Histograms of (a) accumulated adjoint sensitivity for perturbations of surface transfer coefficients, $\partial J/\partial C_E$ (latent heat flux), $\partial J/\partial C_H$ (sensible heat flux), and $\partial J/\partial C_M$ (momentum stress) over entire model domain; (b), as in (a), using dry adjoint model. Effect on 60 h cyclone central pressure (J) is a dot product of a perturbation of C_E, C_H, or C_M and this sensitivity; (c) Nonlinear sensitivity obtained from difference between non-perturbed integrations and nonlinear integrations with surface transfer coefficients increased by 0.5 x 10^{-3} over entire model domain. Moist simulations (a, c) include convective and nonconvective precipitation. Forecast aspect J is pressure at center of 60 h cyclone.

phase of the cyclone development has relatively larger effects on 60 h cyclone intensity. This result is in basic agreement with studies by Danard and Ellenton (1980), Mailhot and Chouinard (1989), Reed and Simmons (1991), Kuo et al. (1991a), and others, who find that surface fluxes early in a cyclone life cycle can provide significant amounts of moisture that later may be directly involved in diabatic heat release in the cyclone.

Between 40 h and 60 h, surface moisture flux has a lesser effect on 60 h cyclone pressure, since F_L is relatively small near the cyclone center, and there is not sufficient time for moisture to be transported from more distant regions of larger fluxes into the area where precipitation processes and diabatic heating influences cyclone intensity at 60 h. Other studies (Kuo and Reed 1988, Manobianco 1989, and Kuo et al. 1991a) have also noted that effects of surface latent heat flux closer to the time or cyclone rapid deepening are relatively small.

The sensitivity to C_E from the nonlinear model (Fig. 3.32c) has a similar pattern to the moist adjoint sensitivity $\partial J/\partial C_E$ depicted in Fig. 3.32a, although the moist adjoint overestimates sensitivity magnitude. Inaccuracy of adjoint sensitivity (compared to nonlinear sensitivity) is largest for the longest forecast interval (e.g., perturbations applied between 0 and 10 h in 60 h forecasts). There would be better correspondence between the adjoint and nonlinear model sensitivities for smaller perturbations.

In this simulation, the domain-total sensitivity related to surface sensible heat flux ($\partial J/\partial C_H$) has positive values during the entire life cycle. This means the surface sensible heat flux (F_S) is *anticyclogenetic*, since an increase in C_H produces increases in 60 h cyclone pressure and F_S. As discussed in Chapt. III.A.4, F_S has a generally

anticyclogenetic effect during the later cyclone development phase, by cooling (downward heat flux) in the warm sector and warming (upward heat flux) in the cold sector. This heating and cooling pattern of F_S opposes the thermal structure of the cyclone warm and cold sectors. The largest sensitivity to F_S in this simulation occurs between 40 h and 50 h in both moist adjoint sensitivity (Fig. 3.32a) and nonlinear sensitivity (Fig. 3.32c).

The effects of sensible heat flux can be highly variable during a cyclone life cycle, and are strongly affected by sea-surface temperature patterns. For example, a sea-surface temperature (SST) perturbation was used in Chapt. III.A.4 to increase F_S in the warm sector, which provided a cyclogenetic pre-conditioning effect early in the cyclone life cycle. Here, the sea-surface temperature is zonally uniform, and there is no pre-conditioning effect from the sensible heat flux.

Sensitivity to the surface momentum transfer coefficient ($\partial J/\partial C_M$) is also positive through the entire life cycle, which implies that the surface stress has an anticyclogenetic effect, as noted in Chapt. III.A.5. In contrast to the sensible and latent heat flux sensitivity, sensitivity to surface stress is largest between 50 and 60 h, when the cyclone is strongest. Thus, the surface stress is a process that acts as a direct brake on cyclone intensification.

For comparison, the sensitivities $\partial J/\partial C_H$ and $\partial J/\partial C_M$ obtained with the dry adjoint model are depicted in Fig. 3.32b. The accuracy provided by the dry adjoint for $\partial J/\partial C_H$ and $\partial J/\partial C_M$ is most acceptable during the period from 40 h to 60 h. Apparently, perturbing C_H and C_M after 50 h does not involve significant interaction with moist physics, in terms of effects on 60 h cyclone pressure. However, accurate sensitivity over longer forecast intervals requires moist processes in the adjoint model.

Sensitivity provided by the dry adjoint model (and perturbation growth in the dry TLM) is too small in magnitude when compared to actual moist nonlinear sensitivity and perturbation growth rates.

This Chapter has examined the development of extratropical cyclone in idealized simulations, through examination of the nonlinear forecast, and by interpretation of information provided by adjoint sensitivity. In the next Chapter, a similar approach is used to examine the life cycle of a cyclone that developed in the North Atlantic Ocean during 20 - 22 January 1995.

IV. NORTH ATLANTIC CYCLONE OF 20-22 JANUARY 1995

The previous Chapter described simulations of idealized extratropical cyclones, and the use of adjoint sensitivity to interpret their development. The focus of this Chapter is on the interpretation of a real cyclone that developed in the North Atlantic ocean during 20 - 22 January 1995 (which will be called the "J95" cyclone). The adjoint sensitivity for this case is expected to be more complex than in the idealized simulations, because of greater uncertainty associated with the initial conditions and the inclusion of a real sea-surface temperature field.

This particular cyclone was selected in part to examine sensitivity for a storm that represents a typical "end-of-stormtrack" cyclone of the type to be studied in the Fronts and Atlantic Storm Track Experiment (FASTEX, Thorpe and Shapiro 1995). These cyclones begin as amplifying waves in baroclinic zones beneath the jet core in the middle or western North Atlantic, and intensify as they move eastward and approach northwestern Europe (Fig. 4.1). During the cyclone development, a large area of low pressure (the Icelandic low) usually remains nearly stationary in the region between Iceland, the U.K., and Norway.

End-of-stormtrack cyclones may experience rapid surface pressure decreases. The cyclone known as the "U.K. Great Storm" (14-16 October 1987) deepened explosively (34 hPa in 24 h) and reached a minimum central pressure of 948 hPa on the western tip of France (Jarraud et al. 1989). A cyclone on 11-13 January 1993 deepened 15 hPa in an 18 h period, including a shorter interval of rapid deepening (Browning and Roberts 1994).
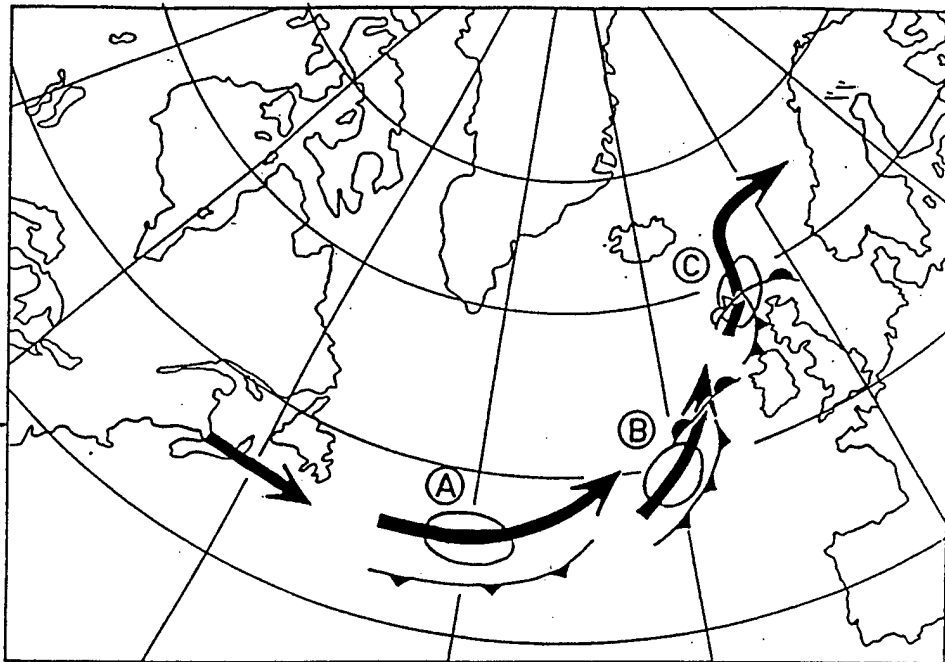
Figure 4.1: Conceptual diagram of North Atlantic end-of-stormtrack cyclone. The black arrows show the jet stream and the isotach (thin solid line) indicates the jet streak position with respect to the evolving surface frontal positions (from FASTEX science plan, Thorpe and Shapiro 1995).

A simulation of the J95 cyclone with the MAMS1 moist nonlinear model will be described in Chapt. IV.A. In Chapt. IV.B, the MAMS1 adjoint (including moist physics) and dry NOGAPS (Navy Operational Global Atmospheric Prediction System) adjoint are used to examine initial condition sensitivity. In Chapt. IV.C, the development of initial condition perturbations is examined with the MAMS1 TLM and nonlinear models, and interpreted in the context of cyclone conceptual models and predictability.

A.   NONLINEAR SIMULATION

The grid configuration of the MAMS1 model is similar to that used in the idealized cyclone simulations in Chapt. III. There are 121 grid points in the east-west
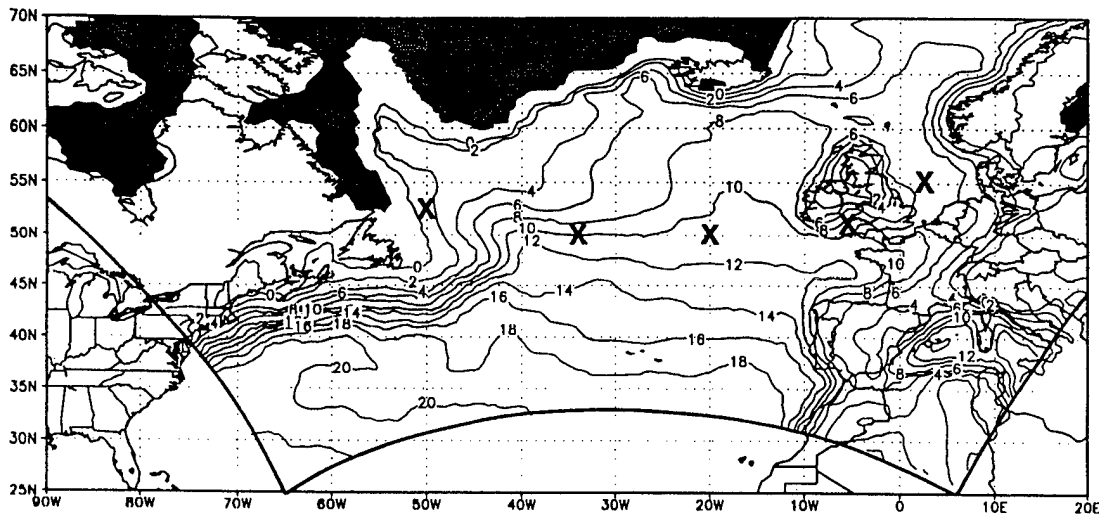
Figure 4.2: Initial surface temperature (minimum contour = 0°C, contour interval = 2°C) at 00UTC 20 Jan 1995. Sea-surface temperature is constant during entire forecast. **X** indicates locations of J95 cyclone at 12 h intervals between 00UTC 20 January and 00UTC 22 January 1995. Areas covered by ice are shaded. Heavy solid line is boundary of Mesoscale Adjoint Modeling System Version 1 (MAMS1) grid.

direction and 82 grid points in the north-south direction with horizontal grid spacing of 60 km, on a Lambert conformal map projection. The model has 14 vertical levels (see Fig. A.1). In this simulation, a version of the relaxed Arakawa-Schubert cumulus parameterization replaces the Hack scheme used in the idealized cyclone study of Chapt. III.B. Other differences in model specifications between this simulation and the idealized simulations are summarized in Appendix A.

Initial conditions for the MAMS1 nonlinear forecast are obtained from a NOGAPS analysis at T79L18 resolution. Interpolation to the MAMS1 grid is bilinear (horizontal) and logarithmic in pressure (vertical). A description of NOGAPS is provided by Hogan and Rosmond (1991). A nonlinear normal mode initialization is performed prior to the forward nonlinear MAMS1 model integration. Lateral boundary conditions for MAMS1 are also obtained from NOGAPS, and are provided

at 12 h intervals, according to a Davies and Turner (1977) relaxation scheme. Model initial conditions include temperature, winds, mixing ratio, terrain pressure, and sea-surface temperature, as well as specification of topography and surface type (land, ocean, ice; Fig. 4.2). In Figs. 4.2 - 4.8, the identifier **X** is used to mark the cyclone position at 12 h intervals. At the initial time, the cyclone signature is too weak to be determined by inspection of the nonlinear model fields, so its position (**X**) is approximated by interpretation of sensitivity from the adjoint model (primarily Fig. 4.12a,b), which are discussed in the next section.

At 00UTC 20 January 1995, a large-scale trough extends from Greenland southeast to the North Sea (Fig. 4.3a). Within this trough, distinct (closed isobar) low pressure centers are found over Scotland (976 hPa) and south of Iceland (972 hPa). Each of these centers has associated cyclonic vorticity in the lower troposphere (850 hPa level) of 10-15 x 10^{-5} s^{-1} (Fig. 4.3a). At 850 hPa, a baroclinic zone extends southwest from the U.K. to 20°W, then northwest to Canada (Fig. 4.4a). At the 250 hPa level, jet speeds above the baroclinic zone exceed 60 m s^{-1} west of 30°W and east of 10°W (Fig. 4.5a). High values of potential vorticity at 250 hPa exist in the trough over the U.K., and over Greenland and northeastern Canada (not shown). Although the J95 cyclone originates almost directly under a 250 hPa jet streak, little evidence exists that the initial cyclone development is related to middle or upper tropospheric features, since the 500 hPa vorticity advection (Fig. 4.6a) and 250 hPa divergence (Fig. 4.5a) are very weak above the most likely position (**X**) of the incipient cyclone.

Based on inspection of the MAMS1 nonlinear forecast, and interpretations of adjoint sensitivity discussed later in this Chapter, it appears that the J95 cyclone may have originated as a small-scale instability in the lower troposphere east of

Newfoundland. The initial increase in cyclonic vorticity may be related to strong surface fluxes of latent and sensible heat occurring above an area of anomalously high sea-surface temperature (Fig. 4.2) in cold northwesterly flow at and prior to 00UTC 20 January (Fig. 4.7a).

At 12UTC 20 January 1995 (12 h forecast), the developing J95 cyclone is a small-scale feature associated with a local maximum in vertical velocity (Fig. 4.4b), but without a strong lower-tropospheric vorticity signature (Fig. 4.3b). The J95 cyclone is now on the south side of the 250 hPa jet (Fig. 4.5b) in an area of positive 500-1000 hPa thickness advection (Fig. 4.7b) and increasing divergence in the upper troposphere (Fig. 4.5b). Vorticity advection at 500 hPa (Fig. 4.6b) is still not well-developed above the incipient cyclone.

At 00UTC 21 January 1995 (24 h forecast), the J95 cyclone is now evident as an area of enhanced vorticity (Fig. 4.3c) and vertical motion (Fig. 4.4c) in an area of strong thickness advection (Fig. 4.7c) near 20°W, 50°N. The cyclone is still under the 250 hPa jet axis, with strong upper-tropospheric divergence (Fig. 4.5c) to the northeast (in the direction of storm motion) in the left-front quadrant of the jet streak.

At 12UTC 21 January 1995 (36 h forecast), the J95 cyclone is just west of Wales and has the characteristics of a well-defined intensifying cyclone. Although 850 hPa vorticity exceeds 20×10^{-5} s^{-1}, the cyclone appears not as a closed isobar system, but as the southernmost tip of the Icelandic low (Fig. 4.3d). Strong upward motion is found above the cyclone in the mid-troposphere (Fig. 4.4d). The cyclone is located under upper-level divergence associated with the left-front quadrant of the 250 hPa jet streak (Fig. 4.5d). Thickness advection in the lower troposphere (Fig. 4.7d) and 500 hPa vorticity advection (Fig. 4.6d) are now quite strong in the cyclone location.
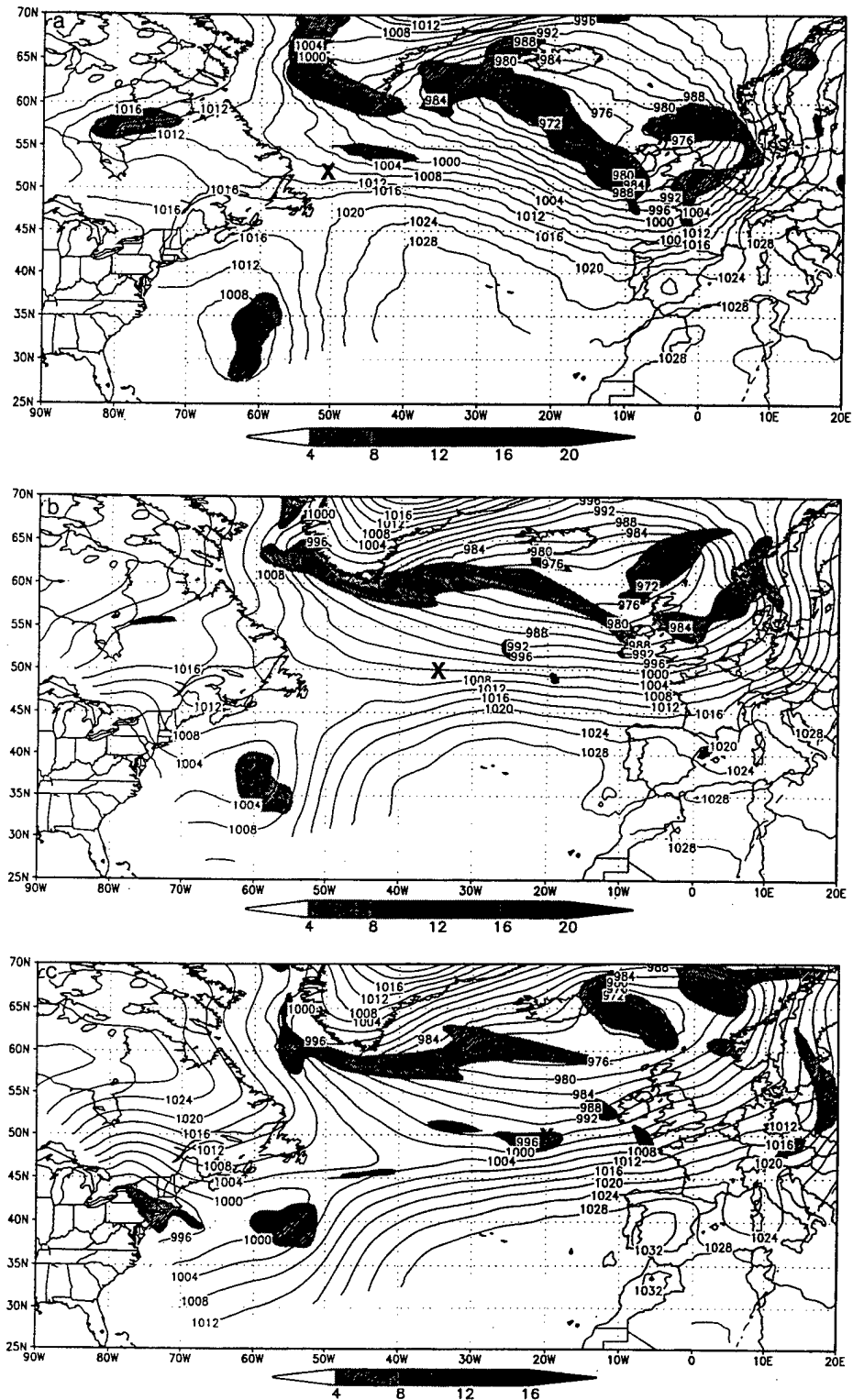
Figure 4.3: Sea-level pressure (hPa) and 850 hPa vorticity (shaded, 10^{-5} s^{-1}); (a) analysis at 00UTC 20 January, and MAMS1 forecasts at 12 h intervals valid at: (b) 12UTC 20 January; (c) 00UTC 21 January; (d) 12UTC 21 January; and (e) 00UTC 22 January 1995. **X** indicates location of J95 cyclone.

106
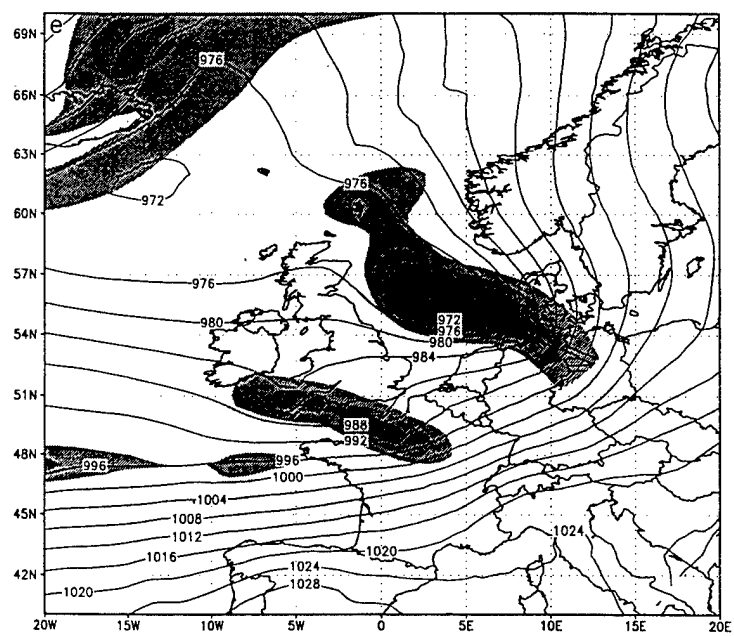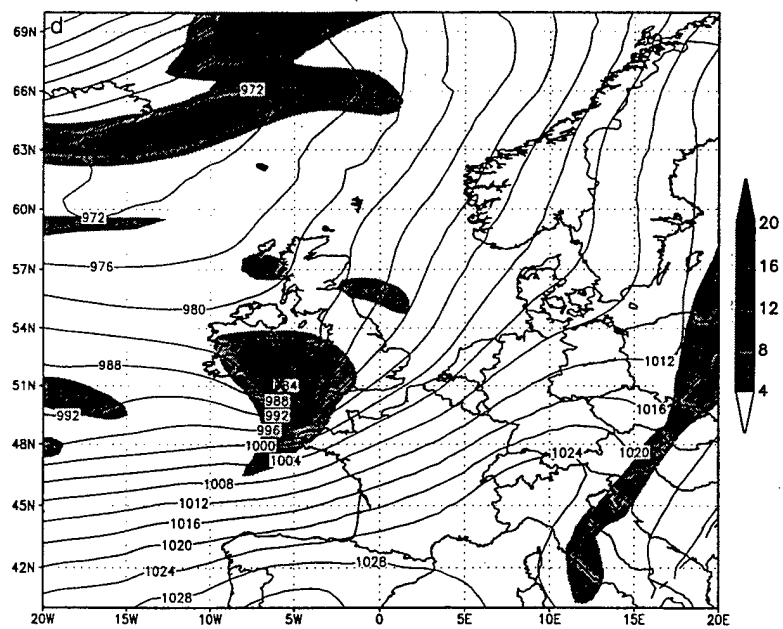
Figure 4.3, continued
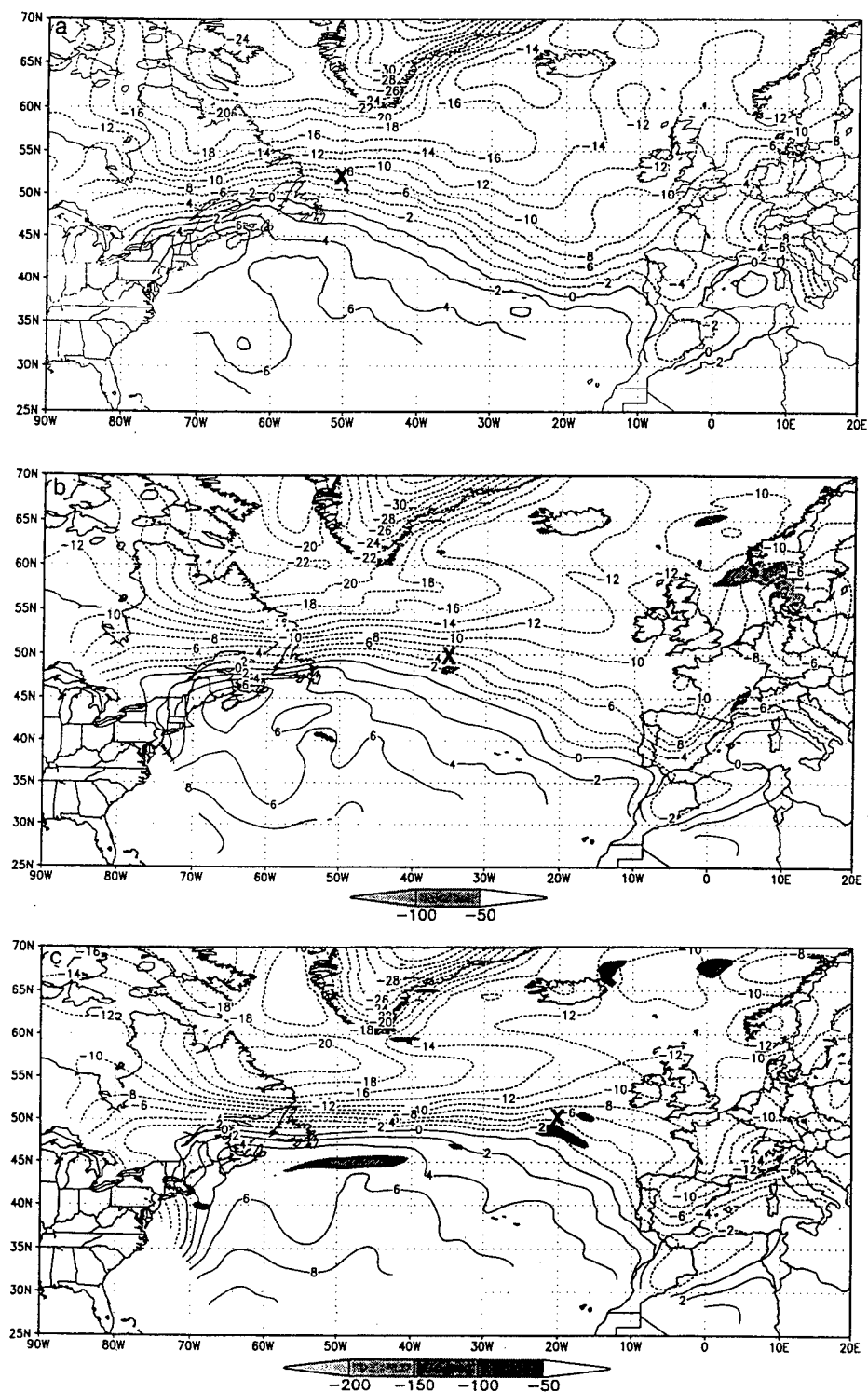
Figure 4.4: 760 hPa Temperature (°C) and omega (shaded, 10^{-4} hPa s^{-1}); (a) analysis at 00UTC 20 January, and MAMS1 forecasts at 12 h intervals valid at: (b) 12UTC 20 January; (c) 00UTC 21 January; (d) 12UTC 21 January; and (e) 00UTC 22 January 1995. Note: omega not plotted for 00UTC 20 January 1995 (initial conditions). **X** indicates location of J95 cyclone.
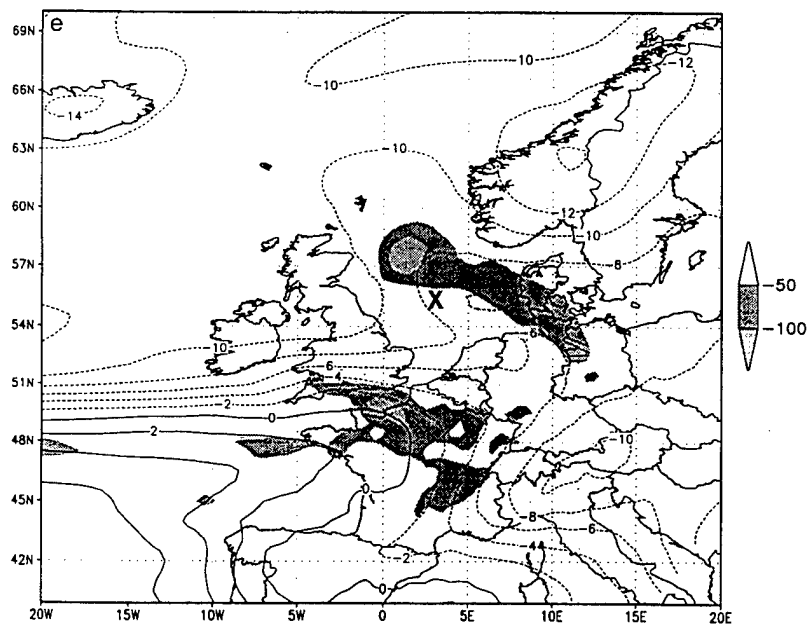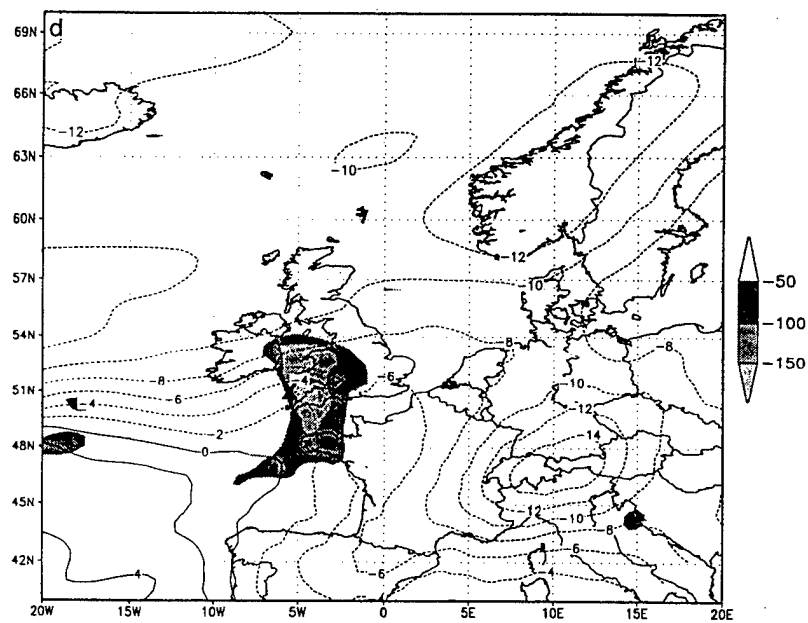
Figure 4.4, continued
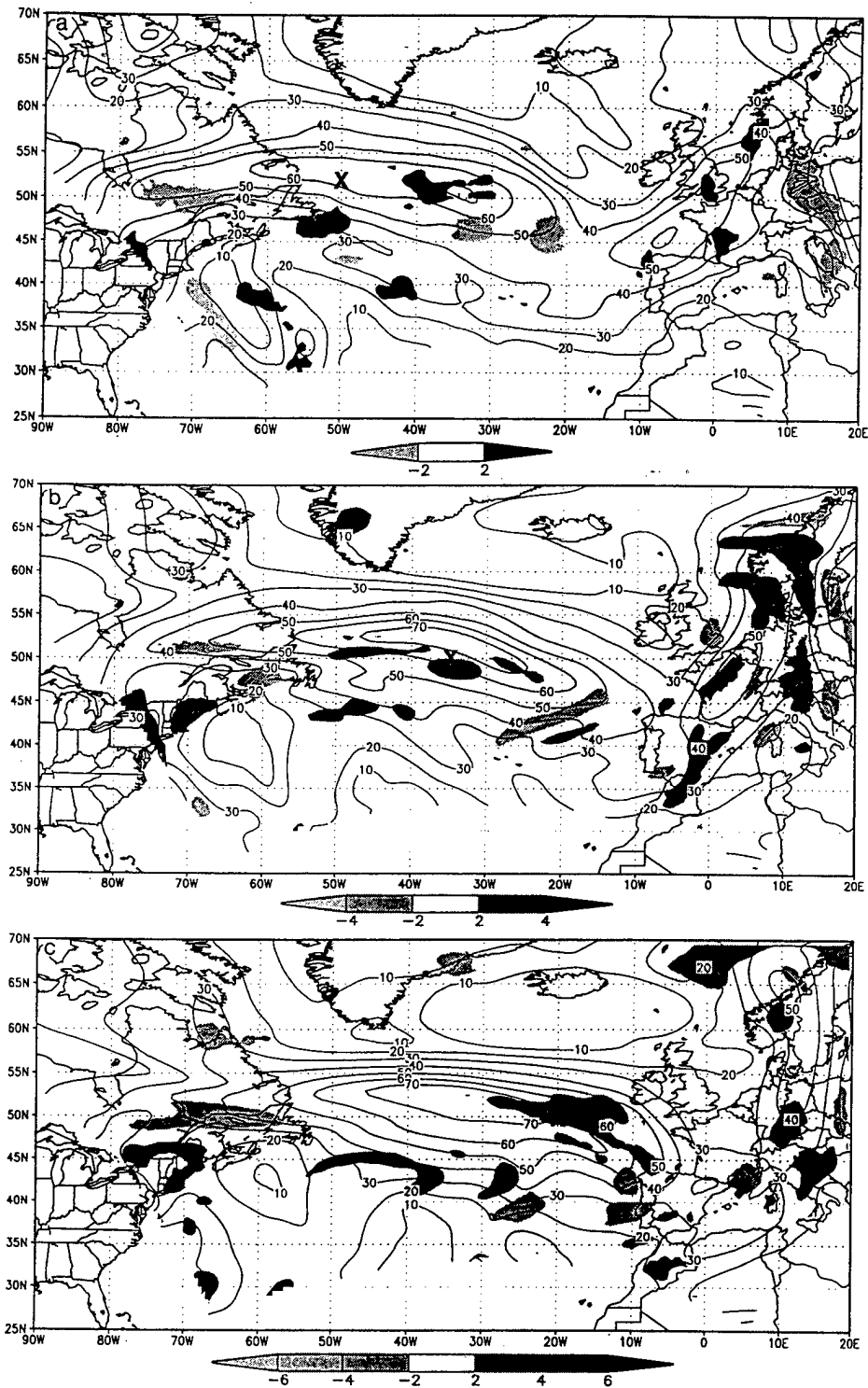
Figure 4.5: 250 hPa wind speed (m s^{-1}) and divergence (shaded, 10^{-5} s^{-1}); (a) analysis at 00UTC 20 January, and MAMS1 forecasts at 12 h intervals valid at: (b) 12UTC 20 January; (c) 00UTC 21 January; (d) 12UTC 21 January; and (e) 00UTC 22 January 1995. **X** indicates location of J95 cyclone. Heavy solid line in (e) indicates area of forecast aspect J referred to in Fig. 4.18.

110
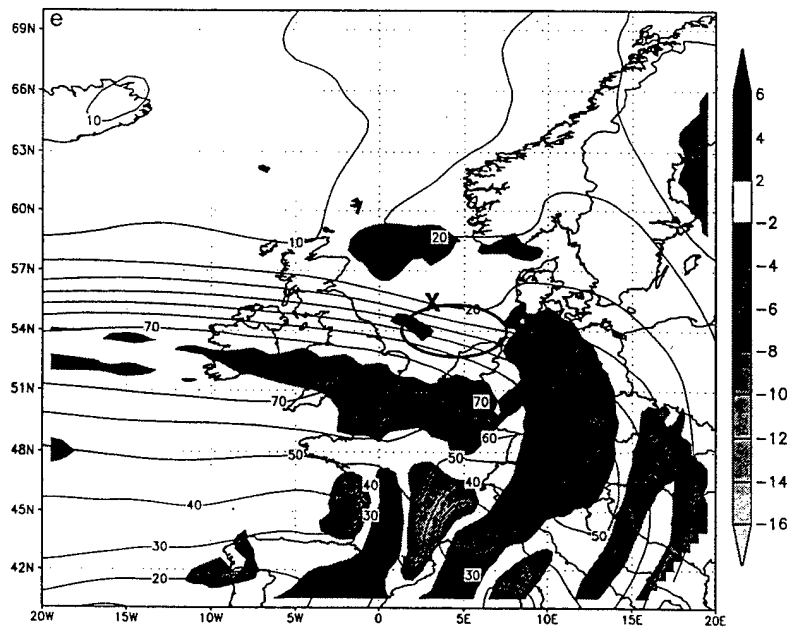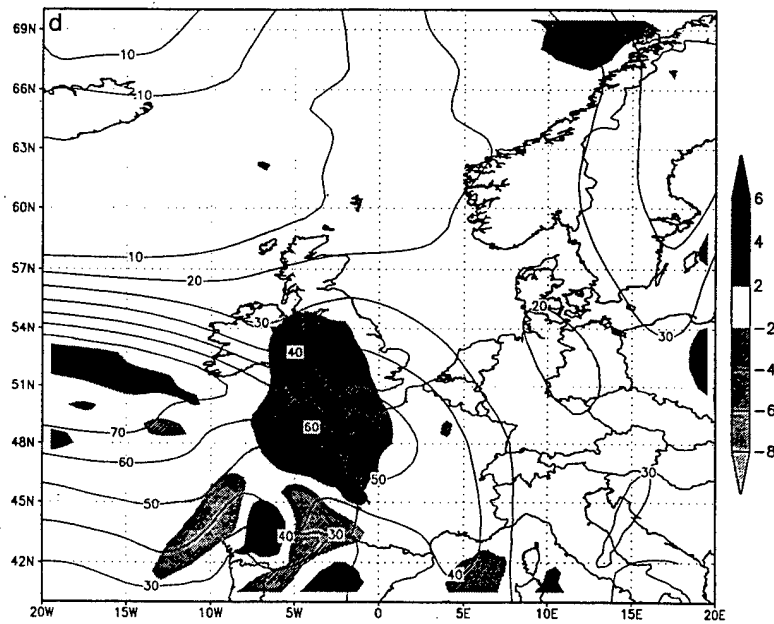
Figure 4.5, continued
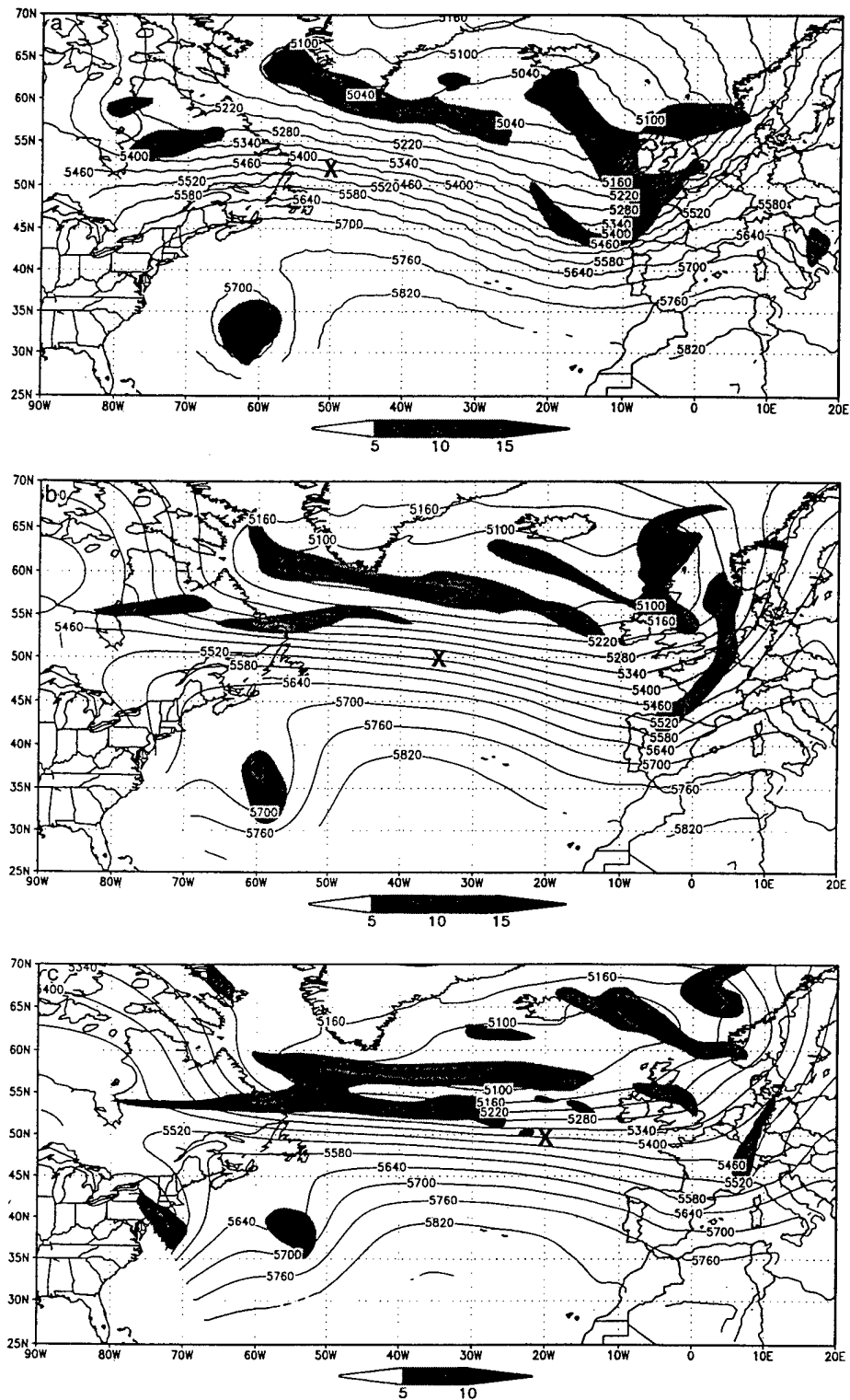
Figure 4.6: 500 hPa height (°C) and cyclonic vorticity (shaded, 10^{-5} s^{-1}); analysis at 00UTC 20 January, and MAMS1 forecasts at 12 h intervals valid at: (b) 12UTC 20 January; (c) 00UTC 21 January; (d) 12UTC 21 January; and (e) 00UTC 22 January 1995. **X** indicates location of J95 cyclone.

112
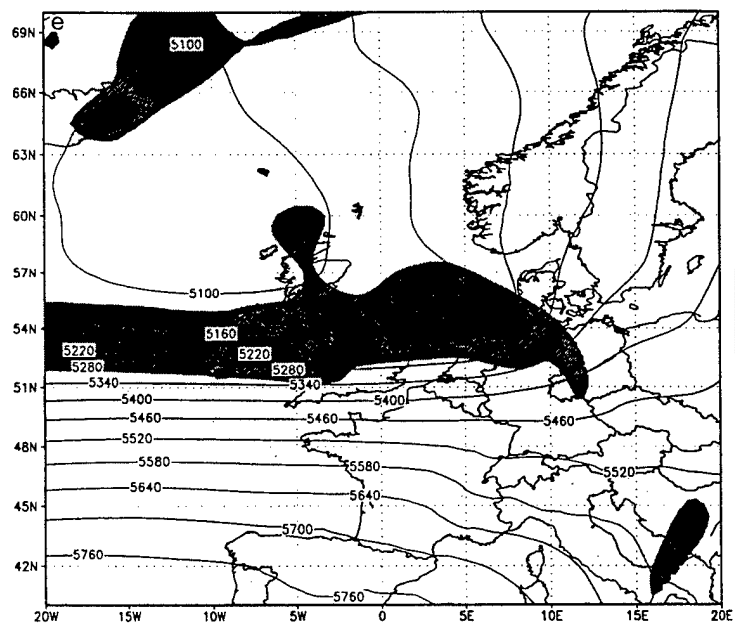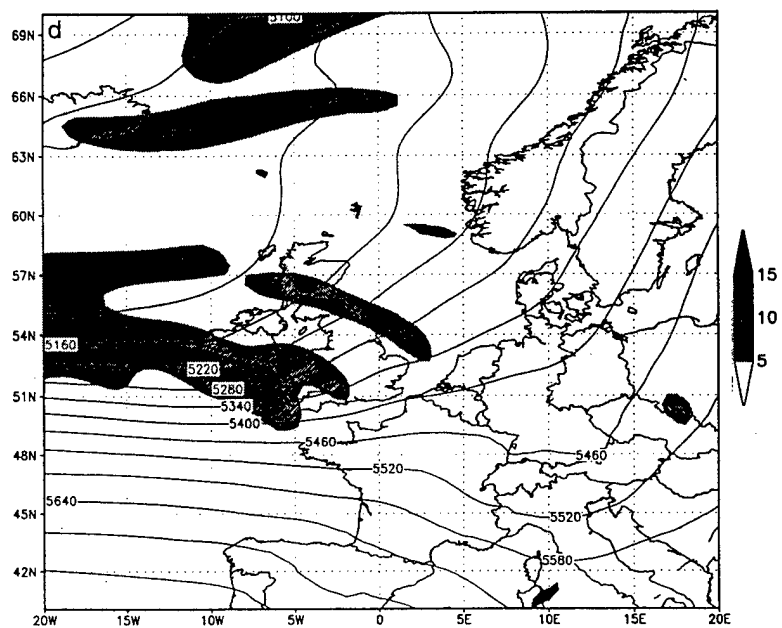
Figure 4.6, continued

113
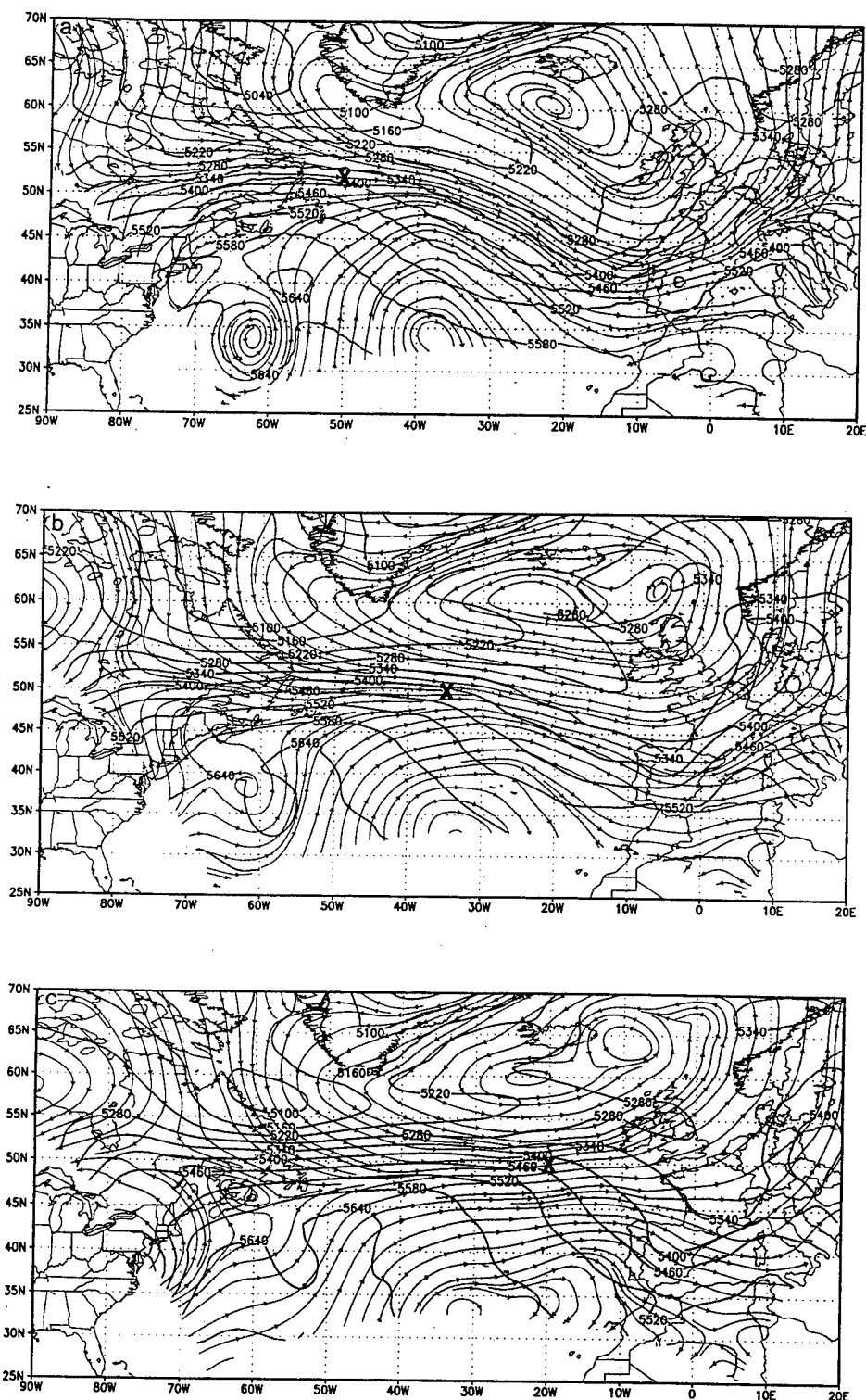
Figure 4.7: 500-1000 hPa thickness (m) and streamlines of 760 hPa wind; analysis at 00UTC 20 January, and MAMS1 forecasts at 12 h intervals valid at: (b) 12UTC 20 January; (c) 00UTC 21 January; (d) 12UTC 21 January; and (e) 00UTC 22 January 1995. **X** indicates location of J95 cyclone.

114
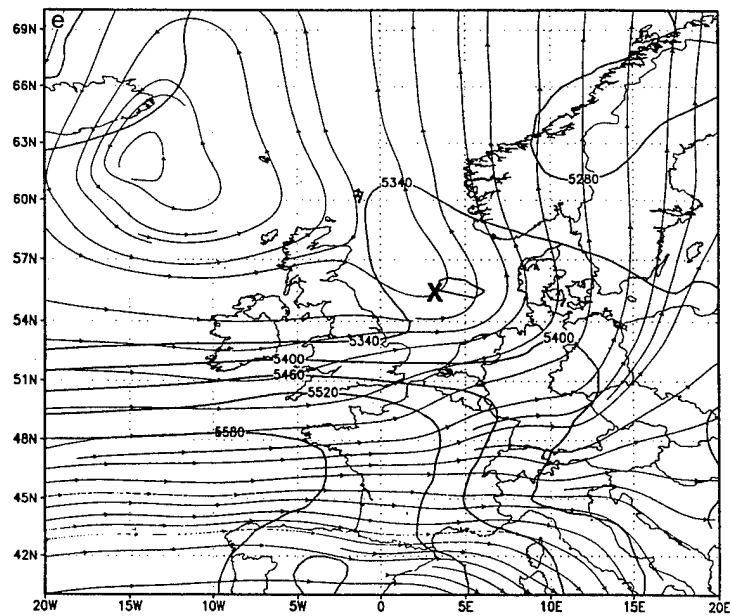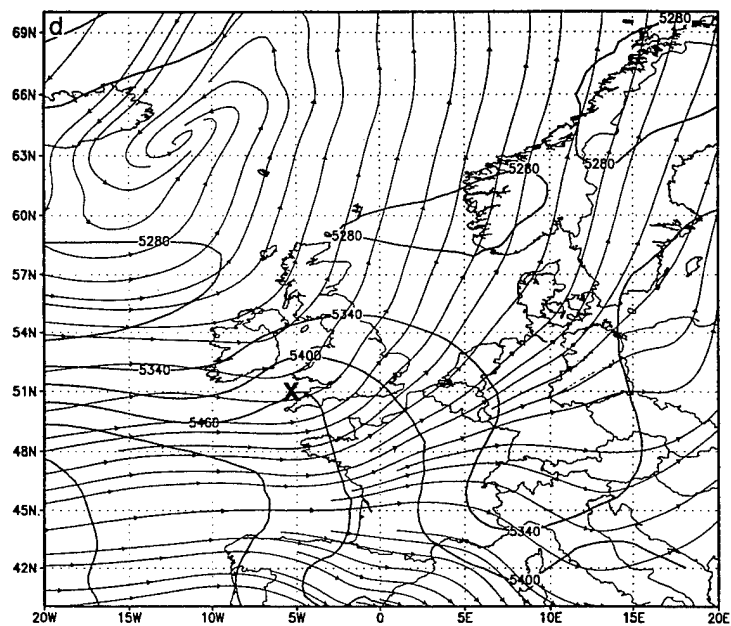
Figure 4.7, continued

At 00UTC 22 January 1995 (48 h forecast), the J95 cyclone (minimum pressure 972 hPa) is located in the North Sea between England and Norway within the larger area of the Icelandic low, which extends northwest toward a secondary 972 hPa pressure minimum near 15°W, 62°N. The associated 850 hPa vorticity is 24 x 10^{-5} s^{-1} (Fig 4.3e), with 850 hPa winds of 25-30 m s^{-1}. Processes associated with the storm have begun to weaken, including vertical motion (Fig. 4.4e), upper-tropospheric divergence (Fig. 4.5e), thickness advection (Fig. 4.7e), and vorticity advection at 500 hPa (Fig. 4.6e).

The total accumulated precipitation during the J95 cyclone forecast is shown in Fig. 4.8. A narrow band of nonconvective precipitation (Fig. 4.8a) between 45°N and 55°N stretches across the Atlantic, south of the cyclone track, and into the North Sea, associated with warm frontal rainfall. A larger area of convective precipitation covers the eastern Atlantic, from Iceland to the European continent. Most of this precipitation appears to be associated with the large-scale Icelandic low, although convective rain occurs along the J95 cyclone path just prior to landfall in Wales, and in the North Sea between Scotland and Norway. The areas of nonconvective and convective precipitation west of 30°N in Figs. 4.8a,b are associated with a different low pressure system that developed separately from the J95 cyclone.

Because the J95 cyclone does not exist as a closed isobar low pressure center at 24 h or 36 h, it is difficult to determine the rate of pressure change for the cyclone as a separate entity. An estimate of the deepening rate is 12 hPa (984 to 972 hPa) during the last 12 h of the forecast, which places the J95 cyclone on the threshold of "explosive" development. The pressure change at the 48 h location of the J95 cyclone
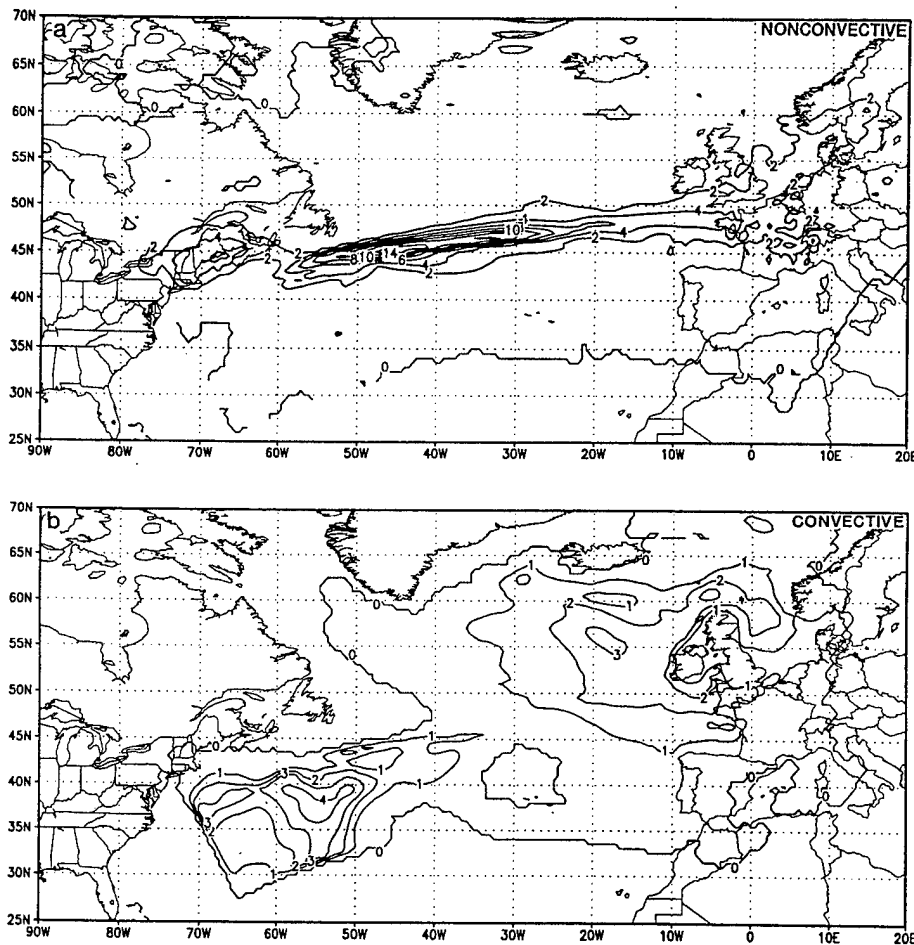
Figure 4.8: (a) Nonconvective rainfall accumulated during 48 h MAMS1 nonlinear forecast from 00UTC 20 January to 00UTC 22 January 1995; (b) as in (a) for convective rainfall. Contour interval = 1.0 cm.

is approximately 20 hPa during the 24 h interval from 00UTC 21 January to 00UTC 22 January 1995.

The 48 h MAMS1 nonlinear model forecast places the J95 cyclone at approximately 3° E, 55° N. Comparison to an analysis of 850 hPa vorticity (Fig. 4.9a) from the European Centre for Medium-range Weather Forecasts (ECMWF) indicates that the cyclone position at 00UTC 22 January is actually 0°E, 58°N. The cyclone position indicated by the ECMWF analysis is confirmed by a satellite image (Fig. 4.9b).

117
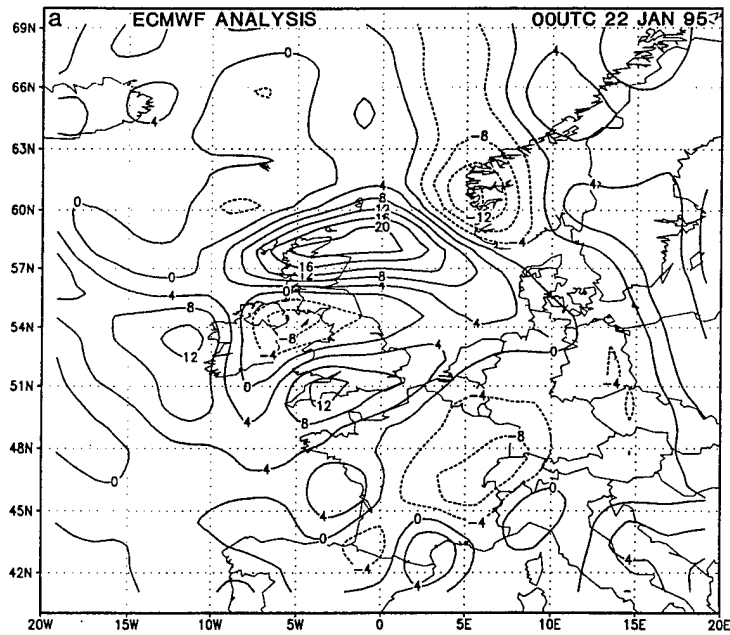
Figure 4.9: (a) Analysis of 850 hPa vorticity (10^{-5} s^{-1}) from European Centre for Medium-range Weather Forecasts (ECMWF) global model at 00UTC 22 January 1995; (b) Defense Meteorological Satellite Program (DMSP) image at 06 UTC 22 January 1995.

The MAMS1 forecast therefore has a positional error of roughly 350 km (to the southeast), although forecast cyclone intensity in terms of 850 hPa vorticity (24×10^{-5} s^{-1}, Fig. 4.3e) compares well to the ECMWF analysis (21×10^{-5} s^{-1}, Fig. 4.9a). The purpose of this study is to interpret physical processes of cyclone development, as simulated by the MAMS1 nonlinear model. The existence of these forecast errors related to cyclone position and intensity does not restrict the use of adjoint sensitivity for interpretation of the cyclone life cycle.

The J95 cyclone life cycle may be compared to the composite Atlantic cyclone described by Rogers and Bosart (1986). Similarities include incipient stage development in the lower troposphere, with the explosive stage involving anomalies in the middle and upper troposphere. The initial increase of lower tropospheric vorticity in the J95 cyclone within a thermally unstable boundary layer above a warm SST anomaly is consistent with mechanisms described by Doyle and Warner (1993a,b) and Bosart et al. (1995) that lead to lower tropospheric fronts and mesoscale cyclones. The cyclones described by Wash et al. (1988) also involve *incipient* cyclone development under fairly straight upper-level flow, without involvement of appreciable cyclonic vorticity advection.

Similarities are also evident between the J95 cyclone and the two-stage cyclone development process described by Gyakum (1991) and Gyakum et al. (1992) in which vorticity in the lower troposphere increases during an "antecedent" phase prior to involvement with upper-tropospheric features. Takayabu (1991) also interprets cyclogenesis in terms of a pre-existing lower-tropospheric vortex interacting with upper-tropospheric forcing. However, the J95 cyclone attains near-explosive deepening rates without a significant short-wave trough in the upper troposphere.

119

The J95 cyclone may be considered in terms of an instability that originates in the lower troposphere. As the cyclone develops over 48 h, the initially small-scale instability and associated flow anomalies grow in horizontal and vertical scale to include the entire depth of the troposphere above the cyclone. As in the idealized cyclone simulation of Chapt. III, thermal advection in the lower troposphere appears to be a critical process in cyclone intensification. It will be shown later that a small perturbation of initial temperature in the lower troposphere can intensify the jet streak at 250 hPa above the cyclone, as well as the surface cyclone.

B. ADJOINT RESULTS

1. MAMS1 (Regional Model) Results

Sensitivity information provided by an adjoint of a nonlinear forecast model can be used to interpret the development of the J95 cyclone, similar to the analysis of the idealized cyclone described in Chapter III. Here, the forecast aspect (J) is selected as relative vorticity over the J95 cyclone in a vertical column extending from approximately 660 hPa to the surface. In this type of end-of-stormtrack cyclone, which forms within the larger Icelandic low, the choice of J as vorticity provides sensitivity that relates directly to the localized feature of interest. Whereas J could be defined as surface pressure at the center of the J95 cyclone, this choice is more appropriate for isolated cyclones that are associated with stronger pressure gradients.

In MAMS1, J = vorticity at 48 h is represented by specifications of $\partial J/\partial u$ and $\partial J/\partial v$, in locations based on maxima and minima of u and v (Fig. 4.10) associated with the cyclone in the 48 h nonlinear forecast. The signs of $\partial J/\partial u$ and $\partial J/\partial v$ at 48 h (Fig. 4.11) are chosen so that a positive J' represents an increase of the vorticity that already exists in the 48 h nonlinear forecast (Fig. 4.3e).
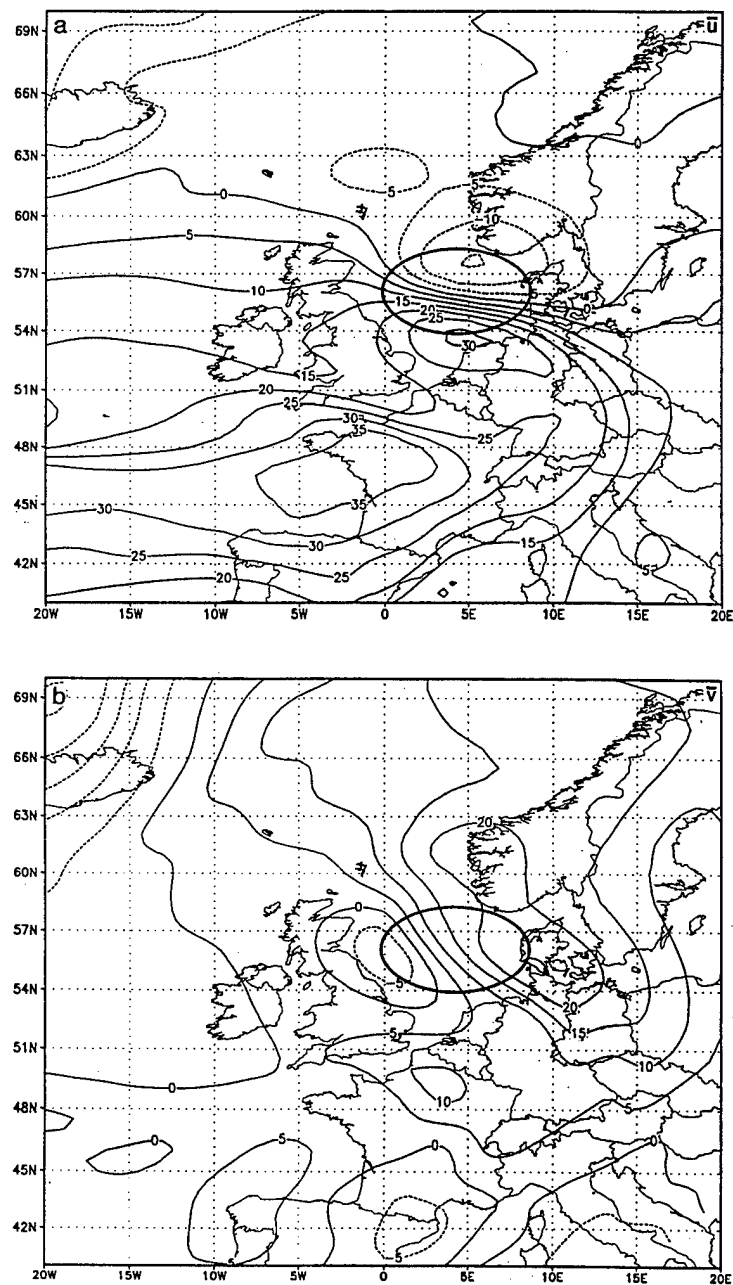
Figure 4.10: MAMS1 48 h nonlinear forecast at 00UTC 22 January 1995 of (a) 850 hPa zonal wind, and (b) 850 hPa meridional wind (contour interval = 5 m s^{-1}). Heavy solid line denotes area in which J represents the average vorticity between 660 hPa and surface.

121
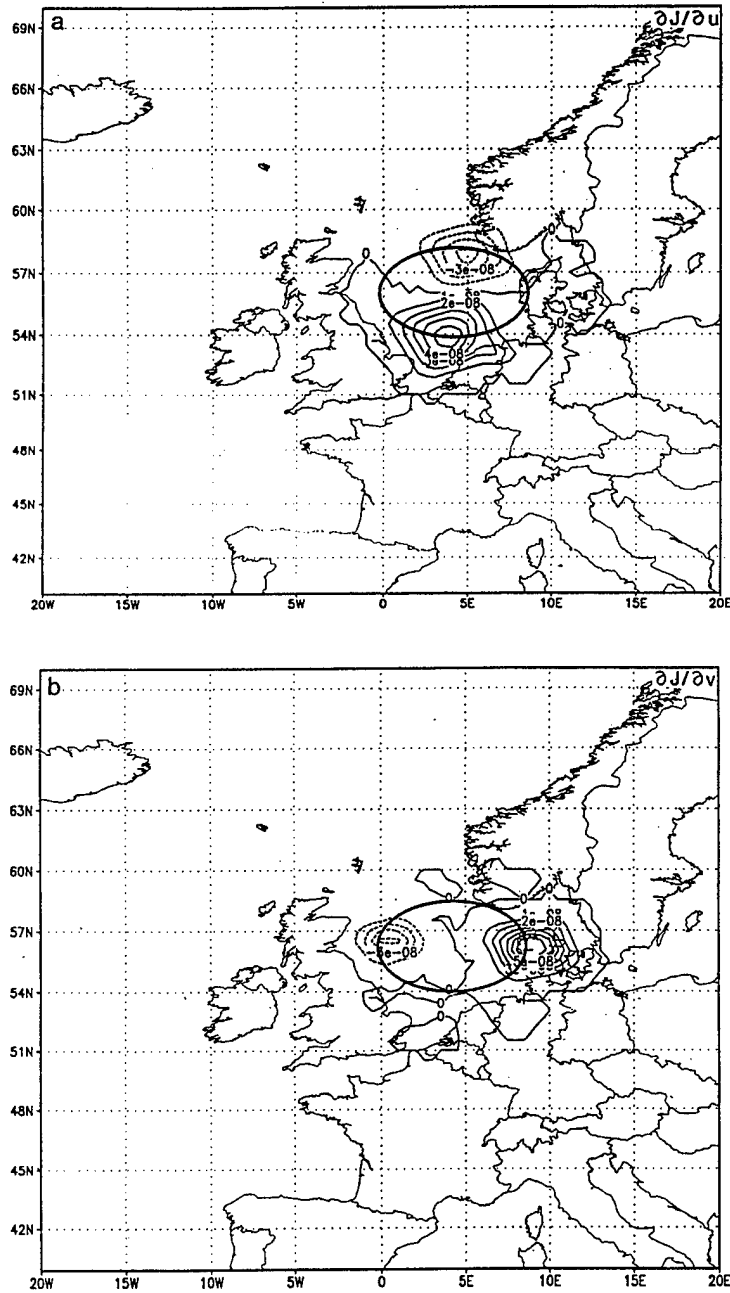
Figure 4.11: Starting values of 850 hPa (a) $\partial J/\partial u$, and (b) $\partial J/\partial v$ (contour interval = 1×10^{-8} m^{-1}) for the MAMS1 adjoint integration at 00UTC 22 January 1995 in which J represents the average vorticity between 660 hPa and surface within area of heavy solid line.

A weighting factor is applied to the starting values of $\partial J/\partial u$ and $\partial J/\partial v$ to account for variations in grid volume mass (the procedure is described in Chapt. II.B). The purpose of this weighting is to have J represent *average vorticity*, by making the starting values of $\partial J/\partial u$ and $\partial J/\partial v$ proportional to mass within grid volumes. *For display purposes*, the sensitivity is normalized by a grid volume mass factor (described in Chapt. II) to remove the effects of differences in grid volume size on sensitivity magnitude. Actual sensitivity within the context of the model grid is still evaluated without the normalization. For the vertical grid configuration used here, the sensitivity normalization introduces minimal change, except for some increase in sensitivity magnitude displayed below 900 hPa.

In this simulation, the basic state coefficients (time-varying nonlinear trajectory) is provided to the adjoint (or tangent linear) model at 15 min intervals. The Jacobian matrices required for adjoint precipitation processes are provided at 30 min intervals (the Jacobians required very large files, which mandated a longer update interval). With this basic state update interval, the tangent linear and adjoint accuracies are quite good during the 48 h forecast interval, as will be shown in section C of this Chapter.

Sensitivity to the initial conditions (at 00UTC 20 Jan 1995) for the J95 cyclone is obtained by a 48 h (backward-in-time) integration of the adjoint model. At the initial time, the maximum sensitivity from the moist MAMS1 adjoint is located between 500 and 800 hPa in an area roughly between 45° - 60° W and 50° - 55° N (Fig. 4.12). A strong spatial correlation exists for $\partial J/\partial T$, $\partial J/\partial v$, and $\partial J/\partial q$ in the mid-troposphere, as noted previously for the idealized cyclone. The interpretation is that in the same location of positive sensitivity, positive perturbations of temperature,

Figure 4.12: Sensitivity at -48 h (00UTC 20 January 1995) with moist MAMS1 adjoint: (a) $\partial J/\partial T$ at 760 hPa, contour interval = 5×10^{-8} s^{-1} deg^{-1}; (b) $\partial J/\partial v$ at 760 hPa, contour interval = 5×10^{-9} m^{-1}; (c) $\partial J/\partial q$ at 760 hPa, contour interval = 1×10^{-4} s^{-1}; and (d) $\partial J/\partial u$ at 350 hPa, contour interval = 5×10^{-9} m^{-1}. Forecast aspect J is the average vorticity between 660 hPa and surface at 48 h cyclone position, as in Fig. 4.11. P1 and P2 in (a) and P3 in (d) refer to perturbations discussed in text. Tic marks labeled "A-B" in (a-c) and "C-D" in (d) are locations of vertical cross-sections in Figs. 4.13a-c, and Fig. 4.14b, respectively.

124
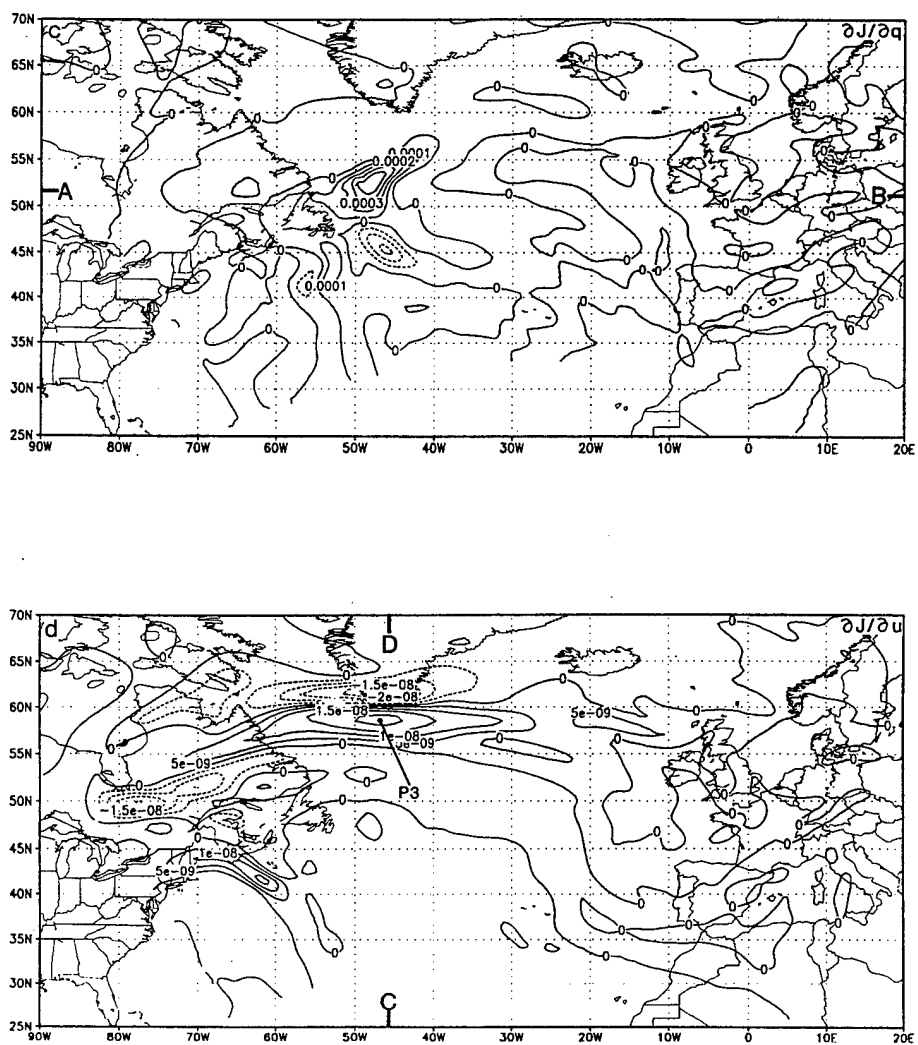
Figure 4.12, continued

meridional wind, and moisture will all have the effect of increasing the vorticity of the J95 cyclone 48 h hence. The sensitivity to zonal wind $\partial J/\partial u$ also has greatest magnitude between 500 - 800 hPa. In Fig. 4.12d, $\partial J/\partial u$ is shown at 350 hPa to illustrate a weaker sensitivity feature that exists in association with a region of high cyclonic vorticity between the jet stream core and southern Greenland. The largest magnitude of $\partial J/\partial u$ at 350 hPa is -23 x 10^{-9} m^{-1}, compared to -49 x 10^{-9} m^{-1} at 660 hPa.

Although regions of lesser sensitivity are found in Fig. 4.12, the locations of maximum sensitivity ($\partial J/\partial T$, $\partial J/\partial v$, and $\partial J/\partial q$) near 52°N, 49°W define the position of the J95 cyclone precursor in the initial conditions at -48 h. For example, the area of positive $\partial J/\partial T$ in the lower troposphere corresponds to the "warm sector" of the incipient cyclone (the correspondence of maximum sensitivity to the cyclone position is also valid at other stages of the life cycle). Without this adjoint-based sensitivity information, it would be difficult to identify the location of the J95 cyclone precursor from analyzed fields at the initial time. In the following section, it will be demonstrated how small perturbations of temperature and wind in the location of the precursor (and in other locations) impact the cyclone forecast 48 h later.

East-west vertical cross sections through the region of maximum sensitivity to temperature, meridional wind, and mixing ratio (Fig. 4.13) depict similar tilted structures to those in the idealized cyclone simulation. The spatial correlations and baroclinic-type structure of these sensitivity fields strongly imply the importance of thermal advection and latent heat release processes to amplification of perturbations in a developing extratropical cyclone, as shown for the idealized simulations in Chapt. III.

126
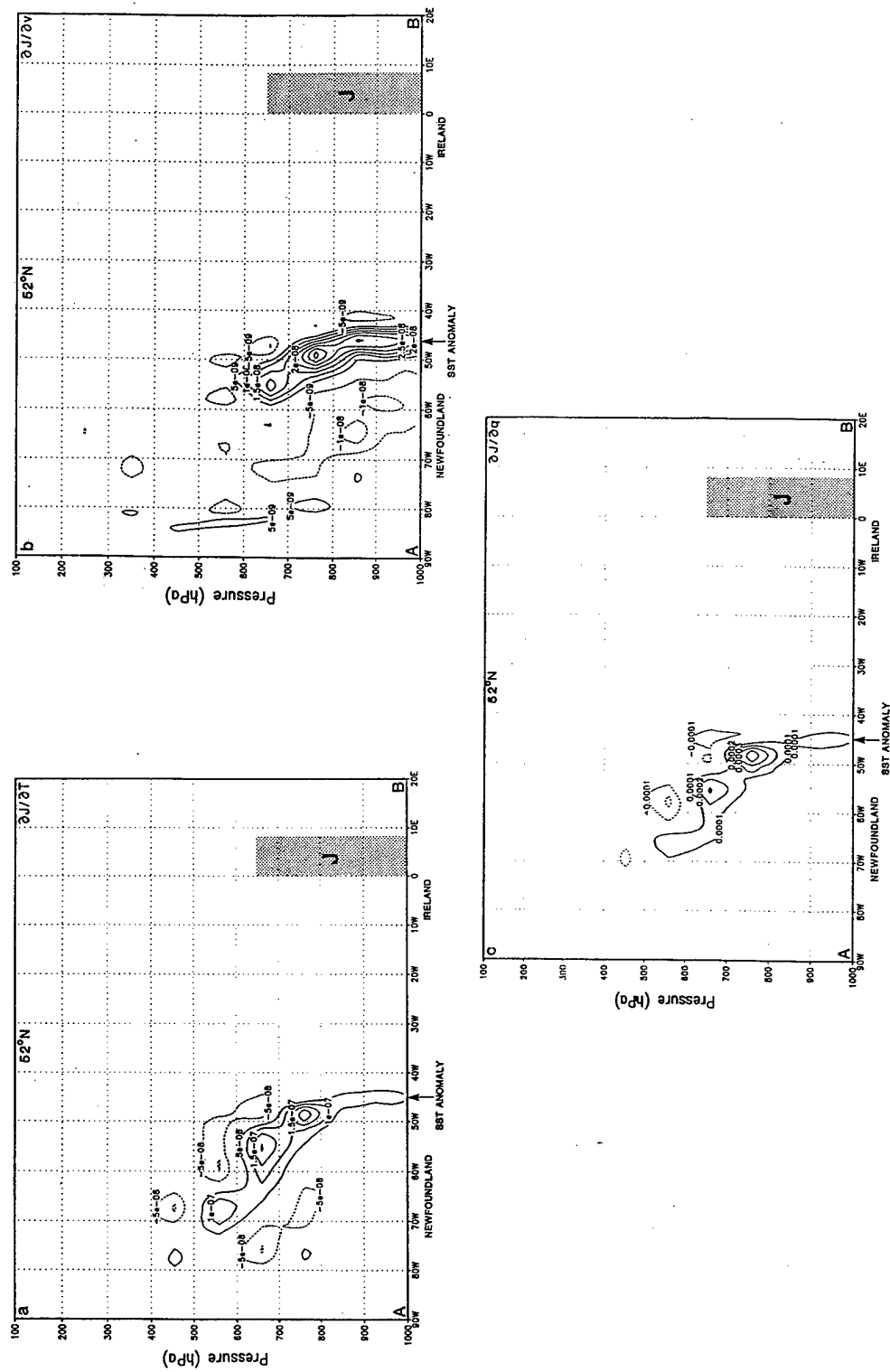
Figure 4.13: Sensitivity at -48 h (00UTC 20 January 1995) with moist MAMS1 adjoint: east-west vertical cross-sections along 52°N of (a) $\partial J/\partial T$, contour interval = 5 x 10^{-8} s^{-1} deg^{-1}; (b) $\partial J/\partial v$, contour interval = 5 x 10^{-9} m^{-1}; and (c) $\partial J/\partial q$, contour interval = 1 x 10^{-4} s^{-1}. Forecast aspect J is the average vorticity between 660 hPa and surface at 48-h cyclone position, as in Fig. 4.11. Location of cross-section "A-B" shown in Fig. 4.12a,b,c. Shaded rectangle indicates area of J, which is centered at 57°N.
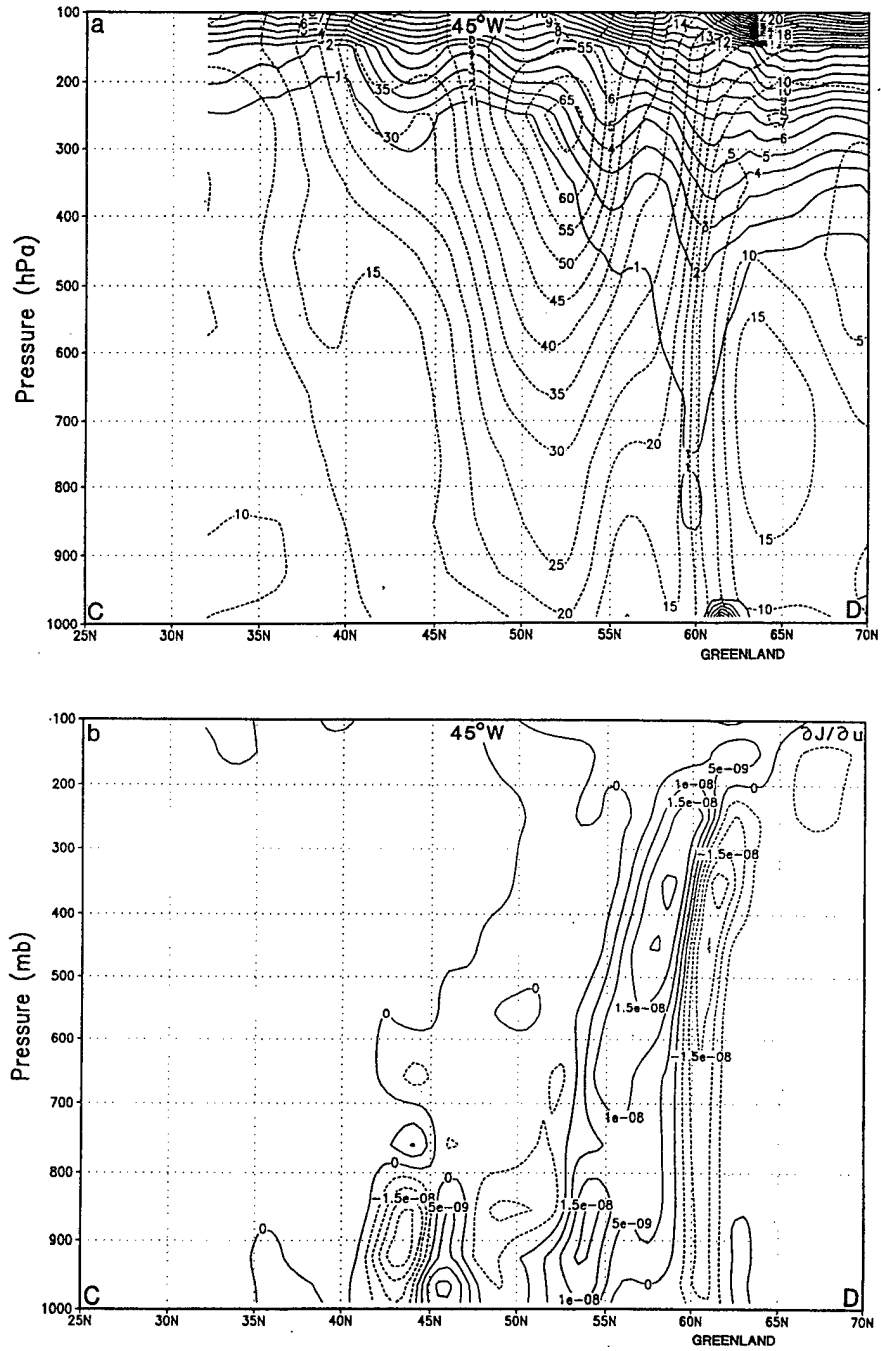
Figure 4.14: North-south vertical cross-sections along 45°W of (a) wind speed (dashed contour = 5 m s⁻¹) and potential vorticity (solid contour = 1 x 10⁻⁶ m²· K s⁻¹ kg⁻¹) at 00UTC 20 January 1995 (initial conditions); and (b) ∂J/∂u (contour interval = 5 x10⁻⁹ m⁻¹) at -48 h (00UTC 20 January 1995) with moist MAMS1 adjoint, where forecast aspect J is the average vorticity between 660 hPa and surface at 48 h cyclone position, as in Fig. 4.11. Location of cross-section "C-D" in (b) shown in Fig. 4.12d.

A second sensitivity feature with smaller magnitudes (Fig. 4.14b) extends upward from the region of strongest zonal wind sensitivity in the lower troposphere into a region of high cyclonic (and potential) vorticity in the upper troposphere on the north side of the jet (Fig. 4.14a). A narrow and deep layer of $\partial J/\partial u$ sensitivity (Fig. 4.14b) at 58° N (62° N) implies that a positive (negative) 350 hPa zonal wind perturbation in the initial conditions can enhance the vorticity of the J95 cyclone 48 h later. Comparison with the isotachs in Fig. 4.14a clearly indicates that this $\partial J/\partial u$ couplet implies a sensitivity to an increase of cyclonic vorticity in a separate shear zone north of the jet, rather than by an increase of zonal wind in the main jet core. In fact, $\partial J/\partial u$ is nearly zero through the axis of largest wind speed above 700 hPa. The vertical tilt of the $\partial J/\partial u$ sensitivity implies a broader region of cyclonic zonal wind shear near 900 hPa with enhanced westerlies (easterlies) at 53°N (61°N) would contribute to enhanced vorticity of the J95 cyclone 48 h later. The physical relationship of the other 900 hPa easterly and westerly zonal wind perturbations between 43°N and 50°N to the cyclone development is not obvious.

The adjoint model can provide sensitivity to perturbations of surface temperature. Since sea-surface temperature is held constant during the simulation of the J95 cyclone in MAMS1, this sensitivity (Fig. 4.15) pertains to perturbations that modify surface temperature at every time step during the 48 h forecast. The J95 cyclone can be intensified by higher sea- surface temperature along the storm track, particularly between 40° W and 10° W, with lesser negative sensitivity north of the cyclone track. This pattern represents enhancement of the cyclone warm and cold sectors, and is similar to sea-surface temperature sensitivity in the idealized cyclone simulation (Fig. 3.15). The maximum sensitivity to sea-surface temperature ($\partial J/\partial T_s$)
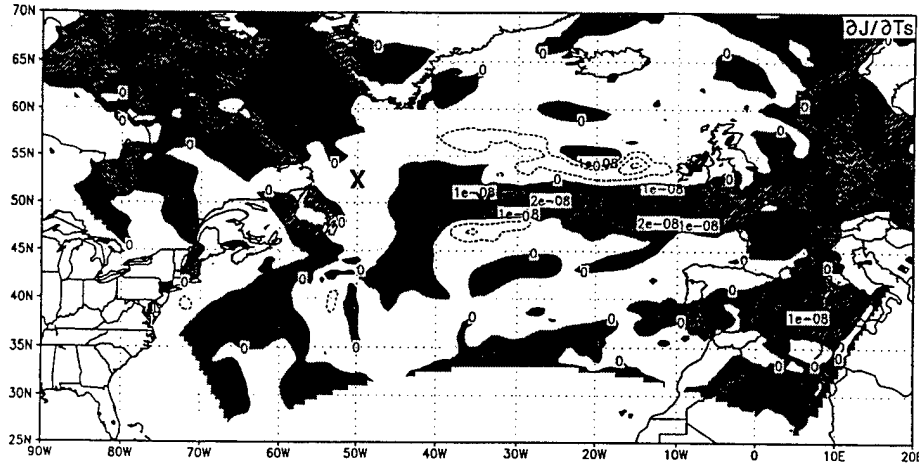
Figure 4.15: Sensitivity to surface temperature ($\partial J/\partial T_S$, positive values shaded, negative values less than -1×10^{-8} s^{-1} deg^{-1} dashed) with moist MAMS1 adjoint. The sensitivity $\partial J/\partial T_S$ represents the effect of a perturbation that remains constant during the 48 h forecast. Forecast aspect J is the average vorticity between 660 hPa and surface at 48 h cyclone position, as in Fig. 4.11. X indicates location of J95 cyclone at 12 h intervals between 00UTC 20 January and 00UTC 22 January 1995.

is approximately 1/10th the magnitude of maximum sensitivity to air temperature ($\partial J/\partial T$), which is found near 700 hPa, but is comparable in magnitude to the maximum sensitivity to zonal or meridional wind ($\partial J/\partial u$, $\partial J/\partial v$).

The sensitivity for the J95 cyclone has a similar vertical structure to that found in a case of Alpine Lee cyclogenesis simulated with a dry version of MAMS1 (Langland and Errico 1996). In both the J95 cyclone (Fig. 4.16) and the alpine lee cyclone (Fig. 4.17), temperature sensitivity reaches a maximum near 700 hPa and is roughly one order of magnitude larger than wind sensitivity in the middle and lower troposphere (note also the peak of sensitivity to mixing ratio near 760 hPa in Fig. 4.16). The similarities of sensitivity vertical structure in these actual cyclone events,

130
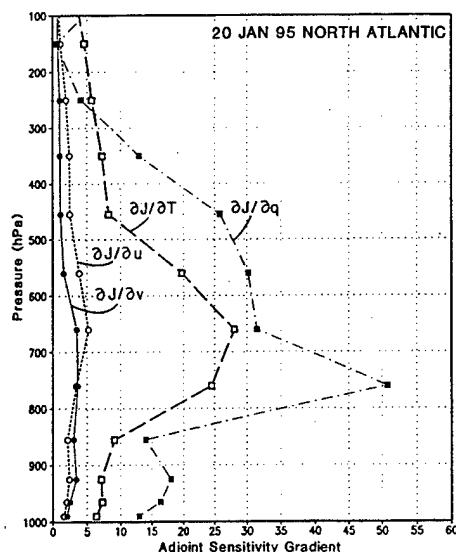
Figure 4.16: Vertical profiles of maximum sensitivity (absolute value) at 00UTC 20 January 1995 (-48 h) with moist MAMS1 adjoint for J95 cyclone: $\partial J/\partial T$ (heavy dashed line, s^{-1} deg^{-1}), $\partial J/\partial u$ (thin dashed line, m^{-1}), $\partial J/\partial v$ (thin solid line, m^{-1}), and $\partial J/\partial q$ (dot-dash line, s^{-1} g^{-1} kg). All values multiplied by 10^8. Forecast aspect J is the average vorticity between 660 hPa and surface at 48 h cyclone position, as in Fig. 4.11. Symbols indicate model levels.
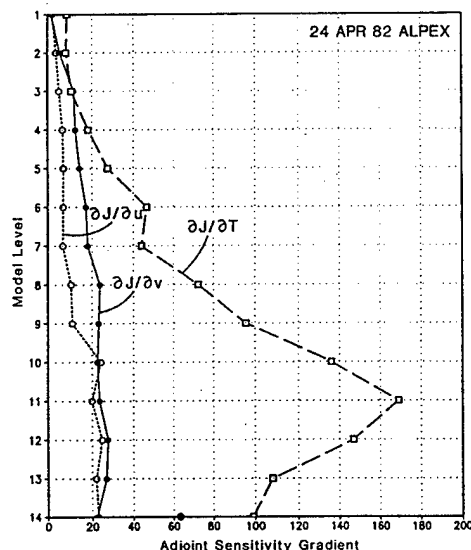
Figure 4.17: Vertical profiles of maximum sensitivity (absolute value) from Langland and Errico (1996) for ALPEX case I (24-25 April 1992) studied by Vukićević and Raeder (1995). $\partial J/\partial T$ (heavy dashed line, 10^{-10} s^{-1} deg^{-1}), $\partial J/\partial u$ (thin dashed line, 10^{-10} m^{-1}), and $\partial J/\partial v$ (thin solid line, 10^{-10} m^{-1}). Solid dot on horizontal axis is maximum sensitivity to terrain pressure ($\partial J/\partial Ps$, 10^{-10} s^{-1} hPa^{-1}). Forecast aspect J is the mean vorticity in lower half of troposphere in a 1000 x 1000 km area. Pressure (P) on model level = $\sigma(Ps-Pt)$ + Pt, where Pt = 50 hPa. Sigma values (σ) for model levels are: 1(.03), 2(.10), 3(.18), 4(.25), 5(.32), 6(.39), 7(.46), 8(.54), 9(.61), 10(.68), 11(.75), 12(.82), 13(.89), and 14(.96).

131

those from the idealized cyclones in Chapt. III, and singular vector results (Buizza and Palmer 1995) suggest that the occurrence of maximum sensitivity in the middle and lower troposphere may be generally characteristic of extratropical baroclinic developments.

The relatively large sensitivity to initial temperature in the lower troposphere may be related to several factors. Temperature perturbations directly modify the height (thickness) and stability structure of the incipient cyclone, as well as temperature gradients that determine the magnitude of thermal advection, which is known to be an important process in baroclinic instability. These thickness changes will alter the height field above the temperature perturbation and thereby (through geostrophic adjustment) change the strength of the wind and vorticity advection at higher levels, including 500 hPa. In contrast, initial temperature perturbations above 500 hPa, or at the tropopause, will not directly alter the 500 hPa height or vorticity, and have no direct effect on thermal advection in critical locations of the lower troposphere. The large sensitivity to lower tropospheric temperature may also be related to effects of temperature perturbations on vertical motion, which can be relatively strong near the 700 hPa level during baroclinic development.

Additional insight concerning development of the J95 cyclone is provided by sensitivity fields for which a new forecast aspect J is selected as zonal wind speed between 200 and 400 hPa above the J95 cyclone at 48 h (position of J shown in Fig. 4.5e). This choice of J relates to intensification of the upper-tropospheric wind speed in a location that is considered important to surface cyclone development (e.g., surface cyclone in the left front quadrant of a 300 hPa jet streak). The initial condition sensitivity for this choice of J has some significant features in common with the
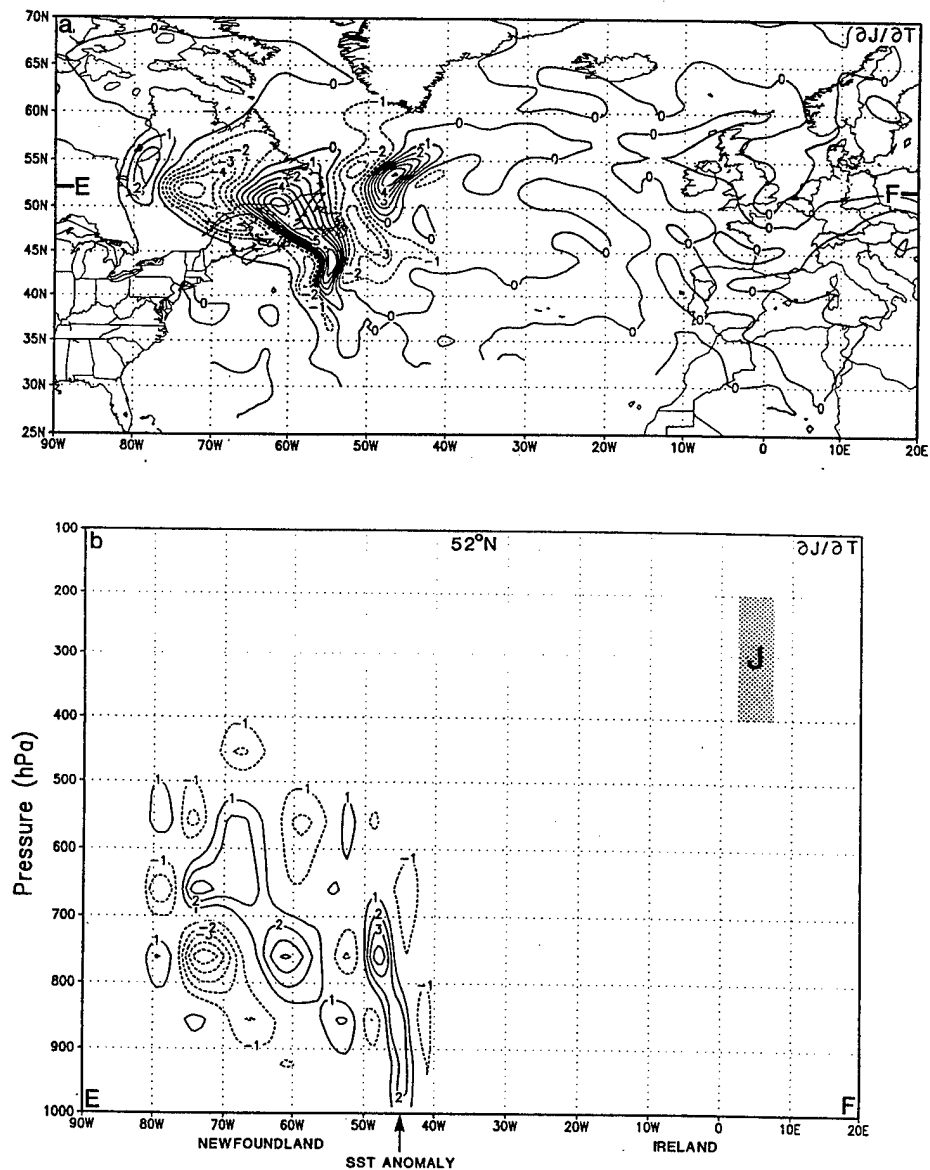
Figure 4.18: Sensitivity at -48 h (00UTC 20 January 1995) with moist MAMS1 adjoint in which forecast aspect J is zonal wind from 200 - 400 hPa above 48 h cyclone position, shown in Fig. 4.5e. (a) $\partial J/\partial T$ at 760 hPa, contour interval = 1 m s^{-1} deg^{-1}; (b) east-west vertical cross-section along 52°N of $\partial J/\partial T$, contour interval = 1 m s^{-1} deg^{-1}. Shaded rectangle in (b) indicates area of J, which is centered at 54°N. Location of cross-section "E-F" in (b) is shown in (a).

133

earlier sensitivity with J defined as lower tropospheric vorticity. In particular, both choices of J result in a concentration of positive $\partial J/\partial T$ (Fig. 4.18a,b - compare to Fig. 4.12a and Fig. 4.13a) and $\partial J/\partial v$ (not shown) in the area around 52°N 48°W in the lower troposphere. The similarity of these sensitivity fields with different choices of J implies that the upper-tropospheric jet streak is intensified by the same baroclinic processes that originate in the lower troposphere and lead to surface intensification of the J95 cyclone.

The sensitivity at -24 h (Fig. 4.19) illustrates again the localized nature of areas in which rapidly growing perturbations can affect a cyclone. Note the correspondence of the -24 h $\partial J/\partial T$ and $\partial J/\partial v$ sensitivity at 760 hPa to features of the incipient cyclone in Fig. 4.3c (850 hPa vorticity), Fig. 4.4c (760 hPa temperature and vertical motion), Fig. 4.5c (250 hPa divergence), and Fig. 4.6c (500-1000 hPa thickness advection). Sensitivities to temperature (Fig. 4.19a) and meridional wind (Fig. 4.19b) have positive values in the warm sector of the developing cyclone so that an increased temperature, or a stronger southerly wind, would amplify the vorticity at the forecast position 24 h hence. Sensitivity to 760 hPa zonal wind at -24 h (not shown) has a smaller magnitude than for $\partial J/\partial T$ and $\partial J/\partial v$, but is localized within the same area.

To evaluate the effects of including moist processes in the adjoint model, sensitivities to initial conditions are obtained using the MAMS1 adjoint with precipitation processes and surface latent heat flux removed. In this dry (near-adiabatic) adjoint, the maximum sensitivity to temperature and meridional wind (Fig. 4.20) is reduced to roughly 25 - 50 percent of that obtained from the moist adjoint, although the location of greatest sensitivity is quite similar to the moist results in terms of horizontal and vertical positions. This result suggests that a dry adjoint
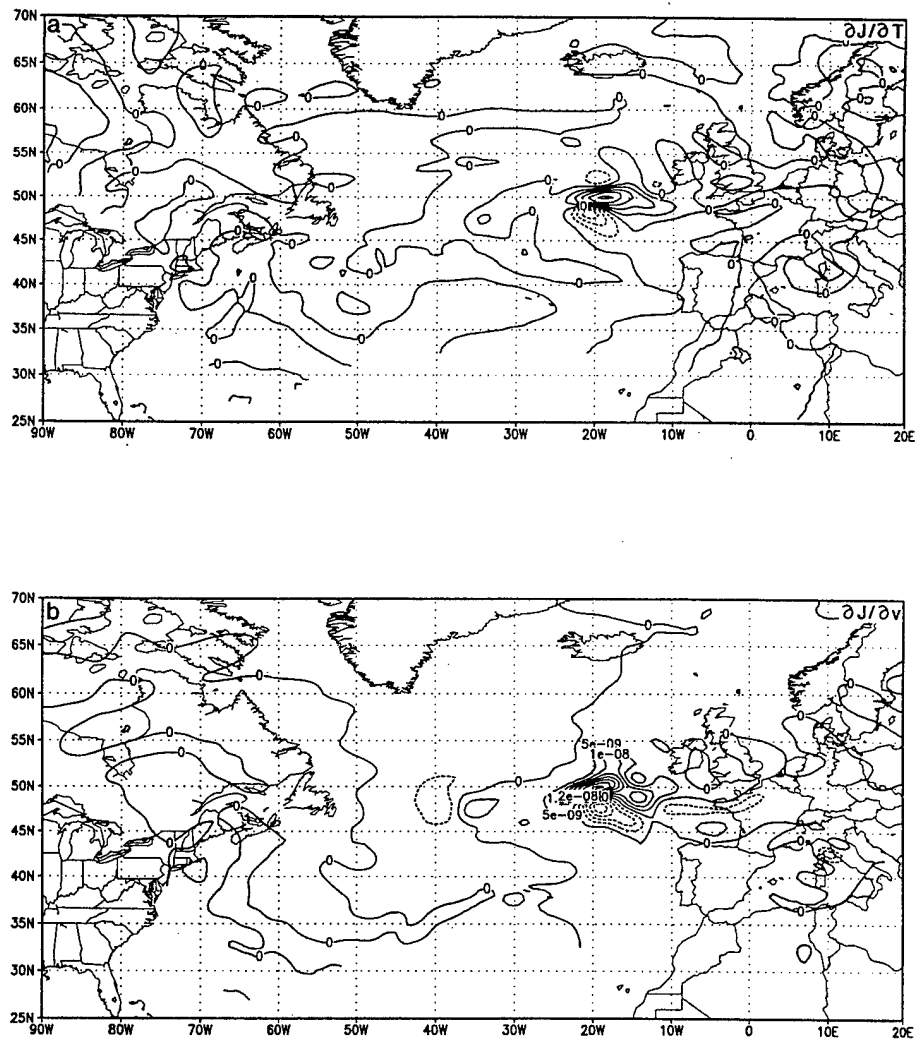
Figure 4.19: Sensitivity at -24 h (00UTC 21 January 1995) with moist MAMS1 adjoint: (a) $\partial J/\partial T$ at 760 hPa, contour interval = 5 x 10^{-8} s^{-1} deg^{-1}; (b) $\partial J/\partial v$ at 760 hPa, contour interval = 5 x 10^{-9} m^{-1}. Forecast aspect J is the average vorticity between 660 hPa and surface at 48 h cyclone position, as in Fig. 4.11.
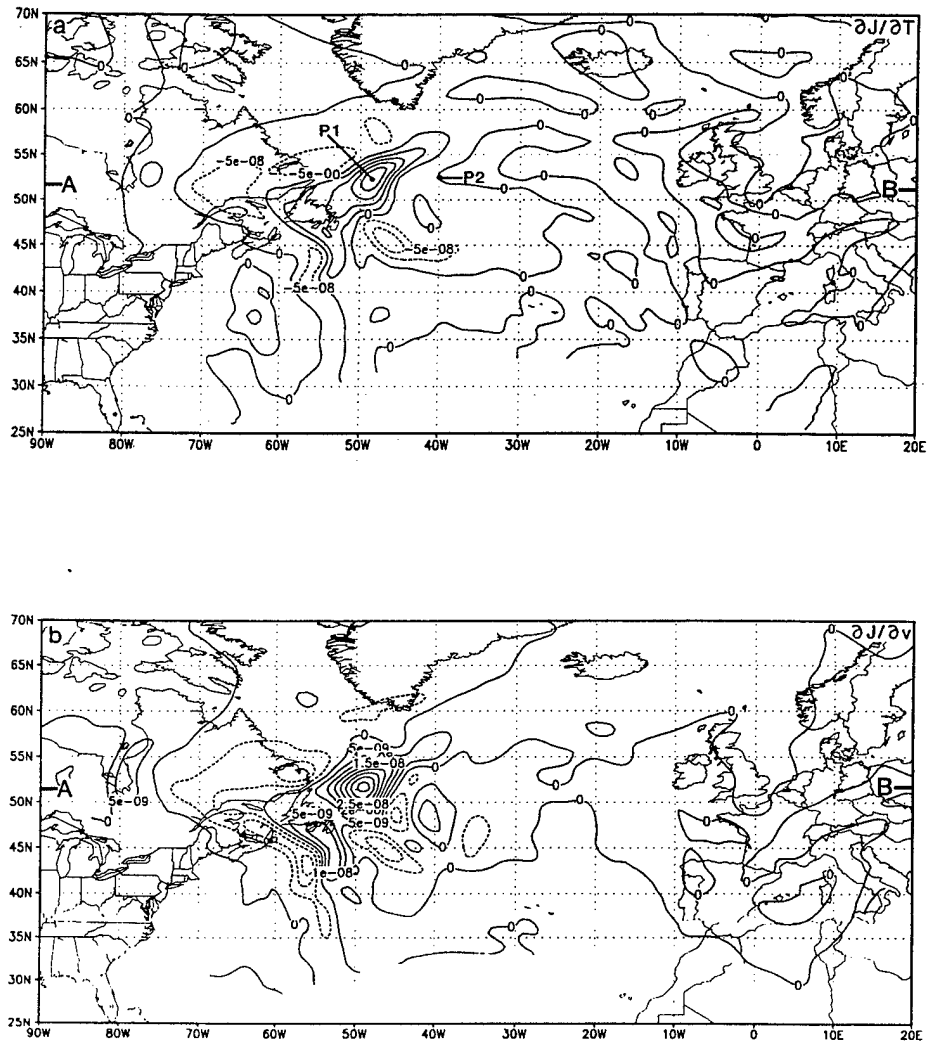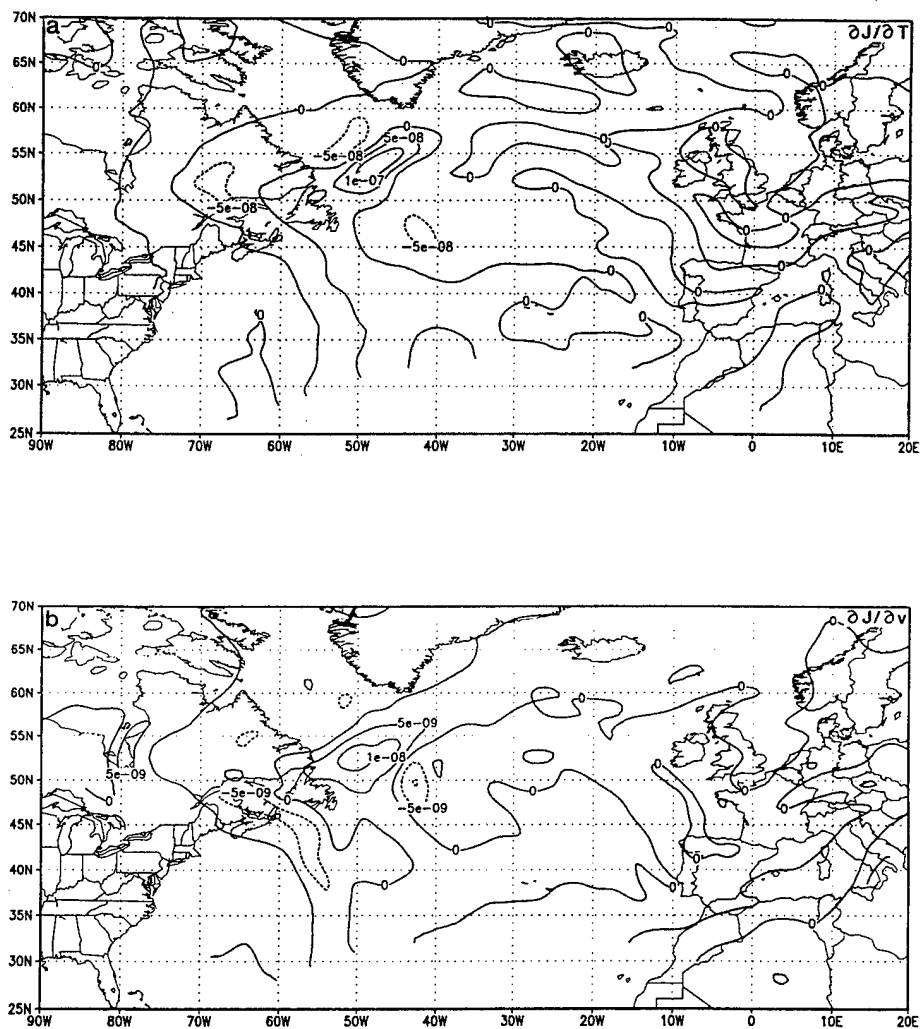
Figure 4.20: Sensitivity at -48 h (00UTC 20 January 1995) with *dry* MAMS1 adjoint: (a) $\partial J/\partial T$ at 760 hPa, contour interval = 5 x 10^{-8} s^{-1} deg^{-1}; (b) $\partial J/\partial v$ at 760 hPa, contour interval = 5 x 10^{-9} m^{-1}. Forecast aspect J is the average vorticity between 660 hPa and surface at 48 h cyclone position, as in Fig. 4.11.

model may be used to identify the *location* of maximum sensitivity for extratropical cyclone situations, even though it will underestimate the actual sensitivity in the nonlinear model.

As suggested by comparison of moist and dry adjoint sensitivity results, and the simulations of the idealized cyclone in Chapt. III, extratropical cyclone intensification is basically controlled by dry baroclinic instability processes of thickness and vorticity advections, with moist processes contributing to more rapid development and more intense cyclones. The effects of moist processes on nonlinear forecasts of cyclones are implied by increases in sensitivity when precipitation processes are included in the adjoint model. The close spatial correspondence of sensitivities to temperature and mixing ratio for this extratropical cyclone may allow the pattern of $\partial J/\partial q$ to be inferred from the pattern of $\partial J/\partial T$ from a dry adjoint model. However, a moist adjoint model gives a better estimate of nonlinear sensitivity magnitude.

2. NOGAPS (Global Model) Results

An important question related to regional model simulations is the effect of lateral boundary conditions (LBCs) on the predictive skill of circulations such as the J95 cyclone. If (in a global sense) the most significant initial condition sensitivity for a particular circulation of forecast aspect (J) is located outside the regional model domain, then the forecast of J may be degraded if an accurate representation of the small-scale features of initial conditions is not transmitted into a regional model via LBCs at fixed time intervals. In this situation, the spatial pattern or magnitude of sensitivity in the regional model will be degraded, compared to the "true" sensitivity pattern that a global model is able to represent, free of LBCs. If the sensitivities to

137

initial conditions derived from global and regional models are basically similar, then prediction of the feature represented by J in the regional model is not expected to be greatly influenced by LBCs, at least when considering forecast time intervals equal to or less than that which has been evaluated.

Here, NOGAPS is used to obtain adjoint sensitivity in a global context for comparison to MAMS1 sensitivity. The nonlinear NOGAPS spectral forecast model is run at T79L18 resolution (about a 1.5° latitude/longitude grid, 18 vertical levels) to provide a full-physics basic state for the adjoint model component, also run at T79L18 resolution. The NOGAPS 48 h forecast of the J95 cyclone is quite similar to the
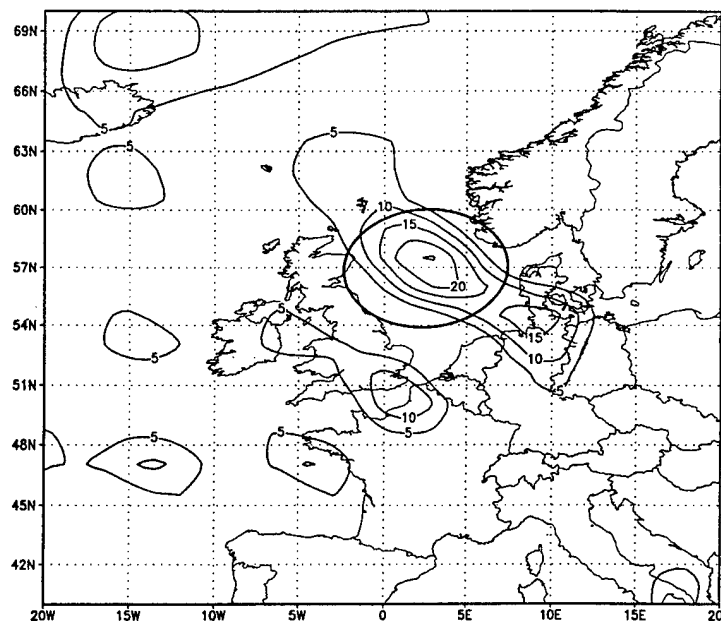
Figure 4.21: Navy Operational Global Atmospheric Prediction System (NOGAPS) T79L18 48 h nonlinear forecast at 00UTC 22 January 1995 of 850 hPa vorticity (contour interval = 5 x 10^{-5} s^{-1}). Heavy solid line denotes area in which forecast aspect J represents the average vorticity between 650 hPa and the surface.

MAMS1 forecast, in that a small-scale cyclone is predicted somewhat north of the MAMS1 position, but with nearly identical vorticity magnitude at 850 hPa (Fig. 4.21).

The NOGAPS adjoint includes a simplified parameterization of vertical mixing and surface stress, but no moist physics (similar to the dry MAMS1 adjoint). The basic state coefficients are provided to the adjoint model at 1800 s (two time step) intervals. As in the MAMS1 sensitivity evaluations, the forecast aspect J is defined as average vorticity over the cyclone center in the lower troposphere (Fig. 4.21), with J weighted by grid volume mass according to the procedure described in Chapt. II and used with MAMS1 in the previous section. In NOGAPS, J can be directly defined as vorticity, since this is a predictive variable in the model.

The NOGAPS initial condition sensitivities to temperature and meridional wind are depicted in Fig. 4.22. Although the T79 NOGAPS sensitivity patterns are somewhat larger in scale, and lack the detail of the 60 km MAMS1 results, the locations of maximum sensitivity in both models are similar. Both NOGAPS and MAMS1 identify largest sensitivity between 500 - 800 hPa. The similarity between the sensitivity patterns in NOGAPS and MAMS1 is remarkable, given that the physical parameterizations, and horizontal and vertical resolution, are significantly different in the two models.

From these results, it may be concluded that the MAMS1 domain used here for simulation of the J95 cyclone is appropriate for a 48 h forecast without significant influences of LBCs, since no critical sensitivity features exist outside the lateral boundaries. It appears (but is not verified here) that a 72 h forecast within the same domain, or a 48 h forecast in a smaller domain (with a western boundary at 40° W, for example) would be subject to problems with LBCs. In addition, for these types of
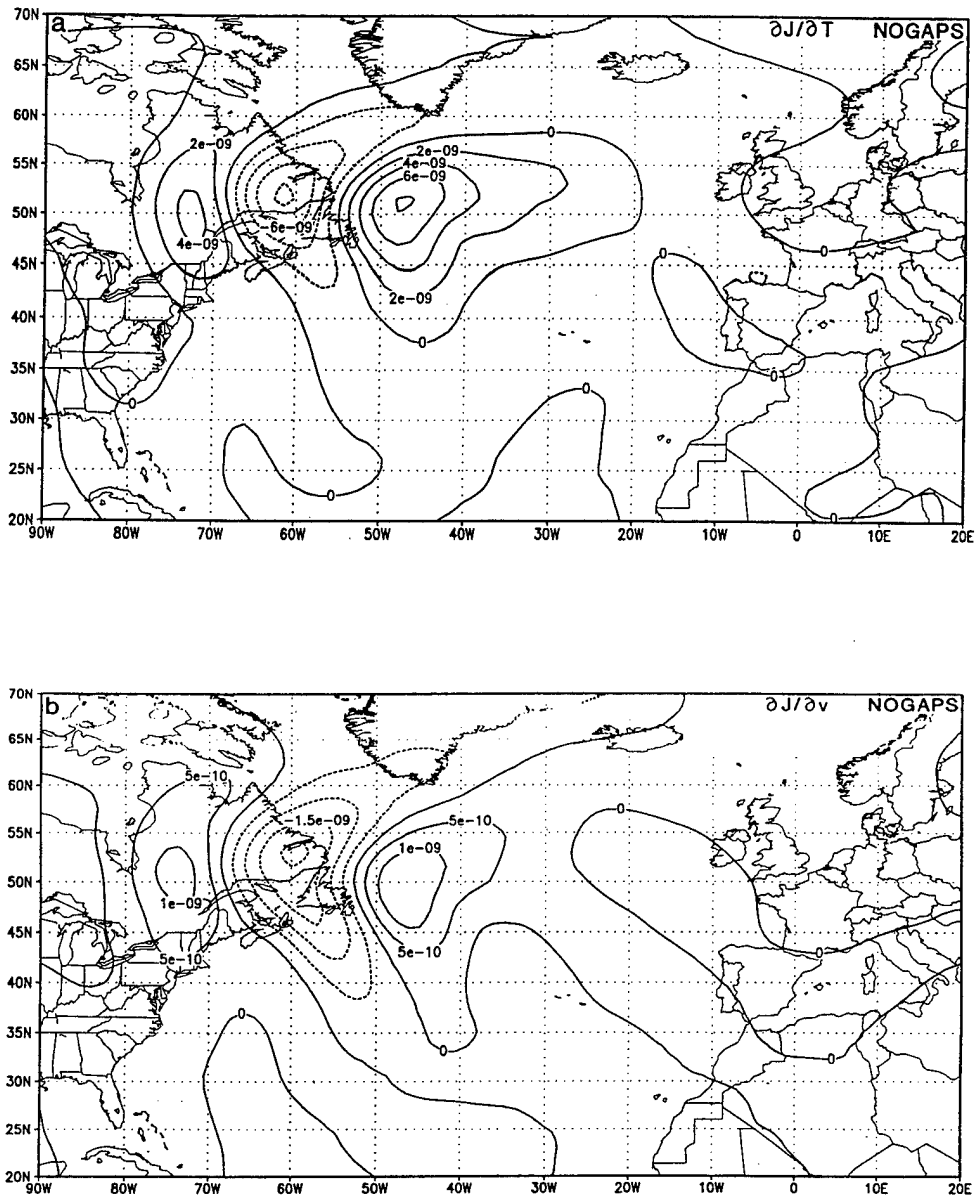
Figure 4.22: Sensitivity at -48 h (00UTC 20 January 1995) with *dry* T79L18 NOGAPS adjoint: (a) $\partial J/\partial T$ at 760 hPa, contour interval = 2 x 10^{-9} s^{-1} deg^{-1}; (b) $\partial J/\partial v$ at 760 hPa, contour interval = 5 x 10^{-10} m^{-1}. Forecast aspect J is the average vorticity between 650 hPa and surface at 48 h cyclone position, as in Fig. 4.21.

frontal wave cyclones, a T79L18 dry adjoint may be adequate to identify the location of primary initial condition sensitivity for nonlinear full physics forecasts in global or regional models.

It is instructive to compare the adjoint sensitivity results to singular vector (SV) patterns obtained by adjoint methods for the J95 cyclone, using a T47L18 version of NOGAPS. The singular vectors considered here use a quadratic energy norm to maximize perturbation total energy growth at 48 h, with a local projection operator (LPO) to constrain the perturbation energy at 48 h in an area surrounding the cyclone, through the entire depth of the troposphere (for a mathematical description of singular vectors, see Buizza and Palmer 1995 or Ehrendorfer and Errico 1995).

Singular vectors can identify more than one unstable (growing) perturbation configuration, which is appropriate when considering the growth of a nonlinear quantity such as perturbation energy. The three leading singular vectors for 760 hPa temperature are shown in Fig. 4.23; each SV identifies locations where initial temperature perturbations can produce energy growth in the region LPO (the SV sign is arbitrary). The singular vector amplitude is maximized in the middle and lower troposphere, and generally is in the same location from Newfoundland into the western Atlantic, as for the sensitivity results in which J = vorticity. The first two SVs (Fig. 4.23a,b) extend farther west, possibly relating to maximization of *upper tropospheric* perturbation energy (compare to Fig. 4.18a with J = zonal wind in the upper troposphere). The third SV (Fig. 4.23c) is located farther east, and may correspond more closely to maximization of *lower tropospheric* energy (compare to Fig. 4.12a with J = lower tropospheric vorticity).
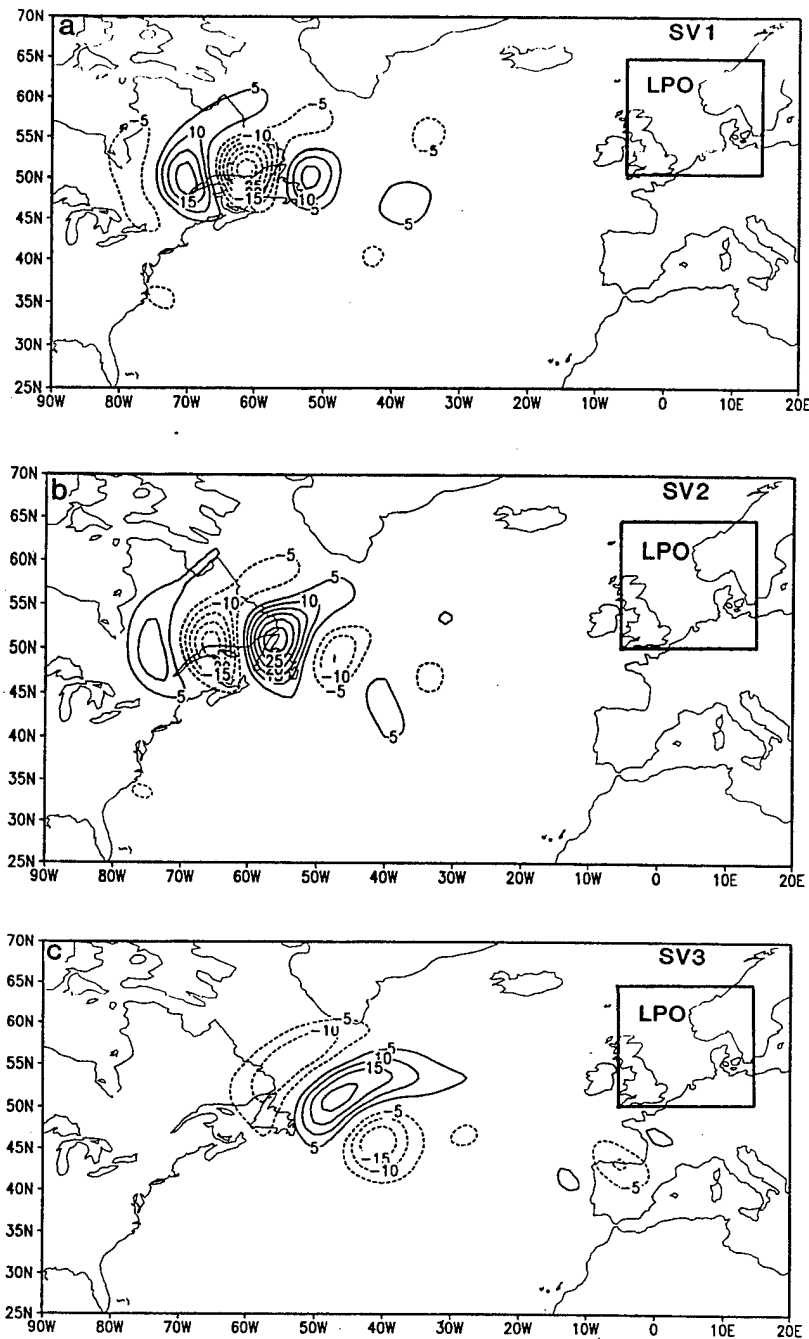
Figure 4.23: The three leading singular vectors (SVs, contour = 5° K) at initial time (00UTC 20 January 1995) representing 760 hPa temperature with adjoint of dry T47L18 NOGAPS forecast model. The SVs indicate where initial temperature perturbations maximize perturbation total energy growth within area "LPO" (local projection operator) at 00UTC 22 January 1995 (courtesy of R. Gelaro, NRL).

For this case, no significant growing singular vectors are located outside the areas shown in Fig. 4.23. This provides confidence that the choice of a linear forecast aspect (J) and the sensitivity approach used throughout this study is appropriate for interpretation of cyclone development, and can identify the most significant initial condition sensitivity in simulations of extratropical cyclones.

C.   PERTURBATION GROWTH

In the previous section, adjoint sensitivity was used to identify horizontal and vertical locations at which small amplitude perturbations of model variables in the initial conditions have the most impact on vorticity associated with the J95 cyclone. These perturbations may be considered to represent: (a) analysis errors in the model initial conditions; (b) arbitrary perturbations; or (c) perturbations that represent, in some sense, physical processes in the original nonlinear simulation. In a simulation of a real cyclone, perturbations in categories (b) and (c) may also represent some component of the actual analysis error.

If some independent knowledge of an error in the initial conditions is available, a perturbation as in (a) should provide a forecast with improved skill. If the sense or magnitude of the initial error is not known, the sensitivity field demonstrates the effect on the nonlinear forecast of an arbitrary perturbation, as in (b). In Chapt. III, the perturbations were based on the magnitude and distribution of tendencies obtained from nonlinear simulations of the idealized cyclone (which has no analysis "error"). These type (c) perturbations are not arbitrary as in (b), but represent a dynamically consistent modification of patterns that existed in the unaltered nonlinear forecast. Thus, the modified nonlinear forecast provides insight into the physical processes of the original nonlinear simulation.

143

Here, arbitrary perturbations of type (b) are used to represent the effects of possible initial condition errors on nonlinear model forecasts of the J95 cyclone. The purpose of these experiments is to determine the possible benefits of improved initial conditions in regions of varying initial condition sensitivity.

Perturbation 1 is specified as a 1°C increase in temperature at nine grid points (120 km x 120 km square) in a single model layer (roughly 100 hPa thick) near 760 hPa (see Figs. 4.12a and 4.24) over the Labrador Sea. It is reasonable to assume that an actual analysis error of this magnitude could exist in the lower troposphere in a data-void region such as this. The boundary layer at P1 is near-moist adiabatic below 700 hPa with a thermally unstable surface layer (note the northward extension of high sea-surface temperature over this area shown in Fig. 4.24), and the 760 hPa wind is northwesterly at about 25 m s^{-1}. An area of enhanced vorticity exists to the northeast of the temperature perturbation (dotted lines in Fig. 4.24). This location of
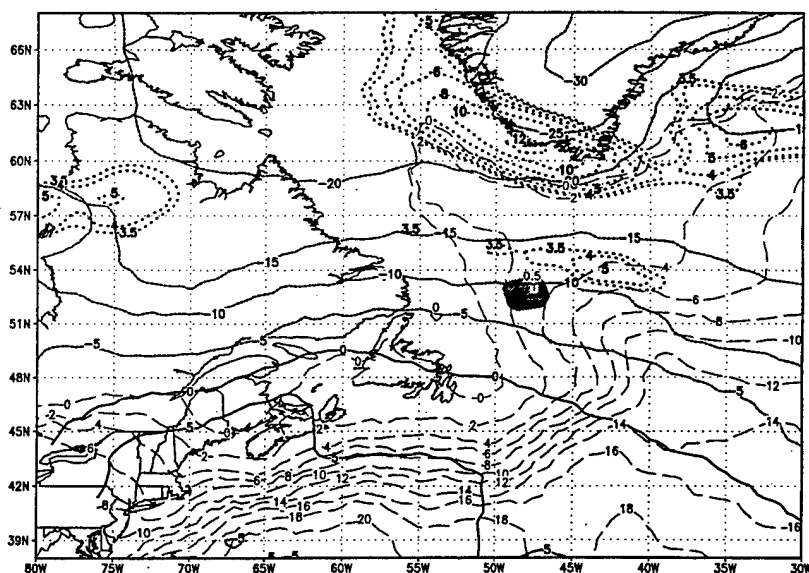
Figure 4.24: Initial 760 hPa temperature (heavy solid contours, °C) and sea-surface temperature (long dashed contours, °C) at 00UTC 20 January 1995. Shaded region near 53°N, 48°W indicates area of 1° C initial temperature perturbation **P1** used in MAMS1 forecasts shown in Figs. 4.25-4.28. Dotted contours correspond to initial cyclonic vorticity (10^{-5} s^{-1}) at 760 hPa.

maximum 760 hPa temperature sensitivity corresponds to the probable location of the J95 precursor, in the lower troposphere. It is expected that the temperature perturbation will amplify the instability that is already present in the area of P1, by altering patterns of thermal advection, vertical stability, and other processes.

The growth of perturbations resulting from P1 during a 48 h forecast is illustrated with temperature and vorticity forecast difference fields (perturbed nonlinear forecast minus non-perturbed nonlinear forecast) at 12 h intervals. These plots (Figs 4.25, 4.26) depict how a lower tropospheric temperature perturbation placed in a location of strong initial condition sensitivity increases in horizontal and vertical scale, and influences other variables and physical processes during the cyclone development. As the forecast progresses, the perturbations move eastward at a speed corresponding to the motion of the J95 cyclone. For example, the maximum 760 hPa temperature and vorticity perturbations at 24 h (Fig. 4.25c) are located close to the J95 cyclone near 50°N, 20°W (compare to Fig. 4.4c). Whereas the temperature perturbations tend to diminish in magnitude during the forecast (Fig. 4.25a,c,e,g), the vorticity perturbations amplify in scale and magnitude, with adjacent areas of positive and negative values (Fig. 4.25b,d,f,h). The amplification of perturbation *vorticity* from P1 is a consequence of the choice of J (average vorticity above the surface cyclone) in this experiment. While the temperature perturbations are *physically consistent* with changes in vorticity, this choice of J is not specifically designed to identify initial perturbation structures that might relate to more significant temperature perturbations in the forecast cyclone location.

Another significant feature related to the growth of perturbation P1 is amplification of forecast perturbations to higher vertical levels with increasing length
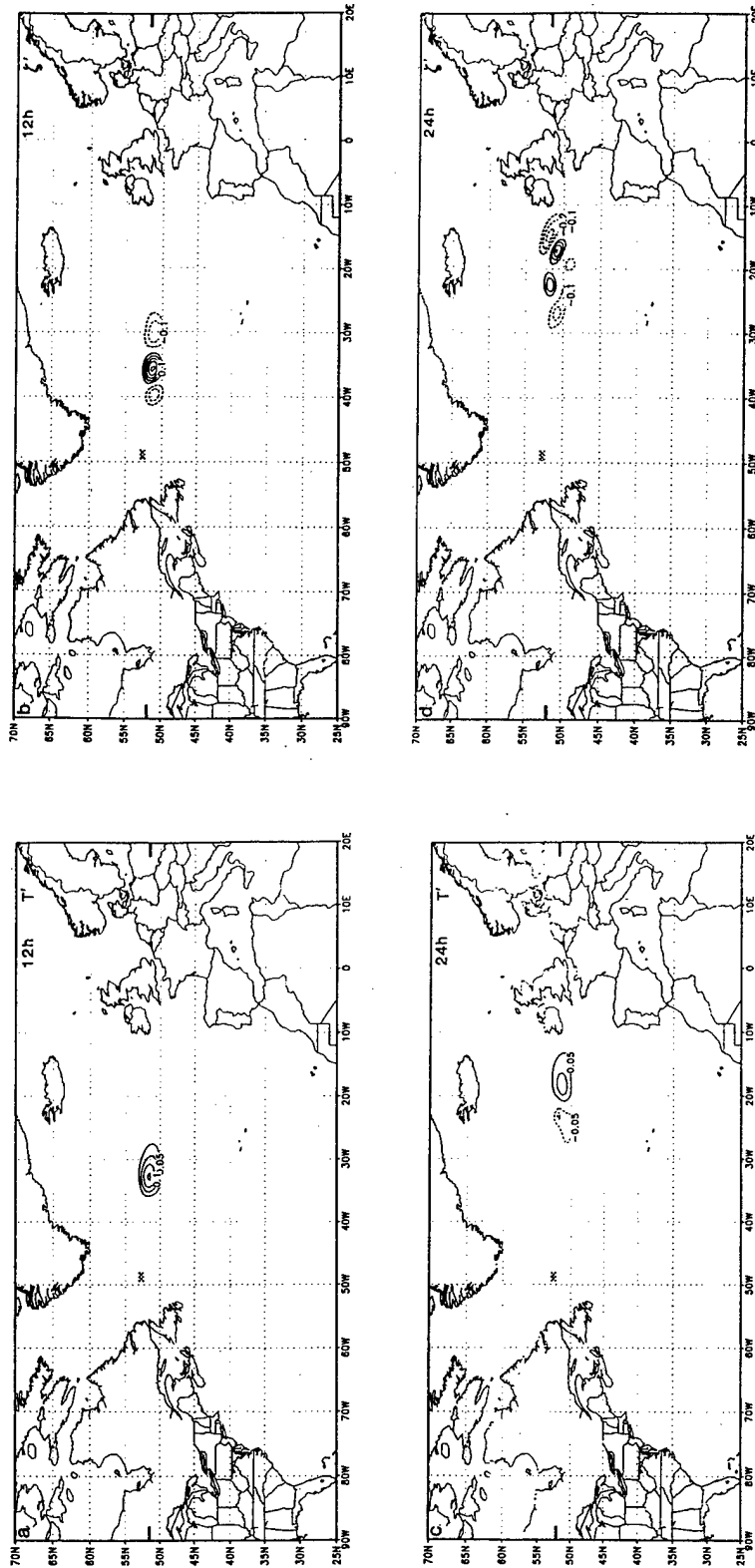
Figure 4.25: MAMS1 nonlinear forecasts of differences in 760 hPa temperature (a,c,e,g, contour interval = 0.05°C) and 760 hPa vorticity (b,d,f,h, contour interval = 0.1 x 10⁻⁵ s⁻¹) resulting from initial temperature perturbation (**P1**) as in Fig. 4.24: (a,b) 12UTC 20 January (12 h forecast); (c,d) 00UTC 21 January (24 h forecast); (e,f) 12UTC 21 January (36 h forecast); and (g,h) 00UTC 22 January (48 h forecast). Shaded square in (a-d) indicates location of 1°C initial temperature perturbation, **P1**. Tic marks on east and west boundaries show locations of cross-sections in Fig. 4.26.

146

Figure 4.25, continued

147
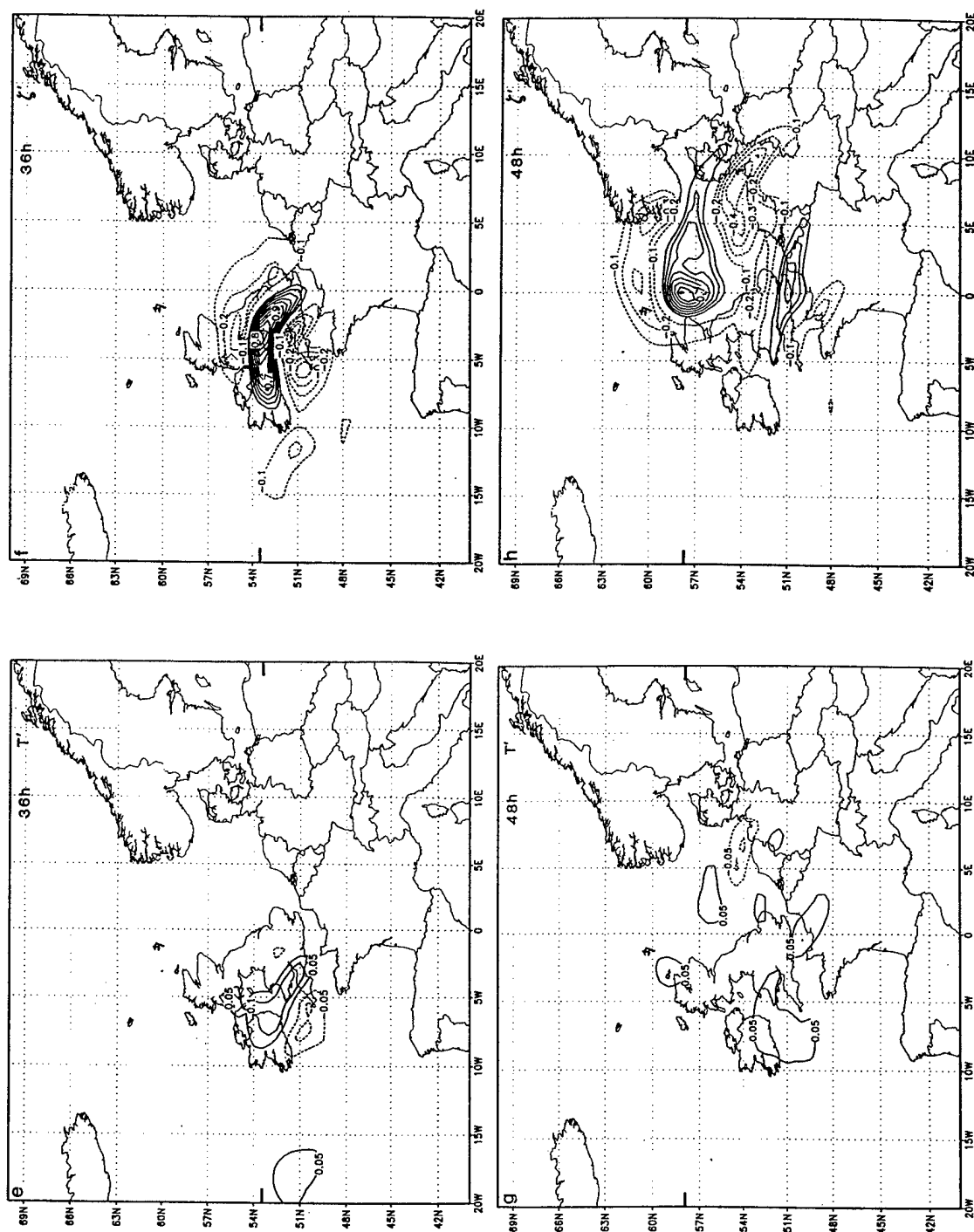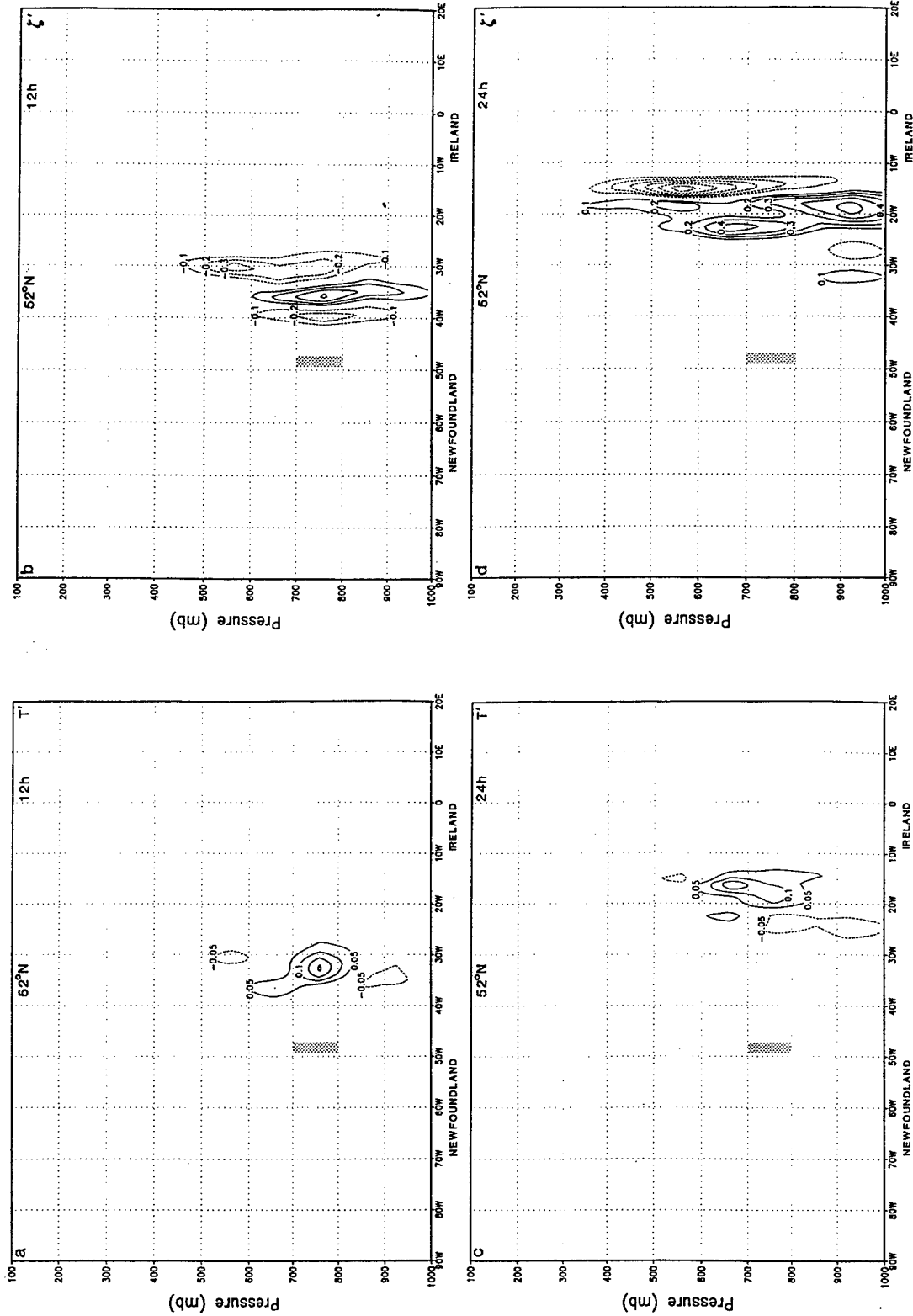
Figure 4.26: As in Fig. 4.25, in east-west vertical cross-sections along (a,b,c,d) 52°N; (e,f) 53°N; (g,h) 58°N. Shaded rectangle in (a-d) indicates location of 1° C initial temperature perturbation (**P1**). Locations of cross-sections shown in Fig. 4.25 (note: a-d extend from 90°W - 20°E, e-h extend from 20°W - 20°E.

148
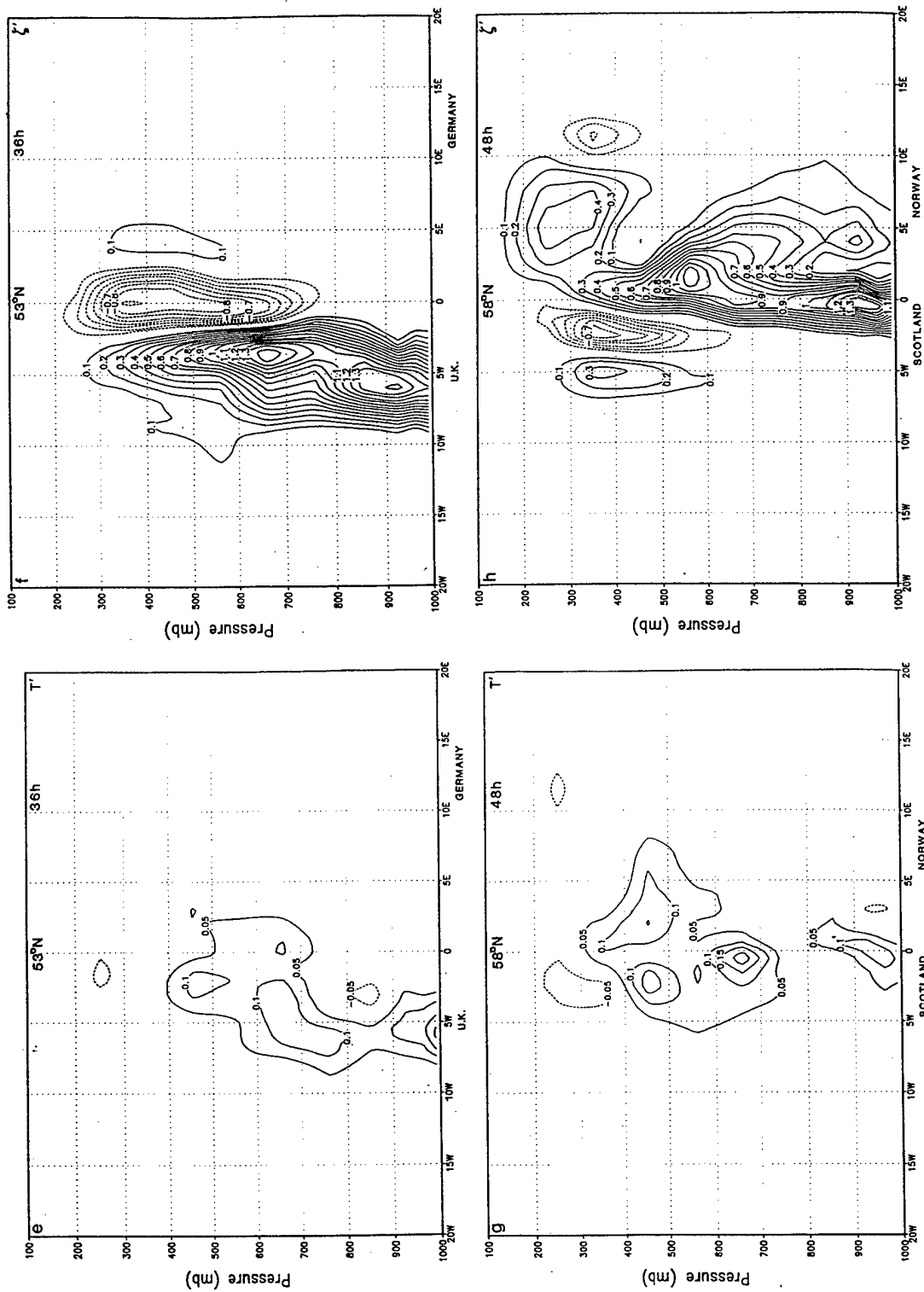
Figure 4.26, continued

of forecast. By 36 h, the vorticity perturbation extends well above 500 hPa (Fig. 4.26f), which implies modification of vorticity advection above the cyclone. At the end of the 48 h forecast, the vorticity perturbation extends through the entire troposphere above the developed cyclone (Fig. 4.26h). From quasi-geostrophic reasoning, low (high) geopotential heights would be expected below (above) a positive temperature perturbation, which would imply cyclonic (anticyclonic) vorticity in the lower (upper) portion of the perturbed column. The vertical structure of the temperature and vorticity perturbations in Fig. 4.26 are consistent with this interpretation.

The nonlinear difference fields may also be compared directly with forecasts of the tangent linear model, which provides an estimate of the TLM (and adjoint) accuracy. Using perturbation P1, 48 h moist TLM forecasts and nonlinear difference fields are compared for zonal wind at 350 hPa (Fig. 4.27a,b), vorticity at 850 hPa (Fig. 4.27c,d), and sea-level pressure (Fig. 4.27e,f). The moist TLM slightly overestimates (roughly 30 percent) 48 h forecast perturbation magnitude compared to the nonlinear model; however, the TLM provides an excellent representation of the nonlinear perturbation spatial pattern.

The magnitude and localization of the vorticity perturbations over the J95 cyclone position at 48 h (compare Figs. 4.3e and 4.27d) is remarkable, given the small amplitude and extent of the initial temperature perturbation (in terms of potential vorticity, the temperature perturbation P1 at initial time corresponds to only 0.05 PV units). At 48 h, the 850 hPa vorticity is increased by as much as 1.2×10^{-5} s^{-1} (Fig. 4.27d), the underlying sea-level pressure is reduced by 0.4 hPa (Fig. 4.27f), and zonal wind at 350 hPa is increased by 0.5 m s^{-1} (Fig. 4.27b).
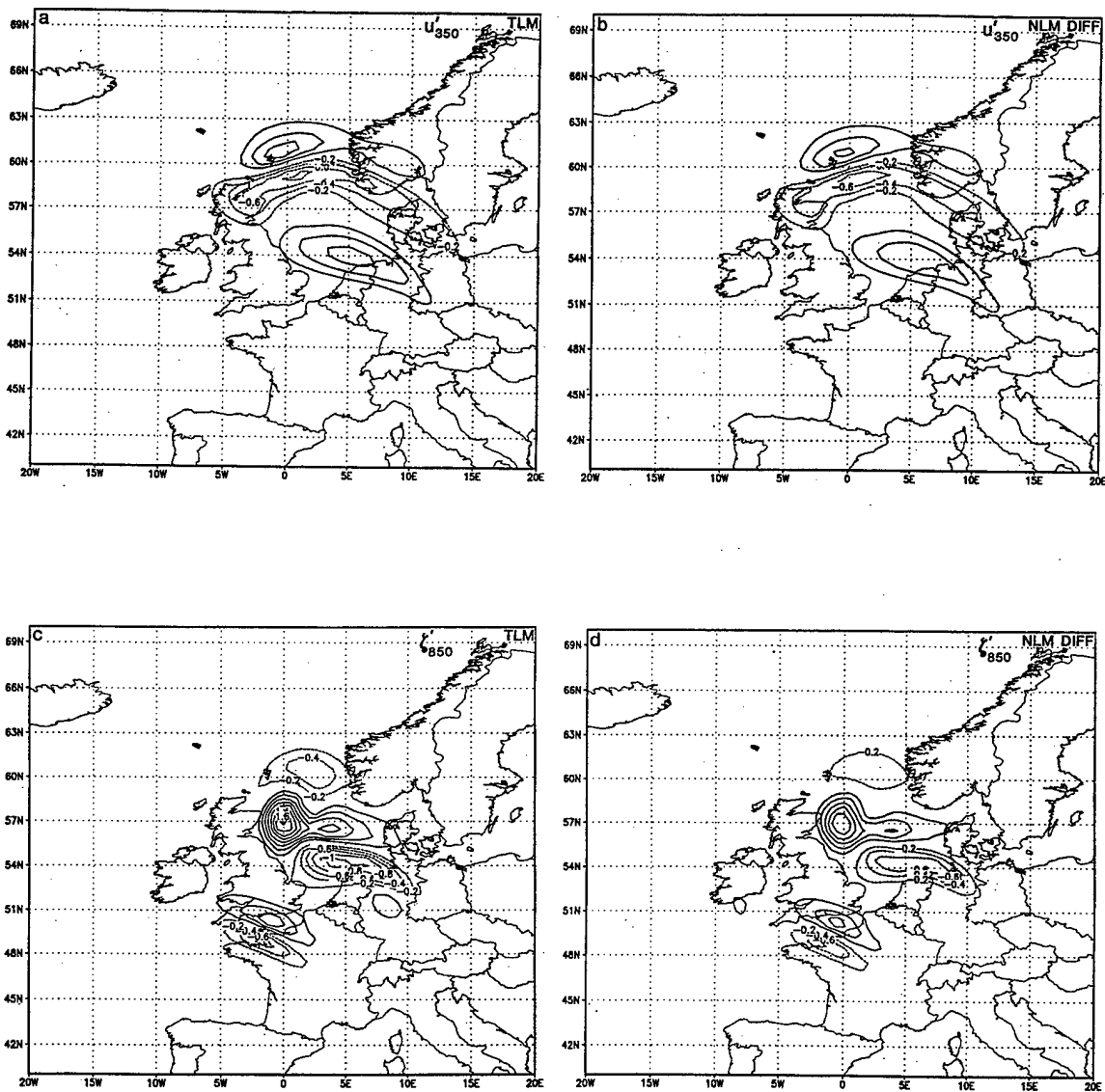
Figure 4.27: (a) MAMS1 48 h tangent linear forecast at 00UTC 22 January 1995 of 350 hPa zonal wind (contour interval = 0.2 m s^{-1}) resulting from 1° C initial 760 hPa temperature perturbation **P1** as in Fig. 4.24; (b) as in (a) except difference between perturbed and non-perturbed nonlinear forecasts; (c,d) as in (a,b) for 850 hPa vorticity (contour interval = 0.2 x 10^{-5} s^{-1}); and (e,f) as in (a,b) for sea-level pressure (contour interval = 0.1 hPa).
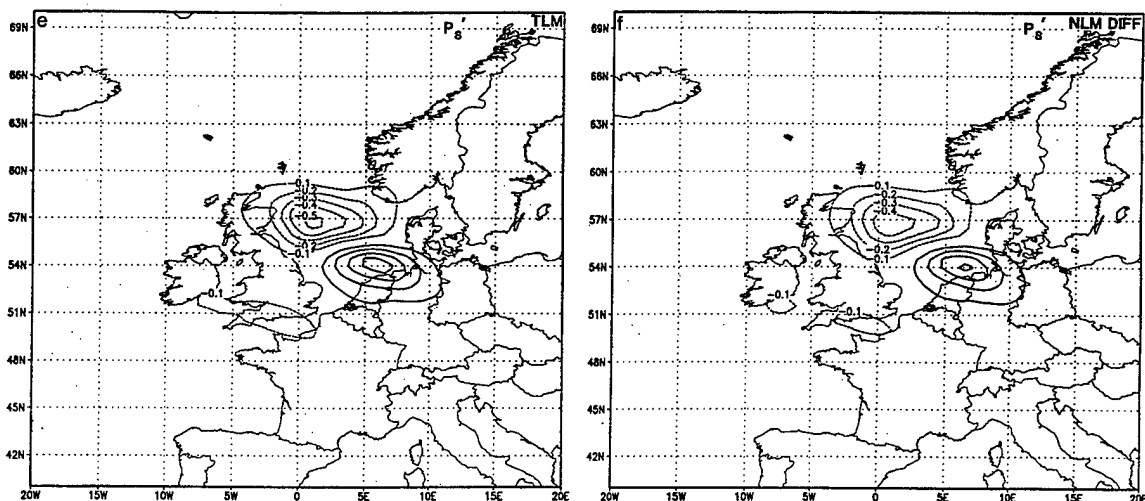
Figure 4.27, continued

These figures demonstrate the growth, physical consistency, and spatial coherence of perturbations resulting from an initial condition modification in a location of strong sensitivity, which the adjoint model can identify. In fact, there is evidence that the initial temperature perturbation P1 is an actual correction to analysis error, based on inspection of the 48 h perturbation vorticity in Fig. 4.27d, which represents a small improvement in cyclone position, according to the ECMWF analysis of Fig. 4.9a. In addition, the ECMWF analysis at the initial time (not shown) indicates that the MAMS1 analysis may be several degrees too cold at the location of perturbation P1, which would correspond to a positive temperature perturbation of 1° C or more.

Perturbation P1 also modifies the patterns of precipitation during the 48 h simulation (Fig. 4.28). Both nonconvective (Fig. 4.28a) and convective (4.28b) precipitation increase in a narrow band extending from the central U.K. northeast into

152
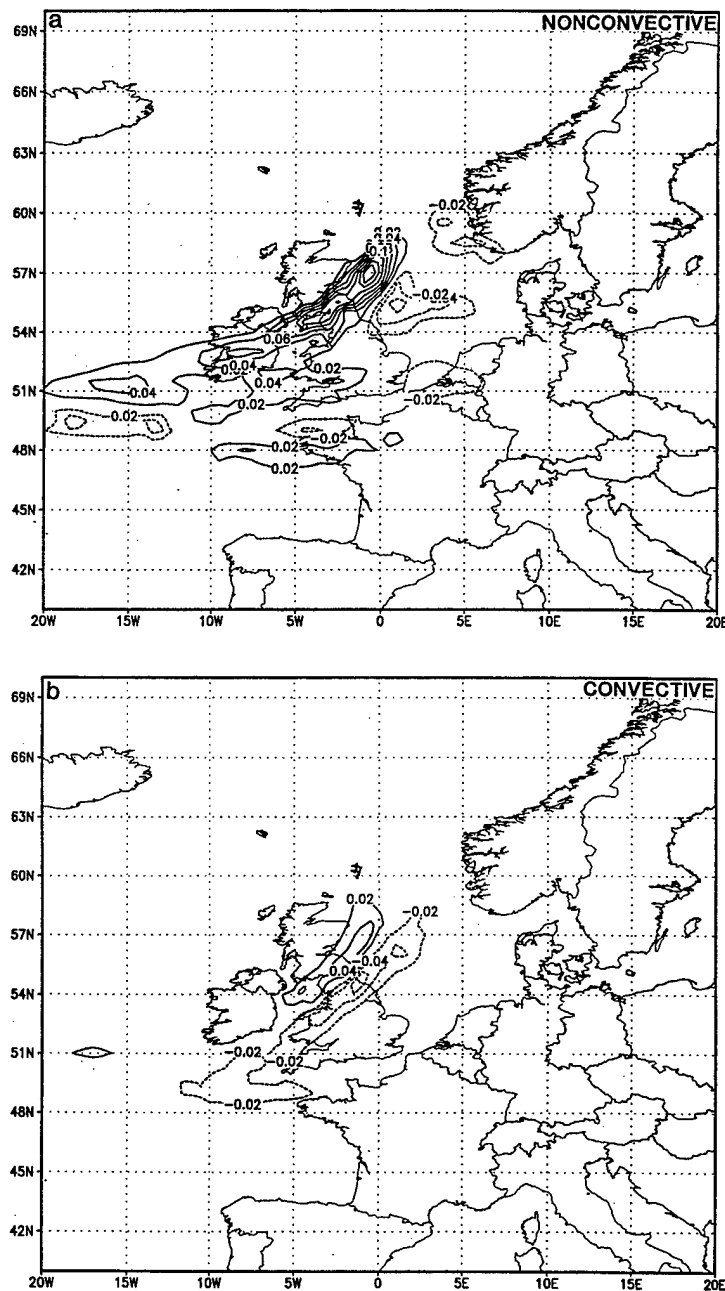
Figure 4.28: As in Fig. 4.8, except (a) nonconvective and (b) convective precipitation differences (contour interval = 0.02 cm) between nonlinear MAMS1 48 h forecast with 1° C initial 760 hPa temperature perturbation **P1** and non-perturbed nonlinear forecast. Increases (decreases) are indicated by solid (dashed) lines.

the North Sea. This pattern is apparently related to the positive perturbation vorticity near $0°$ E, $57°$ N (Fig. 4.27d) and alteration to the cyclone track that is associated with P1. There is a greater increase in nonconvective precipitation than in convective precipitation, although changes to both fields are small compared to the accumulated 48 h precipitation amounts (Fig. 4.8). Precipitation decreases (Fig. 4.28) over the North Sea between the U.K. and Denmark, in locations where the perturbation vorticity (Fig. 4.27d) is negative.

When a temperature perturbation of similar magnitude is placed about $5°$ longitude to the east in a location of weaker sensitivity (P2 in Fig. 4.12a), the effect on the J95 cyclone is quite different. At 48 h, the area affected by perturbations is considerably smaller and perturbations are reduced in magnitude by over 50 percent. For example, the perturbation 350 hPa zonal wind near $2°$E, $59°$N is -0.6 m s^{-1} with P1 (Fig. 4.27b) and only 0.2 m s^{-1} with P2 (Fig. 4.29a). The largest 850 hPa perturbation vorticity is 1.2×10^{-5} s^{-1} with P1 (Fig. 4.27d) and only -0.5×10^{-5} s^{-1} with P2 (Fig. 4.29b). Although P2 is located in the main baroclinic zone, as is P1, the 48 h perturbations for P2 are opposite in sign to those resulting from P1, since P2 includes a region of negative $\partial J/\partial T$ at the initial time (Fig. 4.12a). Thus, the same magnitude of temperature perturbation considered as an error in the initial conditions just $5°$ longitude to the east would decrease the predicted vorticity in the J95 cyclone. This difference between forecasts of increased vorticity (P1) and decreased vorticity (P2) illustrates again the great sensitivity to initial temperature perturbations in the lower and middle troposphere in highly localized areas.

A third perturbation (P3) in a region of maximum positive sensitivity ($\partial J/\partial u$) at the 350 hPa level is a 5 m s^{-1} increase in zonal wind, which corresponds to an
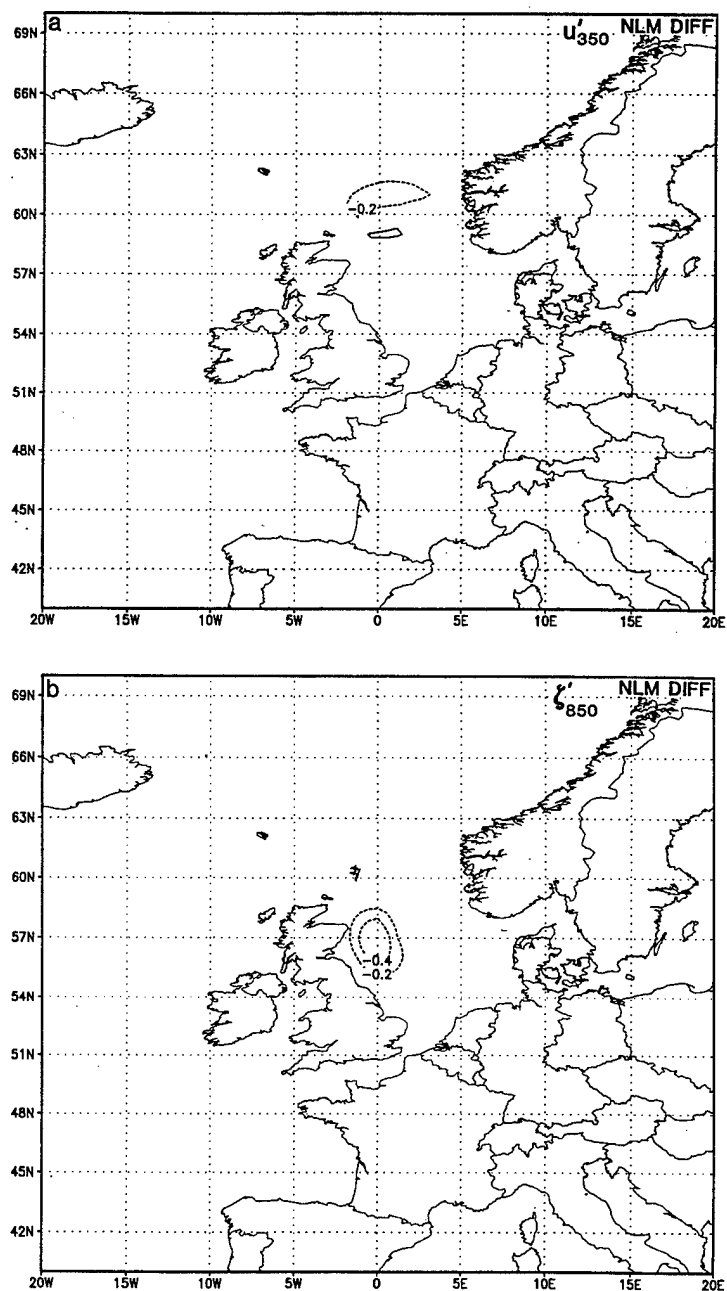
Figure 4.29: MAMS1 48 h nonlinear forecast at 00UTC 22 January 1995 of differences in (a) 350 hPa zonal wind (contour interval = 0.2 m s^{-1}); and (b) 850 hPa vorticity (contour interval = 0.2 x 10^{-5} s^{-1}) resulting from 1° C initial 760 hPa temperature perturbation **P2** (see Fig. 4.12a).

155
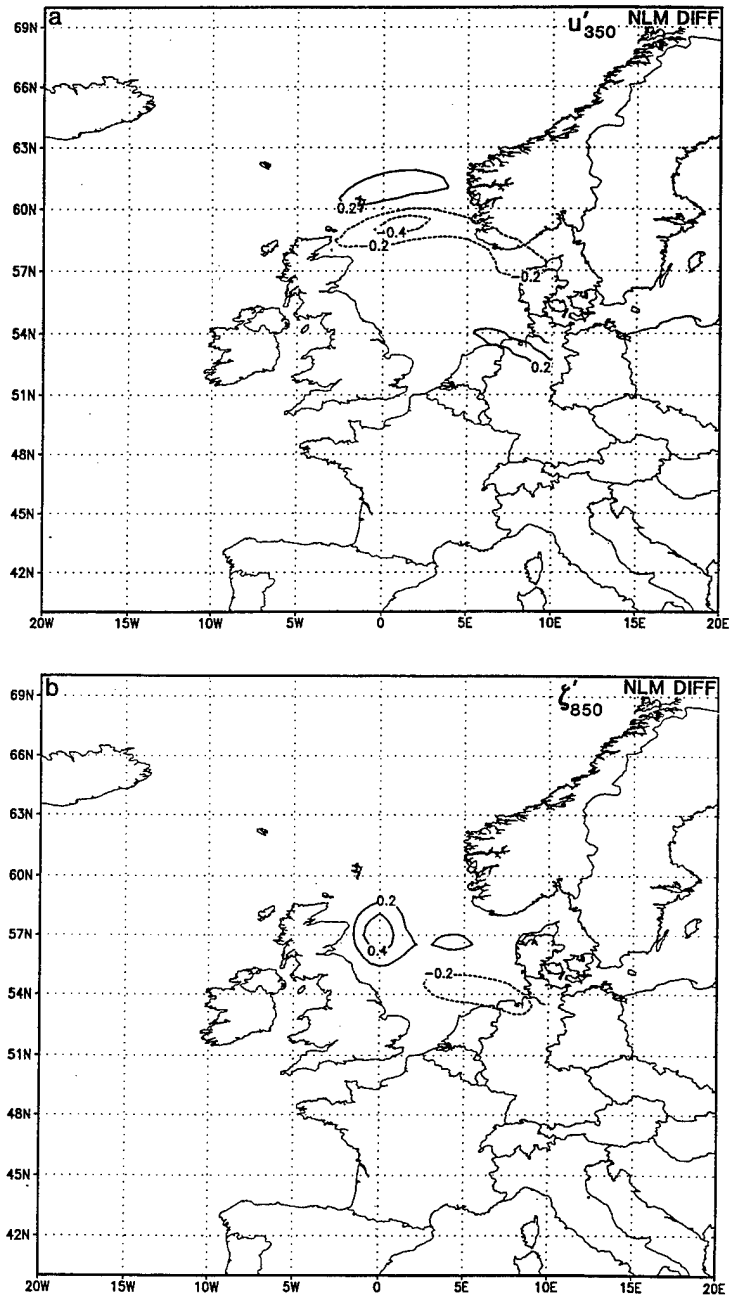
Figure 4.30: As in Fig. 4.29, for 5 m s⁻¹ initial 350 hPa zonal wind perturbation **P3** (see Fig. 4.12d).

increase in cyclonic shear associated with a potential vorticity anomaly north of the jet axis. At 48 h, the perturbation 350 hPa zonal wind is -0.4 m s^{-1} (Fig. 4.30a), and the perturbation vorticity at 850 hPa is 0.4 x 10^{-5} s^{-1} (Fig. 4.30b). Notice that the temperature perturbation P1 and the zonal wind perturbation P3 appear to project onto the same instability, in terms of the 48 h perturbation vorticity pattern. However, the 5 m s^{-1} upper tropospheric initial wind perturbation P3 has *less impact on both upper- and lower-tropospheric winds* at 48 h than result from the 1° C lower tropospheric temperature perturbation P1.

These tests demonstrate that small temperature perturbations in regions of strong sensitivity on a single level in the lower troposphere can initiate significant changes in both upper- and lower-tropospheric circulations. Although not presented, similar effects occur for lower tropospheric perturbations of wind and mixing ratio in locations of strong sensitivity identified by the adjoint model. These results suggest that the cyclone life cycle may be viewed in terms of an instability that propagates upward from the lower troposphere, leading to intensification of anomalies in both the upper- and lower-troposphere at the end of the storm track.

This paradigm of cyclogenesis is consistent with ideas presented in Hoskins et al. (1983) and HMR85 that pertain to steering-level Charney modes and upward propagation of free Rossby waves (see HMR85, pp. 923-928). Studies by Elsberry and Kirchoffer (1988), Davis and Emanuel (1991), and Bush and Peltier (1994) also demonstrate that upper-tropospheric features, including tropopause undulations and associated vorticity advections, may develop concurrently with, and have a dependence on, lower-tropospheric baroclinity and cyclone processes. In these cases, upper-tropospheric anomalies do not necessarily exist prior to, or initiate the cyclone

157

development in the lower troposphere. In the concluding Chapter, the results of interpretations for the idealized simulations of Chapt. III and the real cyclone simulation of Chapt. IV are summarized and presented in terms of a cyclone life cycle conceptual model.

V. SUMMARY AND CONCLUSIONS

A.   INTERPRETATION OF ADJOINT SENSITIVITY

In this study, the technique of adjoint sensitivity analysis is used to interpret development of idealized extratropical cyclones, and a cyclone that developed in the North Atlantic Ocean during January 1995. In many respects, the adjoint sensitivity is consistent with previous physical interpretations of extratropical cyclogenesis. However, adjoint methods can provide unique insights into atmospheric processes, because the sensitivity information provided is quite different from that obtained by conventional forward sensitivity analysis. Adjoint sensitivity also provides different information than is obtained from diagnostic techniques such as height tendency equations, trajectory interpretation, or potential vorticity inversion, which are based on simplified conservation and balance assumptions. The adjoint method allows localized sensitivity features to be identified in a systematic and computationally efficient manner, and provides a perspective on physical processes that is very difficult to obtain from observational or diagnostic studies alone.

In this section, some considerations of adjoint sensitivity interpretation are described. In Chapt. V.B, a conceptual model of extratropical cyclogenesis based on the results of the study is described. In Chapt. V.C, implications for cyclone predictability and some considerations related to future work are summarized.

When interpreting adjoint sensitivity, it is essential to keep in mind that adjoint variables are *gradients* that represent how a specific forecast aspect (J) is influenced by perturbations of model variables or parameters *at earlier times* in a numerical forecast. The largest magnitude adjoint sensitivity corresponds to a

159

location in which initial perturbations have the greatest effect on J at final time, which may not necessarily correspond to locations where largest amplitude flow anomalies (such as jet streaks or potential vorticity features) exist at the initial time. However, large sensitivity values may identify *precursor* features that are dynamically related (over the forecast interval) to J at the final time.

Adjoint sensitivity is a first-order approximation to nonlinear sensitivity, which is obtained along a trajectory that is *tangent* to the actual nonlinear forecast (time-varying basic state). Although adjoint and tangent linear models contain only linear function operators, they differ from purely linear models since the basic state about which they are linearized varies in time. However, the tangent linear assumption implies that adjoint and tangent linear accuracy (compared to nonlinear perturbation behavior) will diminish with increasing length of forecast, and is generally less valid as the perturbation size increases. Although this consideration places limits on adjoint sensitivity evaluation, the benefits that can be obtained from adjoint sensitivity still make it extremely useful. Although some adjoint-related applications (singular vectors, four-dimensional variational analysis) can be computationally expensive, obtaining adjoint sensitivity requires only slightly more resources than a single run of the corresponding nonlinear model.

A single integration of an adjoint model provides sensitivity (for one choice of J) over the entire model domain, for all model prognostic variables and selected parameters. It is impossible, for all practical purposes, to obtain equivalent information by conventional forward sensitivity for models of the size used in numerical weather prediction (on the order of 10^6 degrees of freedom). Without comprehensive adjoint sensitivity information, there is no assurance that the most

significant variables or parameters have been identified via forward sensitivity or other methods.

Another advantage of the adjoint method is that sensitivity can be obtained with respect to a nonlinear forecast that is not modified by removal of physical or dynamical processes. For example, the sensitivity in Chapts. III.B and IV pertains to a basic state that includes dry processes, convective and nonconvective precipitation, surface fluxes of sensible and latent heat, and surface momentum stress. Thus, the separate (*and nonlinear*) contributions of dry and most physical processes can be examined simultaneously, rather than with experiments in which model processes are simply removed or "switched" on and off.

It is re-emphasized that adjoint sensitivity pertains to *effects that occur over a specified forecast interval*, which may be as long as 90 h in the slowly evolving idealized simulation. In contrast, height tendency diagnostic equations, or potential vorticity inversions pertain to *near-instantaneous* cause and effect relations. Therefore, the conclusions inferred from adjoint sensitivity may provide new insights into life cycles of extratropical cyclones.

B. CONCEPTUAL MODEL OF CYCLONE EVOLUTION

In Chapt. III, adjoint sensitivity is used to examine an idealized extratropical cyclone. Baroclinic instability is initiated by a relatively weak, upper-tropospheric wind and temperature anomaly in the initial conditions. The cyclone develops as an amplifying wave on a frontal boundary in an initially zonal baroclinic zone in the lower troposphere. The early phase of the cyclone life cycle is characterized by increasingly strong thermal advection near the lower-tropospheric steering level

(about 800 hPa), with most rapid surface intensification occurring later in the life cycle when the disturbance has also propagated into the upper troposphere.

The interpretation of adjoint sensitivity for the idealized cyclone in Chapt. III clearly identifies the primary elements that can intensify extratropical cyclones and provides insight into spatial and temporal variations of sensitivity related to physical processes of cyclogenesis. To interpret how physical processes influence cyclone development, perturbations that are scaled according to tendencies of temperature and winds in the original nonlinear forecast are projected (using a scalar dot product) onto the adjoint sensitivity. This provides insight into forecast sensitivity that is closely related to physical processes and model dynamics. Physical processes that produce large wind, temperature or pressure tendencies in regions of strong adjoint sensitivity are significant to the feature represented by the forecast aspect (J). Processes that occur in regions of weak sensitivity may be related to the general evolution of the basic state, but changes in their intensity do not have as much effect on J.

In these simulations, J is a linear measure of cyclone central pressure or vorticity. Comparison of sensitivity to singular vectors (obtained with a local projection operator focused on the forecast cyclone) indicates that with a linear choice of J the largest sensitivity corresponds closely to the locations of the leading (most unstable) singular vectors, where initial perturbations cause perturbation energy associated with a cyclone to grow most rapidly over 48 h.

The most significant factors that can intensify the cyclone in the dry simulation are increased thermal advection in the lower troposphere, and lower surface stress. Higher sea-surface temperature in the cyclone warm sector is also a cyclogenetic

effect. Inclusion of moist processes in the idealized cyclone does not change the primary sensitivity features identified in the dry simulation. In both moist and dry simulations, strongest sensitivity exists in the middle and lower troposphere. Sensitivity magnitudes are larger in the moist case, which indicates the potential for greater impact on cyclone development through interaction of moist and dry processes of cyclogenesis. It is significant that inclusion of moist processes does not produce a major change in the sensitivity pattern, since this implies that *the contribution of moist processes to cyclone development can be viewed mainly as an enhancement of dry baroclinic instability.* In the simulations examined here, adjoint and tangent linear model accuracy (compared to nonlinear model sensitivity and perturbation growth rates) is significantly improved by inclusion of moist physical processes.

In the moist cyclone simulation, the effects of precipitation processes on storm intensification are most significant between 700 to 900 hPa (where sensitivity is high), although the heating tendencies from precipitation are generally largest between 500 and 700 hPa. The optimal location for latent heat release is the warm frontal region in the lower troposphere northeast of the cyclone center, which is also a location of strong sensitivity for dry baroclinic development. Diabatic heating near the warm front intensifies thermal and vorticity advections, and net mass divergence in the direction of storm motion. Thus, moist physical processes can interact in a nonlinear and synergistic sense with dry baroclinic processes to increase the cyclone deepening rate, and favorably configured latent heat release can create explosive cyclone deepening rates. Nonconvective precipitation is of particular importance in the simulation examined here, since it is concentrated near the warm front and produces larger heating rates than convective precipitation.

Based on interpretation of adjoint sensitivity and physical processes in the idealized moist cyclone simulation, it is possible to identify the most significant processes, and state whether their effects act to intensify or weaken the cyclone. This information is summarized in Table 5.1. It is important to note that the locations where physical processes are significant in terms of effects on cyclone development can be quite localized. Furthermore, physical processes (e.g., surface sensible heat flux, Chapt. III) can be cyclogenetic in one location and anticyclogenetic in another location at the same time. These types of effects can be identified with adjoint sensitivity, but are difficult to diagnose with other sensitivity methods.

Table 5.1: Effects of various processes on the central pressure at 60 h in simulation of idealized cyclone including moist physical processes. Bold type indicates more significant processes.

	Incipient phase 0 - 40 h	Rapid deepening phase 40 - 60 h
Cyclogenetic:	**Dry baroclinic processes** **Convective precipitation**[1]	**Dry baroclinic processes** Convective precipitation **Nonconvective precipitation**
	Latent heat flux	Latent heat flux
Anticyclogenetic:	Sensible heat flux[2] Surface stress	Sensible heat flux **Surface stress**

[1] Convective precipitation begins after 30 h.
[2] Effects of sensible heat flux can be cyclogenetic if directed upward in warm sector.

Examination of adjoint sensitivity for the North Atlantic cyclone (20-22 January 1995) described in Chapt. IV reveals many similarities to results obtained for the idealized cyclone simulations. Common features include localization of maximum

sensitivity between 500 and 800 hPa in relatively small areas upstream of the forecast cyclone. Close spatial correlations of sensitivity for temperature, meridional wind and mixing ratio imply the importance of thermal advection and latent heat release to cyclone development. The sensitivity in both idealized and real cyclone simulations is characterized by upstream vertical tilt in the lower troposphere, which indicates the relation of perturbation growth to baroclinic instability.

Absence of an initial upper-tropospheric short-wave forcing for the North Atlantic cyclone, and examples of sensitivity and perturbation growth provided in Chapt. IV, strongly suggest that this cyclone involves an initial stage confined to the lower troposphere, probably related to development of a mesoscale thermal and vorticity feature (cyclone precursor) forced by surface heat fluxes within an unstable boundary layer. The incipient North Atlantic cyclone begins to amplify with increasing thermal advection, and propagates upwards as it moves eastward within the baroclinic zone. By the time of most rapid development, the instability involves all levels from the tropopause or jet level to the surface. Cyclone intensification is favored by higher sea-surface temperature to the right of the direction of motion, and by low surface momentum stress found over the sea surface.

The schematic diagram of Fig. 5.1 summarizes the life cycles of the idealized cyclones studied in Chapt. III, and the North Atlantic cyclone examined in Chapt. IV. At the beginning of the storm track, the cyclone instability resembles a Charney mode centered at the steering level in the middle and lower troposphere. Later in the life cycle, there are characteristics of an Eady mode (interaction of tropopause and surface instabilities) with strong vorticity advection in the middle and upper troposphere.

Distance (km) ➤

0   900   1800   2700   3600

| INCIPIENT CYCLONE | UPWARD PROPAGATION OF INSTABILITY | RAPID INTENSIFICATION | BAROTROPIC DECAY |

250

Pressure (hPa)

500

750

1000

Strong divergence and PVA

Divergence and PVA increase

Precursor forms as small-scale thermal wave

Upper ridge amplifies --
Heating by thermal advection, latent heat release

Local vorticity increase within unstable boundary layer (cold air outbreak)

(*Steering Level*)
Increasing thermal advection

Warm Front
Nonconvective rain

F_S F_L

L   L   L

Small surface momentum stress over ocean

0   12   24   36   48

Time (hr) ➤

Figure 5.1: Conceptual diagram of extratropical cyclone development within a storm track, based on idealized simulations (Chapt. III) and North Atlantic cyclone of 20-22 January 1995 (Chapt. IV).

However, thermal advection in the middle and lower troposphere remains important important even in the rapid intensification stage.

The Eady baroclinic model considers cyclogenesis in terms of mutually amplifying instabilities, or potential vorticity anomalies, that exist on upper and lower boundaries (e.g., the tropopause and surface). Since adjoint sensitivity describes how "interior" and non-modal perturbations influence cyclone development, the Eady model is probably too simplistic to provide a complete framework that explains the interpretations based on adjoint information. The Charney baroclinic model does consider effects of interior anomalies; as discussed by HMR85, the "upper" potential vorticity anomaly for the fastest-growing Charney mode is found near the steering level in the middle - lower troposphere (600 - 700 hPa). A number of studies

166

demonstrate the significance of interior and steering level potential vorticity features on surface cyclone development, including Zehnder and Keyser (1991), and Whitaker and Barcilon (1992a,b). The concentration of lower tropospheric sensitivity identified by the adjoint model in this simulation confirms the importance of steering-level processes and the interpretation of baroclinic instability in terms of the Charney mode conceptualization. Instability at the steering level can develop in the absence of moist processes, although latent heat release can produce much stronger thermal and vorticity anomalies.

C. THE PREDICTABILITY QUESTION

A predictability study examines why forecasts of chaotic systems such as the atmosphere that start from slightly different initial states begin to diverge, eventually becoming completely dissimilar. The topic of predictability is closely related to the interpretation of adjoint sensitivity, which can identify locations where small magnitude initial perturbations have greatest effect on the development of atmospheric features over time intervals as long as several days. Predictability is strongly influenced by initial state differences and atmospheric processes that occur in these locations of strong sensitivity.

In the context of numerical weather prediction, the growth of small-scale initial condition (analysis) error is a primary factor that limits deterministic model predictive skill. A better understanding of how initial state differences in various locations cause numerical predictions to diverge during the first several days of a forecast will provide significant insight into longer-range predictability as well.

Previous studies have demonstrated the sensitivity of extratropical cyclone prediction to initial conditions (Mullen and Baumhefner 1989, Kuo and Low-Nam

167

1990), and the existence of localized areas where additional observations can produce dramatic effects on short-range forecast skill in extratropical situations (Heming 1990 and Källén and Huang 1988). As demonstrated in Chapt. IV.C, initial condition perturbations of similar magnitude only a short distance apart may have radically different effects on forecast cyclone features. Thus, figuratively speaking, the "flap of a butterfly's wings" may be significant in one location, and have little or no significance in another, in terms of effect on a particular storm.

The results of this adjoint-based study strongly suggest that predictability of extratropical cyclones is related to the amplification of localized, initially small-scale features in the middle and lower troposphere. In particular, the representation of thermal structure near the incipient cyclone in the lower troposphere appears critical to 48 h cyclone forecasts. For the cases examined here, it does not appear that cyclone prediction depends as strongly on initial conditions at the tropopause. The sensitivity patterns examined in this study do not rule out the effects of upper-tropospheric wind and temperature anomalies at the initial time; rather, they imply that larger perturbations (or analysis errors) are required for these features to have effects as significant as those that arise from smaller initial perturbations in the lower troposphere. No evidence is found here to support the concept that physical processes or anomalies at the tropopause interface dominate cyclone prediction or out-weigh the combined effects that occur in all layers below.

These statements concerning cyclone prediction are consistent with an accepted body of theory which describes perturbation growth and scale interaction in chaotic systems such as the atmosphere. It is clear that small-scale features (and initial errors) in the atmosphere amplify and influence the larger scales represented by

synoptic-scale weather features (Lorenz 1965, 1969). It is also evident that in locations where perturbations grow most rapidly (e.g., locations of strong initial condition sensitivity such as the middle and lower troposphere), initial errors of even small magnitude can have a relatively large effect on numerical forecast skill. Although large-amplitude, upper-tropospheric anomalies can be significant *during* the phase of most rapid cyclone intensification, this does not imply that these features control cyclone development over intervals of 24-48 h. In some situations, the final upper-tropospheric anomalies above the surface cyclone appear to have been strongly influenced by initial perturbations in the lower troposphere at the beginning of the storm track. To improve forecast skill, it may be necessary to include observations of mesoscale features in regions of the lower troposphere where incipient extratropical cyclones form, rather than large-scale features (e.g., jet streaks or tropopause potential vorticity anomalies), which are already evident and usually well-depicted in model initial conditions.

It may be argued that the cyclone cases examined here are not representative of situations involving initial high-amplitude middle- or upper-tropospheric, short-wave troughs, such as those found in cyclones that develop along the east coast of the United States. A more conclusive test will require additional adjoint model simulations. However, several considerations suggest that the sensitivity patterns identified in this study (in particular, strong sensitivity to lower-tropospheric thermal structure) may be fairly representative of extratropical cyclones in general.

First, it is noted that cyclones involving short-wave troughs in the middle or upper troposphere still require interaction of this feature *with a baroclinic zone or vorticity anomaly in the lower troposphere* (e.g., the "phase-locking" of two potential

vorticity anomalies, as described in HMR85). Again, there may be a significant sensitivity to lower-tropospheric thermal structure even when development occurs with a short-wave trough. Perhaps the importance of the short-wave trough to surface cyclogenesis is related to thermal and wind structure *below 500 hPa*, in that the thermal advection and latent heat release patterns control eastward progression and amplification of the short-wave trough. When the short-wave trough advances on the lower-tropospheric baroclinic zone (or potential vorticity anomaly), the thermal waves of the two features are mutually reinforced and combine to create conditions for rapid cyclone intensification.

Second, a general similarity is noted between the vertical distribution of sensitivity in the 20 January 1995 North Atlantic cyclone analyzed in Chapt. IV (Fig. 4.16), and the alpine lee cyclone studied by Vukićević and Raeder (1995; see Fig. 4.17). Although the alpine lee cyclone has a significant upper-tropospheric potential vorticity anomaly at the initial time and develops in a very different environment from the North Atlantic cyclone, the sensitivity patterns of these two cyclone are remarkably similar. Again, this suggests that baroclinic development in general may be characterized by strong sensitivity to lower-tropospheric thermal structure.

Finally, evidence is provided by the structure of singular vectors (e.g., Buizza and Palmer 1995). Singular vectors closely resemble the tilted structures of the sensitivity fields in this study, but do not relate to any one particular cyclone event, and are not based on linear forecast aspects such as those used in this study. Instead, the singular vectors of Buizza and Palmer (1995) relate to perturbation energy growth over most of the Northern Hemisphere, including all types of baroclinic developments and cyclone events. These singular vectors have maximum amplitude between 500 -

170

800 hPa at the initial time, which suggests that this pattern is characteristic of baroclinic processes in mid latitudes.

At the present time, it is generally thought that forecast error in numerical prediction of extratropical cyclones is primarily due to initial condition deficiencies, rather than model imperfections. Over the last two decades, numerical models have improved dramatically, in part by incorporating more sophisticated techniques for representing atmospheric physics and dynamics. In addition, increases in computational power have allowed numerical models to be run with increasingly fine resolution. If additional increases in forecast skill are to be realized, they are likely to result from improvements in observational capability and better analysis methods to provide initial conditions for numerical forecasts.

The results of this study suggest that observational capability might be directed or "targeted" to specific regions of strong initial condition sensitivity, where even small corrections to analysis error could be critical for improvements in numerical forecast skill. A mobile platform such as a jet aircraft with dropwindsondes could be particularly effective for this purpose. These types of adaptive observations might involve a real-time sensitivity analysis for a particular storm, or be based on knowledge of preferential locations of strong sensitivity obtained from evaluation of sensitivity in many storms. The adjoint of a global model may be required to evaluate sensitivity over longer forecast intervals, since a global model is not constrained by lateral boundary conditions, as in a regional model.

An opportunity to test the concept of adaptive observations in forecasts of extratropical cyclones will occur in conjunction with the Fronts and Atlantic Storm Track Experiment (FASTEX), which has a field phase in January and February 1997.

With high-resolution data collected during FASTEX, it will be possible to examine the effects of actual analysis errors on cyclone forecasts, and identify the locations where data are most critical to improvements in forecast skill.

The concept of adjoint-based observational targeting may prove useful for improved prediction of other types of phenomenon that are of importance to Navy operations, including tropical cyclones. The Navy has a unique opportunity to implement an adaptive observation strategy, since it has a capability (in the form of ships and satellite platforms) for data to be collected in areas where observations may be critical, but which are not covered by the conventional observational network. An adjoint-based program could result in improved weather support for the Fleet, as well as for downstream areas over land, and thus minimize damage from these storms.

APPENDIX A: MAMS1 DESCRIPTION

The model is Version 1 of the National Center for Atmospheric Research (NCAR) Mesoscale Adjoint Modeling System (MAMS1, Errico et al. 1994), which includes a nonlinear hydrostatic primitive equation model, a tangent linear model, and an adjoint model. The nonlinear model is similar to the Pennsylvania State University (PSU) / NCAR mesoscale model (MM4), as described by Anthes et al. (1987), Anthes (1990), and Warner and Seaman (1990); differences are described in Errico et al. (1994).

Model dynamics include second order horizonal advection with flux form variables on an Arakawa B-grid, and a time-splitting procedure (Madala 1981) added to allow a larger time step. Horizontal diffusion is fourth order in the interior, and second order near the north and south boundaries. Vertical turbulent mixing is performed with a stability-dependent, first order closure (K-theory) parameterization. Surface transfers of heat, moisture, and momentum involve transfer coefficients and bulk differences of temperature, moisture, and wind. The model vertical coordinate is sigma-pressure $\sigma_p = (p - p_T) / (p_S - p_T)$, where p_S is surface pressure and p_T is a fixed pressure representing the top of the model. A representation of the vertical grid structure used in this study appears in Fig. A.1, and model specifications are summarized in Table A.1.

Table A.1: Mesoscale Adjoint Modeling System Version 1 specifications.

Sigma levels (temperature, mixing ratio, wind): .0125, .0375, .0625, .1275, .23, .33, .44, .55, .65, .75, .85, .925, .965, .99 (see Fig. A.1).
Model top, p_T = 25 hPa.
Predictive variables, p*u, p*v, p*T, p*q, p*=(p_S - p_T).
Time step, Δt = 180 s, leapfrog, split-explicit.
Horizontal grid spacing, Δx=60 km.
Horizontal diffusion coefficient K_H= 3.24 x 10^{14} m^4 s^{-1} (K_H ∇^4).
Vertical turbulent mixing (stability-dependent K-theory, non-implicit solution).
Surface latent heat transfer coefficient, C_E = 1.0 x 10^{-3}.
Surface sensible heat transfer coefficient, C_H = 1.0 x 10^{-3}.
Surface momentum transfer coefficient, C_M = 1.0 x 10^{-3}.
Non-convective (grid-resolvable) precipitation.

Idealized Cyclone Simulations:

Grid points: 121 (east-west), 62 (north-south).
Coriolis parameter, f = 10^{-4} s (f-plane).
Initial conditions, idealized zonal jet and upper tropospheric perturbation.
Boundary conditions, (no-slip channel, see Appendix C).
Cumulus parameterization (Hack et al. 1993).
Basic state update: 30 min (dry simulation); 12 min (moist simulation).

Real Cyclone Simulations:

Grid points: 121 (east-west), 82 (north-south).
Initial conditions, NOGAPS T79L18 analysis.
Nonlinear vertical mode initialization.
Boundary conditions, NOGAPS T79L18 (12 h update), Davies-Turner relaxation method.
Surface topography, ice coverage, sea temperature, NOGAPS data base.
Surface energy budget (force restore with short-wave, long-wave radiation) .
Cumulus parameterization (relaxed Arakawa-Schubert).
Basic state update: 30 min (moist variables), 15 min (dry variables).

174

MAMS1 Vertical Grid
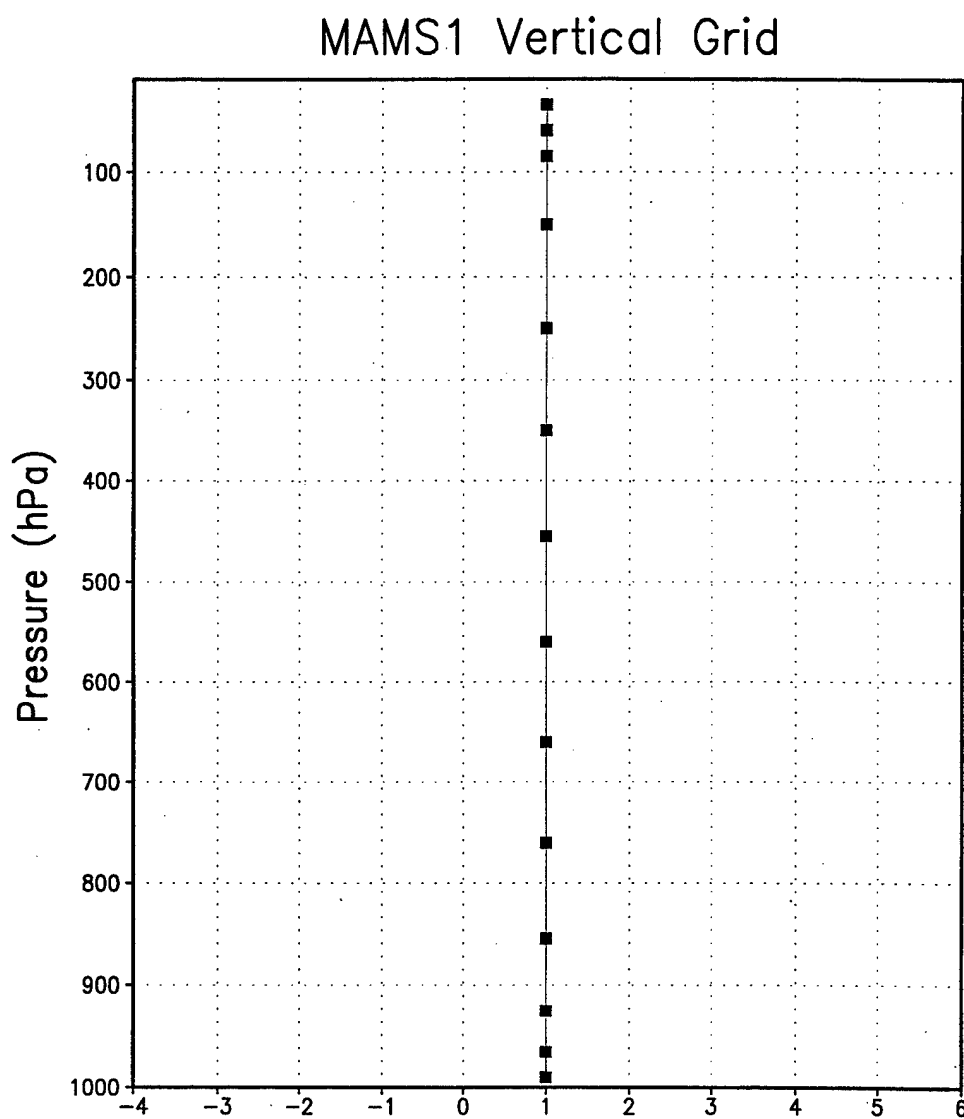
Figure A.1: The 14-level vertical grid structure used in MAMS1 simulations. Solid squares correspond to model levels, assuming a surface pressure of 1000 hPa.

[THIS PAGE INTENTIONALLY LEFT BLANK]

APPENDIX B:
DERIVATION OF IDEALIZED INITIAL CONDITIONS

This Appendix describes the procedure used to derive initial conditions for simulation of an idealized extratropical cyclone. The initial conditions include a background westerly jet in the center of the channel, with a corresponding north-south temperature gradient in hydrostatic and geostrophic balance. The first step in deriving the jet profile is to assign values of the u-wind component in a one-dimensional column. At 1000 hPa (surface level), the initial wind is zero. Proceeding upwards on model sigma surfaces, the zonal wind component is increased by 0.05 m s^{-1} hPa^{-1} until the sigma level at approximately 150 hPa is reached. Above that level, the zonal wind speed is decreased by 0.08 m s^{-1} hPa^{-1} until the uppermost sigma level is reached. Next, the u-component wind is defined on a north-south plane, according to a sine-squared relation

$$u(i,k) = u(c,k) - \sin^2\left\{ \frac{y(i) - y(c)}{h} \frac{\pi}{2} \right\} \cdot u(c,k) \ , \tag{B.1}$$

where i is a gridpoint index in the north-south direction (following MAMS1 notation), k is a vertical gridpoint index, c represents a grid point in the center of the channel (i=32), y is north-south distance, and h is a halfwidth parameter equal to 800 km.

To derive the initial temperature field, a reference column sounding extending from the surface to 28 km at 1 km intervals is defined. This sounding has a surface temperature of 288° K, a temperature lapse rate of 8° K km^{-1} between the surface and 12 km, and a constant temperature of 200° K between 12 km and 20 km. From 20 km to 28 km, temperature increases by 4° K km^{-1}. This temperature profile is interpolated to model sigma surfaces at a grid point on the southern boundary of the model

domain. Then proceeding northwards, temperature increments are obtained according to a form of the thermal wind relation

$$T'_{i,k} = \frac{f(u_{i,k} - u_{i,k+1})}{R_d \ln\dfrac{P_{i,k+1}}{P_{i,k}}} \Delta y \; , \tag{B.2}$$

where P is pressure ($P_{k+1} > P_k$), f is the Coriolis parameter (1.0×10^{-4} s^{-1}), and Δy is the horizontal grid spacing of 60 km. The temperature increments are then added to the original temperature field (including surface temperature) according to

$$T_{i,k} = T_{i-1,k} - 0.5\left(T'_{i,k} + T'_{i,k-1}\right), \; \text{for k} = 2, \text{kk} \, ,$$

$$T_{i,1} = T_{i-1,1} - T'_{i,1} \; , \; \text{for k} = 1 \, , \tag{B.3}$$

$$T_{i,kk+1} = T_{i-1,kk+1} - T'_{i,kk} \; , \; \text{for k} = \text{kk+1 (surface)} \, .$$

The resulting temperature field decreases to the north, with maximum gradient in the center of the channel. The "surface" layer thickness is approximately 50 hPa, or 400 m. The potential temperature difference in the surface layer is approximately 0.85° K, with $\theta_{kk} > \theta_s$. Therefore, the surface layer is initially stable, with weak downward heat fluxes.

To ensure hydrostatic balance, the geopotential heights are derived using the temperature field in the hypsometric equation

$$\phi_{i,k} = \phi_{i,k+1} + R_d \, T_{i,k} \, \ln\left[\frac{P_{i,k+1}}{P_{i,k}}\right] \; . \tag{B.4}$$

To ensure geostrophic balance, the zonal wind field is re-derived according to the geostrophic relation

$$u_{i,k} = -\frac{1}{f \, \Delta y}\left[\phi_{i,k} - \phi_{i-1,k}\right] \, , \tag{B.5}$$

where the zonal wind component u is on model dot points, and geopotential ϕ is on

cross points. The resulting wind profile has a maximum westerly wind speed of 37 m s⁻¹ near 250 hPa, in the center of the channel (Fig. 3.1a). This initial condition is non-divergent, with a maximum relative vorticity of 7×10^{-5} s⁻¹ at 250 hPa on the north side of the jet. Initial surface pressure is 1000 hPa at all grid points. All fields are uniform in the east-west direction.

Using this zonally symmetric initial state, the model was run to 120 h to verify the correctness of the boundary conditions, as well as mass conservation properties. All forecast fields remain zonally symmetric for the entire 120 h, with less than 0.01 percent variation in total mass in the model. Mass conservation was also verified in subsequent model simulations.

As the idealized initial conditions just described are uniform in the east-west direction, a cyclone development will not occur if the nonlinear model is integrated forward without a perturbation. To initiate a cyclogenesis, an anomaly of temperature and wind is placed in the upper troposphere. To define the initial condition anomaly, temperature perturbations are first assigned on pressure surfaces at 50 hPa intervals, using 1.0° C (125 hPa), 1.5° C (175 hPa), 2.0° C (225 hPa), 1.5° C (275 hPa), -1.0° C (325 hPa), -2.0° C (375 hPa), -5.0° C (425 hPa), -4.0° C (475 hPa), -2.0° C (525 hPa). These temperature increments are chosen in such a way that the corresponding net geopotential increment (obtained by vertical integration of the hypsometric equation) is approximately zero. Thus, no initial surface pressure increment is required. The temperature increments are distributed horizontally, with magnitude decreasing outwards from the center of the anomaly, according to a cosine-squared relation

$$T'_{i,j,k} = T^c_k \cos^2\left(\frac{\pi}{2}\frac{d}{r}\right) , \qquad (B.6)$$

179

where T^c is the temperature perturbation at the center of the anomaly, which is located at grid point (36,20), or 240 km north of the jet axis, r is the anomaly radius of 700 km, and d is the horizontal distance of $T'_{i,j,k}$ from the center of the anomaly. The temperature increments are then interpolated to sigma surfaces, and added to the original temperature field. Geopotential heights are recomputed by integrating the hypsometric equation (equation (B.4)), adding a gridpoint index for the east-west direction. Finally, zonal and meridional wind increments corresponding to the anomaly are obtained from the geostrophic relation

$$u_{i,j,k} = -\frac{1}{f \, \Delta y} 0.5 \left[\phi_{i,j-1,k} + \phi_{i,j,k} - \phi_{i-1,j,k} - \phi_{i-1,j-1,k} \right],$$ (B.7a)

$$v_{i,j,k} = \frac{1}{f \, \Delta y} 0.5 \left[\phi_{i-1,j,k} + \phi_{i,j,k} - \phi_{i,j-1,k} - \phi_{i-1,j-1,k} \right].$$ (B.7b)

and added to the original wind fields. Notice that the initial meridional wind (Fig. 3.1d) is entirely due to the anomaly. The wind field is then checked to verify that inertial instability ($\zeta + f < 0$) does not exist. Although a nonlinear normal mode initialization is available in MAMS1, the initial conditions of this idealized cyclone simulation are well-balanced, and it was not necessary to use the initialization procedure for reducing effects of gravity waves that would be present in real-data cases.

The resulting temperature anomaly has a maximum of approximately +1.7° C at 225 hPa and a minimum of - 4.3° C at 425 hPa (Fig. 3.1a, dotted contour). The maximum perturbation of zonal and meridional wind components is 8 m s^{-1} (Fig. 3.1d), which establishes a jet streak of approximately 45 m s^{-1} near 250 hPa (Fig. 3.1b,c), with maximum cyclonic vorticity of 14 x 10^{-5} s^{-1}. Approximating the position of the tropopause by the 2 PVU contour (1 PVU = 10^{-6} m^2 K s^{-1} kg^{-1}), the tropopause is

lowered below the specified initial anomaly (Fig. 3.1a). Although these temperature and wind perturbations may seem relatively weak compared to observed upper-tropospheric anomalies, they lead to a cyclone deepening rate that approaches 0.5 hPa h^{-1} without any effects of moist physical processes.

[THIS PAGE INTENTIONALLY LEFT BLANK]

APPENDIX C:
ADJOINT OF CHANNEL BOUNDARY CONDITIONS

In the idealized model simulations of Chapt. III, the lateral boundary conditions for MAMS1 are determined according to a "channel model" configuration. On the east and west boundaries, periodicity is imposed by an overlap of five grid point columns. On the north and south boundaries, a zero-gradient condition $(d\alpha/dy)=0$ is maintained for all prognostic variables except meridional wind, which is required to be zero on the rows defining the north and south model boundaries.

To include channel boundary conditions in MAMS1, several modifications to the original code are required. The logical variable "lbdry" is set to false. A new subroutine, "chanel" (listed below), is added to the nonlinear and tangent linear models. Calls to "chanel" are made in the main nonlinear and TLM programs after calls to subroutines "nstepf1", "vconvc" ("fconvp"), "sseqnce" ("fseqnce"), "nwavg", "nnconvp" ("fnconvp"). The chanel subroutine is applied to all prognostic variables at the new time level $(t+\Delta t)$, except for the call made after the time filtering in "nwavg", which is applied to the previous time level $(t-\Delta t)$. In subroutine "ststep," the chanel subroutine is used with array delh. In addition, a modification is made to horizontal diffusion along the boundaries in subroutine "ngrid."

In the adjoint model, channel boundary conditions are imposed using the adjoint of subroutine "chanel", called "achanel" (listed below). Whereas "chanel" in the forward model over-writes the outer east and west edge points (1 to 2, nj-2 to nj) with values taken from interior points on the opposite side of the domain, "achanel" in the adjoint model adds the sensitivity on these outer edge points to the interior points and then zeroes the edge points. The sequence of calls to subroutine "achanel" occurs in

reverse order from the forward model. Since "achanel" requires the adjoint model to provide sensitivity on edge points, the logical variable "lbdry" is set to true. Calls to subroutines "cbdry0" and "abdryi" are removed in several locations to ensure that sensitivity on the edges is consistent with channel requirements. A gradient test (equation (2.7)) is used to verify that this method provides the exact adjoint of the TLM channel boundary conditions.

Examples of FORTRAN code statements used to specify the forward and adjoint channel boundary conditions are provided below. Only code for the zonal and meridional wind components are shown; temperature, mixing ratio, pressure and surface temperature use statements that follow the code used for zonal wind. Notice that in MAMS1, the first array index "i" applies to the north-south direction, and the second array index "j" applies to the east-west direction.

```
----------------------------------------------------
      subroutine chanel
c
c impose channel domain boundary conditions on nonlinear or tangent linear arrays
c
      dimension uu(ni,nj,nk), vv(ni,nj,nk)
      zero=0.0
c
      do 200 k=1,nk
c
c east-west periodic boundaries
c
      do 100 i=1,ni
c
c zonal wind component
      uu(i,  1,k) = uu(i,nj-4,k)
      uu(i,  2,k) = uu(i,nj-3,k)
      uu(i, nj,k) = uu(i,    5,k)
      uu(i,nj-1,k) = uu(i,    4,k)
      uu(i,nj-2,k) = uu(i,    3,k)
```

```fortran
c
c  meridional wind component
      vv(i,   1,k) = vv(i,nj-4,k)
      vv(i,   2,k) = vv(i,nj-3,k)
      vv(i,  nj,k) = vv(i,   5,k)
      vv(i,nj-1,k) = vv(i,   4,k)
      vv(i,nj-2,k) = vv(i,   3,k)
  100 continue
c
c  north and south wall conditions
      do 150 j=1,nj
c
c  zonal wind component
      uu(ni  ,j,k) = uu(ni-1,j,k)
      uu(   1,j,k) = uu(    2,j,k)
c
c  meridional wind component
      vv(ni  ,j,k) = zero
      vv(ni-1,j,k) = zero
      vv(   2,j,k) = zero
      vv(   1,j,k) = zero
c
  150 continue
  200 continue
      return
      end
```

```fortran
      subroutine achanel
c
c  impose adjoint of channel domain boundary conditions
c
      dimension uu(ni,nj,nk), vv(ni,nj,nk)
      zero=0.0
c
      do 200 k=1,nk
c
c  east-west periodic boundaries
c
      do 100 i=1,ni
c
c  zonal wind component
      uu(i,nj-4,k) = uu(i,nj-4,k) + uu(i,   1,k)
      uu(i,nj-3,k) = uu(i,nj-3,k) + uu(i,   2,k)
      uu(i,   5,k) = uu(i,   5,k) + uu(i,  nj,k)
      uu(i,   4,k) = uu(i,   4,k) + uu(i,nj-1,k)
      uu(i,   3,k) = uu(i,   3,k) + uu(i,nj-2,k)
```

```
c
      uu(i,    1,k) = zero
      uu(i,    2,k) = zero
      uu(i,   nj,k) = zero
      uu(i,nj-1,k) = zero
      uu(i,nj-2,k) = zero
c
c  meridional wind component
      vv(i,nj-4,k) = vv(i,nj-4,k) + vv(i,    1,k)
      vv(i,nj-3,k) = vv(i,nj-3,k) + vv(i,    2,k)
      vv(i,    5,k) = vv(i,    5,k) + vv(i,   nj,k)
      vv(i,    4,k) = vv(i,    4,k) + vv(i,nj-1,k)
      vv(i,    3,k) = vv(i,    3,k) + vv(i,nj-2,k)
c
      vv(i,    1,k) = zero
      vv(i,    2,k) = zero
      vv(i,   nj,k) = zero
      vv(i,nj-1,k) = zero
      vv(i,nj-2,k) = zero
  100 continue
c
c  north and south wall conditions
      do 150 j=1,nj
c
c  zonal wind component
      uu(ni-1,j,k) = uu(ni-1,j,k) + uu(ni,j,k)
      uu(    2,j,k) = uu(    2,j,k) + uu( 1,j,k)
      uu(    1,j,k) = zero
      uu(  ni,j,k) = zero
c
c  meridional wind component
      vv(ni   ,j,k) = zero
      vv(ni-1,j,k) = zero
      vv(    2,j,k) = zero
      vv(    1,j,k) = zero
c
  150 continue
  200 continue
      return
      end
```

REFERENCES

Anthes, R. A., 1990: Recent applications of the Penn State/NCAR mesoscale model to synoptic, mesoscale and climate studies. *Bull. Amer. Meteor. Soc.*, **71**, 1610-1629.

Anthes, R. A., and D. Keyser, 1979: Tests of a fine-mesh model over Europe and the United States. *Mon. Wea. Rev.*, **107**, 963-984.

Anthes, R. A., Y.-H. Kuo, and J. R. Gyakum, 1983: Numerical simulation of a case of explosive marine cyclogenesis. *Mon. Wea. Rev.*, **111**, 963-984.

Anthes, R. A., E.-Y. Hsie, and Y.-H. Kuo, 1987: *Description of the Penn State/NCAR Mesoscale Model Version 4 (MM4)*. NCAR Technical Note, NCAR/TN-282+STR, 66 pp. (Available from NCAR, P.O. Box 3000, Boulder, Co. 80307).

Atlas, R., 1987: The role of oceanic fluxes and initial data in the numerical prediction of an intense coastal storm. *Dyn. Atmos. Ocean.*, **10**, 359-388.

Bane, J. M., and K. E. Osgood, 1989: Wintertime air-sea interaction processes across the Gulf Stream. *J. Geophys. Res.*, **94**, 10,755-10,772.

Bao, J.-W., and T. T. Warner, 1993: Treatment of on/off switches in the adjoint method: FDDA experiments with a simple model. *Tellus*, **45A**, 525-538.

Bjerknes J., 1919: On the structure of moving cyclones. *Geofys. Publikasjoner*, Norske Videnskaps-Akad. Oslo, **1**(2).

Bjerknes, J. and H. Solberg, 1922: Life cycles of cyclones and the polar front theory of atmospheric circulation. *Geofys. Publikasjoner*, Norske Videnskaps-Akad. Oslo, **3**(1).

Borges, M. D., and D. L. Hartmann, 1992: Barotropic instability and optimal perturbations of observed nonzonal flows. *J. Atmos. Sci.*, **49**, 335-354.

Bosart, L. G., C.-C. Lai, and E. Rogers, 1995: Incipient explosive marine cyclogenesis: coastal development. *Tellus*, **47A**, 1-29.

Bosart, L. F., and S. C. Lin, 1984: A diagnostic analysis of the Presidents' Day storm of February 1979. *Mon. Wea. Rev.*. **112**, 2148-2177.

Boyle, J. S., and L. F. Bosart, 1986: Cyclone-anticyclone couplets over North America. Part II: Analysis of a major cyclone event over the eastern United States. *Mon. Wea. Rev.*, **114**, 2432-2463.

Branscome, L. E., W. J. Gutowski Jr., and D. A. Stewart, 1989: Effect of surface energy fluxes on the nonlinear development of baroclinic waves. *J. Atmos. Sci.*, **46**, 460-475.

Browning, K. A., and N. M. Roberts, 1993: Structure of a frontal cyclone. *Quart. J. Roy. Meteor. Soc.*, **120**, 1535-1557.

Buizza, R., 1994: Sensitivity of optimal unstable structures. *Quart. J. Roy. Meteor. Soc.*, **120**, 429-451.

Buizza, R., 1995: Optimal perturbation time evolution and sensitivity of ensemble prediction to perturbation amplitude. *Quart. J. Roy. Meteor. Soc.*, **121**, 1705-1738.

Buizza, R., and T. N., Palmer, 1995: The singular-vector structure of the atmospheric general circulation. *J. Atmos. Sci.*, **52**, 1434-1456.

Buizza, R., J. Tribbia, F. Molteni, and T. Palmer, 1993: Computation of optimal unstable structures for a numerical weather prediction model. *Tellus*, **45A**, 388-407.

Bush, A. B. G., and W. R. Peltier, 1994: Tropopause folds and synoptic-scale baroclinic wave life cycles. *J. Atmos. Sci.*, **51**, 1581-1604.

Chang, S., K. Brehme, R. Madala, and K. Sashegyi, 1989: A numerical study of the east coast snowstorm of 10-12 February 1983. *Mon. Wea. Rev.*, **117**, 1768-1778.

Charney, J. G., 1947: The dynamics of long waves in a baroclinic westerly current. *J. Meteor.*, **4**, 125-162.

Chen, S.-J., and L. Dell'Osso, 1987: A numerical case study of East Asian cyclogenesis. *Mon. Wea. Rev.*, **115**, 477-487.

Chen, S.-J., Y.-H. Kuo, P.-Z. Zhang, and Q.-F. Bai, 1992: Climatology of explosive cyclones off the east Asian coast. *Mon. Wea. Rev.*, **120**, 3029-3035.

Courtier, P., J.-N., Thépaut, and A. Hollingsworth, 1994: A strategy for operational implementation of 4D-Var, using an incremental approach. *Quart. J. Roy. Meteor. Soc.*, **120**, 1367-1387.

Danard, M. B., 1986: On the sensitivity of predictions of maritime cyclogenesis to convective precipitation and sea temperature. *Atmos.-Ocean*, **24**, 52-72.

Danard, M. B., and G. E. Ellenton, 1980: Physical influences on East Coast cyclogenesis. *Atmos.-Ocean*, **18**, 65-82.

Davies , H. C., and R. E. Turner, 1977: Updating prediction models by dynamical relaxation: An examination of the technique. *Quart. J. Roy. Meteor. Soc.*, **103**, 225-245.

Davis, C. A., and K. A. Emanuel, 1991: Potential vorticity diagnostics of cyclogenesis. *Mon. Wea. Rev.*, **119**, 1929-1953.

Davis, C. A., M. T. Stoelinga, and Y.-H. Kuo, 1993: The integrated effects of condensation in numerical simulations of extratropical cyclogenesis. *Mon. Wea. Rev.*, **121**, 2309-2330.

Doyle, J. D., and T. T. Warner, 1993a: The impact of the sea surface temperature resolution on mesoscale coastal processes during GALE IOP 2. *Mon. Wea. Rev.*, **121**, 313-334.

Doyle, J. D., and T. T. Warner, 1993b: A numerical investigation of coastal frontogenesis and mesoscale cyclogenesis during GALE IOP 2. *Mon. Wea. Rev.*, **121**, 1048-1077.

Eady, E. T., 1949: Long waves and cyclone waves. *Tellus*, **1**, 33-52.

Edmon, H. J., B. J. Hoskins, and M. E. McIntyre, 1980: Eliassen-Palm cross-sections for the troposphere. *J. Atmos. Sci.*, **37**, 2600-2616.

Ehrendorfer, M., and R. M. Errico, 1995: Mesoscale predictability and the spectrum of optimal perturbations. *J. Atmos. Sci.*, **52**, 3475-3500.

Elsberry, R. L., and P. J. Kirchoffer, 1988: Upper-level forcing of explosive cyclogenesis over the ocean based on operationally analyzed fields. *Wea. Forecasting*, **3**, 205-216.

Emanuel, K. A., 1994: Sea-air heat transfer effects on extratropical cyclones. In Proceedings, of *The Life Cycles of Extratropical Cyclones, v. III*, Bergen, Norway, 27 June - 1 July. Aase Grafiske A/S, Stavanger, 67-72.

Errico, R. M., and J. Oortwijn, 1995: The interpretation of adjoint determined sensitivity fields as optimal structures. *Unpublished manuscript.*

Errico, R. M., K. Raeder, and T. Vukićević, 1994: Mesoscale Adjoint Modeling System Version 1 (MAMS1). NCAR Technical Note. [Available from the authors: National Center for Atmospheric Research, P.O. Box 3000, Boulder, CO 80307-3000, USA.]

Errico, R. M., and T. Vukićević, 1992: Sensitivity analysis using an adjoint of the PSU-NCAR mesoscale model. *Mon. Wea. Rev.*, **120**, 1644-1660.

Errico, R. M., T. Vukićević, and K. Raeder, 1993a: Examination of the accuracy of a tangent linear model. *Tellus*, **45A**, 462-477.

189

Errico, R. M., T. Vukićević, and K. Raeder, 1993b: Comparison of initial and lateral boundary condition sensitivity for a limited-area model. *Tellus*, **45A**, 539-557.

Fantini, M., 1990: The influence of heat and moisture fluxes from the ocean on the development of baroclinic waves. *J. Atmos. Sci.*, **47**, 840-855.

Farrell, B. F., 1982: The initial growth of disturbances in a baroclinic flow. *J. Atmos. Sci.*, **39**, 1663-1686.

Farrell, B. F., 1984: Modal and non-modal baroclinic waves. *J. Atmos. Sci.*, **41**, 668-673.

Farrell, B. F., 1985: Transient growth of damped baroclinic waves. *J. Atmos. Sci.*, **42**, 2718-2727.

Farrell, B. F., 1989: Optimal excitation of baroclinic waves. *J. Atmos. Sci.*, **46**, 1193-1206.

Farrell, B. F., 1990: Small error dynamics and the predictability of atmospheric flows. *J. Atmos. Sci.*, **47**, 2409-2416.

Farrell, B. F., and A. M. Moore, 1992: An adjoint method for obtaining the most rapidly growing perturbation to oceanic flows. *J. Phys. Oceanogr.*, **22**, 338-349.

Fleagle, R. G., and W. A. Nuss, 1985: The distribution of surface fluxes and boundary layer divergence in midlatitude ocean storms. *J. Atmos. Sci.*, **42**, 784-799.

Grotjahn, R., and C.-H. Wang, 1989: On the source of air modified by surface fluxes to enhance frontal cyclone development. *Ocean-Air Int.*, **1**, 257-288.

Gyakum, J. R., 1991: Meteorological precursors to the explosive intensification of the QE II storm. *Mon. Wea. Rev.*, **119**, 1105-1131.

Gyakum J. R., P. J. Roebber, and T. A. Bullock, 1992: The role of antecedent surface vorticity development as a conditioning process in explosive cyclone intensification. *Mon. Wea. Rev.*, **120**, 1465-1489.

Hack, J. J., B. A. Boville, B. P. Briegleb, J. T. Kiehl, P. J. Rasch, and D. L. Williamson, 1993: Description of the NCAR Community Climate Model. NCAR Tech. Note NCAR/TN-382+STR, 108 pp. [Available from the authors: National Center for Atmospheric Research, P.O. Box 3000, Boulder, CO 80307-3000, USA.]

Hadlock, R., and C. W. Kreitzberg, 1988: The experiment on rapidly intensifying cyclones over the Atlantic (ERICA) field study: Objectives and plans. *Bull. Amer. Meteor. Soc.*, **69**, 1309-1320.

Hall, M. C. G., 1986: Application of adjoint sensitivity theory to an atmospheric general circulation model. *J. Atmos. Sci.*, **43**, 2644-2651.

Hall, M. C. G., D. G. Cacuci, and M. E. Schlesinger, 1982: Sensitivity analysis of a radiative-convective model by the adjoint method. *J. Atmos. Sci.*, **39**, 2038-2050.

Hartmann, D. L., R. Buizza, and T. N. Palmer, 1995: Singular vectors: The effect of spatial scale on linear growth of disturbances. *J. Atmos. Sci.*, **52**, 3885-3894.

Heming, J. T., 1990: The impact of surface and radiosonde observations from two Atlantic ships on a numerical weather prediction model forecast for the storm of 25 January 1990. *Meteor. Mag.*, **119**, 249-259.

Hines, K. M., and C. R. Mechoso, 1993: Influence of surface drag on the evolution of fronts. *Mon. Wea. Rev.*, **121**, 1152-1175.

Hirschberg, P. A., and J. M. Fritsch, 1991: Tropopause undulations and the development of extratropical cyclones. Part II: Diagnostic analysis and conceptual model. *Mon. Wea. Rev.*, **119**, 518-520.

Hogan, T. F., and T. E. Rosmond, 1991: The description of the Navy Operational Global Atmospheric Prediction System's spectral forecast model. *Mon. Wea. Rev.*, **119**, 1786-1815.

Holton, J. R., 1992: *An Introduction to Dynamic Meteorology*, 3rd ed., Academic Press, 511 pp.

Hoskins, B., and P. Berrisford, 1988: A potential vorticity perspective of the storm of 15-16 October 1987. *Weather*, **43**, 122-128.

Hoskins, B. J., and W. A. Heckley, 1981: Cold and warm fronts in baroclinic waves. *Quart. J. Roy. Meteor. Soc.*, **107**, 79-90.

Hoskins, B. J., and P. J. Valdes, 1990: On the existence of storm-tracks. *J. Atmos. Sci.*, **47**, 1854-1864.

Hoskins, B. J., I. N. James, and G. H. White, 1983: The shape, propagation and mean-flow interaction of large-scale weather systems. *J. Atmos. Sci.*, **40**, 1595-1612.

Hoskins, B. J., M. E. McIntyre, and A. W. Robertson, 1985: On the use and significance of isentropic potential vorticity maps. *Quart. J. Roy. Meteor. Soc.*, **111**, 877-946.

Jarraud, M., J. Goas, and C. Deyts, 1989: Prediction of an exceptional storm over France and southern England (15-16 October 1987). *Wea. Forecasting*, **4**, 517-536.

191

Källén, E., and X.-Y. Huang, 1988: The influence of isolated observations on short-range numerical weather forecasts. *Tellus*, **40A**, 324-336.

Kuo, Y.-H., and S. Low-Nam, 1990: Prediction of nine explosive cyclones over the western Atlantic ocean with a regional model. *Mon. Wea. Rev.*, **118**, 3-25.

Kuo, Y.-H, and R. J. Reed, 1988: Numerical simulations of an explosively deepening cyclone in the Eastern Pacific. *Mon. Wea. Rev.*, **116**, 2081-2105.

Kuo, Y.-H., R. J. Reed, and S. Low-Nam, 1991a: Effects of surface energy fluxes during the early development and rapid intensification stages of seven explosive cyclones in the Western Atlantic. *Mon. Wea. Rev.*, **119**, 457-476.

Kuo, Y.-H., M. A. Shapiro and E. G. Donall, 1991b: The interaction between baroclinic and diabatic processes in a numerical simulation of a rapidly intensifying extratropical marine cyclone. *Mon. Wea. Rev.*, **119**, 368-384.

Lacarra, J.-F., and O. Talagrand, 1988: Short-range evolution of small perturbations in a barotropic model. *Tellus*, **40A**, 81-95.

Langland, R. H., R. L. Elsberry, and R. M. Errico, 1995: Evaluation of physical processes in an idealized extratropical cyclone using adjoint sensitivity. *Quart. J. Roy. Meteor. Soc.*, **121**, 1349-1386.

Langland, R. H., R. L. Elsberry, and R. M. Errico, 1996: Adjoint sensitivity of an idealized extratropical cyclone with moist physical processes. *Quart. J. Roy. Meteor. Soc.* (in press).

Langland, R. H., and R. M. Errico, 1996: Comments on "Use of an adjoint model for finding triggers for Alpine Lee Cyclogenesis." *Mon. Wea. Rev.*, **124**, 757-760.

Lapenta, W. M., and N. L. Seaman, 1992: A numerical investigation of East Coast cyclogenesis during the cold-air damming event of 27-28 February 1982. Part II: Importance of physical mechanisms. *Mon. Wea. Rev.*, **120**, 52-76.

Li, Y., I . M. Navon, W. Yang, X. Zou, J. R. Bates, S. Moorthi, and R. W. Higgins, 1994: Four-dimensional variational data assimilation experiments with a multilevel semi-Lagrangian, semi-implicit general circulation model. *Mon. Wea. Rev.*, **122**, 966-983.

Lindzen, R. S., B. Farrell, and K.-K. Tung, 1980: The concept of wave overreflection and its application to baroclinic instability. *J. Atmos. Sci.*, **37**, 44-63.

Liou, C.-S., C. H. Wash, S. M. Heikkinen, and R. L. Elsberry, 1990: Numerical studies of cyclogenesis events during the second intensive observation period (IOP-2) of GALE. *Mon. Wea. Rev.*, **118**, 218-233.

Lorenz, E. N., 1965: A study of the predictability of a 28-variable atmospheric model. *Tellus*, **17**, 321-333.

Lorenz, E. N., 1969: The predictability of a flow which possesses many scales of motion. *Tellus*, **21**, 289-307.

McIntyre, M., 1988: The use of potential vorticity and low-level temperature/moisture to understand extratropical cyclones. In *The Nature and Prediction of Extra Tropical Weather Systems,* Seminar Proceedings, 7-11 September 1987. ECMWF, Reading, U.K., 261-280.

Madala, R. V., 1981: Efficient time integration schemes for atmosphere and ocean models, Chap. 4. *Finite Difference Techniques for Vectorized Fluid Dynamic Calculations*, ed., David L. Book, Springer Verlag, 56-74.

Mailhot, J., and C. Chouinard, 1989: Numerical forecasts of explosive winter storms: Sensitivity experiments with a meso-α scale model. *Mon. Wea. Rev.*, **117**, 1311-1343.

Manobianco, J., 1989: Explosive east coast cyclogenesis: Numerical experimentation and model-based diagnostics. *Mon. Wea. Rev.*, **117**, 2384-2405.

Marchuk, G.I., 1974: The numerical solution of problems of atmospheric and oceanic dynamics (in Russian), *Gidrometeoizdat,* Leningrad, 387 pp. (English translation, Rainbow Systems, Alexandria, Va.).

Mass, C. F., and D. M. Schultz, 1993: The structure and evolution of a simulated midlatitude cyclone over land. *Mon. Wea. Rev.*, **121**, 889-917.

Molteni, F., R. Buizza, T. N. Palmer, and T. Petroliagis, 1994: The ECMWF ensemble prediction system: methodology and validation. Technical Memorandum No. 202, ECMWF, Reading, U.K., 55 pp.

Molteni, F., and T. N. Palmer, 1993: Predictability and finite-time instability of the northern winter circulation. *Quart. J. Roy. Meteor. Soc.*, **119**, 269-298.

Mullen, S. L., and D. P. Baumhefner, 1988: Sensitivity of numerical simulations of explosive oceanic cyclogenesis to changes in physical parameterization. *Mon. Wea. Rev.*, **116**, 2289-2329.

Mullen, S. L., and D. L. Baumhefner, 1989: The impact of initial condition uncertainty on numerical simulations of large-scale explosive cyclogenesis. *Mon. Wea. Rev.*, **117**, 2800-2821.

Mureau, R., F. Molteni, and T. N. Palmer, 1993: Ensemble prediction using dynamically conditioned perturbations. *Quart. J. Roy. Meteor. Soc.*, **119**, 299-323.

Neiman, P. J., and M. A. Shapiro, 1993: The life cycle of an extratropical marine cyclone. Part I: Frontal-cyclone evolution and thermodynamic air-sea interaction. *Mon. Wea. Rev.*, **121**, 2153-2176.

Neiman, P. J., M. A. Shapiro, and L. S. Fedor, 1993: The life cycle of an extratropical marine cyclone. Part II: Mesoscale structure and diagnostics. *Mon. Wea. Rev.*, **121**, 2177-2199.

Nuss, W. A., and R. A. Anthes, 1987: A numerical investigation of low-level processes in rapid cyclogenesis. *Mon. Wea. Rev.*, **115**, 2728-2743.

Nuss, W. A., and S. I. Kamikawa, 1990: Dynamics and boundary layer processes in two Asian cyclones. *Mon. Wea. Rev.*, **118**, 755-771.

Oortwin, J., and J. Barkmeijer, 1995: Perturbations that optimally trigger weather regimes. *J. Atmos. Sci.*, **52**, 3932-3944.

Park, S. K., K. K. Droegemeier, C. Bischof, and T. Knauff, 1994: Sensitivity analysis of numerically-simulated convective storms using direct and adjoint methods. *Tenth Conf. on Numerical Weather Prediction*, 18-22 July 1994, Portland, Oregon, Amer. Meteor. Soc., 457-459.

Pauley, P. M., and P. J. Smith, 1988: Direct and indirect effects of latent heat release on a synoptic-scale wave system. *Mon. Wea. Rev.*, **116**, 1209-1235.

Petterssen, S., D. L. Bradbury, and K. Pedersen, 1962: The Norwegian cyclone model in relation to heat and cold sources. *Geophys. Norvegica.*, **24**, 243-280.

Petterssen S., and S. J. Smebye, 1971: On the development of extratropical cyclones. *Quart. J. R. Meteor. Soc.*, **97**, 457-482.

Rabier, F., and P. Courtier, 1992: Four-dimensional assimilation in the presence of baroclinic instability. *Quart. J. Roy. Meteor. Soc.*, **118**, 649-672.

Rabier, F., P. Courtier, and O. Talagrand, 1992: An application of adjoint models to sensitivity analysis. *Beiträge zur Physik der Atmosphäre*, **65**, 177-192.

Rabier, F., P. Courtier, J. Pailleux, O. Talagrand, and D. Vasiljevic, 1993: A comparison between four-dimensional variational assimilation and simplified sequential assimilation relying on three-dimensional variational analysis. *Quart. J. Roy. Meteor. Soc.*, **119**, 845-880.

Rabier, F., E. Klinker, P. Courtier, and A. Hollingsworth, 1996: Sensitivity of forecast errors to initial conditions. *Quart. J. Roy. Meteor. Soc.,*, **122**, 121-150.

Reed, R. J., G. A. Grell, and Y.-H. Kuo, 1993: The ERICA IOP 5 storm. Part II: Sensitivity tests and further diagnostics based on model output. *Mon. Wea. Rev.* **121**, 1595-1612.

Reed, R. J., and A. J. Simmons, 1991: Numerical simulation of an explosively deepening cyclone over the North Atlantic that was unaffected by concurrent surface energy fluxes. *Wea. Forecasting*, **6**, 117-122.

Reed, R. J., A. J. Simmons, M. D. Albright, and P. Undén, 1988: The role of latent heat release in explosive cyclogenesis: Three examples based on ECMWF operational forecasts. *Wea. Forecasting*, **3**, 217-229.

Reinhold, B., 1986: Structural determinism of linear baroclinic waves and simple nonlinear equilibrium. *J. Atmos. Sci.*, **43**, 1484-1504.

Robertson, F. R., and P. J. Smith, 1983: The impact of model moist processes on the energetics of extratropical cyclones. *Mon. Wea. Rev.*, **111**, 723-744.

Robinson, W. A., 1989: On the structure of potential vorticity in baroclinic instability. *Tellus*, **41A**, 275-284.

Roebber, P. J., 1984: Statistical analysis and updated climatology of explosive cyclones. *Mon. Wea. Rev.*, **112**, 1577-1589.

Roebber, P. J., 1989: The role of surface heat and moisture fluxes associated with large-scale ocean current meanders in maritime cyclogenesis. *Mon. Wea. Rev.*, **117**, 1676-1694.

Rogers, E., and L. F. Bosart, 1986: An investigation of explosively deepening oceanic cyclones. *Mon. Wea. Rev.*, **114**, 702-718.

Rogers, E., and L. F. Bosart, 1991: A diagnostic study of two intense oceanic cyclones. *Mon. Wea. Rev.*, **119**, 965-996.

Sanders, F., 1986: Explosive cyclogenesis in the west-central north Atlantic Ocean, 1981-1984. Part I: Composite structure and mean behavior. *Mon. Wea. Rev.*, **114**, 1781-1794.

Sanders, F., 1992: Skill of operational dynamical models in cyclone prediction out to five-days range during ERICA. *Wea. Forecasting*, **7**, 3-25.

Sanders, F., and J. R. Gyakum, 1980: Synoptic-dynamic climatology of the "bomb." *Mon. Wea. Rev.*, **108**, 1589-1606.

Sardie, J. M., and T. T. Warner, 1985: A numerical study of the development mechanism of polar lows. *Tellus*, **37A**, 460-477.

Shapiro, M., A., and D. A. Keyser, 1990: Fronts, jet streams and the tropopause. In *Extratropical Cyclones, The Erik Palmén Memorial Volume*, Eds., C. Newton and E. Holopainen, American Meteorological Society, 167-191.

Shutts, G. J., 1990: Dynamical aspects of the October storm, 1987: A study of a successful fine-mesh simulation. *Quart. J. Roy. Meteor. Soc.*, **116**, 1315-1347.

Simmons, A. J., and B. J. Hoskins, 1978: The life cycles of some nonlinear baroclinic waves. *J. Atmos. Sci.*, **35**, 414-432.

Simmons, A. J., and B. J. Hoskins, 1979: The downstream and upstream development of unstable baroclinic waves. *J. Atmos. Sci.*, **36**, 1239-1254.

Simmons, A. J., and B. J. Hoskins, 1980: Barotropic influences on the growth and decay of nonlinear baroclinic waves. *J. Atmos. Sci.*, **37**, 1679-1684.

Takayabu, I., 1991: "Coupling development": an efficient mechanism for the development of extratropical cyclones. *J. Meteor. Soc. Jap.*, **69**, 609-628.

Thépaut, J.-N., R. N. Hoffman, and P. Courtier, 1993: Interaction of dynamics and observations in a four-dimensional variational assimilation. *Mon. Wea. Rev.*, **121**, 3393-3414.

Thomson, N. R., and J. F. Sykes, 1990: Sensitivity and uncertainty analysis of a short-term sea ice motion model. *J. Geophys. Res.*, **95**, 1713-1739.

Thorncroft, C. D., B. J. Hoskins, and M. E. McIntyre, 1993: Two paradigms of baroclinic-wave life-cycle behavior. *Quart. J. Roy. Meteor. Soc.*, **119**, 17-55.

Thorpe, A. J., and M. A. Shapiro, 1995: FASTEX: Fronts and Atlantic Storm Track Experiment: The Science Plan, 25 pp. Available from FASTEX Project Office, Meteo France, 42, Avenue Gustav Coriolis, 31057 Toulouse Cedex, France.

Tracton, M. S., 1973: The role of cumulus convection in the development of extratropical cyclones. *Mon. Wea. Rev.*, **101**, 573-593.

Uccellini, L. W., 1990: Processes contributing to the rapid development of extratropical cyclones. In *Extratropical Cyclones, The Erik Palmén Memorial Volume*, Eds., C. Newton and E. Holopainen, American Meteorological Society, pp. 81-105.

Uccellini, L. W., and P. Kocin, 1987: The interaction of jet streak circulations during heavy snow events along the East Coast of the United States. *Wea. Forecasting*, **2**, 289-308.

Valdes, P. J., and B. J. Hoskins, 1988: Baroclinic instability of the zonally averaged flow with boundary layer damping. *J. Atmos. Sci.*, **45**, 1584-1593.

Verlinde, J., and W. Cotton, 1993: Fitting microphysical observations of nonsteady convective clouds to a numerical model: An application of the adjoint technique. *Mon. Wea. Rev.*, **121**, 2776-2793.

Vukićević, T., and R. M. Errico, 1993: Linearization and adjoint of parameterized moist processes. *Tellus*, **45A**, 493-510.

Vukićević, T., and K. Raeder, 1995: Use of an adjoint model for finding triggers for alpine lee cyclogenesis. *Mon. Wea. Rev.*, **123**, 800-816.

Warner, T. T., and N. L. Seaman, 1990: A real-time mesoscale numerical weather prediction system used for research, teaching and public service at the Pennsylvania State University. *Bull. Amer. Meteor. Soc.*, **71**, 792-805.

Wash, C. H., J. E. Peak, W. F. Calland, and W. A. Cook, 1988: Diagnostic study of explosive cyclogenesis during FGGE. *Mon. Wea. Rev.*, **116**, 431-451.

Whitaker, J. S., and A. Barcilon, 1992a: Type B cyclogenesis in a zonally varying flow. *J. Atmos. Sci.*, **49**, 1877-1892.

Whitaker, J. S., and A. Barcilon, 1992b: Genesis of mobile troughs in the upper westerlies. *J. Atmos. Sci.*, **49**, 2097-2107.

Whitaker, J. S., L. W. Uccellini, and K. F. Brill, 1988: A model-based diagnostic study of the rapid development phase of the Presidents' Day cyclone. *Mon. Wea. Rev.*, **116**, 2337-2365.

Zehnder, J. A., and D. Keyser, 1991: The influence of interior gradients of potential vorticity on rapid cyclogenesis. *Tellus*, **43**, 198-212.

Zou, X., I. M. Navon, and J. Sela, 1993: Variational data assimilation with moist threshold processes using the NMC spectral model. *Tellus*, **45A**, 370-387.

Županski, D., 1993: The effects of discontinuities in the Betts-Miller cumulus convection scheme on four-dimensional data assimilation. *Tellus*, **45A**, 511-524.

Županski, D., and F. Mesinger, 1995: Four-dimensional variational assimilation of precipitation data. *Mon. Wea. Rev.*, **123**, 1112-1127.

Županski, M., 1993: Regional four-dimensional variational data assimilation in a quasi-operational forecasting environment. *Mon. Wea. Rev.*, **121**, 2396-2408.

[THIS PAGE INTENTIONALLY LEFT BLANK]

198

INITIAL DISTRIBUTION LIST

<div align="right">No. of copies</div>

1. Defense Technical Information Center 2
   8725 John J. Kingman Rd., STE 0944
   Ft. Belvoir, VA 22060-6218

2. Dudley Knox Library 2
   Naval Postgraduate School
   411 Dyer Rd.
   Monterey, CA 93943-5101

3. Chairman, Code MR 1
   Department of Meteorology
   Naval Postgraduate School
   Monterey, CA 93943-5101

4. Prof. Russell L. Elsberry 1
   Department of Meteorology
   Naval Postgraduate School
   Monterey, CA 93943-5101

5. Prof. R. Terry Williams 1
   Department of Meteorology
   Naval Postgraduate School
   Monterey, CA 93943-5101

6. Prof. Carlyle H. Wash 1
   Department of Meteorology
   Naval Postgraduate School
   Monterey, CA 93943-5101

7. Prof. Wendell A. Nuss 1
   Department of Meteorology
   Naval Postgraduate School
   Monterey, CA 93943-5101

8. Prof. Roland W. Garwood 1
   Department of Oceanography
   Naval Postgraduate School
   Monterey, CA 93943-5101

9. Prof. Beny Neta 1
   Department of Mathematics
   Naval Postgraduate School
   Monterey, CA 93943-5101

10. Dr. Ronald M. Errico 1
National Center for Atmospheric Research
P.O. Box 3000
Boulder, CO 80307-3000

11. Dr. Rolf H. Langland 8
Naval Research Laboratory
Marine Meteorology Division
7 Grace Hopper Ave.
Monterey, CA 93943-5502

12. Mr. Steven W. Payne 1
Naval Research Laboratory
Marine Meteorology Division
7 Grace Hopper Ave.
Monterey, CA 93943-5502

13. Dr. Simon W. Chang 1
Naval Research Laboratory
Marine Meteorology Division
7 Grace Hopper Ave.
Monterey, CA 93943-5502

14. Dr. Ted L. Tsui 1
Naval Research Laboratory
Marine Meteorology Division
7 Grace Hopper Ave.
Monterey, CA 93943-5502

15. Dr. Richard M. Hodur 1
Naval Research Laboratory
Marine Meteorology Division
7 Grace Hopper Ave.
Monterey, CA 93943-5502

16. Dr. Eric O. Hartwig 1
Code 7000
Naval Research Laboratory
Washington, D.C. 20375-5320

17. Dr. Rao Madala 1
Code 7225
Naval Research Laboratory
Washington, D.C. 20375-5320

18. Dr. Scott Sandgathe 1
    Office of Naval Research
    800 North Quincy St.
    Arlington, VA 22217-5660

19. Dr. Alan Weinstein 1
    Office of Naval Research
    800 North Quincy St.
    Arlington, VA 22217-5660

20. Ms. J. May 1
    Library, Code 84
    Fleet Numerical Meteorology and Oceanography Center
    Monterey, CA 93943-5502

21. Naval Research Laboratory 1
    Ruth H. Hooker Research Library
    4555 Overlook Ave. S.W.
    Washington, D. C. 20375-5000

22. Naval Oceanographic Office 1
    Maury Oceanographic Library
    1002 Balch Blvd.
    Stennis Space Center MS 39522

23. National Center for Atmospheric Research 1
    Attn: Library
    P.O. Box 3000
    Boulder, CO 80307-3000

24. National Oceanic and Atmospheric Administration 1
    Central Library, 2nd floor, SS MC 3
    1315 East West Highway
    Silver Spring, MD 20910

25. Air Weather Service Technical Library 1
    859 Buchannan St.
    Scott AFB, IL 62225-5118

26. European Center for Medium-Range Weather Forecasts 1
    Attn: Library
    Shinfield Park
    Reading, Berkshire RG2 9AX, England

27. The Pennsylvania State University 1
    Physical Sciences Library
    University Park, PA 16802

28.   The Florida State University 1
        Dept. of Meteorology
        Tallahassee, FL 32306

29.   Atmospheric Environment Service 1
        Attn: Library
        4905 Dufferin St.
        Downsview, Ontario, Canada M3H 5T4

30.   Mr. Gregory D. Rohaly 1
        Naval Research Laboratory
        Marine Meteorology Division
        7 Grace Hopper Ave.
        Monterey, CA 93943-5502

31.   Dr. Ronald Gelaro 1
        Naval Research Laboratory
        Marine Meteorology Division
        7 Grace Hopper Ave.
        Monterey, CA 93943-5502

32.   Dr. Roger Daley 1
        Naval Research Laboratory
        Marine Meteorology Division
        7 Grace Hopper Ave.
        Monterey, CA 93943-5502

33.   Dr. Vivek Hardiker 1
        Naval Research Laboratory
        Marine Meteorology Division
        7 Grace Hopper Ave.
        Monterey, CA 93943-5502

34.   Dr. Ralf Geiring 1
        Max-Planck-Institut fuer Meteorologie
        Bundesstrasse 55
        20146 Hamburg
        Germany

35.   Prof. David D. Houghton 1
        Dept. of Meteorology
        University of Wisconsin
        1225 West Dayton St.
        Madison, WI 53706